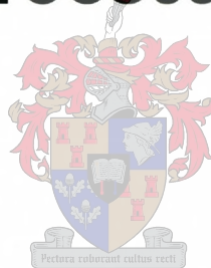


Modelling of Internal Combustion Engine Intake and Exhaust Processes



10 February 2001

C.M. van Vuuren

9204539

Modelling of Internal Combustion Engine Intake and Exhaust Processes

by

Christiaan Michael van Vuuren

Supervisors

Dr. G.D. Thiart

Dr. A.B. Taylor

Department of Mechanical Engineering

Thesis presented in partial fulfilment of the requirements
for the degree of Master of Science in Engineering at the
University of Stellenbosch

February , 2001

Declaration

I, the undersigned, hereby declare that the work contained in this thesis is my own original work and that I have not previously in its entirety or in part submitted it at any university for a degree.

Synopsis

SYNOPSIS

This thesis is concerned with unsteady, one-dimensional flow, which closely mimics those found in the manifolds of internal combustion engines. The physical equations describing problems of this nature are presented and some of the important concepts introduced. These equations and concepts were verified by comparison to published results.

The Method of Characteristics (MOC) for unsteady one-dimensional flow with friction and heat transfer was used to analyse the gas flow through the inlet and exhaust systems of an engine. The theoretical derivation of unsteady gas dynamic boundary conditions is presented and the integration with the unsteady pipe flow explained.

A simulation flow model was developed to analyse the flow by using the MOC. This flow model was then incorporated into an engine simulation program, ESA, to simulate internal combustion engines and to predict the performance of a specific engine. A cam-profile model and an in-cylinder thermodynamic model are used to complete the ESA software.

Experimental work was done on a modified Nissan Z24/NA20 engine to evaluate the simulation model. The manifolds of the Nissan Z24/NA20 were modified to isolate one of the cylinders for a proper single cylinder model. More experimental work was done on a Volkswagen 1.6ℓ 8-valve and a 1.6ℓ 20-valve engine to obtain performance data on two inlet manifolds developed using the ESA software.

Performance data and pressure traces in the inlet manifold of the Nissan Z24/NA20 were recorded for comparison with the ESA software. Good correspondence was found between tested and modelled data and the differences varied between $\pm 5\%$ on engine performance data and pressure wave frequency predictions, and $\pm 10\%$ on pressure pulse amplitudes.

OPSOMMING

Hierdie tesis handel oor bestendige, eendimensionele vloei, wat die gasvloei in spruitstukke van binnebrandenjins naboots. Die nodige vergelykings wat hierdie tipe probleme beskryf asook van die belangrikste konsepte, word bespreek. Hierdie vergelykings en konsepte is met behulp van gepubliseerde data geverifieer.

Die Metode van Karakteristieke (MVK) vir bestendige, eendimensionele vloei met wrywing en warmte oordrag, is gebruik om die gasvloei deur inlaat en uitlaat sisteme van 'n enjin te analiseer. Die teoretiese afleiding van bestendige gasdinamiese randvoorwaardes asook hul integrasie met die bestendige pypvloei, word verduidelik.

'n Simulasie vloei-model is ontwikkel om die vloei met behulp van die metode van karakteristieke te analiseer. Hierdie vloei-model is deel van 'n omvattende enjinsimulasie program, ESA. Dit word gebruik om binnebrandenjins te simuleer en enjinwerkverrigting te voorspel. 'n Nokprofiel-model en 'n termodinamiese ontbrandingsmodel word gebruik om die enjinsimulasie program af te rond.

Eksperimentele toetse op 'n gemodifiseerde Nissan Z24/NA20 enjin is gebruik om die simulasie model te evalueer. Die spruitstukke van die Nissan Z24/NA20 is aangepas om een van die silinders te isoleer om so 'n geskikte enkelsilinder-model te skep. Verdere eksperimentele toetse is gedoen op Volkswagen 1.6ℓ 8-klep en 1.6ℓ 20-klep enjins. Werkverrigtingsdata is verkry op twee nuwe inlaatspruitstukke wat met behulp van die ESA sagteware ontwerp is.

Werkverrigtingsdata en drukverdelingsdata in die inlaatspruitstuk van die Nissan Z24/NA20 is aangeteken om te vergelyk met die resultate van die ESA sagteware. Goeie ooreenstemming is verkry tussen toets- en gemoduleerde data. Die verskille varieer tussen $\pm 5\%$ op enjin werkverrigtingsdata en drukpulsfrekwensie voorspellings, en $\pm 10\%$ op drukpuls-amplitudes.

Acknowledgements

Acknowledgements

The author would like to express his gratitude to the following people and institutions:

University of Stellenbosch, for the use of their test facilities.

Dr. G.D. Thiart, for his theoretical guidance and training.

Dr. A.B. Taylor, for his technical guidance and training.

Mr. P.N.T. Williams, for his guidance and help on computer programming and software development.

Everyone at the Centre for Automotive Engineering, for their assistance on testing in the laboratory.

The product development teams at Nissan South Africa and Volkswagen South Africa for their support in the joint projects.

My family for their unconditional support and help.

Debbie, for her love and understanding.

Table of Contents

TABLE OF CONTENTS	PAGE
SYNOPSIS	i
OPSOMMING	ii
ACKNOWLEDGEMENTS	iii
TABLE OF CONTENTS	iv
NOTATION	viii
ABBREVIATIONS	xi
 CHAPTER 1: INTRODUCTION	 1-1
1.1. BACKGROUND.....	1-1
1.2. SCOPE AND OBJECTIVES.....	1-3
1.3. CLOSURE	1-4
 CHAPTER 2: UNSTEADY HOMETROPIC MOTION IN ONE-DIMENSION	 2-1
2.1. HOMETROPIC FLOW.....	2-1
2.2. THE GOVERNING EQUATIONS.....	2-1
2.3. THE CHARACTERISTIC EQUATIONS	2-2
2.4. UNIT PROCESSES	2-5
2.4.1. Finite difference grids and marching methods	2-5
2.4.2. Finite difference equations	2-7
2.4.3. Interior point	2-8
2.4.4. Solid boundary point	2-10
2.4.5. Open end point.....	2-11
2.4.6. Isentropic nozzle open end.....	2-13
2.5. COMPLEX BOUNDARY CONDITIONS	2-14
2.5.1. Inflow through an open end	2-15
2.5.2. Inflow through a nozzle	2-16
2.5.3. Reverse flow through an exhaust valve	2-17
2.5.4. Reverse flow through an inlet valve	2-17
2.6. COMPUTER SIMULATION CASE STUDIES.....	2-18
2.6.1. Case Study 1: Reservoir and pipe configuration.....	2-18
2.6.2. Case Study 2: Sudden discharge from a cylinder	2-23
2.6.3. Case Study 3: Gradual discharge from a cylinder	2-29
2.7. CLOSURE	2-33

Table of Contents

CHAPTER 3: UNSTEADY NON-HOMENTROPIC MOTION IN ONE-DIMENSION.....	3-1
3.1. NON-HOMENTROPIC FLOW.....	3-1
3.2. THE GOVERNING EQUATIONS.....	3-1
3.3. THE CHARACTERISTIC EQUATIONS.....	3-2
3.4. FANNING FRICTION FACTOR.....	3-3
3.5. HEAT TRANSFER COEFFICIENT.....	3-4
3.6. UNIT PROCESSES.....	3-4
3.6.1. Finite difference equations.....	3-4
3.6.2. Interior point.....	3-5
3.6.3. Flow through poppet valves.....	3-6
3.7. COMPUTER SIMULATION CASE STUDIES.....	3-8
3.7.1. Case Study 1: Simulation of an induction process.....	3-8
3.7.1.1. Test 1.....	3-9
3.7.1.2. Test 2.....	3-11
3.7.2. Case Study 2: Simulation of an exhaust process.....	3-13
3.7.2.1. Test 1.....	3-14
3.7.2.2. Test 2.....	3-16
3.7.2.3. Test 3.....	3-19
3.8. CLOSURE.....	3-21
CHAPTER 4: ENGINE SIMULATION AND ANALYSIS (ESA) SOFTWARE.....	4-1
4.1. MODEL OBJECTIVES.....	4-3
4.2. GENERAL ENGINE MODEL.....	4-3
4.2.1. Overview.....	4-3
4.2.2. Initial conditions, time step and grid size.....	4-4
4.2.3. Indicated output.....	4-4
4.2.4. Combustion gas properties.....	4-6
4.2.5. Cylinder combustion and volume.....	4-6
4.2.6. Heat loss.....	4-8
4.2.7. Engine friction.....	4-8
4.2.8. Flow through valves.....	4-8
4.2.9. Performance calculations.....	4-9
4.3. COMPUTER IMPLEMENTATION.....	4-10
4.3.1. Introduction.....	4-10
4.3.2. Computer hardware and installation procedure.....	4-10
4.4. CONCLUSION.....	4-11

Table of Contents

CHAPTER 5: EXPERIMENTAL VERIFICATION TESTING.....	5-1
5.1. ENGINE SET-UP	5-1
5.2. TESTING PROCEDURE.....	5-4
5.3. TEST RESULTS	5-8
5.3.1. ESA simulation setup	5-8
5.3.2. Engine performance test results.....	5-9
5.3.3. Inlet manifold pressure pulse trace results	5-11
5.4. CONCLUSION	5-18
CHAPTER 6: EXPERIMENTAL VERSATILITY TESTING	6-1
6.1. OPTIMUM INLET MANIFOLD DIMENSIONS	6-1
6.1.1. Inlet manifold length.....	6-1
6.1.2. Inlet manifold diameter.....	6-3
6.2. OPTIMUM VALVE TIMING CHARACTERISTICS.....	6-5
6.3. INLET PLENUM DESIGN	6-7
6.4. INLET TRUMPET OR DIFFUSER DESIGN.....	6-8
6.5. EXHAUST MANIFOLD DESIGN	6-10
6.6. ENGINE DESIGN USING ESA SIMULATIONS	6-10
6.6.1. FAW-VW China Jetta inlet manifold development	6-11
6.6.2. FAW-VW China Bora inlet manifold development	6-19
6.7. CONCLUSION	6-27
CHAPTER 7: CONCLUSIONS AND RECOMMENDATIONS.....	7-1
7.1. MULTI-CYLINDER BRANCH TYPE FLOW.....	7-1
7.2. OTHER COMPLEX BOUNDARY CONDITION, VOLUMES AND COMBUSTION MODELS.....	7-2
7.3. OTHER NUMERICAL SCHEMES AND SOLUTION METHODS	7-3
7.4. EXHAUST SYSTEM DESIGN.....	7-3
7.5. VALVE FRICTION MODELS	7-3
7.6. INLET VELOCITY & EXHAUST PRESSURE MEASUREMENTS	7-4
7.7. GENERAL ESA LIMITATIONS	7-5
APPENDIX A - Case Study 1: Reservoir and pipe configuration	A-1
APPENDIX B - Case Study 2: Sudden discharge from a cylinder	B-1
APPENDIX C - Case Study 3: Gradual discharge from a cylinder	C-1

Table of Contents

APPENDIX D - Case Study 1: Simulation of an induction process.....	D-1
APPENDIX E - Case Study 2: Simulation of an exhaust process	E-1
APPENDIX F - User manual for Engine Simulation and Analysis (ESA) software.....	F-1
APPENDIX G - New fuel injected inlet manifold drawings.....	G-1
APPENDIX H - Tested and modelled performance data on Nissan test engine	H-1
APPENDIX I - Tested and modelled pressure data on Nissan test engine.....	I-1
APPENDIX J - Inlet manifold prototype pictures.....	J-1
APPENDIX K - Inlet manifold pressure and velocity graphs	K-1
REFERENCES.....	Ref-1

Notation**NOTATION**

Given below are all the **Standard symbols** used in this document. Where the text deviates from this, special comment and re-definition are given.

A	Pipe cross-sectional or valve area [m^2]
B	Equation variable
b	Bore [m]
C	Characteristic line
C_d	Valve discharge coefficient
C_p	Constant pressure specific heat [J/kg K]
C_v	Constant volume specific heat [J/kg K]
c	Speed of sound [m/s]
D	Hydraulic diameter of pipe [m]
d	Diameter [m] or differential or increment
f	Fanning friction factor or function
h	Coefficient of heat transfer [$\text{W/m}^2 \text{K}$] or enthalpy [J/kg K]
k	Coefficient of conductivity [W/m K]
L	Effective pipe length [m]
L_k	Lift ratio
l	Pipe or conrod length [m]
M	Mach number or mass [kg]
m	Mass [kg]
min	Minimum
\dot{m}	Mass flow [kg/s]
N	Engine speed [rpm]
Nu	Nusselt number
P	Stagnation pressure [Pa] or power [kW]
P_w	Power [kW]
Pr	Prandtl number
p	Pressure or static pressure [Pa]
Q	Equation variable or heat transfer [kJ/s]
q	Heat transfer [kJ/s]
R	Universal gas constant [J/kg K] or ratio

Notation

R_e	Reynolds number
R_p	Pressure ratio
rev	<i>Revolution</i>
S	Equation variable
s	Entropy [kJ/ kg K] or stroke [m]
T	Temperature [°C] or equation variable or torque [Nm]
T_q	Torque [Nm]
t	Time [s]
u	Velocity [m/s]
V	Volume [m ³]
W	Total Work [W]
x	Distance [m]

Greek symbols

β	Friction equation variable
Δ	Increment
ϕ	Area ratio of valve to port or fuel/air equivalence ratio
∂	Partial differential
γ	Ratio of specific heats; C_p/C_v
η	Efficiency [%]
λ_{\pm}	Slope of the Mach lines
λ_o	Slope of the pathline
μ	Dynamic viscosity [kg/m s]
θ	Crank angle [°]
θ_b	Burn angle [°]
θ_s	Spark angle [°]
ω	Angular velocity [rad/s]
ρ	Density [kg/m ³]

Superscript

*	Pressure variable
---	-------------------

Subscripts

a	Atmospheric conditions or condition at a specified point
-----	--

Notation

<i>amb</i>	Ambient conditions
<i>atm</i>	Atmospheric conditions
<i>b</i>	Condition at a specified point or burned properties
<i>c</i>	Conditions at cylinder
<i>cr</i>	Critical value or state
<i>cyl</i>	Conditions at cylinder
<i>d</i>	Displacement
<i>e</i>	Conditions at valve entrance or exit
<i>f</i>	Fuel
<i>g</i>	Gas in pipe
<i>i</i>	Grid point
<i>in</i>	In flowing
<i>is</i>	Isentropic conditions
<i>max</i>	Maximum
<i>mech</i>	Mechanical efficiency
<i>min</i>	Minimum
<i>o</i>	Pathline
<i>pipe</i>	Conditions in pipe
<i>r</i>	Stagnation conditions
<i>resv</i>	Reservoir conditions
<i>t</i>	Partial differential to time or conditions at valve throat
<i>te</i>	Effective throat area
<i>u</i>	Unburned properties
<i>vol</i>	Volumetric efficiency
<i>w</i>	Pipe wall
<i>x</i>	Partial differential with respect to distance
<i>+</i>	Right-running Mach line
<i>–</i>	Left-running Mach line
<i>±</i>	Right- and left-running Mach lines

Abbreviations**ABBREVIATIONS**

AF	Air/Fuel Ratio
ABDC	After Bottom Dead Centre
ATDC	After Top Dead Centre
BBDC	Before Bottom Dead Centre
BTDC	Before Top Dead Centre
BMEP	Break Mean Effective Pressure [Pa]
CA	Crank Angle
CFD	Computational Fluid Dynamics
CFL	Courant-Friedrichs-Lewy
CR	Compression Ratio
Displ	Displacement
ESA	Engine Simulation and Analysis
EVC	Exhaust Valve Closes [°CA BTDC]
EVO	Exhaust Valve Opens [°CA BBDC]
IC	Internal Combustion
IMEP	Indicated Mean Effective Pressure [Pa]
IVC	Inlet Valve Closes [°CA ATDC]
IVO	Inlet Valve Opens [°CA ABDC]
MEP	Mean Effective Pressure [Pa]
MOC	Method of Characteristics
SFC	Specific Fuel Consumption [g/kW.hr]

CHAPTER 1: INTRODUCTION

1.1. BACKGROUND

Internal-combustion engines are classified according to the cycle of operations, two- or four-stroke cycle, and their respective modes of combustion, petrol or diesel [1, 2, 3, 4]. The cycle of operations can be subdivided into the gas exchange process, where the products of combustion are exhausted and replaced by a fresh charge of air/fuel mixture, and the power process, where the air/fuel mixture is compressed, ignited and the hot gas expanded to produce useful work. In thermodynamic terms, during the gas exchange process the cylinder is an open system and during the power process it is a closed system.

In the four-stroke cycle engine the gas exchange process is caused by the pumping action of the piston motion, although there may also be interactions with the intake and exhaust system. It is convenient to analyse the mode of operations commencing with the gas exchange process followed by the power process [4].

The flow paths in the manifolds and past the valves of internal combustion engines are extremely complex. If the flow is analysed in two or three dimensions, complex simulation models such as the CFD packages STAR-CD [5] and PowerFLOW [6] must be used (these models need a great deal of computing power and is best served running on a main frame computer). The flow paths are often simplified by considering the flow to be one-dimensional [4, 7]. In one-dimensional flow, pulsation, pressures, velocities and temperatures in manifolds and past valves can still be accurately predicted. In general, the gas is highly turbulent and fluid frictional forces are present within the fluid and at the walls. In simple analyses, the fluid is assumed to be inviscid and wall friction is allowed for by use of a friction factor [4, 8, 9]. Furthermore, the gas is taken to be perfect for the examination of many flow processes and the fluid properties are assumed to be uniform over each cross-sectional area of the passage. For this the perfect gas law, $P = \rho R t$ applies, where R and c_p are taken to be constant.

Chapter 1: Introduction

The gas flow in internal combustion engines is non-steady and changes in the fluid properties take place in space and time. The understanding of the gas flow through an internal combustion engine is essential for the development of intake and exhaust systems for modern internal combustion engines. A measure of the quality of gas flow through an engine is the volumetric efficiency [1, 2, 3, 4]. Volumetric efficiency is defined as the mass of air and fuel inducted into the cylinder, divided by the mass that would occupy the displaced volume at a density equalling that in the plenum chamber or the atmospheric density [1, 2, 3, 4]. The volumetric efficiency of a specific engine is heavily influenced by the manifold design, porting and the camshaft characteristics of the engine. It is therefore important to design and develop inlet- and exhaust manifolds that will enhance airflow through the engine to get optimal volumetric efficiency; obtaining maximum mean effective pressure and peak performance [4, 8].

As early as the 1950's engineers were trying to simulate internal combustion engine processes [4, 9]. Simulation started on the in-cylinder processes to investigate energy released by fuel, energy lost, engine work and other in-cylinder characteristics [9]. Engineers then realised that the amount of energy entering the cylinder (fuel) and the energy leaving the cylinder (hot gas) were controlled by the flow phenomena of the intake and exhaust processes. They first used graphical methods to simulate the intake and exhaust processes by means of the MOC, which is a marching type solution method applicable to quasi-linear partial differential equations [10, 11].

Later, computers were used to simulate and solve this complex flow type [8, 9]. Engineers started to develop computer software packages such as SPICE II (Simulation Program for Internal Combustion Engines) [12] and DYNOMATION [13] to simulate internal combustion engine processes to assist in the design of engines. SPICE II is a software package that was originally developed for use with compression ignition or diesel engines. It also has the capability to simulate petrol engines, but with reduced success and accuracy. The one important disadvantage of SPICE II is that it does not consider pressure pulses in the intake and exhaust manifolds and only uses square box volumes to simulate pipes. DYNOMATION was developed exclusively for spark ignition or petrol engines. It

Chapter 1: Introduction

does consider pressure pulse flow in the manifolds using a simple pulse tracking method, but shortcomings in the in-cylinder model also makes this software package unreliable. Neither of the two software packages can therefore be used to simulate IC engines with a high degree of accuracy and reliability.

At the University of Stellenbosch an in-cylinder computer model, consisting of a single-zone combustion model, was developed by Williams [14]. Unfortunately this model is lacking in the following departments: (1) the single-zone combustion model is an idealised combustion model and a better two-zone combustion model [15] had to be implemented and (2) no simulation model existed to simulate the unsteady flow processes in the intake and exhaust systems.

1.2. SCOPE AND OBJECTIVES

The main objectives that were envisaged for this thesis:

- Construct and verify a computer simulation model that implements the MOC and the necessary boundary conditions.
- Verify the computer model by doing simple theoretical case studies and comparing the numerical computer results with published data.
- Develop a full engine simulation model, based on the MOC, and containing the following:
 - A two-zone in-cylinder thermodynamic model providing pressures and temperatures during compression, combustion and expansion developed by Williams [15].
 - A dynamic model of valve train response to an input cam profile, providing valve lift profiles at various speeds developed by Williams [14, 15].
 - An empirical valve and port flow loss model developed by Williams [14, 15].
 - A computational fluid dynamics flow model, simulating the gas flow in the inlet and exhaust manifolds and past the valves, using the MOC. This model allows calculation of the amount of gas and fuel mixture transferred in and out of the cylinder during induction, exhaust and valve overlap.

Chapter 1: Introduction

- Do experimental work to provide actual flow data: pressures and velocities. A modified Nissan Z24/NA20 engine was available for this purpose.
- Do experimental work to provide engine performance data. Two Volkswagen engines, a 1.6ℓ 8-valve and a 1.6ℓ 20-valve were available for this purpose.
- Compare computer simulation data with experimental data to test the reliability and accuracy of the simulation program.
- Make recommendations on the use and accuracy of the engine simulation software.

The computer model must be capable of simulating the following aspects of engine operation:

- Pressure pulses
- Flow velocities
- Mass transfer through inlet and exhaust valves
- Intake and exhaust manifold length changes
- Intake and exhaust manifold flow area changes
- Different intake and exhaust camshaft timings
- Different intake and exhaust camshaft profiles
- Different intake and exhaust valve diameters
- Different intake and exhaust valve lifts
- Different plenum and exhaust back pressures and temperatures

The effects on IMEP, SFC, power, torque and volumetric efficiency can then be investigated. By means of all these tests a certain engine could be “fine tuned” to achieve the prescribed optimum performance.

1.3. CLOSURE

In chapter 2 a detailed study of unsteady one-dimensional homentropic flow and the implementation of the MOC are presented. A detailed explanation of all the relevant boundary conditions in an internal combustion engine is also given in this chapter, as well as a few computer case studies and the numerical results for homentropic flow. A detailed discussion on one-dimensional non-

Chapter 1: Introduction

homentropic flow and the influence it has on the homentropic flow data is presented in chapter 3. More computer case studies and the numerical results are presented in this chapter. In chapter 4 the computer software and the integration of the CFD model with the other simulation models are discussed. In chapter 5 all the experimental work and tests done on the Nissan Z24/NA20 are presented and the simulation results are compared with the experimental results. In chapter 6 the performance tests done on the two Volkswagen engines are discussed and the comparative computer simulation results are presented. The final conclusion and recommendations for future work are presented in chapter 7.

CHAPTER 2: UNSTEADY HOMENTROPIC MOTION IN ONE-DIMENSION

In this chapter unsteady one-dimensional flow in which large amplitude changes in the properties of the gas occur, is discussed. This flow phenomenon is usually found in the flow systems of internal combustion engines [2, 4]. The governing equations for unsteady one-dimensional homentropic flow and quasi-one-dimensional homentropic flow of a compressible fluid are presented as well as the corresponding characteristic and compatibility equations. Numerical algorithms are presented for applying the characteristic and compatibility equations to several unit processes and boundary conditions that occur commonly in unsteady flow [4, 10, 11]. Case studies are presented to illustrate the application of these unit processes to several unsteady one-dimensional flow problems.

2.1. HOMENTROPIC FLOW

A special case of generalised flow is homentropic flow [4, 10, 11]. In homentropic flow the entropy level remains constant throughout the flow field [18]. For homentropic flow, all the other properties of the fluid can change with respect to distance and time. Homentropic flow implies no friction, no heat transfer and no mass addition to the system [10]. The idealisation to homentropic flow is an advantage in inlet and exhaust systems, because it saves computer computing time when only the total entropy of the system has to be calculated and not the entropy at every grid point and time step.

2.2. THE GOVERNING EQUATIONS

A truly one-dimensional flow is one where the flow properties depend only on one space co-ordinate, x , and the time, t . Consequently, the pathlines of the fluid particles are straight lines. Flow in a duct having a slowly varying cross-section where the hydraulic diameter is small compared to the radius of curvature of the axis of the duct, is termed quasi-one-dimensional flow. The flow area is therefore a function of x and t [10].

Chapter 2: Unsteady Homentropic Motion in One-Dimension

The governing equations for unsteady quasi-one-dimensional homentropic flow are as follows [4, 10, 18]:

Continuity equation:

$$\rho_t + u\rho_x + \rho u_x + \frac{\rho u}{A} \frac{dA}{dx} = 0 \quad (2.1)$$

Momentum equation:

$$u_t + uu_x + \frac{1}{\rho} p_x = 0 \quad (2.2)$$

Energy equation:

$$\rho_t + u\rho_x - c^2(\rho_t + u\rho_x) = 0 \quad (2.3)$$

Entropy equation:

$$s_t + us_x = 0 \quad (2.4)$$

Equation of state:

$$p = \rho RT \quad (2.5)$$

Speed of sound equation (for an isentropic process):

$$c^2 = \frac{\gamma p}{\rho} \quad (2.6)$$

The only difference between unsteady one-dimensional flow and unsteady quasi-one-dimensional flow is in the continuity equation where the area variation term, $\frac{\rho u}{A} A_x$, disappears for unsteady one-dimensional flow. The other three governing equations are the same for both cases. Unsteady quasi-one-dimensional flow will be considered in this section.

2.3. THE CHARACTERISTIC EQUATIONS

The following so-called characteristic equations can be obtained from the governing equations [7, 10, 11]:

$$\left(\frac{dt}{dx} \right)_o = \lambda_o = \frac{1}{u} \quad (2.7)$$

$$\left(\frac{dt}{dx} \right)_\pm = \lambda_\pm = \frac{1}{u \pm c} \quad (2.8)$$

Chapter 2: Unsteady Homentropic Motion in One-Dimension

These characteristic equations describe characteristic lines, which are the curves along which information of the changes of properties of the flow are transmitted, due to a disturbance in the flowing gas.

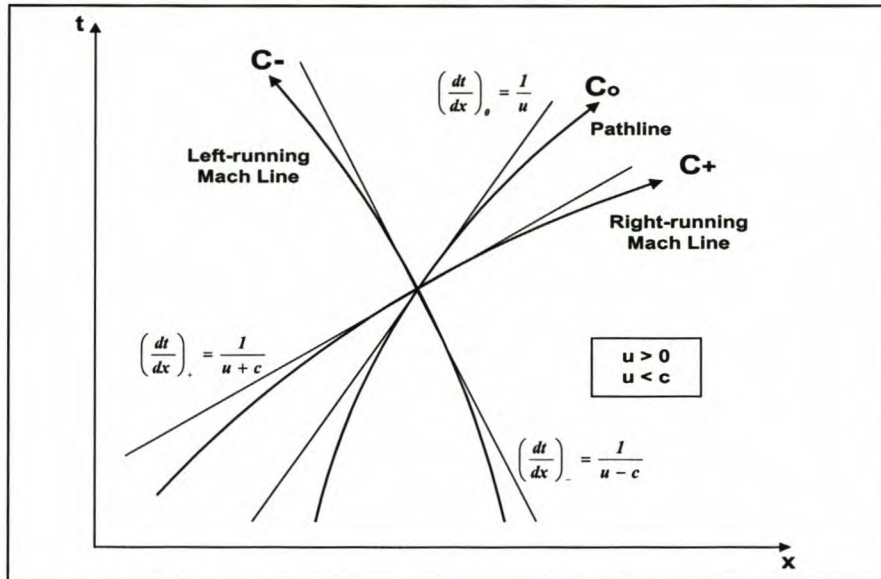


Figure 2-1: Characteristics for unsteady one-dimensional flow [subsonic flow from left to right]

Figure 2-1 illustrates schematically the characteristics in the xt -plane (that is the physical plane) for subsonic flow in the positive x -direction.

One of the properties of a characteristic curve is that it defines the path along which information is propagated through a flow field. Along the C_+ and C_- characteristics, the speed of propagation is given by equation (2.8). The propagation speeds along the C_+ and C_- characteristics are equal to the speed of sound relative to the moving fluid. In this regard, the C_{\pm} characteristics in unsteady flow are analogous to the Mach lines in steady flow, and are called the Mach lines of the unsteady flow [10].

In an unsteady one-dimensional or quasi-one-dimensional flow, three characteristic curves pass through each point of the flow field: the pathline C_0 and the right- and left-running Mach lines C_{\pm} , illustrated in Figure 2-1. Physically it implies that C_+ and C_- are the propagation paths of disturbances and that C_0 is the path of a fluid particle with respect to time.

Four possible cases are illustrated in Figures 2-1 to 2-4, depending on whether u is positive or negative and whether $|u|$ is less than or greater than the local

Chapter 2: Unsteady Homentropic Motion in One-Dimension

speed of sound c , that is whether the flow is subsonic or supersonic [10]. Although all the characteristics exist [10] for $|u| > c$ and $|u| < c$, only the case for $|u| < c$, i.e. subsonic flow, is of importance for this thesis, because the flow is always subsonic in the inlet and exhaust systems of engines [4].

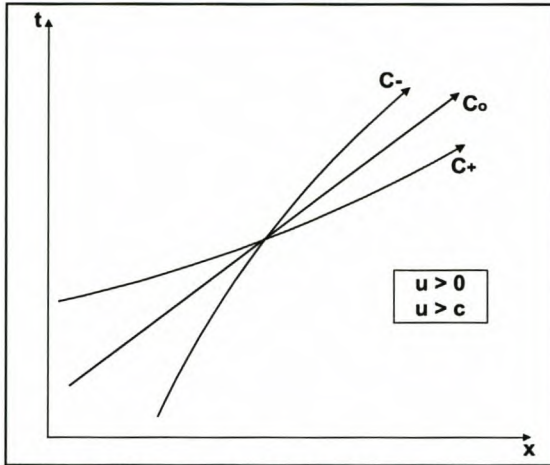


Figure 2-2: Supersonic flow from left to right

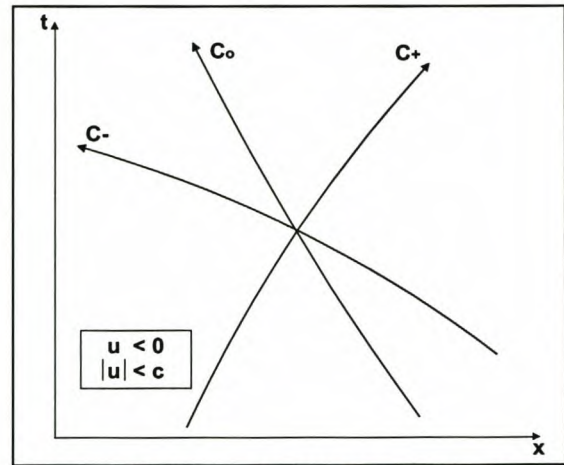


Figure 2-3: Subsonic flow from right to left

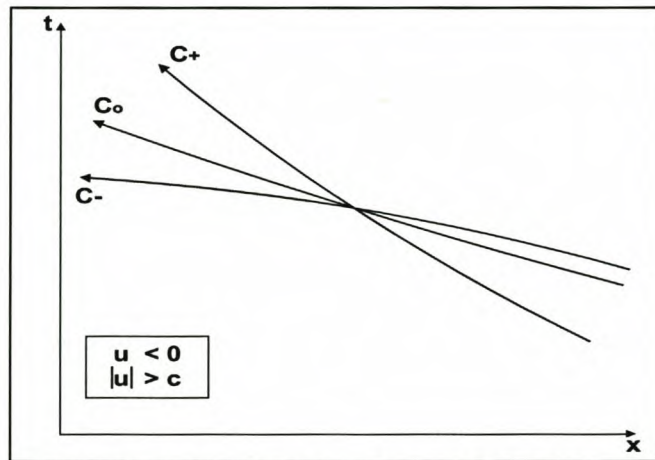


Figure 2-4: Supersonic flow from right to left

The so-called compatibility equations, which are basically alternative versions of the governing equations, are valid along the characteristic curves, and are given by Shapiro [7]:

$$dp_0 - c^2 dp_0 = 0 \quad (2.9)$$

$$dp_{\pm} = \mp(\rho c) du_{\pm} - \frac{u \rho c^2}{A} \left(\frac{dA}{dx} \right) dt_{\pm} \quad (2.10)$$

Equation (2.9) is applicable along the pathline and expresses the change in density, dp_0 , along an infinitesimal section of the pathline, dx , if the corresponding change in pressure is equal to dp_0 . The density also depends on

Chapter 2: Unsteady Homentropic Motion in One-Dimension

the speed of sound, which is a function of p and ρ (equation of state). Equation (2.10) is applicable along the C_{\pm} characteristics and expresses the change in pressure, dp_{\pm} , along an infinitesimal section of the pathline, dx , if the corresponding change in velocity is equal to du_{\pm} in a time step dt_{\pm} . The pressure also depends on the speed of sound, density and change in cross sectional area at the characteristic. Since each of the compatibility equations describes the conservation of fluid properties and is written in terms of differentials, the intersection of the characteristics implies that these equations are all valid at the same point. The three compatibility equations may therefore be solved simultaneously at the point of intersection for the flow properties u , p and ρ at that point, if the flow properties are known at "previous" points on the characteristics.

2.4. UNIT PROCESSES

In this section the numerical approach to solve a problem with the characteristic and compatibility equations, called a unit process, is discussed. Unit processes are developed for determining the flow properties for the following types of points:

- a) A point interior to the flow field termed an *interior point*.
- b) A point on a solid boundary termed a *solid boundary point*.
- c) A point at an open end termed an *open end point*.
- d) Subsonic outflow through an isentropic nozzle termed a *nozzle point*.

2.4.1. Finite difference grids and marching methods

The governing equations may be integrated by a marching type of numerical method, such as the method of characteristics. The application of this numerical method requires the development of numerical algorithms that are appropriate to the problem under consideration [10].

It was shown in Section 2.3 (Figures 2-1 to 2-4) that three characteristics pass through every point in the xt -plane: the pathline C_0 and a right- and left-running Mach lines, C_+ and C_- , respectively. In numerical algorithms for applying the MOC, the characteristics are approximated by means of straight-line segments, as illustrated in Figure 2-5.

Chapter 2: Unsteady Homentropic Motion in One-Dimension

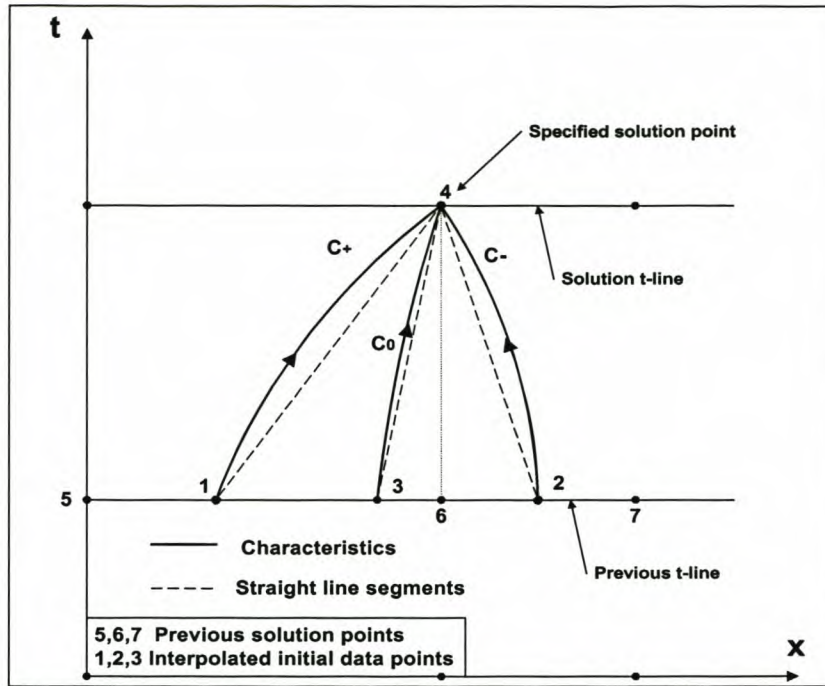


Figure 2-5: Straight-line segments for an interior point

There are two different methods for proceeding (marching) through a flow field with a numerical algorithm: the *direct marching method* and the *inverse marching method* [10]. In this thesis the *inverse marching method* is used, because the method uses a constant grid size and progressive stepping through time which makes it easier to implement into a computer simulation model [9, 18].

In this method the locations of the solution points, such as point 4 in Figure 2-5, are specified a priori. The three characteristics intersecting at point 4 are extended rearward to intersect a line on which initial-data points from previous calculations are located. In the study of unsteady flow, it is advantageous to determine the flow properties at pre-specified points located on lines of constant time, termed *t-lines*.

Calculation of the flow properties at the initial-data points (points 1, 2 and 3 in Figure 2-5) requires interpolation employing previous solution points (points 5, 6 and 7 in Figure 2-5). The interpolation reduces the accuracy of the results obtainable by the numerical algorithm. Furthermore, to ensure that the solution is stable, the Courant-Friedrichs-Lewy (CFL) stability criterion must be satisfied [4, 7, 10]. The criterion requires that the initial data points (points 1, 2 and 3) fall between the previous solution points (points 5, 6 and 7) that are employed in the interpolation for determining the flow properties at points 1, 2 and 3.

Chapter 2: Unsteady Homentropic Motion in One-Dimension

To satisfy the CFL-criterion, the recommended time step must be less than or equal to

$$\Delta t_{\min} = \min \left[\frac{\Delta x_i}{(|u_i| + c_i)} \right] \quad (2.11)$$

The subscript, i , is for the grid points. The largest velocity ($|u_i| \leq c_i$) and sonic velocity will result in the smallest time step.

2.4.2. Finite difference equations

The numerical procedure for solving an unsteady one-dimensional flow problem is similar to solving a steady two-dimensional supersonic irrotational flow problem [10, 11]. To illustrate the construction of the numerical algorithms for the unit processes listed in Section 2.4, the inverse marching method illustrated in Figure 2-5 is employed.

The finite difference equations corresponding to the characteristic and compatibility equations presented in Section 2.3 are presented in Table 2-1.

Table 2-1: Finite difference equations for unsteady one-dimensional and quasi-one-dimensional flow

$\Delta t_0 = \lambda_0 \Delta x_0$	(pathline)	(2.12)
$\lambda_0 = \frac{1}{u_0}$		(2.13)
$\Delta p_0 - B_0 \Delta \rho_0 = 0$	(along a pathline)	(2.14)
$B_0 = c^2$		(2.15)
$\Delta t_{\pm} = \lambda_{\pm} \Delta x_{\pm}$	(Mach lines)	(2.16)
$\lambda_{\pm} = \frac{1}{u_{\pm} \pm c_{\pm}}$		(2.17)
$\Delta p_{\pm} \pm Q_{\pm} \Delta u_{\pm} = S_{\pm} \Delta t_{\pm}$	(along a Mach line)	(2.18)
$Q_{\pm} = \rho c$		(2.19)
$S_{\pm} = -\frac{u \rho c^2}{A} \left(\frac{dA}{dx} \right)$		(2.20)

Chapter 2: Unsteady Homentropic Motion in One-Dimension

The finite time step Δt is calculated so that the intersections of the rearward projected Mach lines 1-4 and 2-4 lie between the previous solution points (points 5 and 7). These points are to be employed in interpolating for the value of the flow properties at the initial-data points: points 1, 2 and 3. The size of the time step Δt to the solution t -line is calculated by means of the CFL-criterion so that it corresponds to the smallest value of Δt for all of the solution points located on the previous t -line.

The numerical algorithms for applying equations (2.12) to (2.20) of Table 2-1 are based on the *Modified Euler Predictor-Corrector* method discussed in [10, 20]. In the predictor step, all of the coefficients in the finite difference equations are calculated at the known initial-data points. The corrector step employs the average values of the three primary dependent variables u , p and ρ for each characteristic curve. The coefficients of the finite difference equations are calculated for the aforementioned average values of the flow properties. Hence, the resulting numerical algorithms are average property algorithms.

2.4.3. Interior point

Figure 2-5 illustrates schematically, in the xt - plane, the finite difference grid for determining the location and properties of point 4, an interior point.

The locations of the initial-data points 1, 2 and 3 are determined by writing equations (2.12) and (2.16) in finite difference form in terms of values at points 1, 2, 3 and 4. Thus,

$$\Delta t_0 = \lambda_0(x_4 - x_3) \quad (2.21)$$

$$\Delta t_+ = \lambda_+(x_4 - x_1) \quad (2.22)$$

$$\Delta t_- = \lambda_-(x_4 - x_2) \quad (2.23)$$

where $\Delta t = \Delta t_0 = \Delta t_+ = \Delta t_-$ for the inverse marching finite difference grid. Since Δt and x_4 are known, equations (2.21) to (2.23) may be solved simultaneously for x_1 , x_2 and x_3 , if λ_0 , λ_+ and λ_- are known. The properties u , p and ρ at points 1, 2 and 3 are then obtained by linear interpolation.

Chapter 2: Unsteady Homentropic Motion in One-Dimension

The slopes λ_0 , λ_+ and λ_- are given by equations (2.12) and (2.16). Since they are not known, they must be determined iteratively. For the Euler *predictor*, the initial estimates for the slopes are calculated using the following approximation:

$$\lambda_0 = \frac{1}{u_6} \quad \lambda_+ = \frac{1}{u_5 + c_5} \quad \lambda_- = \frac{1}{u_7 - c_7} \quad (2.24)$$

Equations (2.21) and (2.23) may then be solved for x_1 , x_2 and x_3 , and the corresponding values of u , p and ρ at those points may be determined by linear interpolations. Then,

$$\lambda_0 = \frac{1}{u_3} \quad \lambda_+ = \frac{1}{u_1 + c_1} \quad \lambda_- = \frac{1}{u_2 - c_2} \quad (2.25)$$

The procedure may be repeated to obtain improved values, of x_1 , x_2 and x_3 and the corresponding values of u , p and ρ . The procedure is repeated until the values of x_1 , x_2 and x_3 change by less than a specified tolerance between iterations.

The compatibility equations, which is valid along the Mach lines (2.18), can be expressed in finite difference form in terms of values at points 1, 2 and 4.

Thus,

$$p_4 + Q_+ u_4 = T_+ \quad (2.26)$$

$$p_4 - Q_- u_4 = T_- \quad (2.27)$$

where

$$T_+ = S_+ \Delta t + p_1 + Q_+ u_1 \quad (2.28)$$

$$T_- = S_- \Delta t + p_2 - Q_- u_2 \quad (2.29)$$

For the Euler *predictor*

$$Q_+ = \rho_1 c_1 \quad S_+ = -\frac{u_1 \rho_1 c_1^2}{A_1} \left(\frac{dA}{dx} \right)_1 \quad (2.30)$$

$$Q_- = \rho_2 c_2 \quad S_- = -\frac{u_2 \rho_2 c_2^2}{A_2} \left(\frac{dA}{dx} \right)_2 \quad (2.31)$$

Equations (2.26) and (2.27) are solved for p_4 and u_4 . The compatibility equation which is valid along pathlines (2.14), expressed in finite difference form in terms of values at points 3 and 4, yields

$$p_4 - B_0 p_4 = T_0 \quad (2.32)$$

Chapter 2: Unsteady Homentropic Motion in One-Dimension

where

$$T_0 = p_3 - B_0 \rho_3 \quad (2.33)$$

For the Euler *predictor*

$$B_0 = c_3^2 \quad (2.34)$$

Equation (2.32) is now solved for ρ_4 .

The steps presented above are repeated according to the Euler corrector algorithm, to furnish corrected values for the flow properties at point 4. The coefficients of the compatibility equations presented in Table 2-1 are determined by applying the Euler *corrector* algorithm employing average values of u , p and ρ along each characteristic.

Thus,

$$\lambda_0 = \frac{1}{u_0} \quad \lambda_+ = \frac{1}{u_+ + c_+} \quad \lambda_- = \frac{1}{u_- - c_-} \quad (2.35)$$

where

$$u_0 = \frac{u_3 + u_4}{2} \quad u_+ = \frac{u_1 + u_4}{2} \quad u_- = \frac{u_2 + u_4}{2} \quad (2.36)$$

From Benson [4]

$$c_+ = c(p_+, \rho_+) \quad c_- = c(p_-, \rho_-) \quad (2.37)$$

where

$$\rho_+ = \frac{\rho_1 + \rho_4}{2} \quad \rho_- = \frac{\rho_2 + \rho_4}{2} \quad p_+ = \frac{p_1 + p_4}{2} \quad p_- = \frac{p_2 + p_4}{2} \quad (2.38)$$

The coefficients Q_+ , Q_- , S_+ , S_- , T_+ , T_- and B_0 are determined in a similar manner. The corrector may be applied only once, or iterated to achieve a specified convergence tolerance.

2.4.4. Solid boundary point

The unit process for a solid boundary point is applicable at the closed end of a flow passage, such as a closed valve, and at the surface of a moving solid object, such as a piston. In this thesis only the stationary solid boundary will be used. Figure 2-6 illustrates the case where the solid boundary is stationary and located at the left-hand side of the flow field [4]. An analogous unit process may be developed when the closed end of the duct is on the right-hand side of the flow field.

Chapter 2: Unsteady Homentropic Motion in One-Dimension

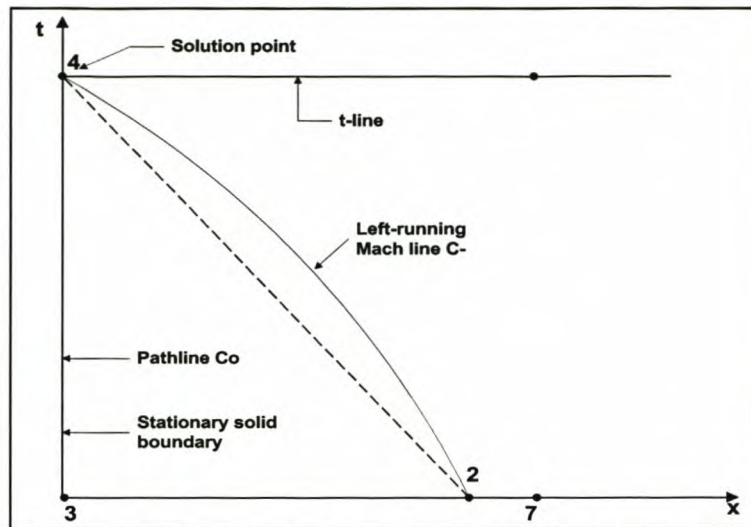


Figure 2-6: Unit process for a stationary solid boundary

For the stationary boundary illustrated in Figure 2-6 the location of x_4 of the solution point is known and at x_4 the fluid velocity is $u_4 = 0$. The pathline 3-4 corresponds to the path on the boundary. A stationary boundary is a special case of a moving boundary for which x_4 is fixed and $u_4 = 0$. The pressure p_4 and density ρ_4 are determined from the compatibility equations, (2.27) and (2.32).

Values at points 2 and 4 are determined from the characteristic equations, (2.21) and (2.23), by applying the Euler predictor method as explained in Section 2.4.3 for an interior point. The values of p_4 and ρ_4 are obtained by applying the Euler predictor method, but may be improved by applying the Euler corrector method.

2.4.5. Open end point

The unit process for determining the flow properties at the open end of a duct is more complicated than that for the closed end. At an open end, the flow may be either an inflow or an outflow. The general features of wave interaction at the open end of a duct are discussed in Benson [4]. Figure 2-7 illustrates the unit process for an open end point with outflow at the right-hand side of the internal flow field. An analogous unit process may be developed when the open end of the duct is on the left-hand side of the internal flow field.

The unsteady two- and three-dimensional external flow field, surrounding the exit plane of the duct, determines the boundary condition at the open end. As discussed in Benson [4], for subsonic outflow, a reasonable approximation may be obtained by assuming that the pressure p_4 at the open end is equal to the

Chapter 2: Unsteady Homentropic Motion in One-Dimension

ambient or exit pressure. Figure 2-7 illustrates the unit process for an open end with subsonic outflow. The boundary condition imposed on the internal flow is that the static pressure $p_4 = p_{amb}$. When the details of the external flow field must be considered, their overall effect on the open-end boundary condition is still expressed by specifying the pressure p_4 that the external flow field presents to the internal flow. In that case, however, the determination of p_4 requires obtaining the solution of the unsteady two- or three-dimensional external flow field. Consequently, it may be assumed that the boundary condition for an open end with subsonic outflow is that p_4 is known.

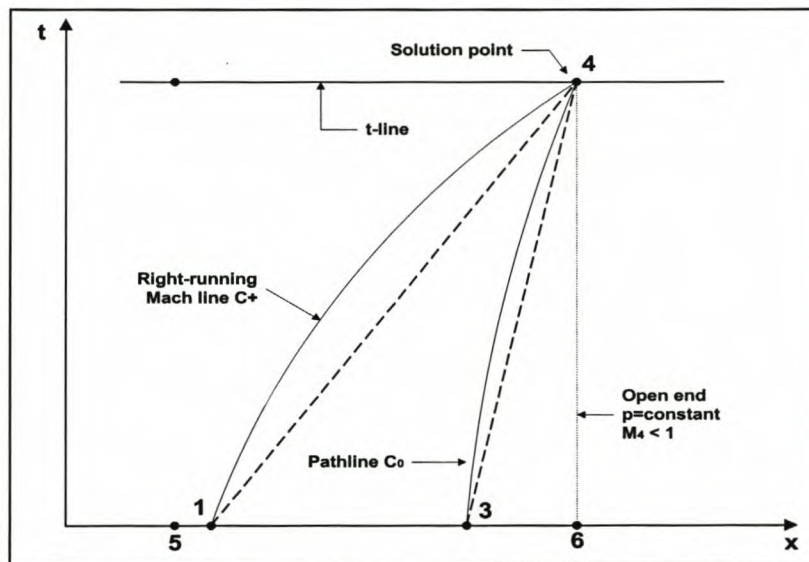


Figure 2-7: Unit process for subsonic outflow at an open end

For subsonic outflow, x_4 and p_4 are specified. Points 1 and 3, in Figure 2-7, are located by applying the characteristic equations, (2.21) and (2.22), employing the Euler predictor method presented in Section 2.4.3. At point 4, u_4 and p_4 are determined from the corresponding compatibility equations, (2.25) and (2.31). Improved values for the properties at point 4 may be obtained by the repetitive application of this past procedure.

Figure 2-8 illustrates the unit process for inflow at an open end point. In the case of subsonic inflow only a single characteristic, the right-running Mach line C_+ , reaches point 4 from inside the flow passage. Consequently, two boundary conditions must be specified from the external flow field [17]. This more complex type of boundary will be discussed in Section 2.5.

Chapter 2: Unsteady Homentropic Motion in One-Dimension

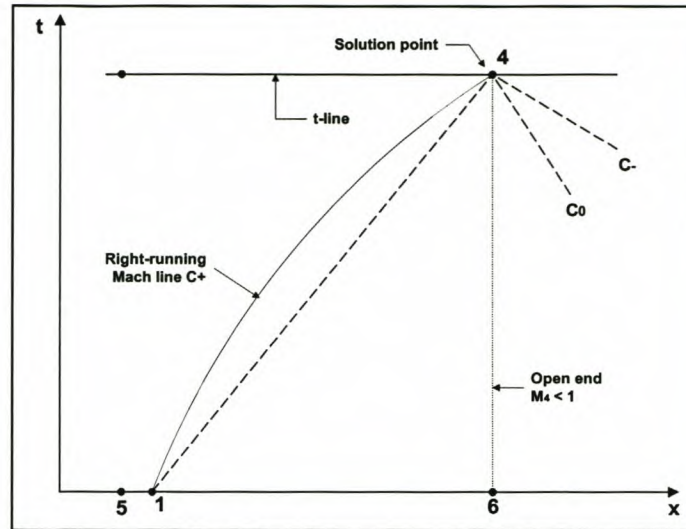


Figure 2-8: Subsonic inflow at an open end

2.4.6. Isentropic nozzle open end

Figure 2-9 illustrates diagrammatically the flow model for a duct having an outflow of gas through a short converging nozzle (typical to an inlet valve of an internal combustion engine).

The flow in the nozzle may be considered to be quasi-steady. If the flow is also inviscid and adiabatic, it is isentropic. The assumption that the flow is quasi-steady, one-dimensional and isentropic means that the instantaneous values of the stagnation properties of the gas flowing in the nozzle are equal to those at the nozzle entrance plane. Hence, the flow properties at the nozzle entrance plane, e , can be related to those at the nozzle throat, t [4, 10], for both perfect and imperfect gases. The boundary conditions at the nozzle throat plane are that $p_t \geq p_{amb}$. If $M_t < 1$, then $p_t = p_{amb}$. If $M_t = 1$ then $p_t = p^* \geq p_{amb}$. These are the steady-state boundary conditions discussed in Zucrow [10] with outflow at the nozzle.

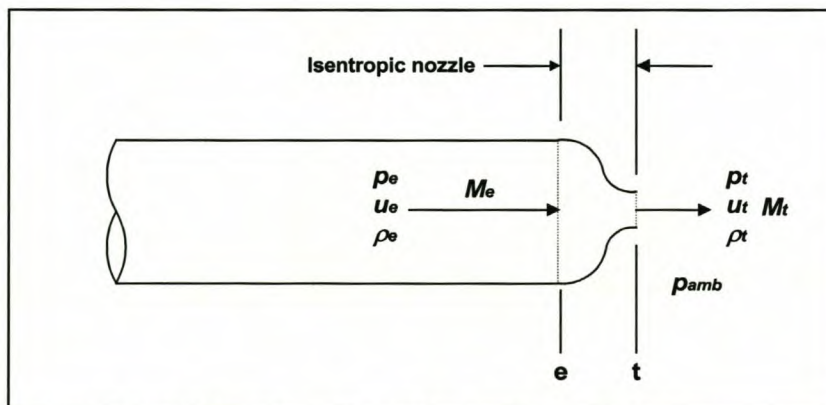


Figure 2-9: Outflow through an isentropic nozzle

Chapter 2: Unsteady Homentropic Motion in One-Dimension

The unit process for subsonic outflow through an isentropic nozzle is therefore analogous to the unit process for subsonic outflow through the open end of a duct, discussed in Section 2.4.5. There is, however, the modification that p_e is determined by the quasi-steady properties of the nozzle.

There are two possible flow cases in the nozzle. The flow in the nozzle can be either sonic or subsonic. This is determined by the pressure ratio, between the throat and entrance to the nozzle, and the area ratio of the nozzle. Equation (2.39) gives the relationship of the critical pressure ratio and the area ratio ϕ . The equation is solved by iterative techniques, such as Newton-Raphson [20].

$$\phi^2 \left[\frac{\gamma-1}{\gamma+1} \left(\frac{P_t}{P_e} \right)_{cr}^{\frac{2}{\gamma}} \right] + \frac{2}{\gamma+1} \left(\frac{P_t}{P_e} \right)_{cr}^{\frac{1-\gamma}{\gamma}} = 1 \quad (2.39)$$

First, if the nozzle is choked, then $M_t = 1$, and M_e and p_e may be determined from the nozzle area ratio $\frac{A_e}{A_t}$ by the classical gas dynamic equations presented in Zucrow [10]. Secondly, if the nozzle is not choked, then $p_t = p_{amb}$ and M_t may be determined from the pressure ratio $\frac{P_t}{P_t}$ where $P_t = P_e$ for quasi-steady isentropic flow. Knowing M_t and the area ratio $\frac{A_e}{A_t}$, M_e and p_e may be determined by the classical gas dynamic equations in Zucrow [10]. Hence, in both cases p_e is determinable, and the unit process for an open end may be employed for determining v_e and p_e .

It is important to note that this analysis neglects unsteady flow effects inside the nozzle, which is justified if the nozzle length is extremely short compared to the length of the duct.

2.5. COMPLEX BOUNDARY CONDITIONS

Three simple boundary conditions have already been discussed in Sections 2.4.4, 2.4.5 and 2.4.6, namely for the closed end, outflow at a constant area open-end and at the isentropic nozzle. In the case of the closed end it was assumed that

Chapter 2: Unsteady Homentropic Motion in One-Dimension

the velocity is zero at the boundary, while at the open end and nozzle throat, atmospheric conditions were assumed for subsonic outflow.

To model any boundary condition it is necessary to make certain assumptions about the boundary condition; the quasi-steady assumption is a usual one for one-dimensional flow, but others might be necessary [17]. These assumptions must be validated by comparison with experiments. The boundaries described in this chapter are typical boundaries found in internal combustion engines.

2.5.1. Inflow through an open end

This boundary is typical of inflow at the inlet pipe or reverse flow at the exhaust pipe exit. When there is flow into the open end of the duct from a large and relatively stagnant atmosphere, a workable approximation is to assume that the flow from the reservoir/atmosphere into the duct may be treated as though it was quasi-steady at each time step [7].

With the assumption of quasi-steady flow from the reservoir/atmosphere to the duct inlet plane (Figure 2-10), we may write the energy equation of steady flow as [7]:

$$T_r = T_i + \frac{u_i^2}{2C_p} \quad (2.40)$$

where subscript, r , denotes stagnation conditions in the reservoir/atmosphere and subscript, i , denotes the duct inlet plane.

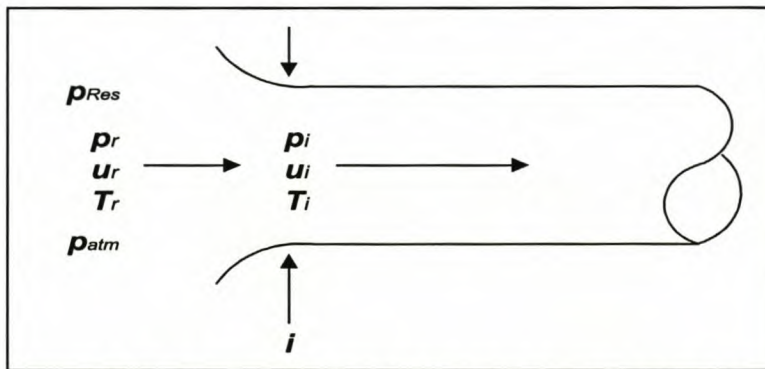


Figure 2-10: Inflow at an open end from a reservoir/atmosphere

Eliminating the temperature, T , in favour of the speed of sound, c , by means of equation 2.5, we obtain the equation of steady state [7]:

$$c_i^2 + \frac{\gamma-1}{2}(u_i)^2 = (c_r)^2 \quad (2.41)$$

Chapter 2: Unsteady Homentropic Motion in One-Dimension

It is also assumed that the stagnation pressure, P_i , at the entrance is equal to the reservoir/atmospheric pressure. Figure 2-11 illustrates the MOC Mach lines for subsonic inflow at an open end [4].

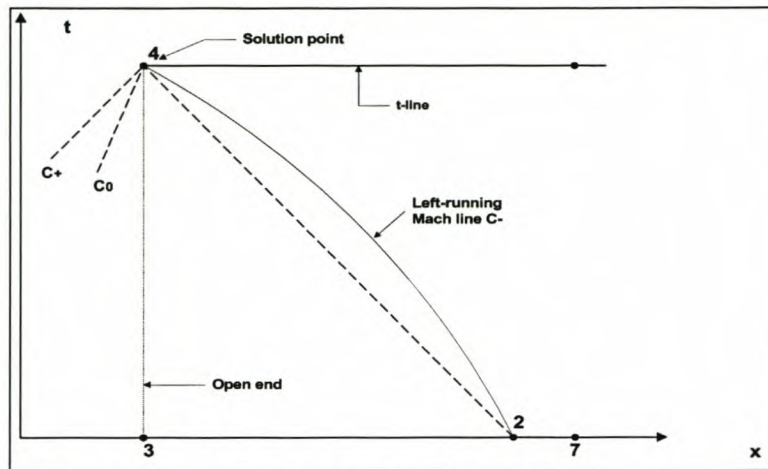


Figure 2-11: Subsonic inflow at an open end

With equations (2.40) and (2.41), known reservoir/atmospheric conditions and the characteristic and compatibility equations of the MOC, the velocity u_i or the speed of sound c_i at the entrance of the open end can be solved iteratively. New pressure and density can then be calculated from the new velocity and speed of sound, using the classical gas dynamic equations [10].

2.5.2. Inflow through a nozzle

Inflow through a nozzle is typical to outflow through an exhaust valve in an internal combustion engine [22]. Figure 2-12 shows the flow from a cylinder through a nozzle into a long pipe. The flow in the throat of the nozzle can be either sonic or subsonic.

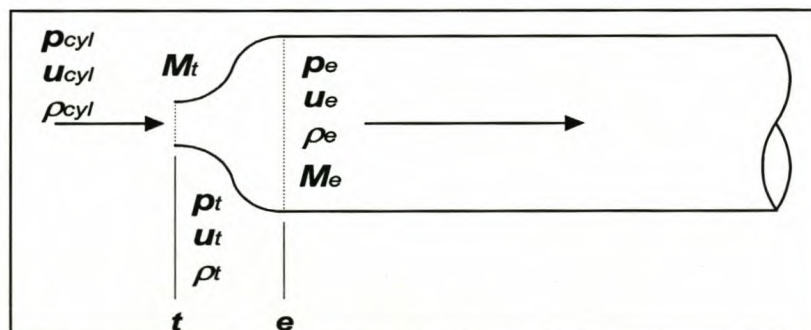


Figure 2-12: Inflow through a nozzle

To check for subsonic or sonic flow in the throat, the stagnation pressure ratio between the cylinder and pipe entrance is calculated and compared to the

Chapter 2: Unsteady Homentropic Motion in One-Dimension

critical pressure ratio [21, 22]:

$$\left(\frac{P_{cyl}}{P_e} \right)_{cr} = \left(\frac{\gamma + 1}{2} \right)^{\frac{\gamma}{\gamma - 1}} \quad (2.42)$$

If the calculated pressure ratio is equal to or higher than the critical pressure ratio, the flow will be sonic and if not, the flow is subsonic in the throat.

For subsonic flow in the throat, flow from the cylinder to the throat is isentropic and adiabatic (non-isentropic) between the throat and the pipe entrance [18, 19]. The values of the properties in the throat are calculated with the classical isentropic gas laws [10] and $M_t < 1$. The properties at the entrance of the pipe are calculated with expressions, derived from the governing gas flow equations and using the assumptions specified in this paragraph, presented by Benson [4] and by using the characteristic and compatibility equations of the MOC.

For sonic flow in the throat, flow from the cylinder to the throat is isentropic and the Mach number in the throat is unity. The values of the properties in the throat are calculated with the classical isentropic gas laws [10] and $M_t = 1$. The properties at the entrance of the pipe are calculated with expressions, derived from the governing gas flow equations and using the assumptions specified in this paragraph, presented by Benson [4] and by using the characteristic and compatibility equations of the MOC.

2.5.3. Reverse flow through an exhaust valve

A badly designed exhaust system will cause high exhaust back pressure, which can cause reverse flow at the exhaust valve. Reverse flow through the exhaust valve will occur when the pressure in the cylinder drops below the static throat pressure (usually just before the exhaust valve closes). Reverse flow is also outflow through a nozzle, or similar to forward flow through an inlet valve [8]. Therefore, all the relationships and assumptions that were used for flow through an inlet valve (Section 2.4.6) can now be used and implemented [4].

2.5.4. Reverse flow through an inlet valve

Reverse flow through the inlet valve will only occur when the pressure in the cylinder rises above the stagnation pressure of the pipe at the inlet valve

Chapter 2: Unsteady Homentropic Motion in One-Dimension

entrance. This can occur just after the inlet valve opened or just before it closes and is usually related to low engine speeds. A well-designed inlet manifold will minimise reverse flow by using the pulsating ramming effect to keep the average pressure at the inlet valve above the cylinder pressure. Reverse flow is also inflow through a nozzle, or similar to normal flow through an exhaust valve [8]. Therefore, all the relationships and assumptions that were used for flow through an exhaust valve (Section 2.5.2) can now be used and implemented [4].

2.6. COMPUTER SIMULATION CASE STUDIES

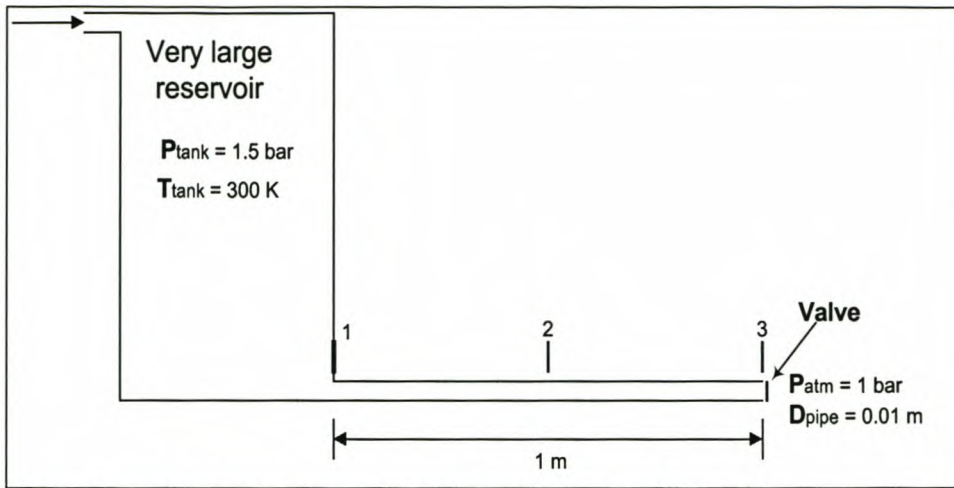
The first stage in developing an accurate and reliable computer simulation program, is to develop and test subroutines for each one of the unit processes and boundary conditions described in Sections 2.4 and 2.5. By repeating case studies reported by Benson [4], the different subroutines were used and tested in different combinations.

2.6.1. Case Study 1: Reservoir and pipe configuration

The first case study is that of flow in a pipe connected to a reservoir (Figure 2-13) on the left end of the pipe and the atmosphere at the right. The valve at the right end of the pipe suddenly opens to full pipe bore to the atmosphere. The air inside the pipe is subjected to this change in boundary condition. It is assumed that the reservoir pressure and temperature are maintained constant and the ratio of specific heats, γ , is equal to 1.4. The flow in the pipe is then analysed with the MOC and the results are reported at three points, marked 1, 2 and 3 in Figure 2-13.

This example makes use of two boundary conditions: (1) open end inflow and (2) open end outflow and includes the use of an interior solution point. These three subroutines were included in a computer program, **ReservoirPipe.exe**. The program was created in a Delphi4 compiler environment (program installation included on CD). A flow chart of this program is presented in Figure 2-14.

Benson [4] used two methods to solve this problem. First he used the old graphical solution method and then compared it to his numerical solution by using the MOC. His data was used to evaluate this case study and make an evaluation on the accuracy of the results.

Chapter 2: Unsteady Homentropic Motion in One-Dimension**Figure 2-13:** Diagram of the reservoir and pipe configuration

The problem was analysed with the initial data, just after the valve opens, as given in Table 2-2.

Table 2-2: Initial data for *ReservoirPipe.exe* just after valve opens

	Reservoir	Point 1	Point 2	Point 3	Atmosphere
Pressure [bar]	1.5	1.5	1.5	1	1
Temperature [K]	300	300	300	?	?
Velocity [m/s]	0	0	0	?	0
Density [kg/m ³]	1.74	1.74	1.74	?	?
Speed of Sound [m/s]	347.2	347.2	347.2	?	?

By using the equation of state as given by equations (2.5) and (2.6) in conjunction with the following expression for isentropic flow

$$\frac{T_a}{T_b} = \left(\frac{P_a}{P_b} \right)^{\frac{\gamma-1}{\gamma}} \quad (2.43)$$

the temperature of the atmospheric air can be calculated from Zucrow [10]:

$$T_{atm} = T_{resv} \left(\frac{P_{atm}}{P_{resv}} \right)^{\frac{\gamma-1}{\gamma}} = \underline{\underline{267.18 \text{ K}}} \quad (\text{with } \gamma = 1.4)$$

By using equations (2.5) and (2.6), the density and speed of sound can be calculated for the atmosphere,

$$\rho_{atm} = 1.304 \text{ kg/m}^3$$

$$c_{atm} = 327.65 \text{ m/s}$$

Chapter 2: Unsteady Homentropic Motion in One-Dimension

The conditions at point 3 are equal to that of the atmosphere after the valve has opened, except for the velocity (Section 2.4.3).

The critical pressure ratio for choked flow is (similar to equation (2.42)):

$$\left(\frac{P_{pipe}}{P_{atm}}\right) = \left(\frac{\gamma + 1}{2}\right)^{\frac{\gamma}{\gamma - 1}} = \underline{\underline{1.893}} \quad (\text{with } \gamma = 1.4)$$

The given pressure ratio for this example is

$$\left(\frac{P_{pipe}}{P_{atm}}\right) = 1.5 < 1.893$$

implying that the flow is subsonic at the pipe exit.

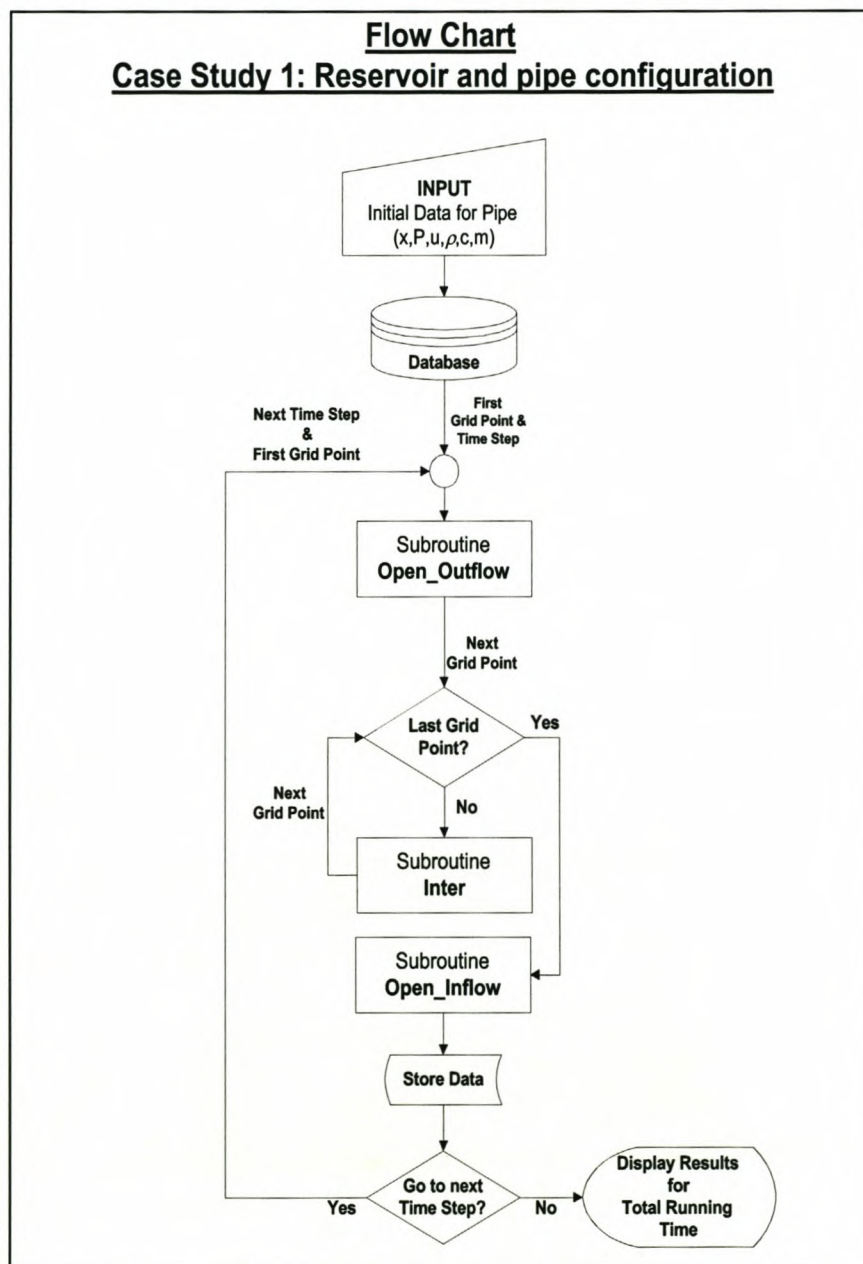


Figure 2-14: Flow chart of the program *ReservoirPipe.exe*

Chapter 2: Unsteady Homentropic Motion in One-Dimension

To calculate the velocity at the pipe exit when the valve opened, we use the constant area flow equation [4] and $\gamma = 1.4$:

$$U = \frac{2}{\gamma - 1} C_{atm} \left[\left(\frac{P_{pipe}}{P_{atm}} \right)^{\frac{\gamma-1}{2\gamma}} - 1 \right] = \underline{\underline{97.71 \text{ m/s}}}$$

In the analysis three different grids with 10, 30 and 50 grid points respectively were used to investigate the influence on the accuracy of the results. Two time steps of 0.05 ms and 0.025 ms were also used to investigate the difference in result accuracy.

By implementing the boundary condition of Section 2.5.1 and constructing a quadratic velocity equation at the entrance, the open-end inflow boundary on the reservoir side can be solved. Any iteration method can be used to solve the velocity equation.

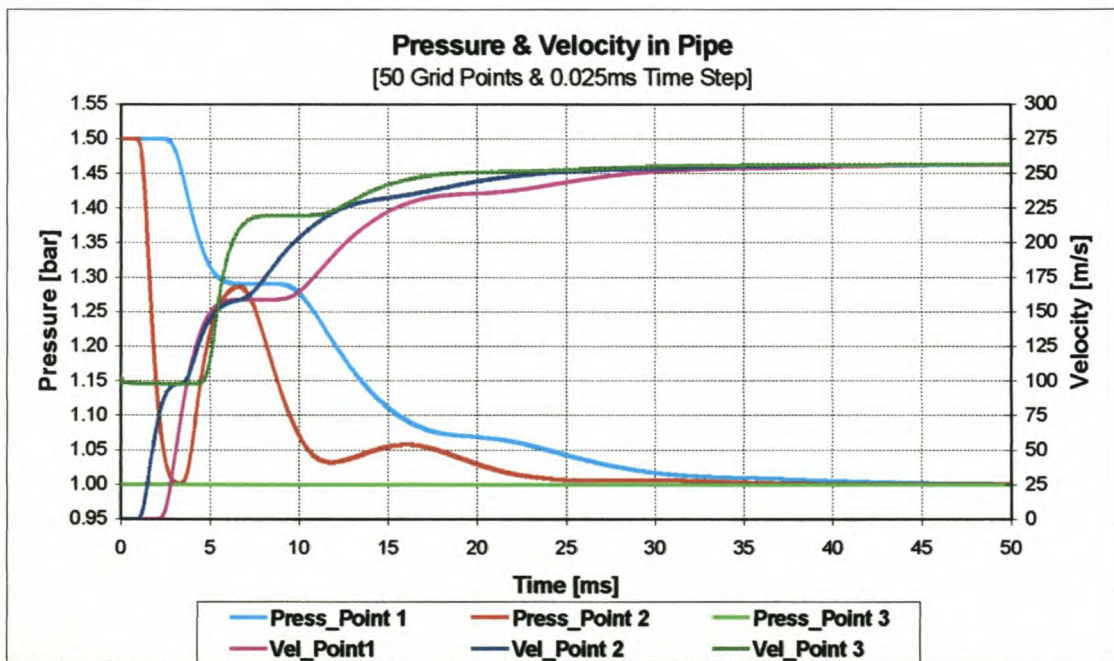


Figure 2-15: Pressure and velocity in pipe [50 grid points & 0.025ms time step]

In Figure 2-15 the pressures and velocities at the three different measurement points are shown. It is clear from Figure 2-15 that an expansion wave runs up the pipe, returns from the inflow open end as a compression wave running down the pipe where it returns again from the open outflow boundary as an expansion wave. This process repeats itself until the wave has diminished away and pipe conditions have reached equilibrium.

Chapter 2: Unsteady Homentropic Motion in One-Dimension

In Figure 2-16 and Figure 2-17 the pressure and velocity distributions are shown as contour graphs of time and position in the pipe.

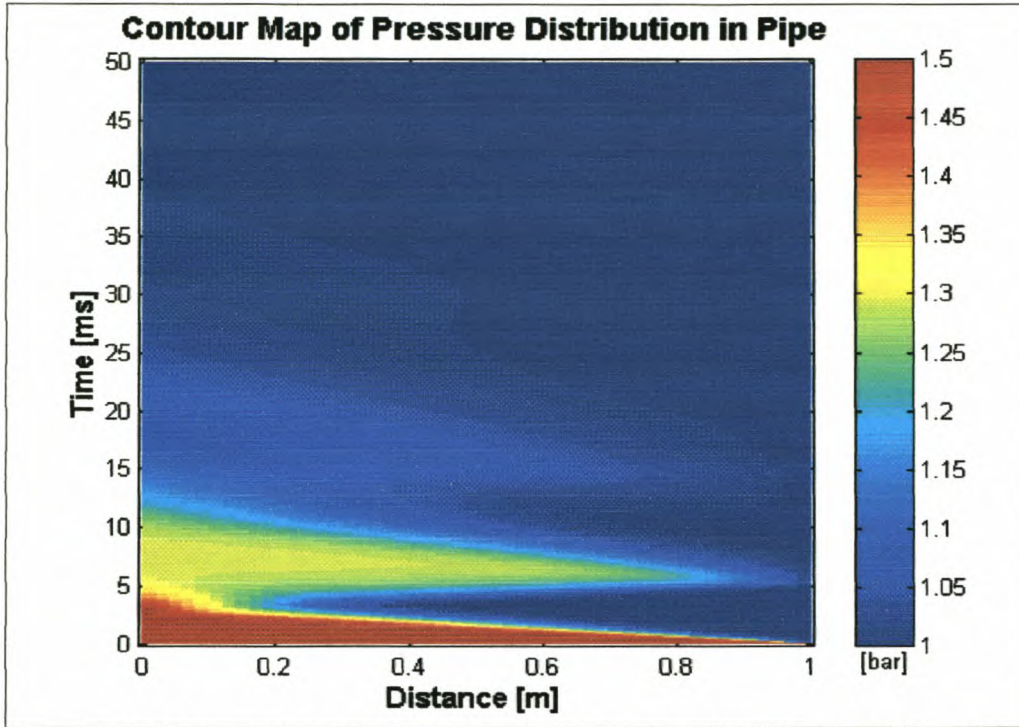


Figure 2-16: Pressure distribution in pipe vs. time [50 grid points & 0.025ms time step]

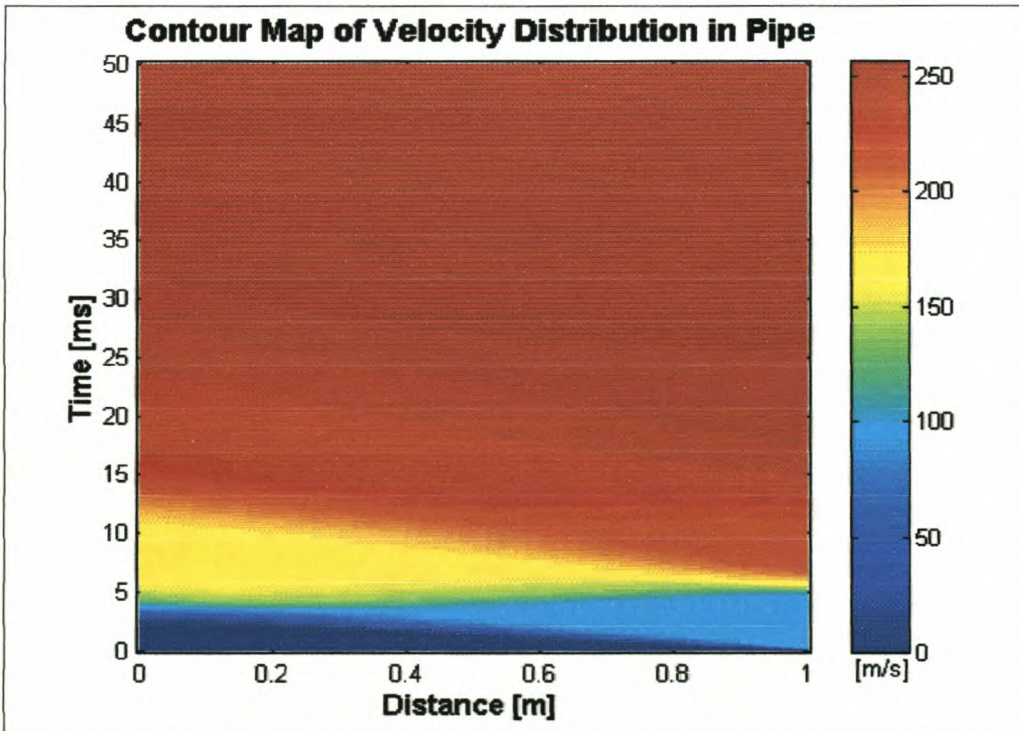


Figure 2-17: Velocity distribution in pipe vs. time [50 grid points & 0.025ms time step]

A typical set of results for different grids and time steps are presented in Appendix A, Figures A-1 to A-6. From these results the following general

Chapter 2: Unsteady Homentropic Motion in One-Dimension

conclusions on the number of grid points and size of time steps could be made.

It is clear that for a given time step an increase in the number of grid points results in an increase in result accuracy. The level of accuracy is constrained by the CFL-criterion, though, and the maximum number of grid points for a time step of 0.025 ms is 65 grid points.

It is also evident from the graphs that when the number of grid points is kept constant and the time step is made smaller, the solution becomes less accurate, but not significantly so. A smaller time step though permits more grid points and therefore a more accurate result.

Direct comparisons of the simulated data and the results presented by Benson [4] are shown in Figures A-7 to A-9. Agreement between the two sets of results is good, proving that the MOC works well for this type of unsteady flow.

2.6.2. Case Study 2: Sudden discharge from a cylinder

The sudden discharge from a cylinder through a constant area isentropic nozzle is illustrated in Figure 2-18. The valve at the right end of the cylinder is suddenly opened to full nozzle diameter to the atmosphere and the air inside the cylinder is subjected to a change of boundary condition. The flow in the cylinder is then analysed with MOC and the results are reported at two points inside the cylinder, marked 1 and 2 in Figure 2-18. The cylinder can also be considered as a pipe with a nozzle at the one end.

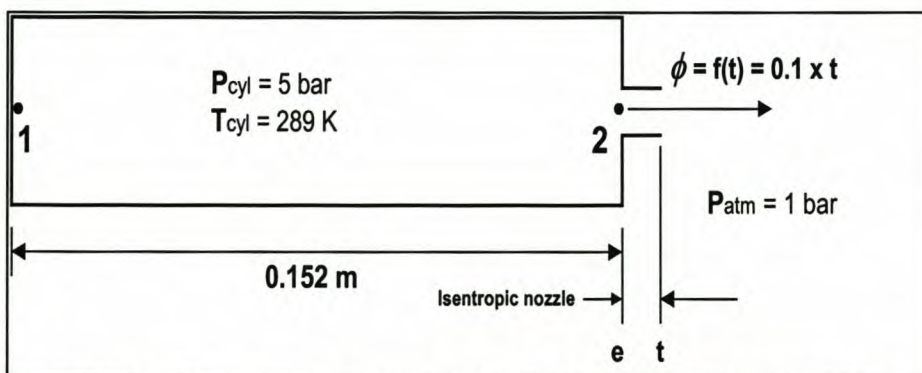


Figure 2-18: Diagram of sudden discharge from a cylinder through a nozzle

In this example two boundary conditions are used: (1) closed end at the left of the cylinder and (2) an isentropic nozzle with outflow/inflow conditions at the right. It also includes the use of an interior solution point. These three subroutines

Chapter 2: Unsteady Homentropic Motion in One-Dimension

were included in a computer program, **Cylinder1.exe**. The program was created in a Delphi4 compiler environment (program installation included on CD). A flow chart of this program is presented in Figure 2-19.

The example was taken from Benson [4] where he used the same two methods (graphical and numerical) to solve the problem as for case study 1. His data was used to evaluate this case study and make an evaluation on the accuracy of the results.

The problem was then analysed with the initial data, just after the valve opens, as given in Table 2-3.

The unknown values at the specified points were calculated by means of equations (2.5) to (2.6), as well as the following expression from Zucrow [10]:

$$\frac{1}{\phi} = \frac{A_e}{A_t} = \frac{1}{M_e} \left[\left(\frac{2}{\gamma+1} \right) \left(1 + \frac{\gamma-1}{2} M_e^2 \right) \right]^{\frac{\gamma+1}{2(\gamma-1)}} \quad (2.44)$$

The critical pressure ratio for choked flow ($\gamma = 1.4$) is the same as for case study 1, i.e. $P_{cr} = 1.893$.

The given pressure ratio for this example is

$$\left(\frac{P}{P_{atm}} \right) = 3.041 > 1.893$$

implying that the flow is choked in the nozzle throat at the start of the blow-down process.

To calculate the velocity at the nozzle exit when the valve opened, we define two critical points in the nozzle, the entrance to the nozzle, e , and the nozzle throat, t . Now by knowing that $M_t = 1$ and $\phi = 0.25$ we get from equation (2.44) that $M_e = 0.1465$.

Now the pressure at the throat is, from Zucrow [10],

$$p_t = p^* = P \left(\frac{2}{\gamma+1} \right)^{\frac{\gamma}{\gamma-1}} = \underline{\underline{1.607 \text{ bar}}}$$

The temperature at the throat can now be calculated with equation (2.43). The density and speed of sound of the throat point can be calculated with equations (2.5) and (2.6).

Chapter 2: Unsteady Homentropic Motion in One-Dimension

It is now possible to calculate, from Zucrow [10], the pressure at the nozzle entrance, e ,

$$p_e = \frac{P}{\left[1 + \frac{\gamma-1}{2} M_e^2\right]^{\frac{\gamma}{\gamma-1}}} = \underline{\underline{2.996 \text{ bar}}}$$

These values, calculated in this section, are used to complete Table 2-3.

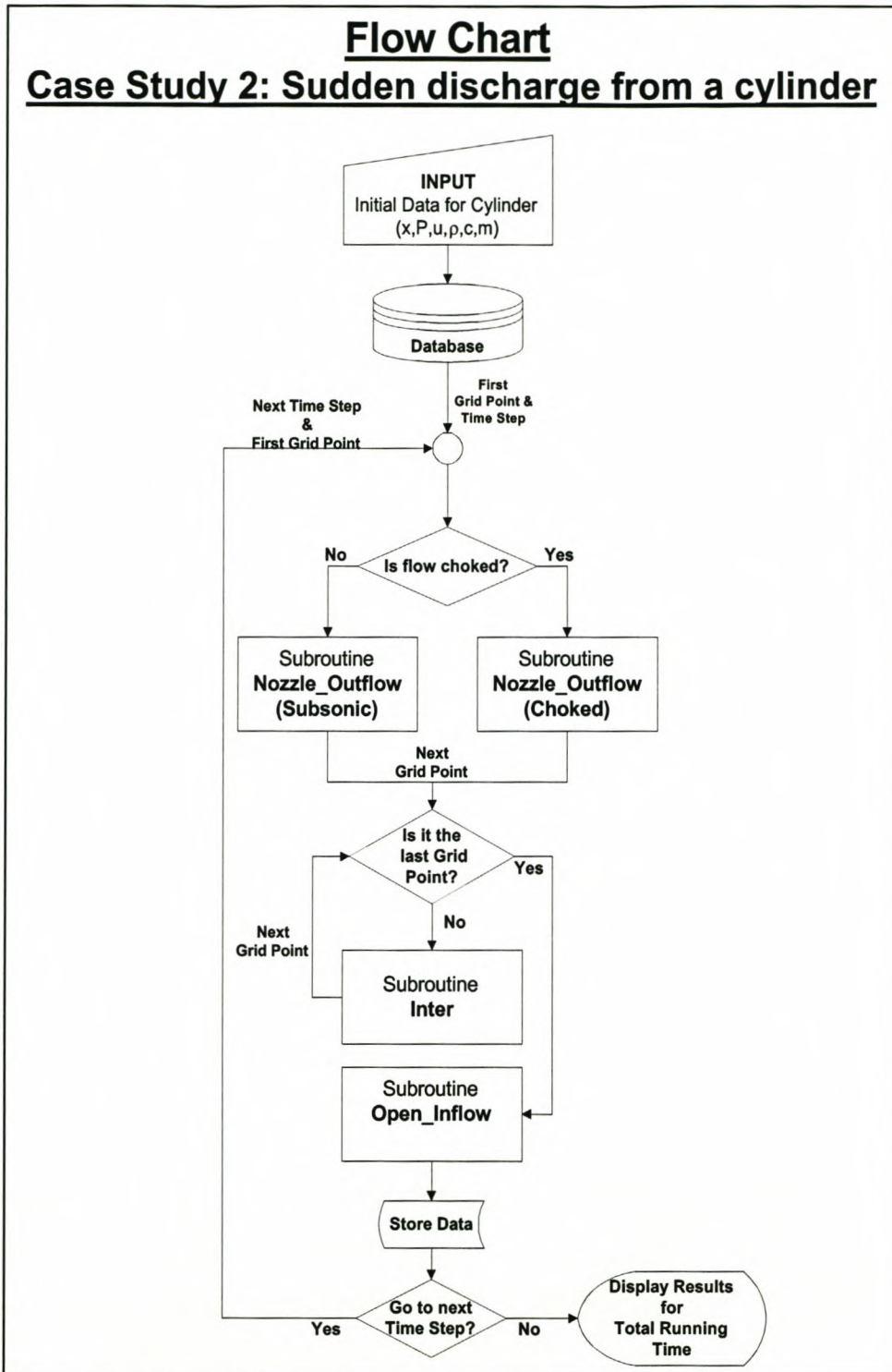
Table 2-3: Initial data for *Cylinder1.exe* after valve opens

	Point 1	Point 2	Point, e	Point, t	Atmosphere
Pressure [bar]	3.041	3.041	2.996	1.607	1
Temperature [K]	412.22	412.22	410.46	343.54	300
Velocity [m/s]	0	0	54.43	371.53	0
Speed of Sound [m/s]	406.98	406.98	406.11	371.53	347.2
Mach Number	0	0	0.147	1	0

When the pressure ratio drops below the critical pressure ratio, the flow goes subsonic again at the nozzle. The Mach number and other variables at the nozzle throat are then recalculated and the values at the entrance changes accordingly. The values are recalculated using the methods described in Section 2.4.6.

Towards the end of the blow-down of the cylinder the static pressure in the cylinder drops below that of the atmosphere, because of the sudden discharge and the kinetic energy of the flowing air. This causes the air to flow back into the cylinder. The nozzle boundary condition now becomes an inflow nozzle end and the methods presented in Section 2.5.2 are used. The pressure in the cylinder then again rises above that of the atmospheric air and air then starts to flow out again. These phenomena continue until the cylinder has blown down fully and an equilibrium state is reached.

In Figures 2-21 and 2-22 the pressures and velocities at the two points marked in Figure 2-18 are shown.

Chapter 2: Unsteady Homentropic Motion in One-Dimension**Figure 2-19:** Flow chart of the program *Cylinder1.exe*

In Figures 2-23 and 2-24 the pressure and velocity distributions are shown as contour graphs of time and position in the cylinder. Figure 2-22 shows an expansion wave moving down the cylinder and returning from the closed end as another expansion wave. This process repeats itself until the cylinder has blown down fully.

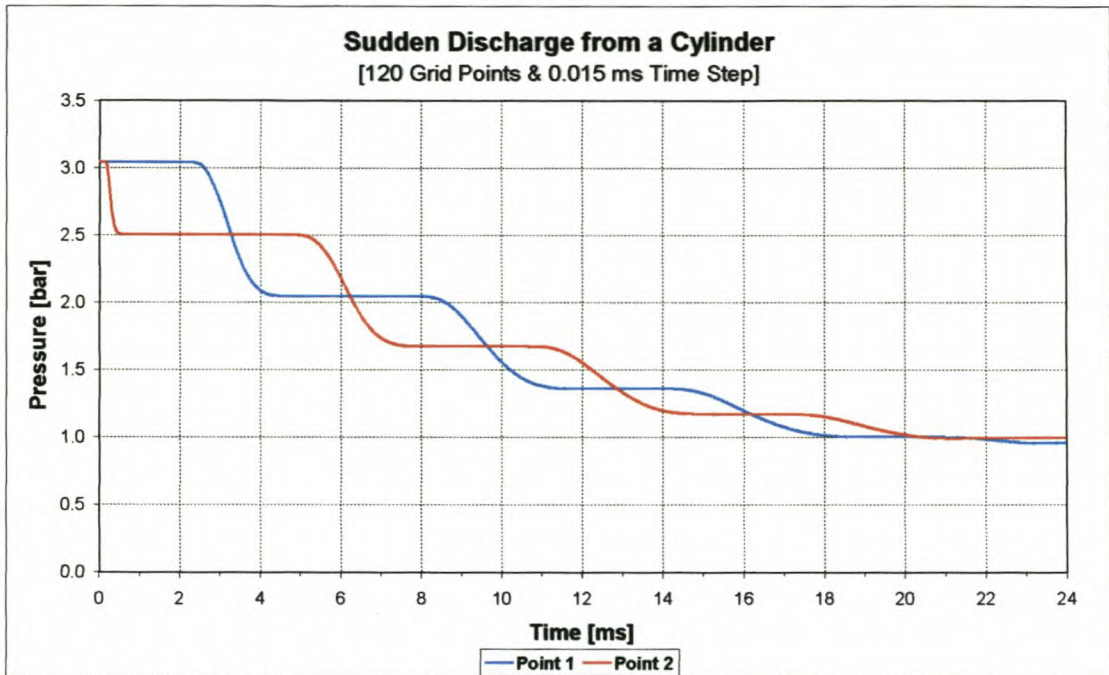
Chapter 2: Unsteady Homentropic Motion in One-Dimension

Figure 2-20: Pressure in sudden discharge of a cylinder
[120 grid points & 0.015 ms time step]

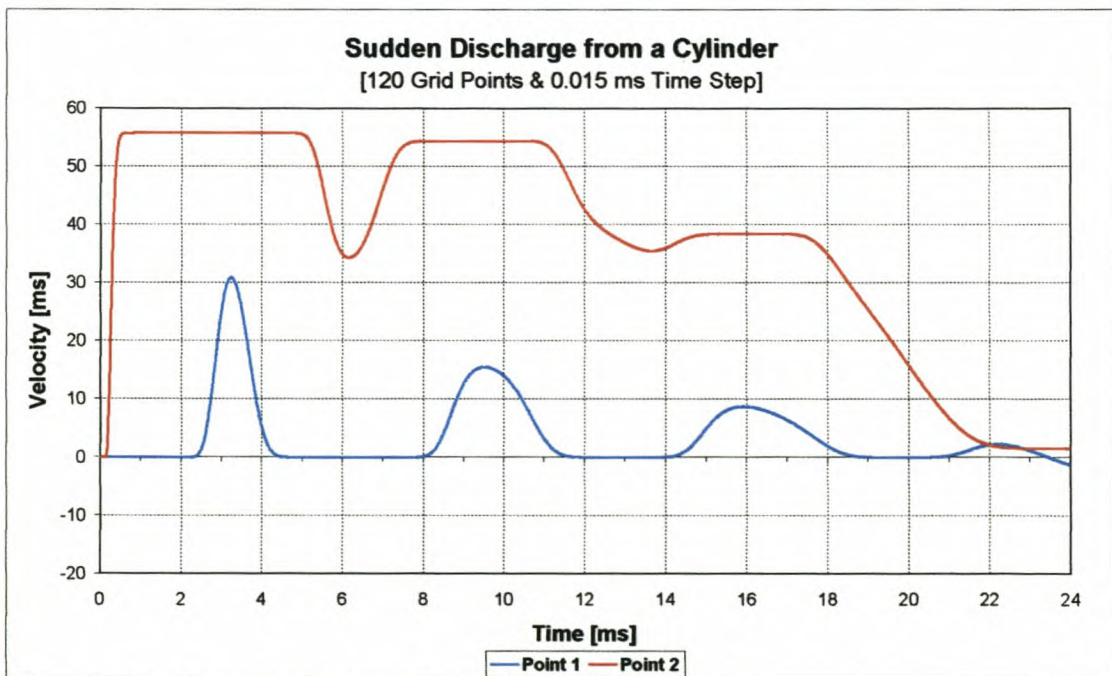


Figure 2-21: Velocity in sudden discharge of a cylinder
[120 grid points & 0.015 ms time step]

Direct comparisons of the simulated data and the results presented by Benson [4] are presented in Figures B-1 to B-4. Once again good agreement between the two sets of results is found.

Chapter 2: Unsteady Homentropic Motion in One-Dimension

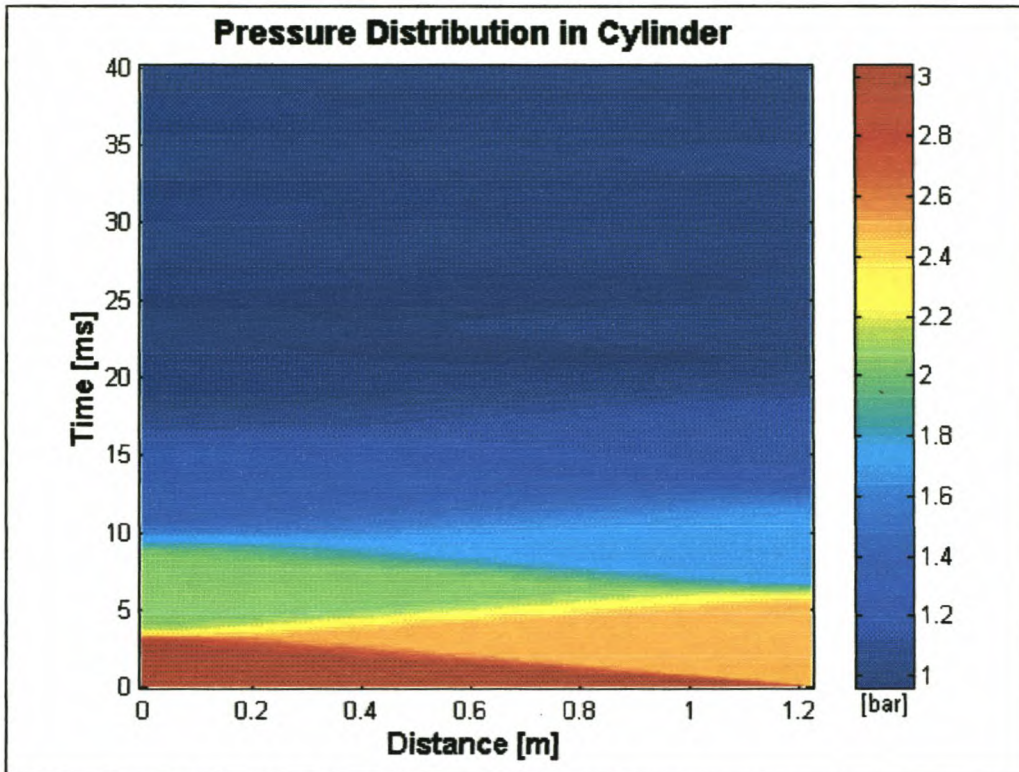


Figure 2-22: Pressure distribution in cylinder vs. time
[120 grid points & 0.015 ms time step]

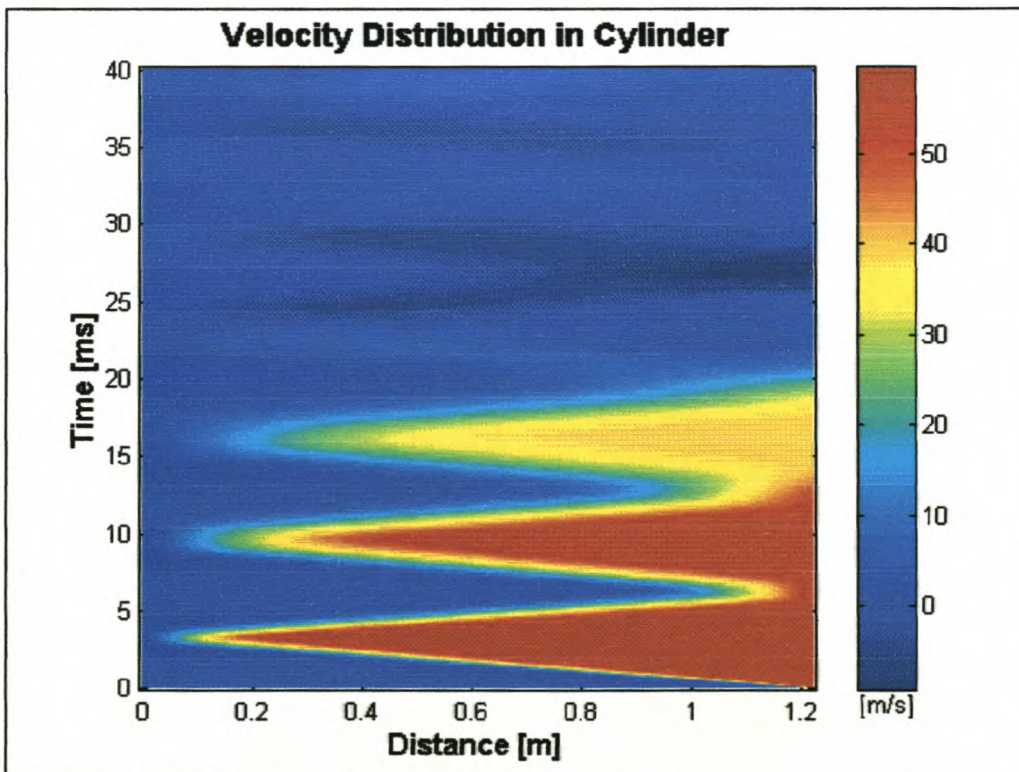


Figure 2-23: Velocity distribution in cylinder vs. time
[120 grid points & 0.015 ms time step]

Chapter 2: Unsteady Homentropic Motion in One-Dimension

2.6.3. Case Study 3: Gradual discharge from a cylinder

In this case study the gradual discharge from a cylinder through a variable area isentropic nozzle, Figure 2-24, is analysed. The valve at the right end of the cylinder is opened linearly with respect to time. The flow in the cylinder is then analysed by the MOC and the results reported at two points in the cylinder, marked 1 and 2 in Figure 2-24. The cylinder can also be considered as a pipe with an isentropic nozzle at the exit end.

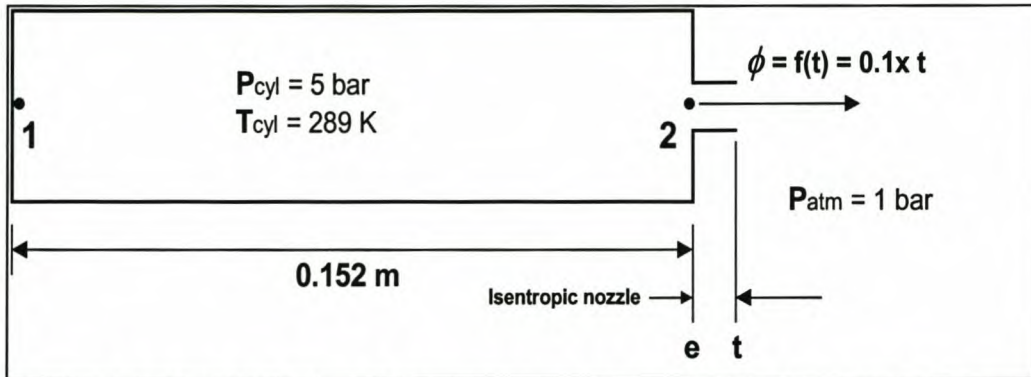


Figure 2-24: Diagram of gradual discharge from a cylinder through a nozzle

This example makes use of two boundary conditions: (1) closed end at the left of the cylinder and (2) a variable area isentropic nozzle with outflow/inflow at the right. It also includes the use of an interior solution point. These three subroutines were included in a computer program, **Cylinder2.exe**. The program was created in a Delphi4 compiler environment (program installation included on CD). The flow chart of this program is similar to the one presented in Figure 2-19, the only difference being the variable area of the nozzle.

The example was taken from Benson [4] where he used the same two methods (graphical and numerical) to solve the problem as for case studies 1 and 2. His data was used to evaluate this case study and make an evaluation on the accuracy of the results.

The problem was then analysed and the initial data, just after the valve started to open, were calculated. The unknown values at the specified points were calculated by means of equations (2.5) to (2.6) and (2.44) from Zucrow [10].

The critical pressure ratio for choked flow ($\gamma = 1.4$) is the same as for case studies 1 and 2, i.e. $P_{cr} = 1.893$.

Chapter 2: Unsteady Homentropic Motion in One-Dimension

The given pressure ratio for this example is

$$\left(\frac{P}{P_{atm}}\right) = 5 > 1.893$$

implying that the flow is choked in the nozzle throat at the start of the blow-down process.

To calculate the velocity at the nozzle exit when the valve opened, we define two critical places at the nozzle, the entrance to the nozzle, e , and the nozzle throat, t . Now by knowing that $M_t = 1$ and $\phi = f(t)$ we get from equation (2.44) that $M_e = f(t)$ and can be iteratively calculated at each time step.

Now the pressure at the throat is calculated from Zucrow [10],

$$p_t = p^* = P \left(\frac{2}{\gamma + 1} \right)^{\frac{\gamma}{\gamma - 1}} = \underline{\underline{2.641 \text{ bar}}}$$

The temperature at the throat can now be calculated with equation (2.43). The density and speed of sound of the throat point can be calculated with equations (2.5) and (2.6).

It is now possible to calculate the pressure at the nozzle entrance for each time step, from Zucrow [10],

$$P_e = \frac{P}{\left[1 + \frac{\gamma - 1}{2} M_e^2 \right]^{\frac{\gamma}{\gamma - 1}}}$$

These values, calculated in this section, are used to complete the problem as in case study 2.

When the pressure ratio drops below the critical pressure ratio the flow goes subsonic again at the nozzle. The Mach number and other variables at the nozzle throat is then recalculated and the values at the entrance change accordingly. The values are recalculated using the methods in Section 2.4.6.

Towards the end of the blow-down of the cylinder the static pressure in the cylinder drops below that of the atmosphere, because of the sudden discharge and the kinetic energy of the flowing air. This causes the air to flow back into the cylinder. The nozzle boundary condition now becomes an inflow nozzle end and the methods presented in Section 2.5.2 are used. The pressure in the cylinder

Chapter 2: Unsteady Homentropic Motion in One-Dimension

then again rises above that of the atmospheric air and air then starts to flow out again (Figures 2-26 and 2-27). These phenomena continue until the cylinder has blown down fully and an equilibrium state is reached.

The pressures and velocities at the two cylinder measurement points are presented in Figures 2-26 and 2-27.

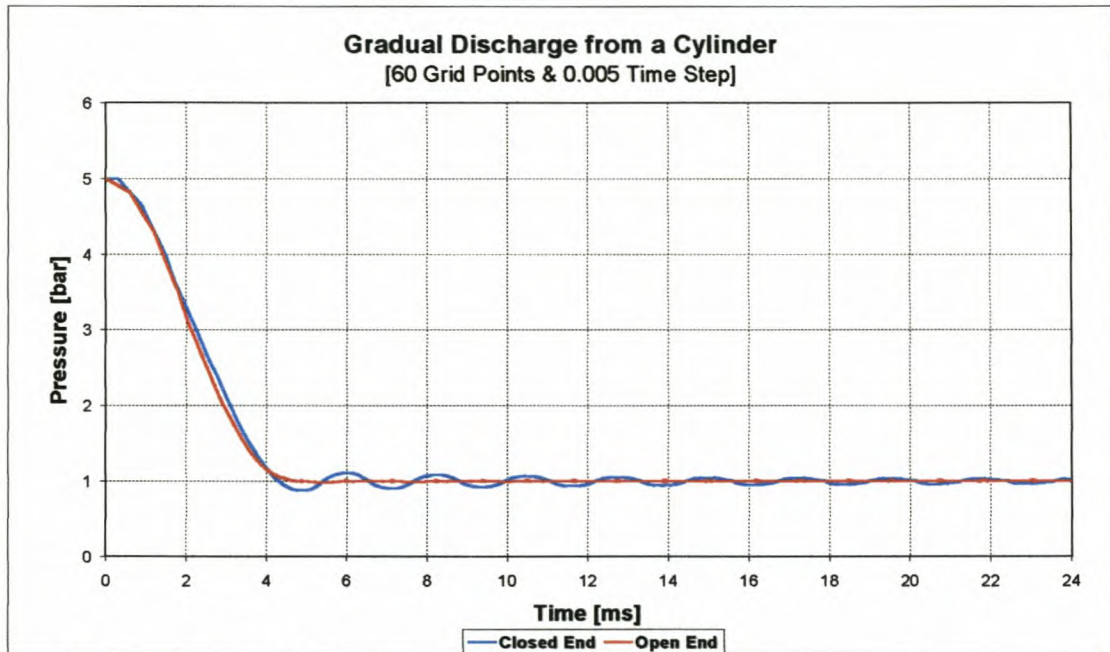


Figure 2-25: Pressure in gradual discharge of a cylinder
[60 grid points & 0.005 ms time step]

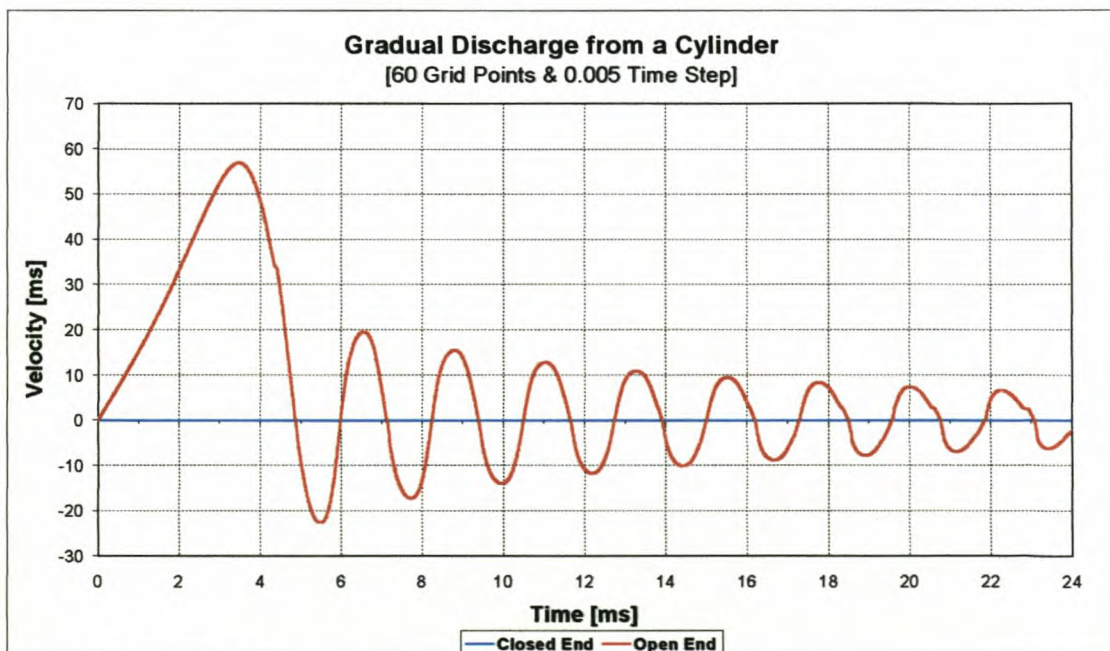


Figure 2-26: Velocity in gradual discharge of a cylinder
[60 grid points & 0.005 ms time step]

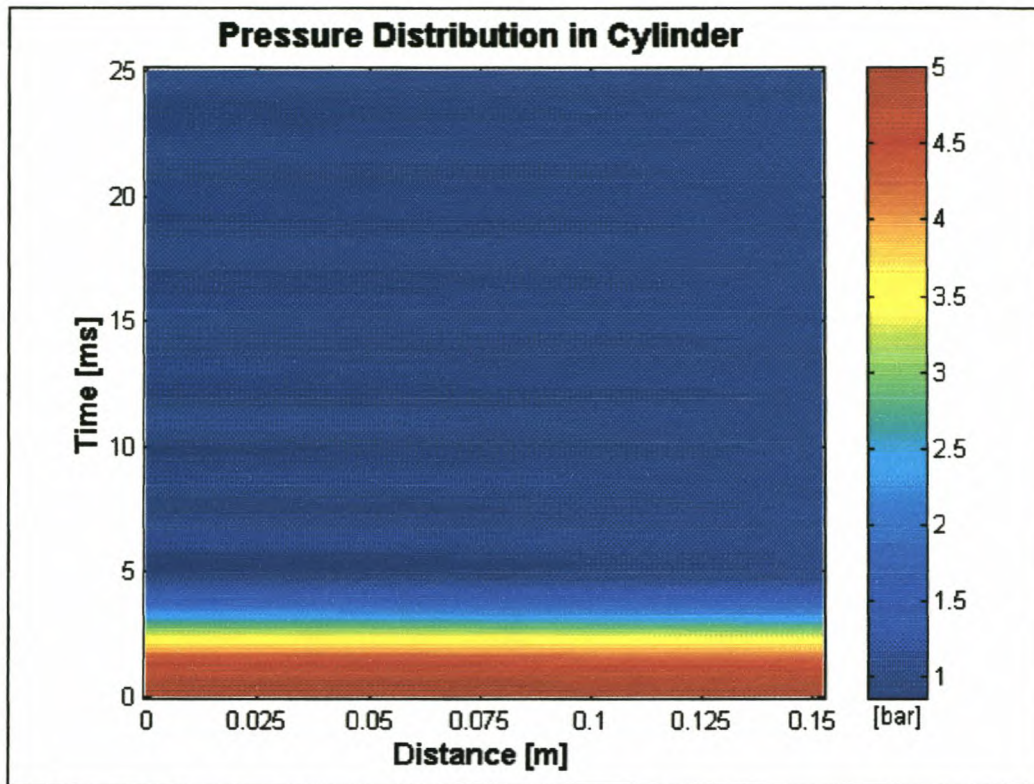
Chapter 2: Unsteady Homentropic Motion in One-Dimension

Figure 2-27: Pressure distribution in cylinder vs. time
[60 grid points & 0.005 ms time step]

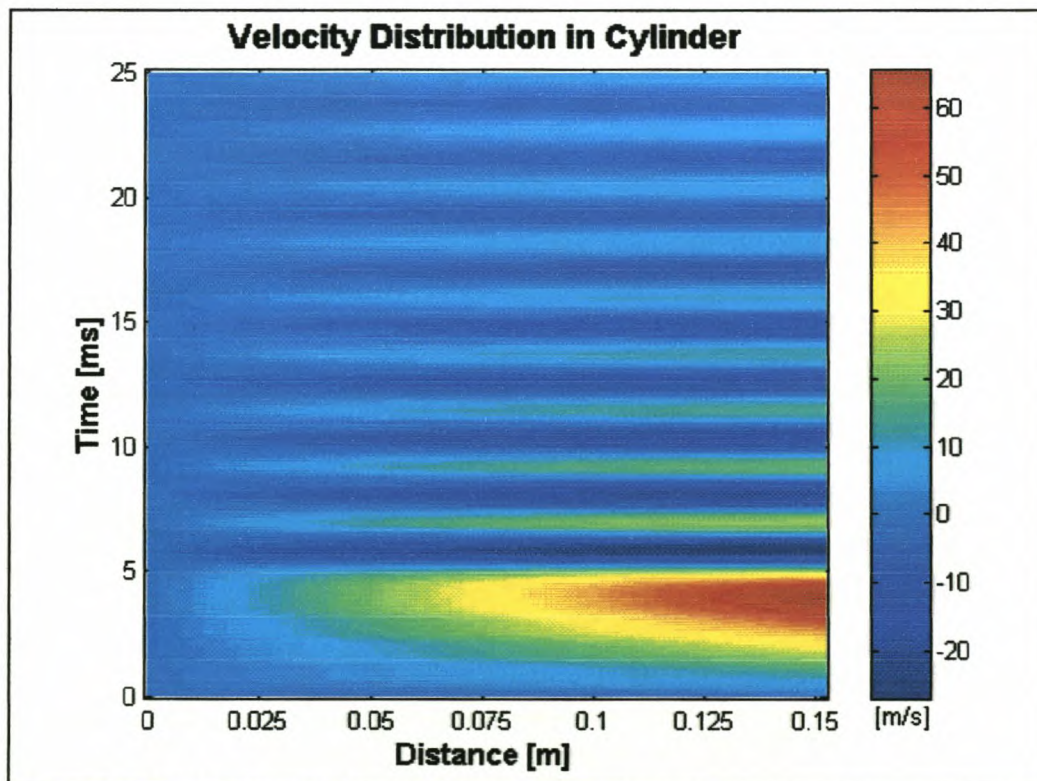


Figure 2-28: Velocity distribution in cylinder vs. time
[60 grid points & 0.005 ms time step]

The cylinder in this example is very short, therefore it appears as if the cylinder only blows down. It appears as if no pressure waves are formed, but the waves

Chapter 2: Unsteady Homentropic Motion in One-Dimension

are there, they only reflect very fast. In Figures 2-28 and 2-29 the pressure and velocity distributions are shown as contour graphs of time and position in the cylinder.

Direct comparisons of the simulated data and the results presented by Benson [4] are presented in Figures C-1 and C-2. Once again good agreement between the two sets of results is found.

2.7. CLOSURE

In chapter 2 it is shown that the MOC could predict flow phenomena quite accurately. In the case studies it was also proven that the grid size and time step has a significant influence on the accuracy of the results. The results obtained with the case studies compared well with the published data of Benson [4]. This gave us confidence in the MOC as well as in the simulation of the boundary conditions. The subroutines developed in this chapter are used as foundation for the rest of the development of the final computer simulation program.

A detailed discussion on one-dimensional non-homentropic flow and the influence it has on the flow is presented in chapter 3. The inclusion of friction and heat transfer in the numerical algorithms are presented and case studies are submitted to verify the numerical data with published results.

CHAPTER 3: UNSTEADY NON-HOMENTROPIC MOTION IN ONE-DIMENSION

In Chapter 2, unsteady one-dimensional homentropic flow in which large amplitude changes in the properties of the gas occur, was discussed. Unfortunately, the disadvantage of homentropic flow is that no friction, heat transfer or mass addition are considered. In the flow systems of internal combustion engines it is especially friction, heat transfer, temperature gradients and the irreversibility of flow through valves that influence the flow properties in the engine ducting [4, 10]. In the present chapter the governing equations for unsteady one-dimensional non-homentropic flow of a compressible fluid as well as the corresponding characteristic and compatibility equations are presented. Case studies are presented to illustrate the application of unsteady one-dimensional non-homentropic flow problems.

3.1. NON-HOMENTROPIC FLOW

Non-homentropic flow is also known as generalised flow [4, 10]. The difference between non-homentropic flow and homentropic flow is that with homentropic flow the total entropy remains constant throughout the flow field [18]. With non-homentropic flow the total entropy and the entropy levels of each grid point in the flow field changes with time [4]. Non-homentropic flow implies friction, heat transfer and mass addition to the system [10]. The idealisation to homentropic flow is an advantage in inlet and exhaust systems, because it saves computing time when only the total entropy of the system has to be calculated and not the entropy of every grid point. Non-homentropic flow is more accurate, especially when working with very high gas velocities and temperature gradients in the flow field.

3.2. THE GOVERNING EQUATIONS

One-dimensional flow is still assumed, as discussed in Chapter 2, i.e. the flow properties depend only on one space co-ordinate, x , and the time, t . The governing equations for unsteady one-dimensional non-homentropic flow are as follows [4, 10, 18]:

Chapter 3: Unsteady Non-Homentropic Motion in One-Dimension

Continuity equation:

$$\rho_t + u\rho_x + \rho u_x + \frac{\rho u}{A} \frac{dA}{dx} = 0 \quad (3.1)$$

Momentum equation:

$$u_t + uu_x + \frac{1}{\rho} p_x + \frac{u|u|}{2} \cdot \frac{4f}{D} = 0 \quad (3.2)$$

Energy equation:

$$\rho_t + u\rho_x - c^2(\rho_t + u\rho_x) = \rho(\gamma - 1) \left[\frac{\pi Dh}{\rho A} (T_w - T_g) + \frac{u^2|u|}{2} \cdot \frac{4f}{D} \right] \quad (3.3)$$

Entropy equation:

$$s = s(t) \quad (3.4)$$

Equation of state:

$$p = \rho RT \quad (3.5)$$

Speed of sound equation (for an isentropic process):

$$c^2 = \frac{\gamma p}{\rho} \quad (3.6)$$

3.3. THE CHARACTERISTIC EQUATIONS

The characteristic equations for non-homentropic flow are exactly the same as for homentropic flow, as given by the equations (2.7) and (2.8) in Chapter 2.

The compatibility equations for non-homentropic flow are different from that of homentropic flow and are given by Shapiro [7] and Zucrow [10].

Along each pathline,

$$dp_0 - c^2 d\rho_0 = (\gamma - 1) \left(\frac{\rho}{u} q - \beta \right) dx_0 \quad (3.7)$$

where

$$\beta = -\frac{\rho u|u|}{2} \cdot \frac{4f}{D} \quad (\text{friction}) \quad (3.8)$$

$$q = \pi Dh \frac{T_w - T_g}{\rho A} \quad (\text{heat transfer}) \quad (3.9)$$

Chapter 3: Unsteady Non-Homentropic Motion in One-Dimension

Also, along each Mach line

$$dp_{\pm} \pm (\rho c) du_{\pm} = \left[-\frac{u\rho c^2}{A} \left(\frac{dA}{dx} \right) \pm c\beta + (\gamma - 1)(\rho q - u\beta) \right] dt_{\pm} \quad (3.10)$$

Equation (3.7) is applicable along the pathline and expresses the change in density, $d\rho_0$, along an infinitesimal section of the pathline, dx , if the corresponding change in pressure is equal to $d\rho_0$. The density also depends on (1) the speed of sound, which is a function of p and ρ (equation of state), (2) the pipe friction, which is a function of the Fanning friction factor, f , and the gas velocity and (3) the heat transfer between the gas and pipe wall. Equation (3.10) is applicable along the C_{\pm} characteristics and expresses the change in pressure, dp_{\pm} , along an infinitesimal section of the pathline, dx , if the corresponding change in velocity is equal to du_{\pm} in a time step dt_{\pm} . The pressure also depends on the speed of sound, density, friction, heat transfer and change in cross sectional area at the characteristic.

Here the intersection of the characteristics also implies that these equations are all valid at the same point. The three compatibility equations may therefore be solved simultaneously at the point of intersection for the flow properties u , p and ρ at that point, if the flow properties are known at "previous" points on the characteristics.

3.4. FANNING FRICTION FACTOR

The Fanning friction factor is dependent on the flow type: laminar, transitional or turbulent flow, which is determined by the Reynolds number [10, 38, 39].

$$Re = \frac{\rho|u|d}{\mu} \quad (3.11)$$

Laminar flow ($Re < 2300$),

$$f = \frac{16}{Re} \quad (3.12)$$

Transitional flow ($2300 \leq Re < 4000$),

$$f = \frac{0.0791}{Re^{0.25}} \quad (3.13)$$

Turbulent flow ($Re \geq 4000$),

$$f = \frac{0.04}{Re^{0.16}} \quad (3.14)$$

Chapter 3: Unsteady Non-Homentropic Motion in One-Dimension

These equations, 3-11 to 3-14, are incorporated into the compatibility equations for the simulation program to calculate friction.

3.5. HEAT TRANSFER COEFFICIENT

The convective heat transfer coefficient needs to be calculated for every time step of the simulation. For heat transfer in pipes, the Reynolds number also determines the equation for calculating this coefficient.

For laminar flow ($Re < 2300$) [19],

$$h = 10 \quad (3.15)$$

and for transitional and turbulent flow the Reynolds' analogy is used [4],

$$h = \frac{f}{2} C_p u_p \quad (3.16)$$

With this approximate method, it is assumed that the heat transfer under unsteady conditions is the same as for steady conditions [4]. These equations, 3-15 and 3-16, are incorporated into the compatibility equations for the simulation program to calculate heat transfer.

3.6. UNIT PROCESSES

In this section the numerical approach to solve a problem with the characteristic and compatibility equations, called a unit process, is discussed. Unit processes are developed for determining the flow properties for the following types of points:

- A point interior to the flow field termed an *interior point*.
- Subsonic outflow through the *poppet valve* of an engine.

3.6.1. Finite difference equations

The finite difference equations corresponding to the characteristic and compatibility equations presented in Section 3.3 are presented in Table 3-1.

Table 3-1: Finite difference equations for unsteady one-dimensional flow

$\Delta t_0 = \lambda_0 \Delta x_0$	(pathline)	(3.17)
$\lambda_0 = \frac{1}{u_0}$		(3.18)

Chapter 3: Unsteady Non-Homentropic Motion in One-Dimension

$\Delta p_0 - B_0 \Delta \rho_0 = T_0 \Delta x_0$	(along a Pathline)	(3.19)
$B_0 = c^2$		(3.20)
$T_0 = (\gamma - 1) \left[\frac{4h}{uD} (T_w - T_g) + \frac{\rho u u }{2} \cdot \frac{4f}{D} \right]$		(3.21)
$\Delta t_{\pm} = \lambda_{\pm} \Delta x_{\pm}$	(Mach lines)	(3.22)
$\lambda_{\pm} = \frac{1}{u_{\pm} \pm c_{\pm}}$		(3.23)
$\Delta p_{\pm} \pm Q_{\pm} \Delta u_{\pm} = S_{\pm} \Delta t_{\pm}$	(along a Mach line)	(3.24)
$Q_{\pm} = \rho c$		(3.25)
$S_{\pm} = -\frac{u \rho c^2}{A} \left(\frac{dA}{dx} \right) \mp c \frac{\rho u u }{2} \cdot \frac{4f}{D} + (\gamma - 1) \left[\frac{4h}{D} (T_w - T_g) + \frac{\rho u^2 u }{2} \cdot \frac{4f}{D} \right]$		(3.26)

The numerical algorithms for applying equations (3.17) to (3.26) are based on the *Modified Euler Predictor-Corrector* method discussed in Zucrow [10].

3.6.2. Interior point

Figure 2-5 illustrates schematically, in the x t - plane, the finite difference grid for determining the location and properties of point 4, an interior point.

The locations of the initial-data points 1, 2 and 3 and the slopes λ_0 , λ_+ and λ_- are determined in exactly the same way as described in Section 2.4.3 by considering $\Delta t = \Delta t_0 = \Delta t_+ = \Delta t_-$ and using equations (3.17) to (3.26).

The compatibility equations, which is valid along the Mach lines (3.24), can be expressed in finite difference form in terms of values at points 1, 2 and 4.

Thus,

$$p_4 + Q_+ u_4 = T_+ \quad (3.27)$$

$$p_4 - Q_- u_4 = T_- \quad (3.28)$$

where

$$T_+ = S_+ \Delta t + p_1 + Q_+ u_1 \quad (3.29)$$

$$T_- = S_- \Delta t + p_2 - Q_- u_2 \quad (3.30)$$

Chapter 3: Unsteady Non-Homentropic Motion in One-Dimension

For the Euler *predictor*

$$Q_+ = \rho_1 c_1 \quad (3.31)$$

$$S_+ = -\frac{u_1 \rho_1 c_1^2}{A_1} \left(\frac{dA}{dx} \right)_1 - c_1 \frac{\rho_1 u_1 |u_1|}{2} \cdot \frac{4f_1}{D_1} + (\gamma - 1) \left[\frac{4h_1}{D_1} (T_W - T_1) + \frac{\rho_1 u_1 |u_1|}{2} \cdot \frac{4f_1}{D_1} \right] \quad (3.32)$$

$$Q_- = \rho_2 c_2 \quad (3.33)$$

$$S_- = -\frac{u_2 \rho_2 c_2^2}{A_2} \left(\frac{dA}{dx} \right)_2 - c_2 \frac{\rho_2 u_2 |u_2|}{2} \cdot \frac{4f_2}{D_2} + (\gamma - 1) \left[\frac{4h_2}{D_2} (T_W - T_2) + \frac{\rho_2 u_2 |u_2|}{2} \cdot \frac{4f_2}{D_2} \right] \quad (3.34)$$

Equations (3.27) and (3.28) are solved for p_4 and u_4 . The compatibility equation which is valid along pathlines (3.19), expressed in finite difference form in terms of values at points 3 and 4, yields

$$p_4 - B_0 \rho_4 = T_0 \quad (3.35)$$

where

$$T_0 = p_3 - B_0 \rho_3 \quad (3.36)$$

For the Euler *predictor*

$$B_0 = c_3^2 \quad (3.37)$$

Equation (3.35) is now solved for ρ_4 .

The steps discussed in Section 2.4.3 are repeated according to the Euler corrector algorithm, to furnish corrected values for the flow properties at point 4. The coefficients of the compatibility equations presented in Table 3-1 are determined by applying the Euler *corrector* algorithm iteratively, employing average values of u , p and ρ along each characteristic (Chapter 2).

3.6.3. Flow through poppet valves

Figure 3-1 illustrates diagrammatically the flow model for a duct having an outflow of gas through a short converging nozzle, typical to an inlet valve of an internal combustion engine, similar to that of Chapter 2.

Chapter 3: Unsteady Non-Homentropic Motion in One-Dimension

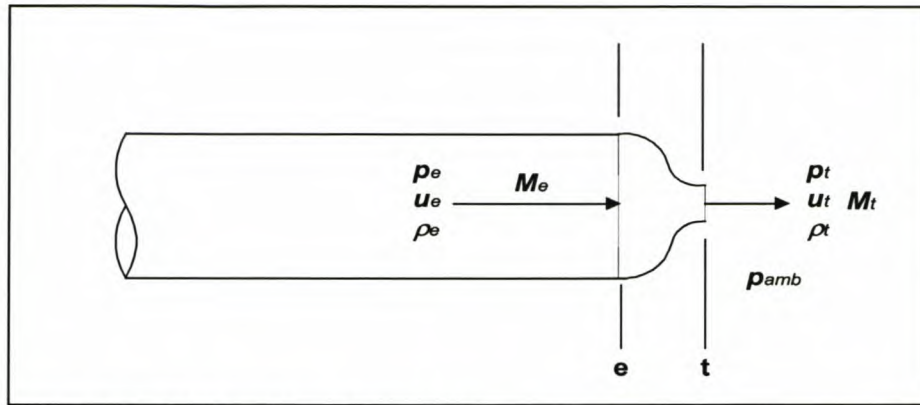


Figure 3-1: Outflow through a nozzle

The flow in the nozzle or valve may be considered to be steady. This is justified if the nozzle length is extremely short compared to the length of the duct wherein the unsteady flow effects may be important.

The development of any engine simulation model is incomplete and thus inaccurate without modelling the effects of the flow losses through the valves. As an overwhelming proportion of modern engines make use of overhead poppet valves, it is the subject of this investigation.

The development of the CFD code for manifold flow is the subject of this thesis, with Williams [15] being responsible for the in-cylinder model, cam and valve lift simulation. It is obvious that these two fields overlap with the flow through the valves.

In all practical situations the flow that passes between a cylinder and a duct through a valve experiences a decrease in area [15]. In such a case it is customary to describe this behaviour by using a discharge coefficient, symbolised as C_d . This coefficient is presented as

$$C_d = \frac{A_{te}}{A_t} \quad (3.38)$$

where A_t is the measured valve throat area and A_{te} the effective valve throat area [15]. It has been shown that the discharge coefficient varies primarily with changes in valve lift ratio, L_k , and pressure ratio, R_p , across the valve [15]. The discharge coefficient must thus be presented to the simulation software in the form of a three dimensional map of C_d vs. R_p and L_k as illustrated in Figure F-16.

The discharge coefficient is traditionally measured in a steady flow experiment and then applied to an unsteady flow simulation in a quasi-steady fashion so as

Chapter 3: Unsteady Non-Homentropic Motion in One-Dimension

to enhance the realism and accuracy of the predictions it provides [15]. A point of concern is the difference between the coefficients for steady state and pulsed flow, but no data regarding this could be found.

3.7. COMPUTER SIMULATION CASE STUDIES

In developing an accurate and reliable computer simulation program it is necessary to evaluate the subroutines for each one of the unit processes and boundary conditions described in Section 3.7. This is done by repeating a case study reported in a SAE paper by Kirkpatrick et al. [18].

The experimental setup of Kirkpatrick et al. [18] (also see Blair [40]) consisted of a single cycle pressure wave generator consisting of a cylinder, connected via a sliding valve to a long duct. The pressure waves it creates closely mimic, in amplitude and profile, those to be found in IC engines. In the experiments air was used throughout as the working gas. A perfect seal exists between the cylinder and the valve, thus enabling mass flow correlation. The initial cylinder pressure may be set to simulate an induction or an exhaust process of an engine. The duct attached to the pressure wave generator can simulate virtually any configuration to be found on an IC engine. Pressure and temperature are recorded by transducers positioned at various locations in the apparatus and stored using a high speed data acquisition system.

Unfortunately some test information is not available or is not clear, e.g. the valve port area vs. time had to be estimated from a very small graph. The 3-dimensional C_d map data was also not available, so that C_d values had to be estimated at each maximum pressure ratio, depending on the valve lift.

3.7.1. Case Study 1: Simulation of an induction process

The first case study is that of flow in a pipe connected to a cylinder on the right end of the pipe and the atmosphere at the left (Figure 3-2). The valve at the cylinder end of the pipe is opened linearly to full pipe bore and closed again. The air inside the pipe is subjected to this change of boundary condition. It is assumed that the pressure and temperature in the cylinder simulate that of a real engine. The flow in the pipe is then analysed with the MOC and the results are reported at two points, marked 1 and 2 in Figure 3-2.

Chapter 3: Unsteady Non-Homentropic Motion in One-Dimension

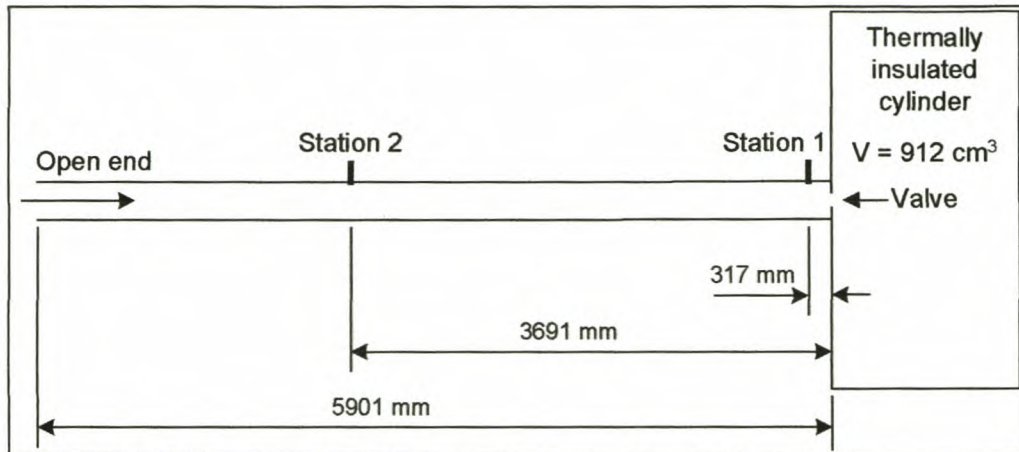


Figure 3-2: Diagram of the cylinder and pipe configuration

This example makes use of three boundary conditions: (1) valve inflow, (2) open end inflow and (3) a closed end when the valve is closed. These subroutines were included in a computer program, *Inlet.exe*. The program was created in a Delphi4 compiler environment (program installation included on CD).

3.7.1.1. Test 1

In the first test the initial cylinder pressure and temperature are 0.5 bar and 293 K respectively. The conditions in the pipe, before the valve opens, are a pressure of 1 bar and a temperature of 293 K respectively. This condition usually exists in IC engines at mid to high engine speeds. The pressures in the cylinder, point 1 and point 2, as well as the velocities at the two specified points are shown in Figures 3-4 and 3-5.

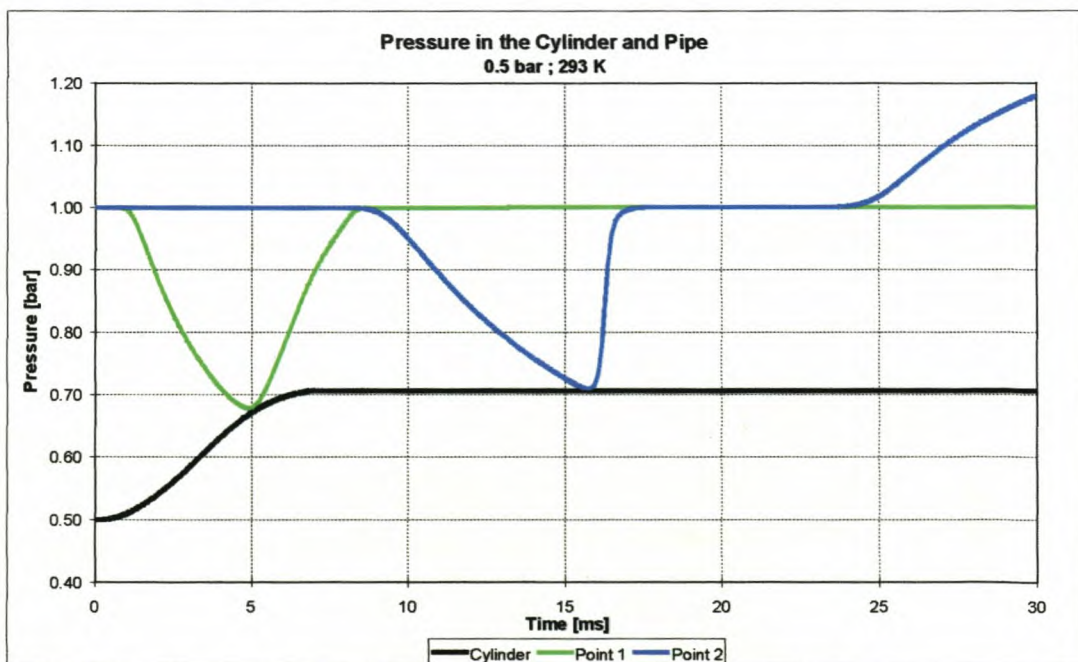


Figure 3-3: Pressure in the cylinder and at point 1 and 2 in the pipe

Chapter 3: Unsteady Non-Homentropic Motion in One-Dimension

It is clear from Figures 3-4 and 3-5 that an expansion wave runs up the pipe and returns from the inflow open end as a compression wave running down the pipe towards the cylinder.

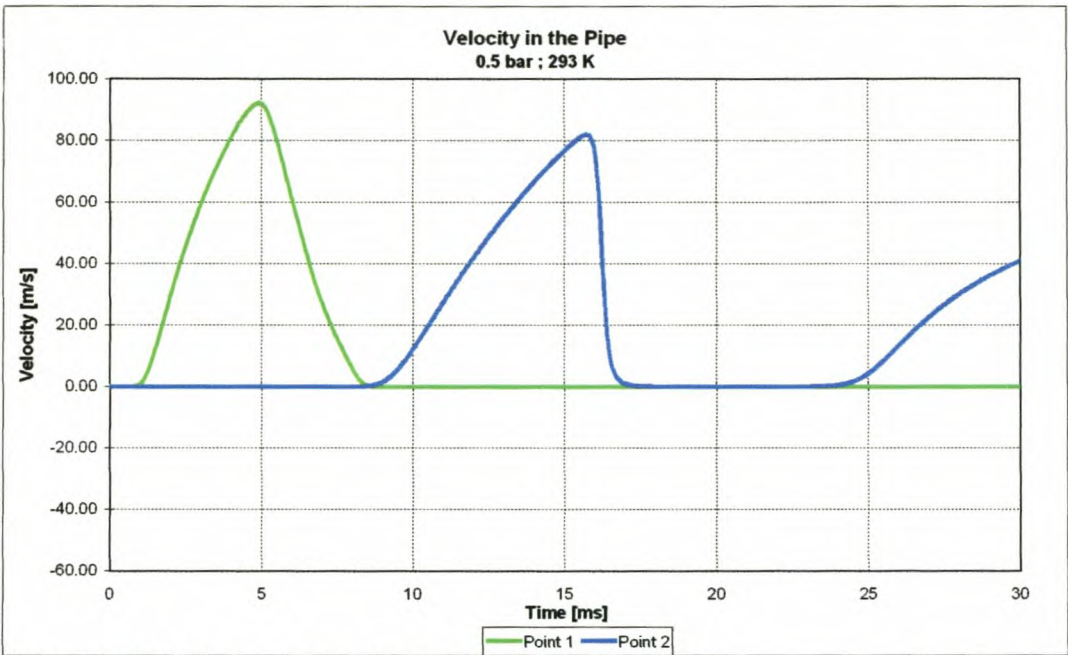


Figure 3-4: Velocity at point 1 and 2 in the pipe

In Figures 3-6 and 3-7 the pressure and velocity distributions are shown as a contour graphs of time and position in the pipe. More detailed information is presented in Appendix D at the cylinder and the two selected measurement points.

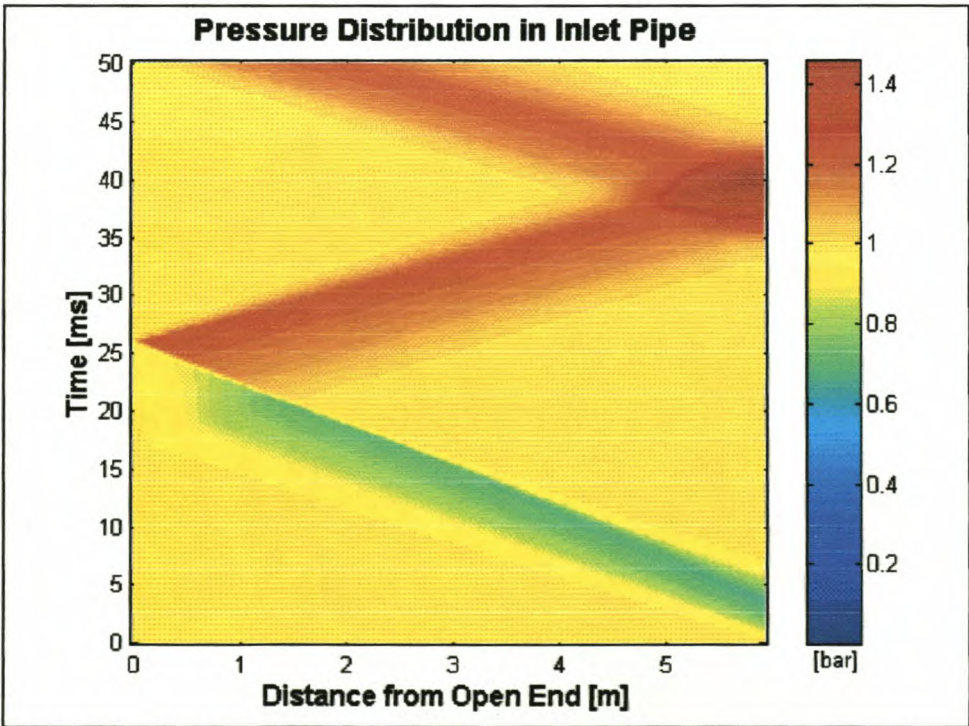


Figure 3-5: Pressure distribution in the pipe vs. time

Chapter 3: Unsteady Non-Homentropic Motion in One-Dimension

Direct comparisons of the simulated data and the results presented by Kirkpatrick et al. [18] and Blair [40] are shown in Figures D-1 to D-3. Agreement between the two sets of results is good. The differences that do exist can be attributed to the fact that not all the detailed information is available, i.e. the correct valve lift profile and C_d map values.

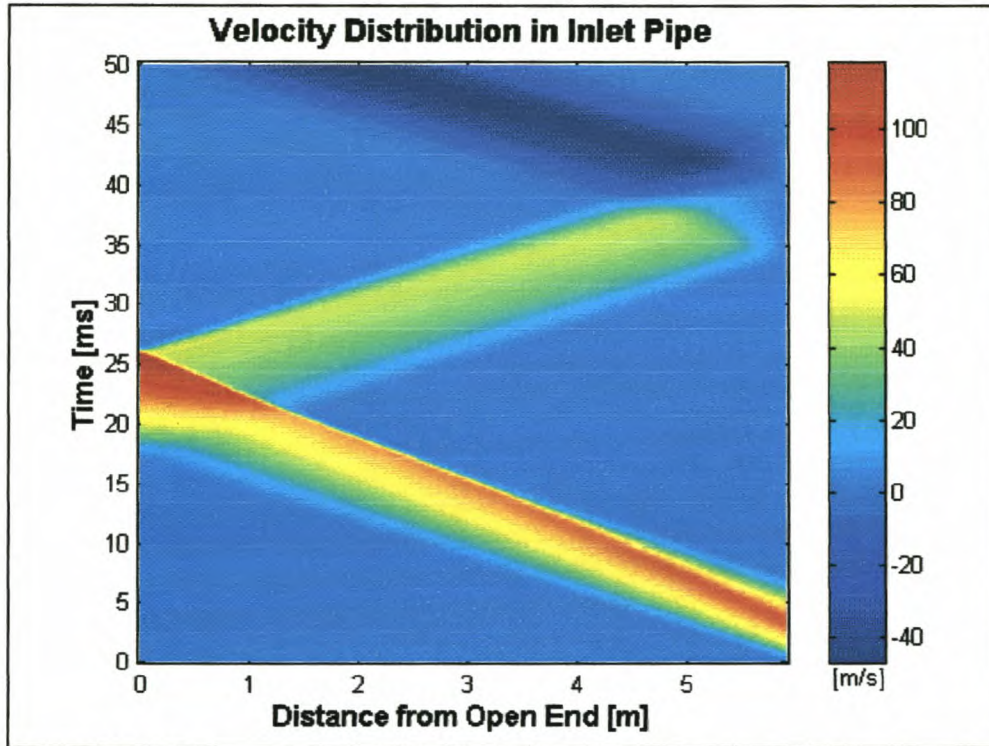


Figure 3-6: Velocity distribution in the pipe vs. time

3.7.1.2. Test 2

In the second test the initial cylinder pressure and temperature are 0.8 bar and 293 K respectively. The conditions in the pipe, before the valve opens, are a pressure of 1 bar and a temperature of 293 K respectively. This condition usually exists in IC engines at low engine speeds and it is important to compare it to Test 1, because of the difference in pressure and the subsequent lower gas velocities. The pressures in the cylinder, point 1 and point 2, as well as the velocities at the two measured points are shown in Figures 3-8 and 3-9.

It is clear from Figures 3-8 and 3-9 that an expansion wave runs up the pipe and returns from the inflow open end as a compression wave running down the pipe towards the cylinder.

In Figures 3-10 and 3-11 the pressure and velocity distributions are shown as contour graphs of time and position in the pipe.

Chapter 3: Unsteady Non-Homentropic Motion in One-Dimension

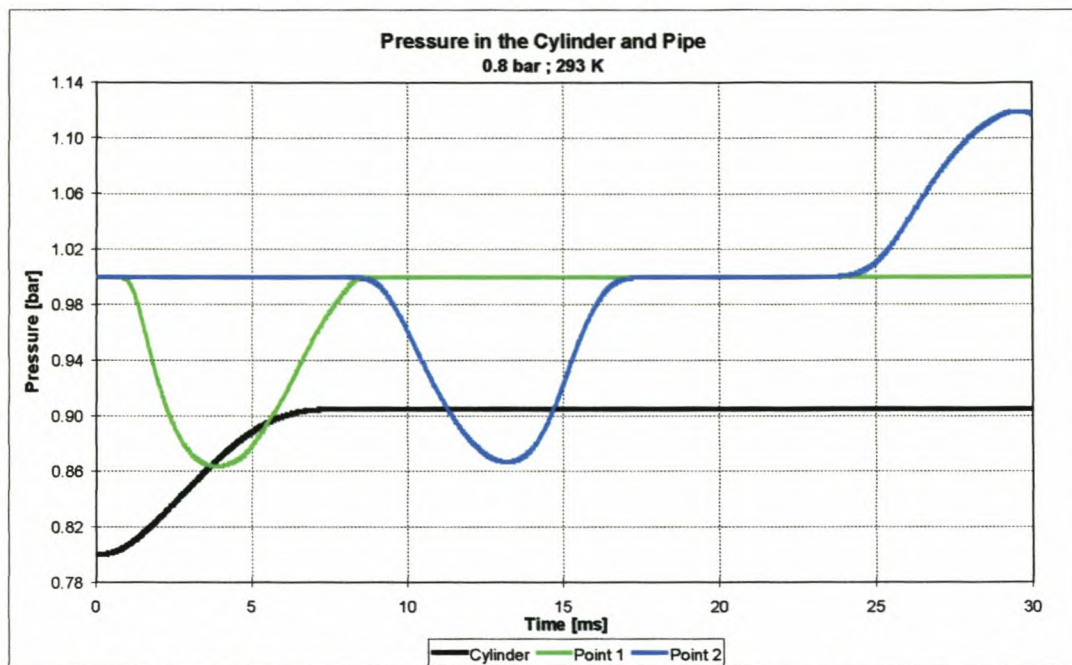


Figure 3-7: Pressure in the cylinder and at point 1 and 2 in the pipe

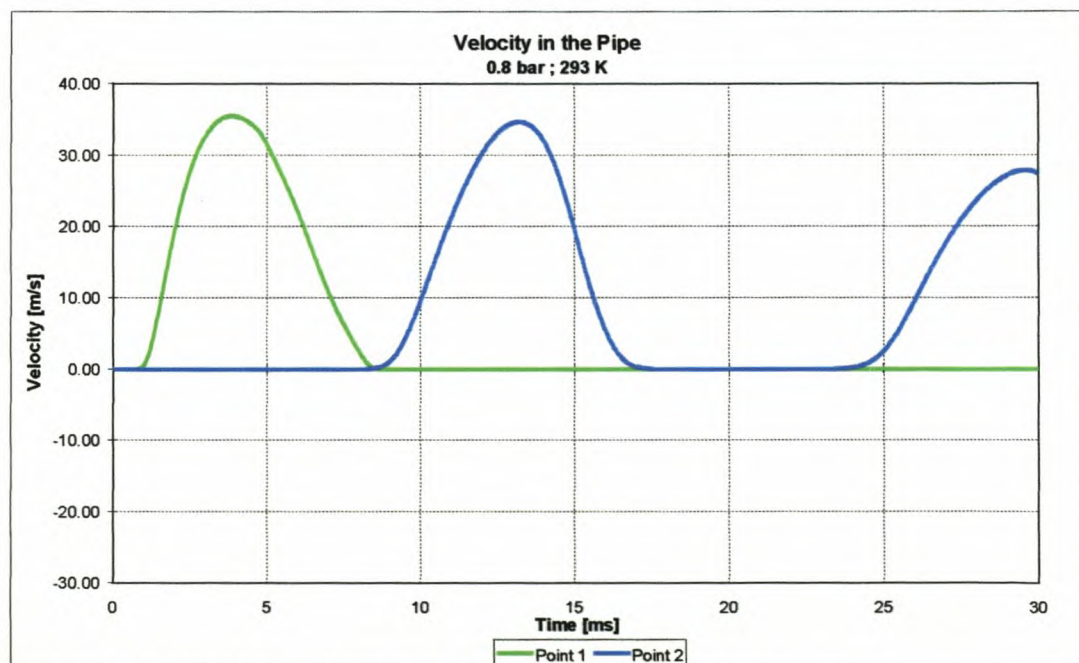
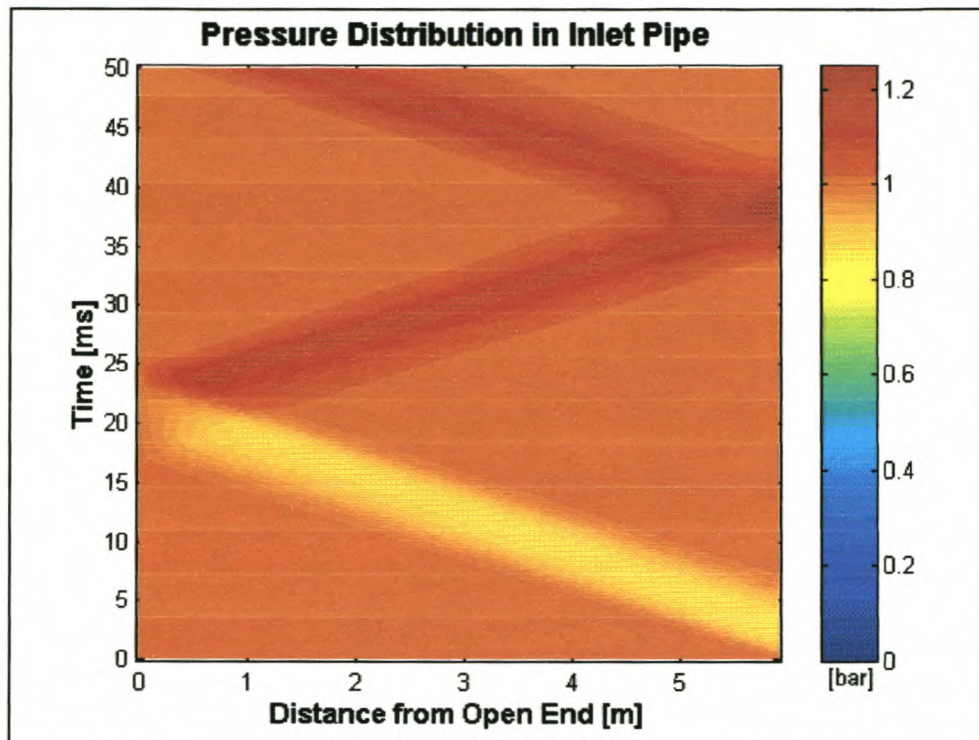
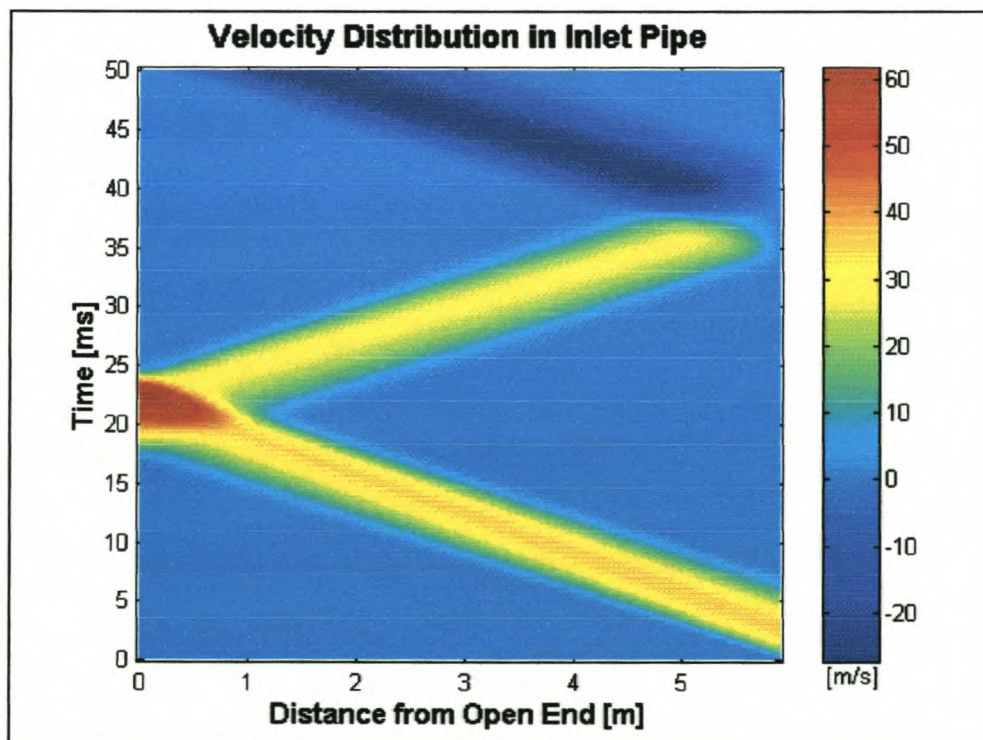


Figure 3-8: Velocity at point 1 and 2 in the pipe.

More detailed information is presented in Appendix D at the cylinder and the two selected measurement points.

Direct comparisons of the simulated data and the results presented by Kirkpatrick et al. [18] and Blair [40] are presented in Figures D-4 to D-6. Once again good agreement between the two sets of results is found.

Chapter 3: Unsteady Non-Homentropic Motion in One-Dimension**Figure 3-9:** Pressure distribution in the pipe vs. time**Figure 3-10:** Velocity distribution in the pipe vs. time**3.7.2. Case Study 2: Simulation of an exhaust process**

The second case study is that of flow in a pipe connected to a cylinder on the right end of the pipe and the atmosphere at the left (Figure 3-11). The valve at

Chapter 3: Unsteady Non-Homentropic Motion in One-Dimension

the cylinder end of the pipe is opened linearly to full pipe bore and closed again. The air inside the pipe is subjected to this change of boundary condition. It is assumed that the pressure and temperature in the cylinder simulate that of a real engine. The flow in the pipe is then analysed with the MOC and the results are reported at two points, marked 1 and 2 in Figure 3-11.

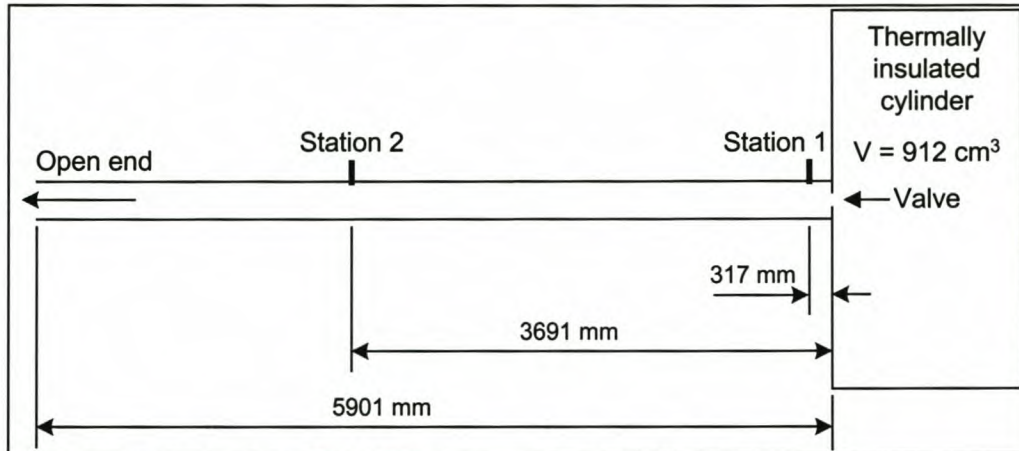


Figure 3-11: Diagram of the cylinder and pipe configuration

This example makes use of three boundary conditions: (1) valve outflow, (2) open end outflow and (3) a closed end when the valve is closed. These subroutines were included in a computer program, **Exhaust.exe**. The program was created in a Delphi4 compiler environment (program installation included on CD).

3.7.2.1. Test 1

In the first test the initial cylinder pressure and temperature are 1.5 bar and 293 K respectively. The conditions in the pipe, before the valve opens, are a pressure of 1 bar and a temperature of 293 K respectively. This condition usually exists in IC engines at low engine speeds or engines with a low compression ratio.

The pressures in the cylinder, point 1 and point 2, as well as the velocities at the two specified points are shown in Figures 3-13 and 3-14. It is clear from Figures 3-13 and 3-14 that a compression wave runs up the pipe and returns from the outflow open end as an expansion wave running down the pipe towards the cylinder.

In Figures 3-15 and 3-16 the pressure and velocity distributions are shown as contour graphs of time and position in the pipe.

Chapter 3: Unsteady Non-Homentropic Motion in One-Dimension

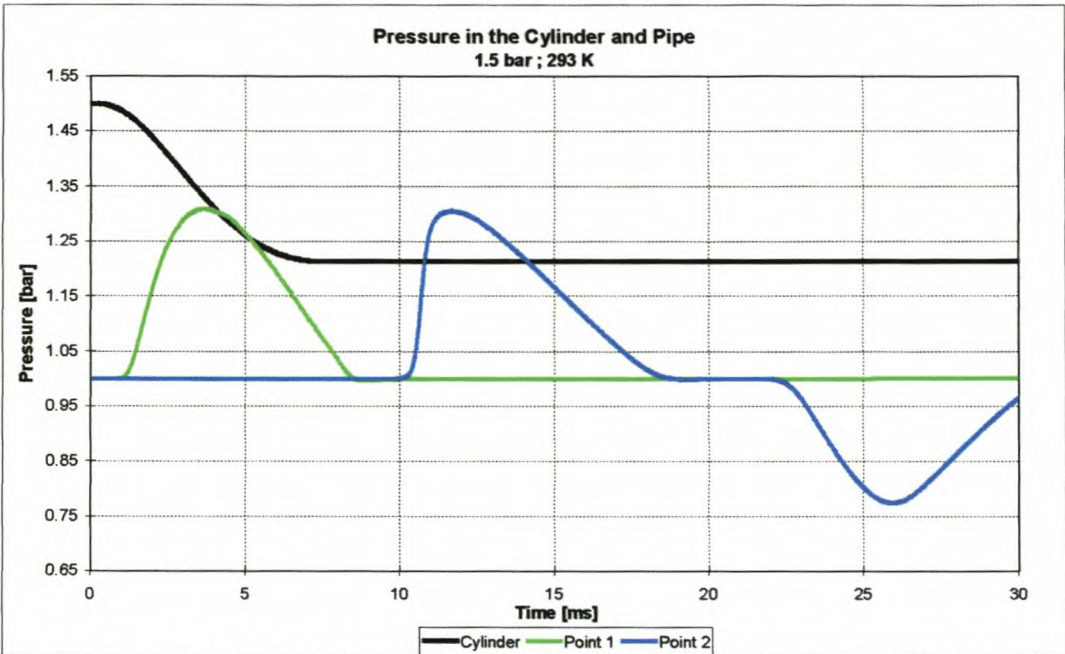


Figure 3-12: Pressure in the cylinder and at point 1 and 2 in the pipe

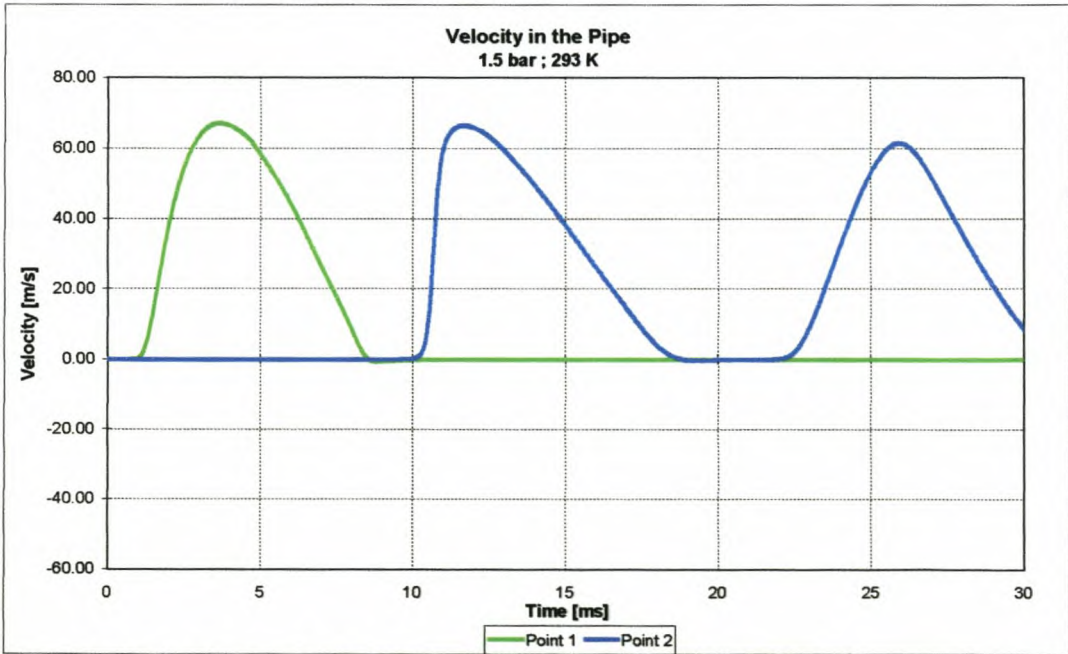
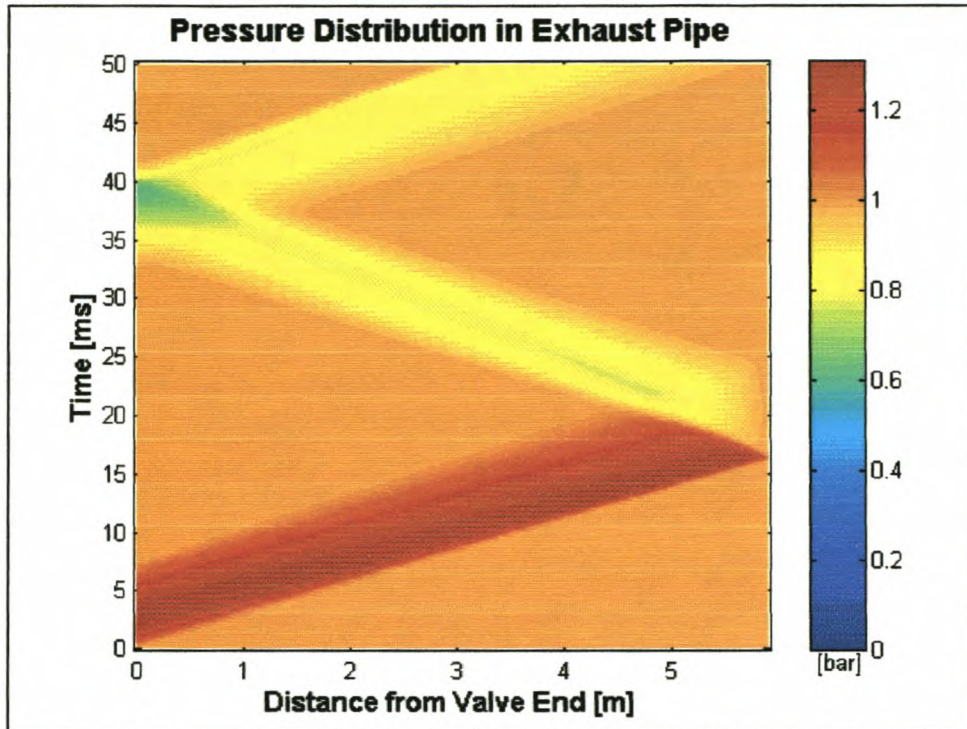
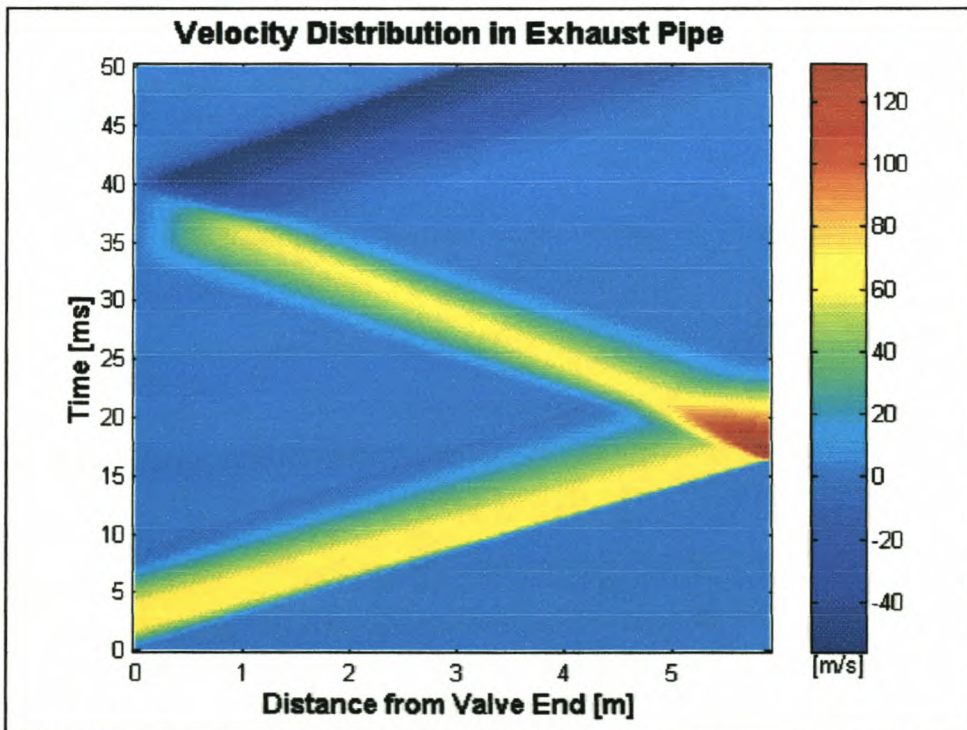


Figure 3-13: Velocity at point 1 and 2 in the pipe

More detailed information is presented in Appendix E at the cylinder and the two selected measurement points. Direct comparisons of the simulated data and the results presented by Kirkpatrick et al. [18] and Blair [40] are shown in Figures E-1 to E-3. Agreement between the two sets of results is good. Here also the differences that do exist can be attributed to the fact that not all the detailed information is available.

Chapter 3: Unsteady Non-Homentropic Motion in One-Dimension**Figure 3-14:** Pressure distribution in the pipe vs. time**Figure 3-15:** Velocity distribution in the pipe vs. time**3.7.2.2. Test 2**

In the second test the initial cylinder pressure and temperature are 2.4 bar and 293 K respectively. The conditions in the pipe, before the valve opens, are a pressure of 1 bar and a temperature of 293 K respectively. This condition

Chapter 3: Unsteady Non-Homentropic Motion in One-Dimension

usually exists in IC engines at higher engine speeds or engines with a high compression ratio and it is important to compare it to Test 1, because of the difference in pressure and the subsequent higher gas velocities.

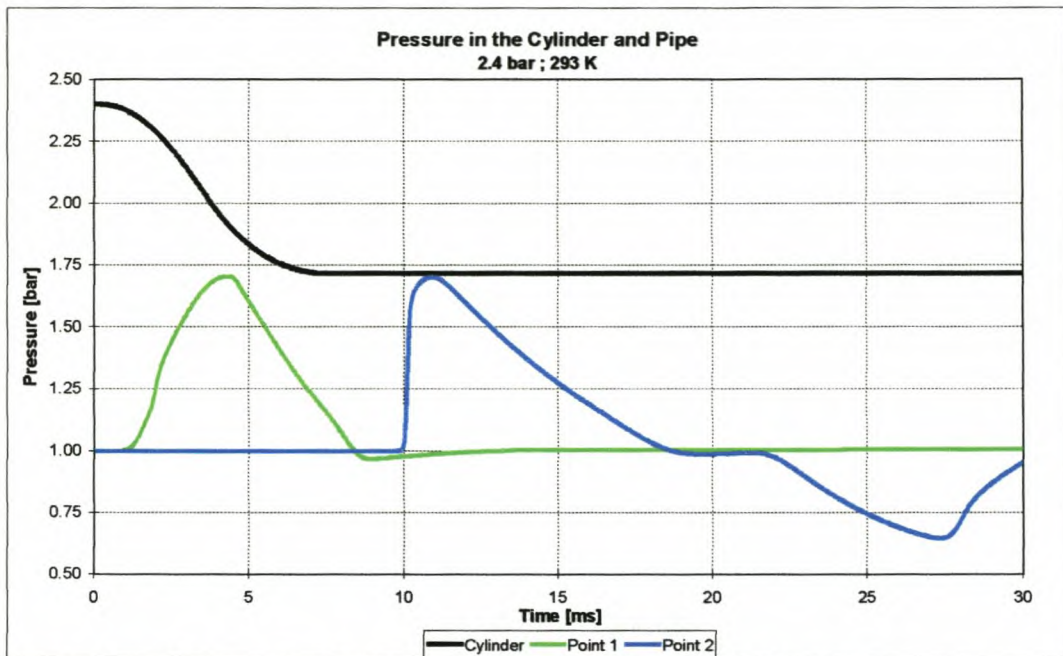


Figure 3-16: Pressure in the cylinder and at point 1 and 2 in the pipe

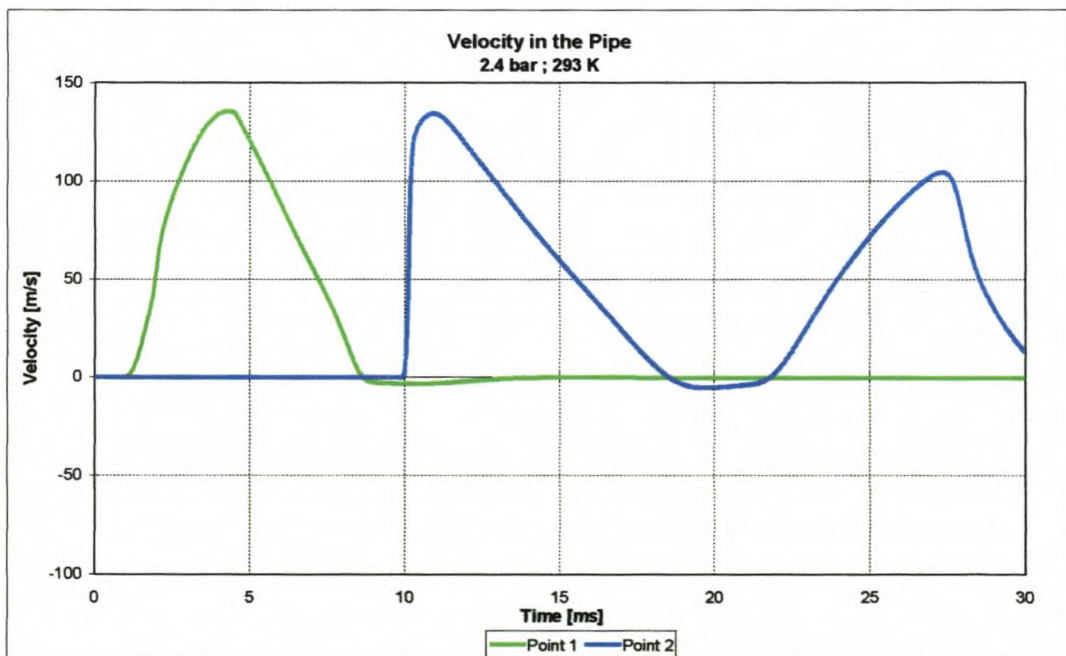


Figure 3-17: Velocity at point 1 and 2 in the pipe

The pressures in the cylinder, point 1 and point 2, as well as the velocities at the two specified points are shown in Figures 3-17 and 3-18.

It is clear from Figures 3-17 and 3-18 that a compression wave runs up the pipe and returns from the outflow open end as an expansion wave running down the

Chapter 3: Unsteady Non-Homentropic Motion in One-Dimension

pipe towards the cylinder. In Figures 3-19 and 3-20 the pressure and velocity distribution is shown as a contour graphs of time and position in the pipe.

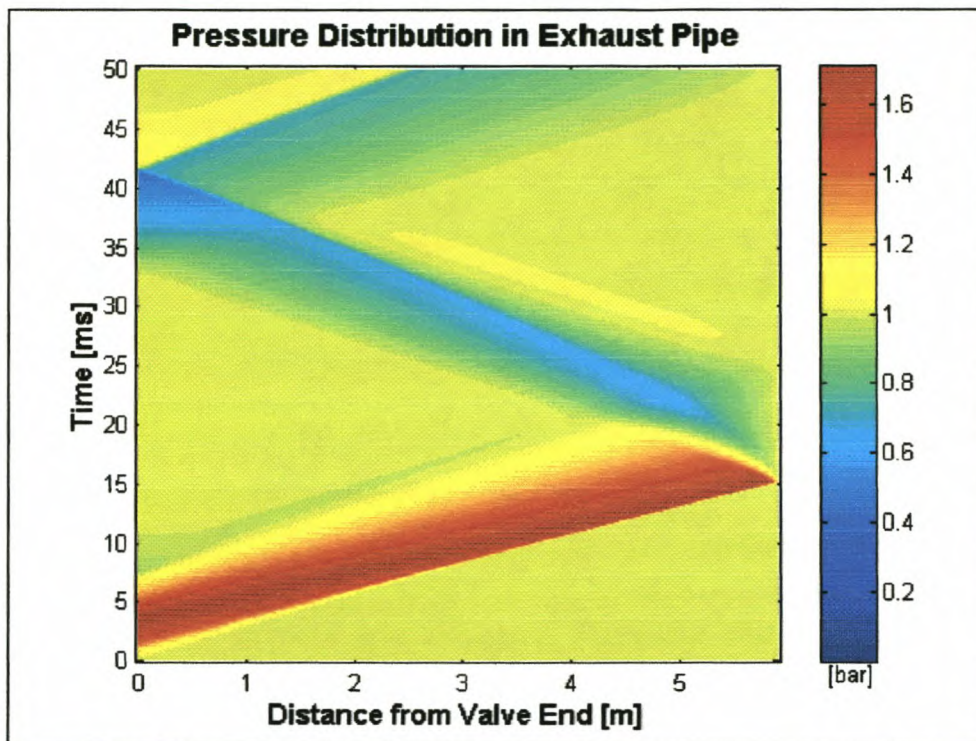


Figure 3-18: Pressure distribution in the pipe vs. time

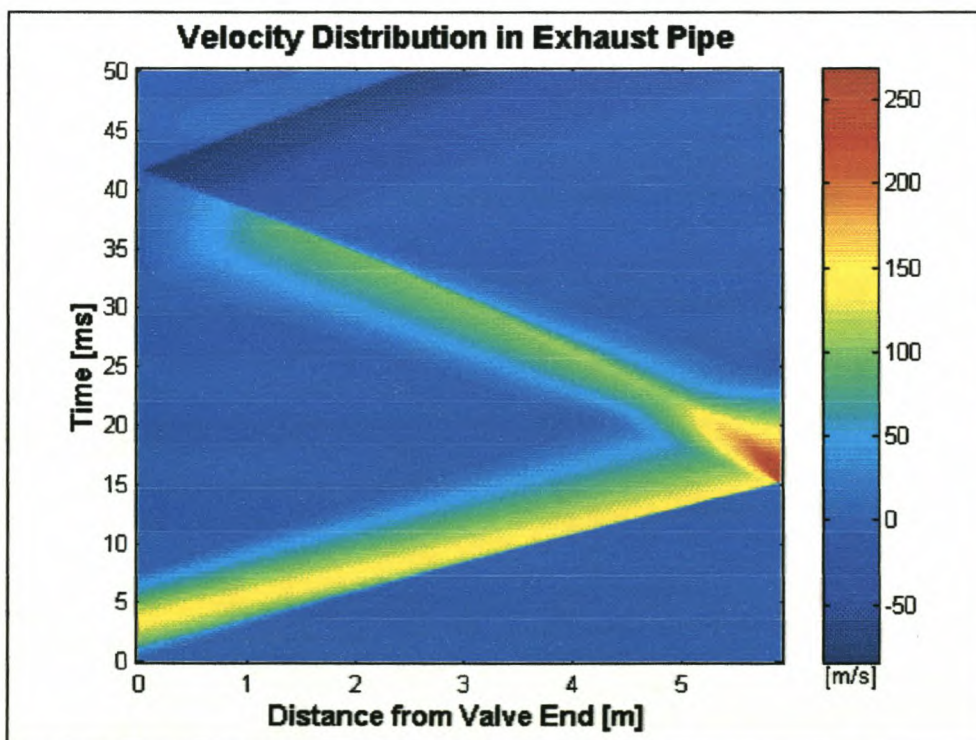


Figure 3-19: Velocity distribution in the pipe vs. time

Chapter 3: Unsteady Non-Homentropic Motion in One-Dimension

More detailed information is presented in Appendix E at the cylinder and the two selected measurement points. Direct comparisons of the simulated data and the results presented by Kirkpatrick et al. [18] and Blair [40] are presented in Figures E-4 to E-6. Once again good agreement between the two sets of results is found.

3.7.2.3. Test 3

In the third test the initial cylinder pressure and temperature are 2.0 bar and 473 K respectively. The conditions in the pipe, before the valve opens, are a pressure of 1 bar and a temperature of 293 K respectively. This condition needs to be compared to Tests 1 and 2, because of the difference in temperature and the subsequent change in gas velocity.

The pressures in the cylinder, point 1 and point 2, as well as the velocities at the two specified points are shown below in Figures 3-21 and 3-22.

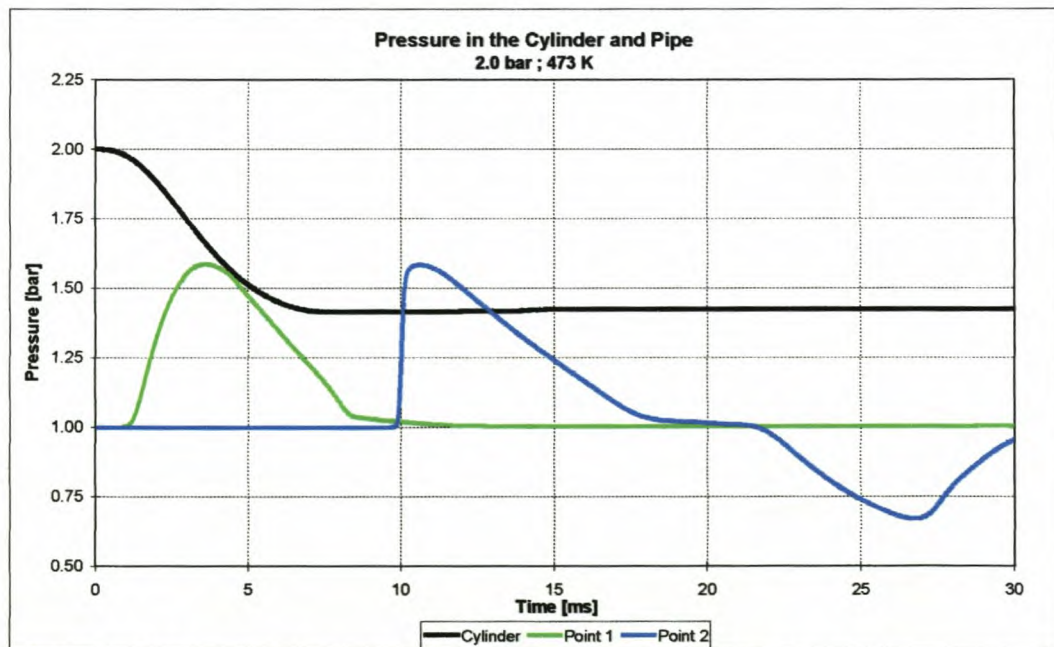
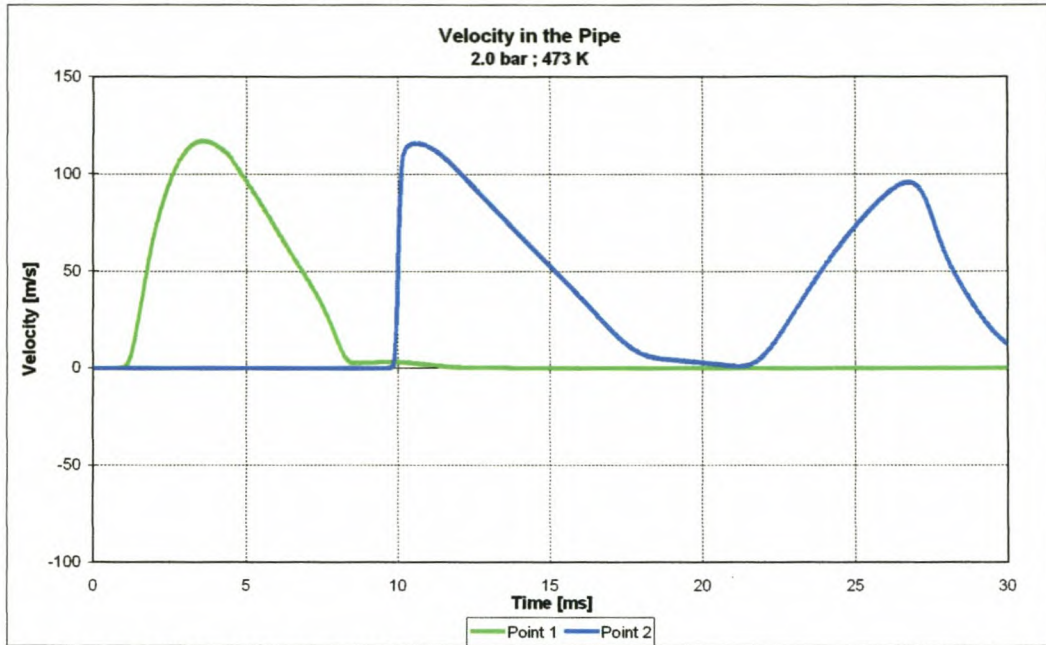
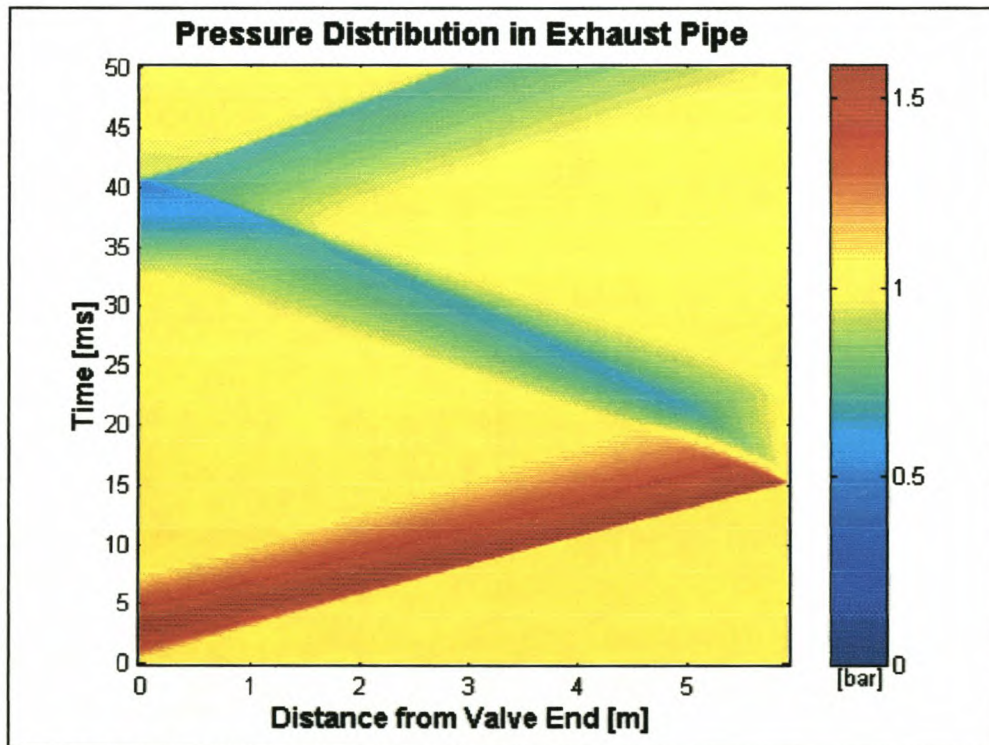


Figure 3-20: Pressure in the cylinder and at point 1 and 2 in the pipe

It is clear from Figures 3-21 and 3-22 that a compression wave runs up the pipe and returns from the outflow open end as an expansion wave running down the pipe towards the cylinder.

In Figures 3-23 and 3-24 the pressure and velocity distribution is shown as contour graphs of time and position in the pipe.

Chapter 3: Unsteady Non-Homentropic Motion in One-Dimension**Figure 3-21:** Velocity at point 1 and 2 in the pipe**Figure 3-22:** Pressure distribution in the pipe vs. time

More detailed information is presented in Appendix E at the cylinder and point 1. Direct comparisons of the simulated data and the results presented by Kirkpatrick et al. [18] and Blair [40] are presented in Figures E-7 to E-8. Once again good agreement between the two sets of results is found.

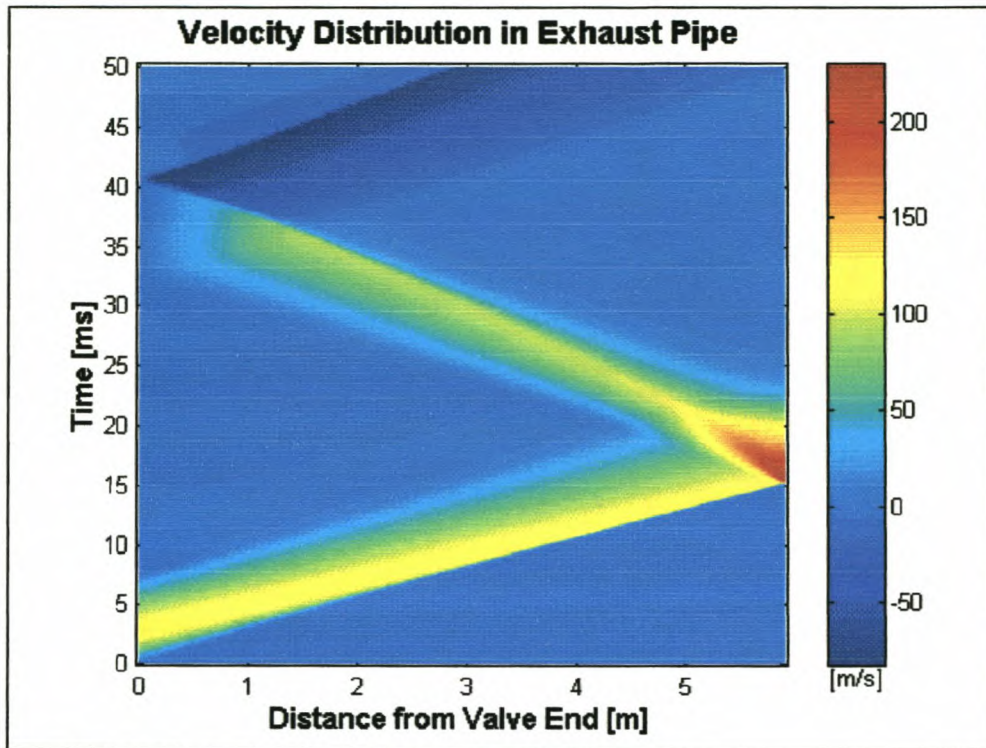
Chapter 3: Unsteady Non-Homentropic Motion in One-Dimension

Figure 3-23: Velocity distribution in the pipe vs. time

3.8. CLOSURE

In this chapter it was shown that the MOC could predict flow phenomena with friction losses and heat transfer quite accurately. The results obtained with the case studies compared well with the published data of Blair [18, 40]. This gave us confidence in the MOC for non-homentropic flow as well as the simulation of complex boundary conditions.

The simulation code developed in this chapter and Chapter 2 is used as the foundation for the final simulation software, Engine Simulation and Analysis (ESA). The further development of the ESA software is discussed in Chapter 4.

CHAPTER 4: ENGINE SIMULATION AND ANALYSIS (ESA) SOFTWARE

The development of computer based internal combustion engine models has been the subject of much research, particularly with the recent increases in memory capacity and computing power of both mainframe and personal computers. The internal combustion engine is primarily a thermodynamic system into which a fuel and air mixture is introduced, compressed and burned to release energy which is used for the expansion of a cylinder volume, producing torque at the crankshaft.

Modelling this system thus requires development of thermodynamic and gas flow models for compression, combustion, expansion, heat transfer, friction and transfer of gasses through the induction and exhaust systems of the engine.

Software codes for engines therefore make use of various models, from extremely simple empirical based theory, through single dimensional models to full three dimensional computational fluid dynamic calculations. Each step in this progression requires vast increases in processing power, the full CFD codes requiring extremely large mainframe computers for realistic processing time for even the simplest cases.

One-dimensional thermodynamic models for in-cylinder pressure [4] and temperature calculations are reasonably simple and have been used in PC based models (e.g. SPICE II [12] and DYNOMATION [13]) for many years now. Often these models make use of very simple in-cylinder and wave action codes to predict engine performance, given a simple set of engine dimensions and operating conditions. These simplifications are made in order to reduce processing time, for example to produce a simple torque curve in only a few minutes. Only recently have developments in personal computer capacity lead to the possibility of developing codes for the PC that can simulate the complex, unsteady, pulsed flows in manifolds.

ESA is an internal combustion engine simulation package developed during the course of this thesis. The flow chart of this simulation program is shown in Figure 4-1: it consists of a two-zone thermodynamic combustion model linked to a computation fluid dynamics manifold and pipe flow model and is also integrated

Chapter 4: Engine Simulation and Analysis (ESA) Software

with a camshaft analysis model. The combination of these three models allows accurate simulation of all the effects of variation of cam profiles, manifold and exhaust pipe dimensions as well as geometric, fuel and other properties of the engine and its environment.

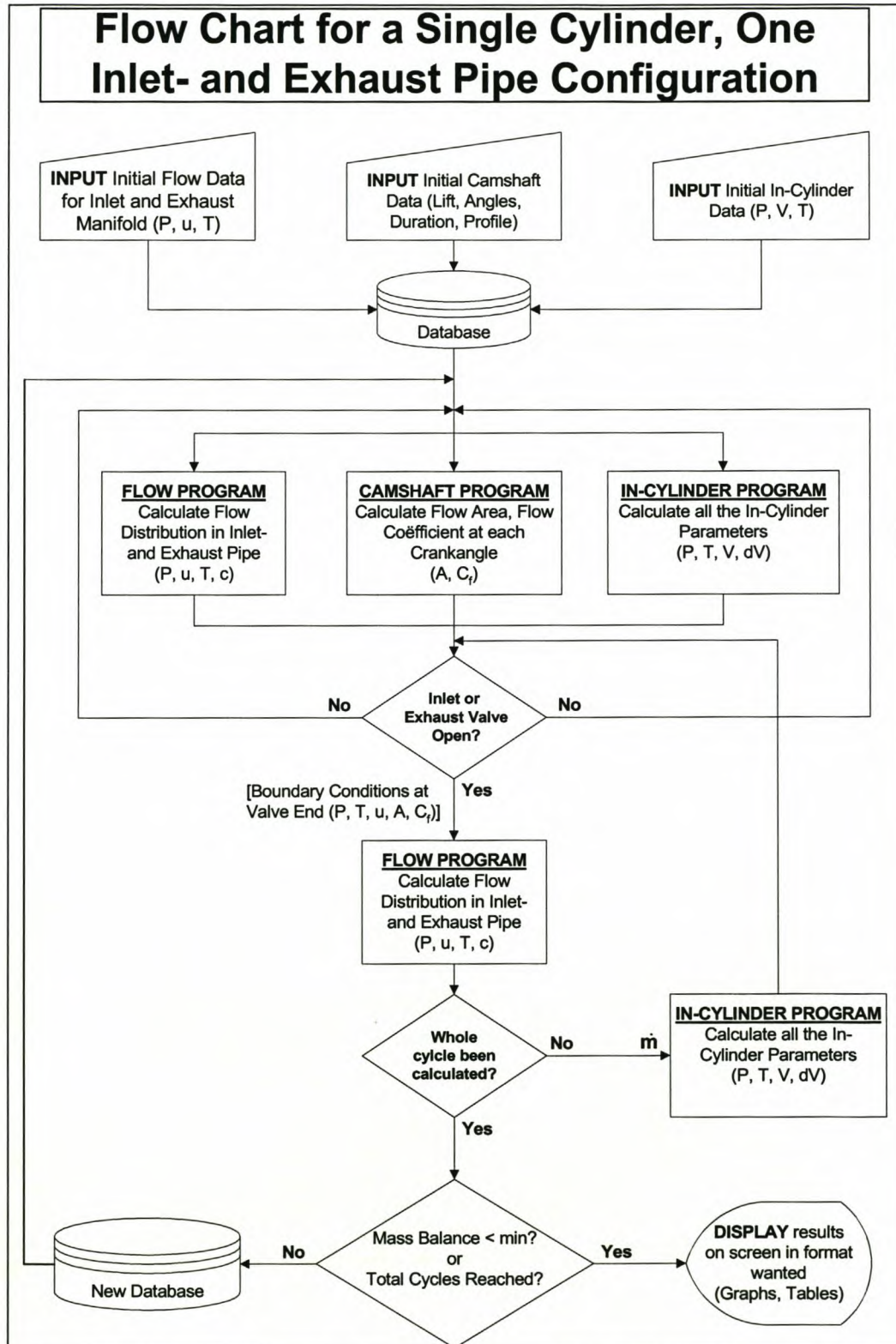


Figure 4-1: Flow chart of engine simulation computer model ESA

Chapter 4: Engine Simulation and Analysis (ESA) Software

The simulation program was developed as an engineering design tool. It can be used to optimise an existing or new engine, to study different design parameters, to further the understanding of the interactions between the engine and the inlet and exhaust systems and to determine the areas where research and development would be most beneficial.

4.1. MODEL OBJECTIVES

The objective of the simulation program is to enable a design engineer to test his proposed design on an interactive computer and to arrive at an optimum condition for the engine, designed to meet certain requirements. To reach this objective, the following requirements were set for the simulation program:

- Be flexible to accommodate automotive engines of various designs.
- Be capable of being geometrically versatile and as close as possible to the actual structure of the engine.
- Be capable of simulating a wide range of operating conditions.
- Produce results that can be used with confidence in the design process and compared to real engine data with a high degree of accuracy.

4.2. GENERAL ENGINE MODEL

4.2.1. Overview

The domain of the model extends from the plenum end of the inlet tract, through the manifold tract, inlet valves, cylinder, exhaust valves, and exhaust tract up to the first expansion of the exhaust at a silencer box or catalyst. It incorporates modelling of one cylinder only, with no interaction between cylinders in the form of pressure pulses being accounted for. The model computes simultaneous solutions of the governing equations of all the sub-models at small time steps throughout the 720 crankshaft degrees of the engine operation (4-stroke operation is assumed). These time-steps are chosen as one-crankshaft degree increments for ease of calculation, data-input and graphics display. The thermodynamic and flow conditions at the end of each time-step are calculated from the values at the previous time-step as well as the boundary conditions of the system, by use of an integration method.

Chapter 4: Engine Simulation and Analysis (ESA) Software

4.2.2. Initial conditions, time step and grid size

Initial gas properties in the intake system, exhaust system and in the cylinder are taken to be the atmospheric conditions. The simulation starts when the inlet valve closes and compression starts. This process and the rest of the simulation method are demonstrated by the flowchart in Figure 4-1.

Because time-steps are chosen as one-crankshaft degree increments, the time step varies according to engine speed. To maintain stability with a constant CFL number, this means that the grid sizes of the inlet and exhaust systems have to be changed at each engine speed. The grid size is changed in the program by entering a grid size equation, which is dependent on the engine speed and manifold length (Figures F-8 and F-10). A varying grid size has the drawback that comparisons at specific grid points in the manifolds at different engine speeds are not possible. It also results in a large grid size at high engine speed and small grid size at low engine speed. A small grid size has the drawback on result accuracy at low engine speeds. It has the inability to react to area changes at low engine speeds, because of the small number of grid points available to compute the unsteady flow. Nevertheless, at medium to high engine speeds the program produce accurate results that compare very well with test data, as shown in Chapters 5 and 6.

For each time-step the following calculations are carried out:

- Solution of equations of state to obtain the gas properties inside the cylinder.
- Solution of the pressures, temperatures and velocities present inside the inlet and exhaust tracts.
- Calculations of the mass flow through the valves, based on the pressure difference across the valve, the valve lift and valve discharge coefficient.
- A mass and energy balance inside the cylinder, with heat addition where there is combustion, and losses where there is heat transfer and friction.

The output of the engine can then be summed across the whole engine cycle.

4.2.3. Indicated output

The pressure vs. volume diagram of an engine is known as the indicator diagram. The area within this cycle is a measure of the work done by the

Chapter 4: Engine Simulation and Analysis (ESA) Software

combustion gas and is given by [1, 2, 3]

$$W_{ab} = \int_a^b P \cdot dV \quad (4.1)$$

where a and b are the start and end points of the calculation, usually defined in terms of engine crankshaft angle. In comparing the performance of internal combustion engines it is also useful if the terms used to express this performance, are independent of the size of the engine. For these reasons, the performance can be given in terms of mean effective pressures, defined as

$$MEP = \frac{W}{V_d} \quad (4.2)$$

where V_d is the displaced volume of the engine. Indicated Mean Effective Pressure (IMEP) is therefore defined as

$$IMEP = \frac{\int_{IVC}^{EVO} P \cdot dV}{V_d} \quad (4.3)$$

which is determined directly from the indicator diagram of the engine. We define Break Mean Effective Pressure (BMEP) as the MEP calculated from dynamometer measurable brake torque as follows

$$BMEP = \frac{\text{Work per rev}}{\text{Displ per rev}} = \frac{2\pi T}{V_d / 2} \quad (4.4)$$

for a 4-stroke engine.

Three other forms of MEP's can also be defined: Friction Mean Effective Pressure (FMEP), Pumping Mean Effective Pressure (PMEP) and Auxillary Mean Effective Pressure (AMEP), which are the power losses to engine friction, gas pumping and engine auxiliaries (not implemented in ESA) respectively. We can then write the following expression [1, 2, 3]:

$$IMEP = BMEP + PMEP + FMEP + AMEP \quad (4.5)$$

and show that the mechanical efficiency of the engine is equal to

$$\eta_{mech} = \frac{BMEP}{IMEP} \quad (4.6)$$

These performance indicators, equations (4.1) to (4.6), provide the framework for determination of the results (Section 4.2.9) of the ESA model.

Chapter 4: Engine Simulation and Analysis (ESA) Software

4.2.4. Combustion gas properties

The fuel / air mixture inside the cylinder is divided into two zones, a burned zone and an unburned zone (Figure 4-2). The instantaneous gas properties of each of these zones are calculated and stored separately, the exception being the pressure, which is assumed uniform throughout the cylinder, and is therefore identical for the two zones. Equilibrium gas properties are assumed, because the reactions take place on a time scale far smaller than that present in the engine combustion process [15].

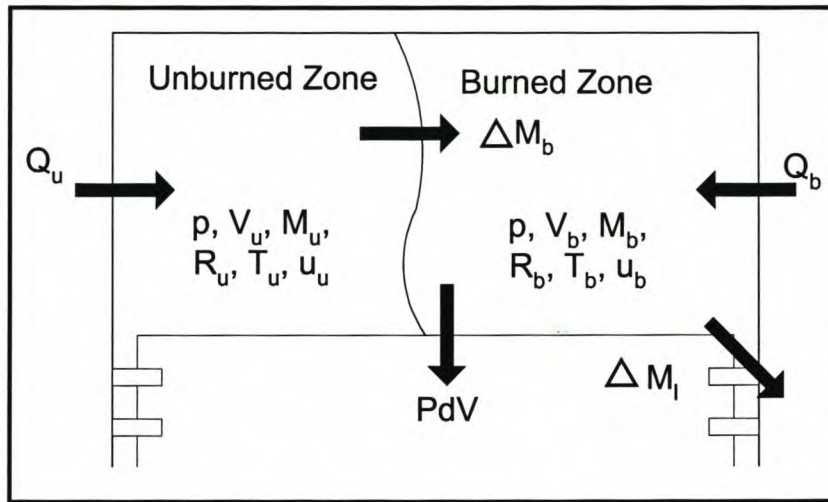


Figure 4-2: Two-zone combustion model

This in-cylinder model, developed by Williams [15], is an extension of the model of Bell [42], which is based on the model of Olikara and Borman [41].

4.2.5. Cylinder combustion and volume

The thermodynamic model is based on an energy balance within the cylinder, a control volume with a moving wall. At completion of this balance, the energy produced by the engine in terms of indicated mean effective pressure (IMEP) is calculated from an integration of the energy transferred to the piston as work. After deduction of losses, this is used to calculate engine torque and thus power. The cylinder combustion model is based on the first law of thermodynamics for a varying adiabatic control volume having a uniform state [4]:

$$\frac{dQ_c}{dt} - p_c \frac{dV_c}{dt} = \frac{\partial}{\partial t}(m_c e_c) - h_a \left(\frac{dm}{dt} \right)_a + h_e \left(\frac{dm}{dt} \right)_e \quad (4.7)$$

Mass enters and leaves the control volume at a rate determined by conditions in the cylinder, the manifolds and the valve flow area. Now the rate of change of

Chapter 4: Engine Simulation and Analysis (ESA) Software

cylinder pressure is a function of the intake and exhaust mass flow rates, the cylinder pressure and volume, the rate of change of cylinder volume and the stagnation speeds of sound:

$$\frac{dp_c}{dt} = \frac{1}{V_c} \left[c_a^2 \left(\frac{dm}{dt} \right)_a - c_e^2 \left(\frac{dm}{dt} \right)_e - \gamma p_c \frac{dV_c}{dt} + (\gamma - 1) \frac{dQ_c}{dt} \right] \quad (4.8)$$

The cylinder volume and the rate of change of the cylinder pressure at a given crank angle are determined from the engine dimensions. The cylinder volume, V , and rate of change of cylinder volume, $\frac{dV}{dt} = \omega \frac{dV}{d\theta}$ are calculated from the geometry of the standard piston, conrod, and crankshaft. Heywood [2] shows that

$$\frac{V}{V_c} = 1 + \frac{1}{2} (R_c - 1) \left[R + 1 - \cos\theta - (R^2 - \sin^2\theta)^{\frac{1}{2}} \right] \quad (4.9)$$

where $R = \frac{2l}{s}$ is the ratio of conrod length to crank radius (stroke/2). The cylinder clearance volume can be calculated from the compression ratio and the swept volume as

$$V_c = \frac{R_c}{R_c + 1} \left(\frac{\pi b^2 s}{4} \right) \quad (4.10)$$

The cylinder volume at a given crank angle can then be calculated as

$$V(\theta) = \left(\frac{R_c}{R_c + 1} \left(\frac{\pi b^2 s}{4} \right) \right) \cdot \left\{ 1 + \frac{1}{2} (R_c - 1) \left[\frac{2l}{s} + 1 - \cos\theta - \left(\left(\frac{2l}{s} \right)^2 - \sin^2\theta \right)^{\frac{1}{2}} \right] \right\} \quad (4.11)$$

The term $dV/d\theta$ is then obtained by taking the derivative of equation (4.11) with respect to crank angle and it reduces to

$$\frac{dV}{d\theta} = \frac{\pi b^2 s}{8} \sin\theta \cdot \left(1 + \frac{\frac{s}{2l} \cos\theta}{\sqrt{1 - \left(\frac{s}{2l} \sin\theta \right)^2}} \right) \quad (4.12)$$

Chapter 4: Engine Simulation and Analysis (ESA) Software

4.2.6. Heat loss

Heat loss occurs due to heat transfer to the walls of the cylinder, piston and head of the engine. This heat is then transferred to the cooling water of the engine, or, in the case of an air-cooled engine, to the air passing over the cooling fins of the cylinder head and sleeve. Models for this heat transfer vary from complex multiple resistance to simple empirical based models. The basic heat transfer equation is

$$\frac{dQ_l}{dt} = h \cdot A \cdot (T_{gas} - T_{wall}) \quad (4.13)$$

In this equation, the wall temperature is known from the input data, and the gas temperature and contact area from the flow model. The heat transfer coefficient is calculated from equations (3.15) and (3.16).

4.2.7. Engine friction

The Total Friction Mean Effective Pressure (TFMEP) is calculated using a simplistic speed based model [2]. This is given by

$$TFMEP = 0.97 + 0.15 \frac{N}{1000} + 0.05 \left(\frac{N}{1000} \right)^2 \quad (4.14)$$

where N is engine speed in rpm. As this definition of TFMEP includes the pumping work, the PMEP as calculated in Section 4.2.9, equation (4.15), is subtracted from this to obtain FMEP. This is also a simplistic approach, and in the case of a detailed development, the user should measure the engine friction and modify this equation accordingly.

4.2.8. Flow through valves

Flow through engine ports has generally been calculated by use of the quasi-steady flow approximation that assumes that steady-flow equations and steady-flow coefficients may be applied at each instant. Evaluation of this assumption is hampered by the lack of sound methods to determine instantaneous values of unsteady mass flow rate experimentally.

One of the obstacles during this thesis was therefore to get reliable discharge coefficient data for valves. Many papers have been published on valve discharge coefficients, but up to now all the data presented is measured on a steady-state flow bench [18, 22, 40]. No data could be found on C_d -values

Chapter 4: Engine Simulation and Analysis (ESA) Software

measured under unsteady flow conditions. Discharge coefficient valve data by Williams [15], was used in the simulation model and for all the modelled examples.

4.2.9. Performance calculations

The performance calculations are performed at the end of the simulation for comparison of different engine configurations. During the engine cycle the following equations are summed or integrated.

$$PMEP = \frac{\int_{EVO}^{IVC} P dV}{V_d} \quad (4.15)$$

$$\dot{m} = \int_{IVO}^{IVC} \dot{m}_{in} d\theta = \int_{EVO}^{EVC} \dot{m}_{out} d\theta \quad (4.16)$$

$$Q = \int_{EVO}^{IVC} (\dot{Q}_b + \dot{Q}_v) d\theta \quad (4.17)$$

Note that Mass Flow In = Mass Flow Out (a mass balance) is the measure of convergence of the solution. When the mass balance is less than 0.5%, the solution is regarded as converged. This is usually reached within 5 to 10 simulation cycles.

Equations (4.3), (4.5) and (4.13) are used to calculate the BMEP. From equation (4.4), the torque and power for a 4-stroke engine are calculated as

$$T = \frac{BMEP \times V_d \times N_{cyl}}{4\pi} \quad (4.18)$$

$$P = \frac{2 \times T \times N \times \pi}{60} \quad (4.19)$$

where V_d is the displaced volume of one cylinder, N_{cyl} is the number of cylinders and N is the engine speed in rpm.

The volumetric efficiency is calculated as discussed in Chapter 1 [1, 2, 3]

$$\eta_{vol} = \left[\frac{m_{IVC}}{\left(\frac{P_{atm} V_d}{R_{atm} T_{atm}} \right)} \right] \times \frac{100}{1} \quad (4.20)$$

Chapter 4: Engine Simulation and Analysis (ESA) Software

The fuel consumption is calculated from

$$\dot{m}_f = \dot{m}_{in} \times \frac{1}{AF + 1} \times \frac{2 \times N}{60} \quad (4.21)$$

and the specific fuel consumption is given by

$$SFC = \frac{\dot{m}_f}{P} \quad (4.22)$$

The thermal efficiency is calculated from

$$\eta_{thermal} = \frac{P}{\frac{2 \cdot N}{60} \cdot Q_{fuel} \cdot m_{fuel}} \times \frac{100}{1} \quad (4.23)$$

Equations (4.1) to (4.23) are all used in the ESA program code to calculate different engine performance parameters. These engine parameters are displayed by ESA at the completion of a simulation as illustrated in Appendix F.

4.3. COMPUTER IMPLEMENTATION

4.3.1. Introduction

The computer code for the model was written in Pascal in the object oriented 32 bit Borland Delphi 4 environment and compiled to a user friendly, full 32 bit Windows 95/98 and NT application. The code is in the form of a self-contained object, driven from the main engine simulation interface. The object contains the in-cylinder code simulating combustion chamber properties from inlet valve closure to exhaust valve opening as well as the routines to interface with the manifold flow code during the valve events.

4.3.2. Computer hardware and installation procedure

One of the challenges of this thesis was to write a simulation program that could run efficiently on a personal computer. The program runs on any Pentium PC, but it is important to note that better hardware (memory, CPU and graphics card) enables the user to run simulations faster. Throughout the programming phase it was clear that the biggest limitation of the running speed of the ESA software, is not the processor speed of the computer, but the graphics speed of the SVGA card (if running with graphs on). Most of the tests were therefore run with no graphics display during simulations. The graphics would only update and show at completion of a simulation run.

Chapter 4: Engine Simulation and Analysis (ESA) Software

4.4. CONCLUSIONS

Throughout the development and evaluation period of the ESA software it was clear that an accurate engine data file and using good boundary condition assumptions were necessary to produce accurate results.

The ESA software has already been used extensively on different engine configurations and has been proven to be versatile and accurate. This is illustrated in Chapters 5 and 6 where comparisons between the data obtained from actual engine tests are compared with that predicted by means of the ESA software.

Chapter 5: Experimental Verification Testing

CHAPTER 5: EXPERIMENTAL VERIFICATION TESTING

In design engineering, a theoretical simulation process that has not been checked for accuracy against relevant experiments is, depending on its intended purpose, at best potentially misleading and at worst inapplicable as a design tool. In this chapter some experiments that were done to provide data for testing the ESA software, are described.

5.1. ENGINE SETUP

The engine used for the experiments is a modified Nissan four cylinder carburettor, 8-valve, over-head cam, 2.4ℓ with a Nissan Z24 block and Nissan NA20 head, cross-flow engine. Its inlet manifold was changed to a purpose-designed, fabricated fuel injection inlet manifold (Figure 5-1), because of more freedom in the intake system design, better mixture distribution and better response. Each cylinder has its own inlet pipe, connected to a common intake chamber or plenum that opens to atmosphere through a short air duct.

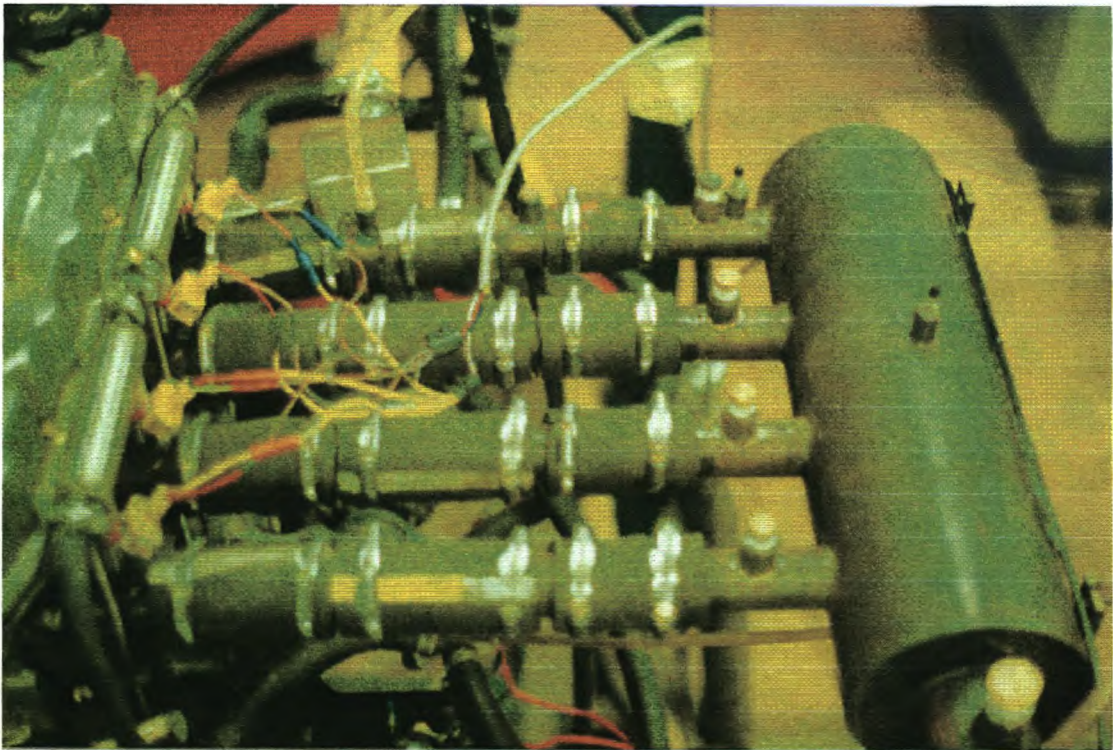


Figure 5-1: New fuel injected inlet manifold installed on engine

The manifold allows the length of the inlet pipes to be varied in 100mm increments from 210 to 410mm. The manifold also allows isolation of a single inlet

Chapter 5: Experimental Verification Testing

pipe from the remaining 3 pipes when necessary. Fuel injection nozzles were mounted on all inlet pipes, and pressure fittings were located in the plenum of the manifold and at different positions along the inlet pipe of cylinder 1. The detailed manifold drawings are presented in Appendix G. The manifold was also equipped with high-speed DYTRAN dynamic pressure sensors that were used to measure the pressure pulses in the manifold (Figure G-7).

Outputs from the dynamic pressure sensors shown in Figure 5-2 were recorded every degree of crank angle during 89 cycles. This data was translated and recorded using a high-speed data-acquisition system called RACER (Rapid Acquisition of Combustion and Engine Results) [43] running on a separate computer to the one controlling and monitoring the engine and the computer running the engine control unit (ECU).

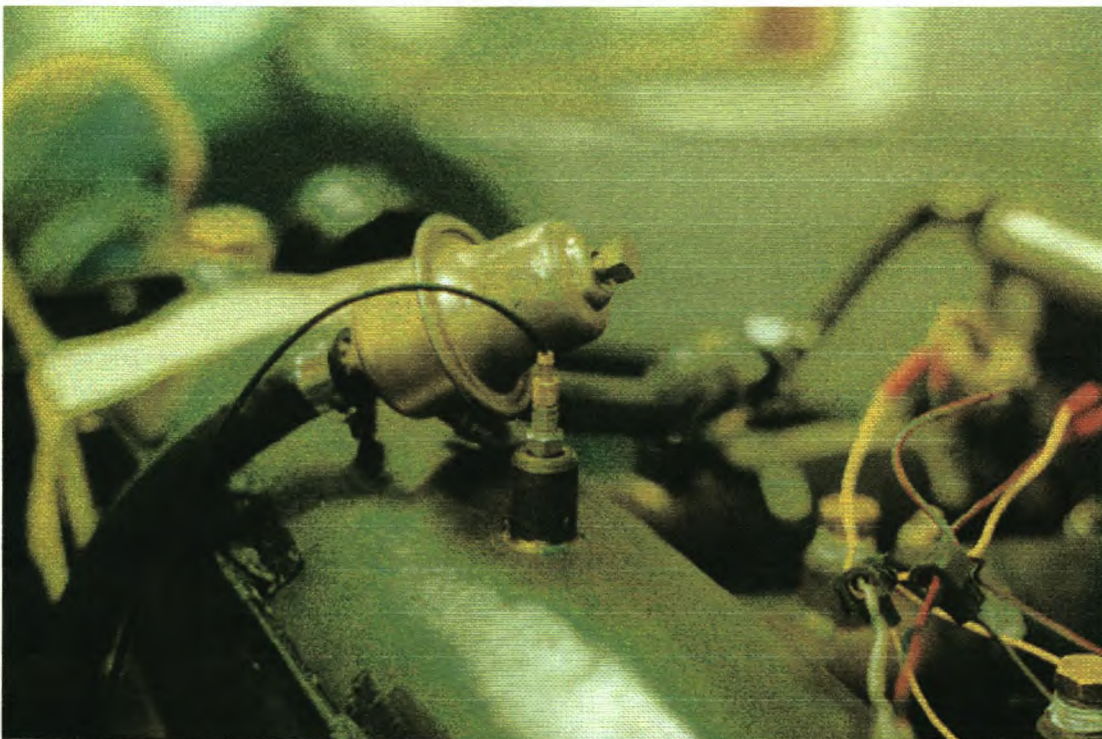


Figure 5-2: Pressure transducer installed in inlet manifold plenum

A Dupec Defita 2000 ECU, controlled the fuel injection system and ignition timing. Hall-effect pickups on a degree-wheel and a TDC mark on the crankshaft provided crank-angle reference to RACER and inlet manifold pressure data were averaged over 89 engine cycles. An additional exhaust manifold and exhaust system were also fabricated, allowing isolation of one cylinder from pulses present in the other cylinders exhaust pipes (Figures 5-3 and 5-4).

Chapter 5: Experimental Verification Testing

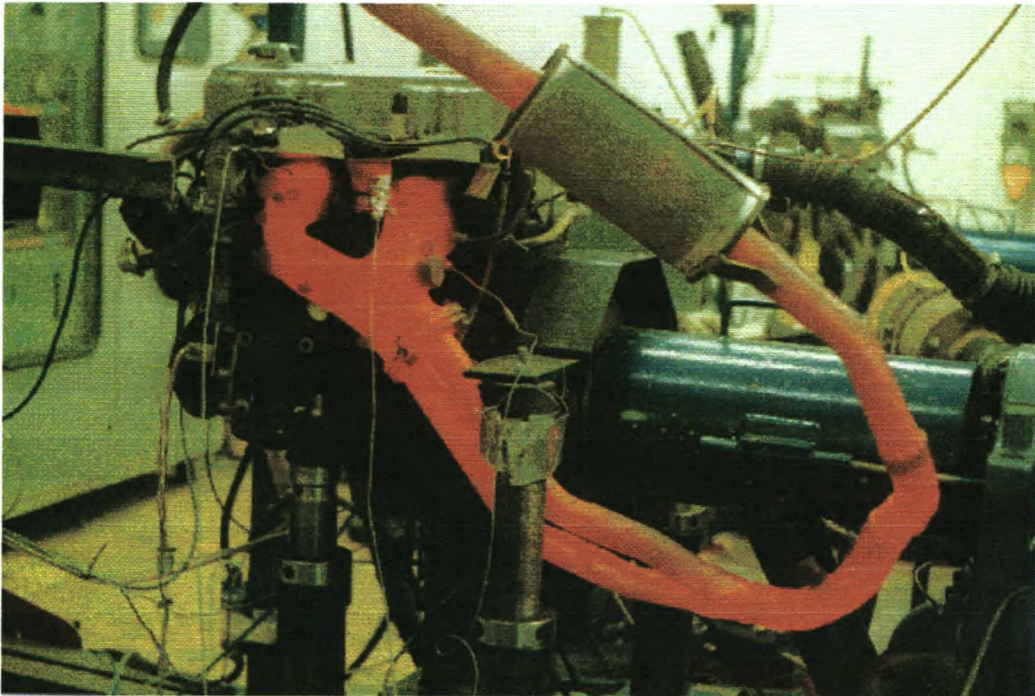


Figure 5-3: Standard exhaust system (4-2-1)



Figure 5-4: New modified exhaust system

Chapter 5: Experimental Verification Testing

Measurements recorded also included manifold absolute pressure, exhaust CO (carbon monoxide), spark advance, brake torque, as well as engine oil, water and exhaust temperatures. To get velocity results of the flow in cylinder 1 turned out to be quite a problem. The only equipment available for this measurement was a hotwire anemometer probe. This equipment is unfortunately very fragile and the heating element kept breaking, because of the severe pulses in the inlet manifold. Because no other equipment was available and the engine setup such that the pulses could not be changed, no velocity recordings could be made. The pressure and performance measurements from the engine are found to be sufficient to compare with the ESA software, though.

5.2. TESTING PROCEDURE

The entire testing procedure was divided into 7 tests as summarised in Table 5.1. The details of the tests were as follows:

- **Test 1**

The Nissan test engine was set up with the standard Nissan exhaust system (Figure 5-3) and with the designed inlet manifold (Figure 5-1). The inlet manifold was connected to the engine in normal working method with all four pipes connected to the head of the engine and to the manifold plenum. The ignition timing and fuel injection of the engine was mapped with the Dupec ECU system for each engine speed at full load condition, to obtain optimum performance with the specified setup.

The custom-made inlet manifold was setup with a length of $\pm 210\text{mm}$ from the cylinder head to the plenum. This gave a total inlet flow length of $\pm 290\text{mm}$. The DYTRAN pressure transducers were installed in the manifold to measure pressure traces at points A, B and C. A is situated at the cylinder head ($\pm 10\text{mm}$ from the cylinder head face), B is situated at the entry to the plenum ($\pm 210\text{mm}$ from the cylinder head face) and C is situated at the top of the plenum chamber to measure pressure variation in the manifold plenum.

- **Test 2**

The engine setup and testing procedure were similar to Test 1, except for increasing the inlet manifold length by 100mm by adding a piece of inlet pipe, connected with rubber mountings. The inlet manifold length was increased to

Chapter 5: Experimental Verification Testing

$\pm 310\text{mm}$ from cylinder head to plenum. This gave a total inlet flow length of $\pm 390\text{mm}$.

The DYTRAN pressure transducers were installed in the manifold to measure pressure traces A, B, C and D. A is situated at the cylinder head ($\pm 10\text{mm}$ from the head face), B is situated in the middle of the inlet pipe ($\pm 160\text{mm}$ from the head face), C is situated at the plenum ($\pm 310\text{mm}$ from the head face) and D is installed at the top of the manifold plenum volume.

• Test 3

The engine setup and testing procedure were similar to Tests 1 and 2, except for increasing the inlet manifold length by another 100mm by adding a piece of inlet pipe, connected with rubber mountings. The inlet manifold length was increased to $\pm 410\text{mm}$ from cylinder head to plenum. This gave a total inlet flow length of $\pm 490\text{mm}$.

A DYTRAN pressure transducer was installed in the manifold to measure the pressure trace at point A. A is situated at the cylinder head ($\pm 10\text{mm}$ from the head face).

After the completion of the pressure measurements, the exhaust system was changed to the custom designed exhaust system (Figure 5-4) to try and isolate cylinder 1 from the other 3 cylinders. The engine was re-mapped (ignition timing and fuel injection were modified for each engine speed at full load conditions) for the new exhaust system and the pressure measurements at point A was recorded.

• Test 4

The engine setup and testing procedure were similar to Tests 1, 2 and 3. The manifold on the plenum side was then shifted 1 pipe left towards cylinder 4. The open piece of pipe on the plenum end was blanked-off. The inlet pipe on cylinder 1 was now open to the atmosphere (Figure 5-5). This setup would ensure that cylinder 1 is as close as possible to a single cylinder setup. This would benefit the correspondence of pressure data between the ESA model and actual measured data.

The inlet manifold length was kept at $\pm 410\text{mm}$ from cylinder head to the atmosphere, keeping a total flow length of $\pm 490\text{mm}$.

Chapter 5: Experimental Verification Testing

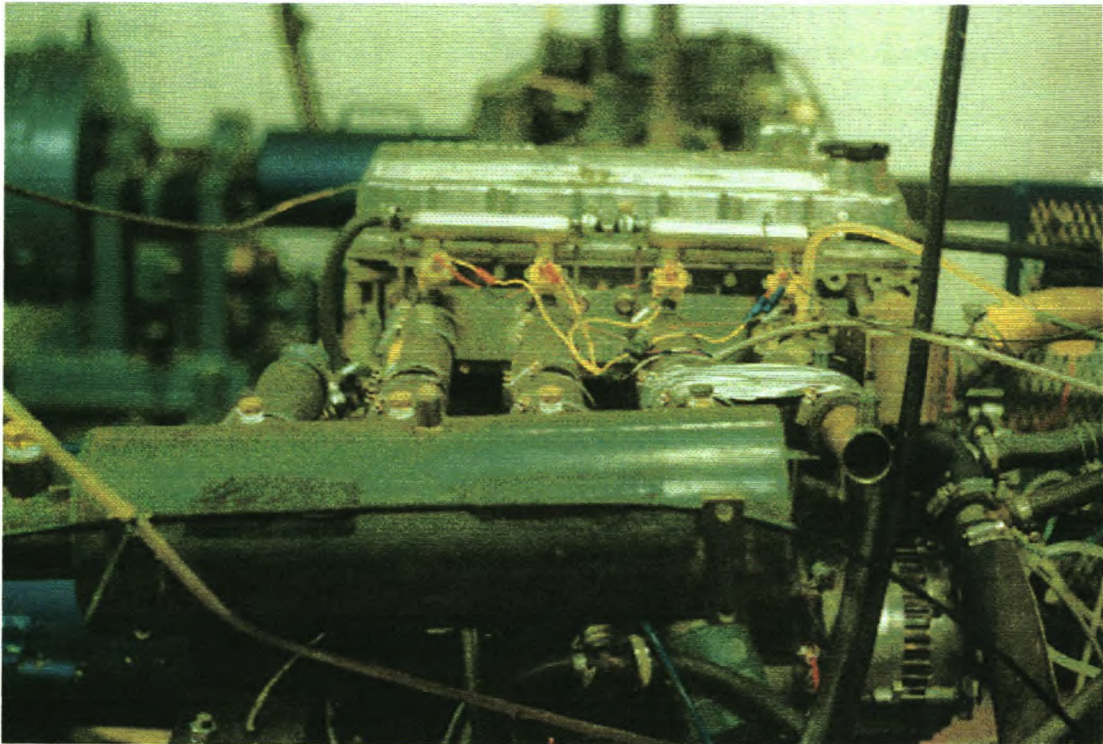


Figure 5-5: Inlet manifold modified to isolate cylinder 1



Figure 5-6: Pressure transducer at pipe open end

Pressure traces at points A, B and D were measured. A is situated at the cylinder head ($\pm 10\text{mm}$ from the head face), B is situated in the middle of the

Chapter 5: Experimental Verification Testing

inlet pipe ($\pm 160\text{mm}$ from the head face) and D is situated $\pm 10\text{mm}$ from the pipe open end at the atmosphere ($\pm 410\text{mm}$ from the head face) as illustrated in Figure 5-6.

• **Test 5**

The engine setup and testing procedure were similar to Test 4, except for decreasing the inlet length by 100mm to an inlet manifold length of $\pm 310\text{mm}$ from cylinder head face to atmosphere and a total inlet flow length of $\pm 390\text{mm}$. The pressure trace was recorded at point A. A is situated at the cylinder head ($\pm 10\text{mm}$ from the head face).

• **Test 6**

The engine setup and testing procedure were similar to Tests 4 and 5, except for decreasing the inlet length by another 100mm to an inlet manifold length of $\pm 210\text{mm}$ from cylinder head to atmosphere and a total inlet flow length of $\pm 290\text{mm}$. Pressure in the inlet manifold was measured similar to Test 5 at point A.

• **Test 7**

The engine setup and testing procedure were similar to Test 6. The camshaft was indexed and caused the camshaft to advance by 12° crank angle. Pressure in the inlet manifold was measured similar to Tests 5 and 6 at point A.

Table 5.1: Summary of testing procedure

Test	Inlet system	Exhaust system	Camshaft	Pressure measurement point(s)
1	Custom inlet; 210 mm	Std. Nissan exhaust	Std. setup	A, B, C
2	310 mm	Std. Nissan exhaust	Std. setup	A, B, C, D
3a	410 mm	Std. Nissan exhaust	Std. setup	A
3b	410 mm	Custom exhaust	Std. setup	A
4	Modified inlet; 410 mm	Custom exhaust	Std. setup	A, B, D
5	310 mm	Custom exhaust	Std. setup	A
6	210 mm	Custom exhaust	Std. setup	A
7	210 mm	Custom exhaust	12° CA advance	A

Chapter 5: Experimental Verification Testing

During all these tests a dedicated PC recorded all the engine parameters e.g. torque, power, exhaust temperature, etc., monitored the engine and would stop the engine if an alarm were signalled. Using the Dupec ECU software, the injection timing and ignition timing of the fuel injection system was optimised at each engine speed and full load condition.

5.3. TEST RESULTS

All the engine performance graphs and pressure trace results, tested and ESA simulated, are presented in Appendixes H and I. Only some of the results will be discussed in this section.

5.3.1. ESA simulation setup

For the ESA simulation to be used confidently, some detailed information was needed, as explained in Chapter 4. Some of the engine information e.g. exhaust temperatures and pressures, ignition timing, etc. were only available after completion of the engine testing and some physical engine detail had to be obtained using drawings, engine handbooks, etc. The following physical engine information was used for all the ESA simulations:

- Bore = 89 mm
- Stroke = 96 mm
- Conrod Length = 165 mm
- Compression Ratio = 8.3
- Inlet Valve Diameter = 38 mm
- IVO = 20° BTDC
- IVC = 40° ABDC
- Inlet Valve Lift = 9.5 mm
- Exhaust Valve Diameter = 34 mm
- EVO = 60° BBDC
- EVC = 30° ATDC
- Exhaust Valve Lift = 9.5 mm
- Burnangle = 55° CA
- A/F Ratio = 14.5
- QFuel = 43 MJ/kg
- Atmospheric Temperature = 25° C

Chapter 5: Experimental Verification Testing

This information was used as basis for the entire group of ESA engine files. More detailed information can be found in any of the Nissan engine simulation files, *.eng, supplied on the installation CD.

5.3.2. Engine performance test results

The one objective of the engine tests is to obtain performance data that can be compared to the results created by the ESA software. The engine is also used to investigate the effect of inlet manifold length on engine torque. This change in engine setup is also evaluated with the results created by the ESA software. In Figures H-1 to H-4 the engine performance with different inlet manifolds, exhaust systems and camshaft setup are shown. Figures H-5 and H-6 illustrate the results created by ESA. From Figure 5-7 the difference between the fuel injected, new manifold Nissan engine and standard carburettor engine are presented. It is

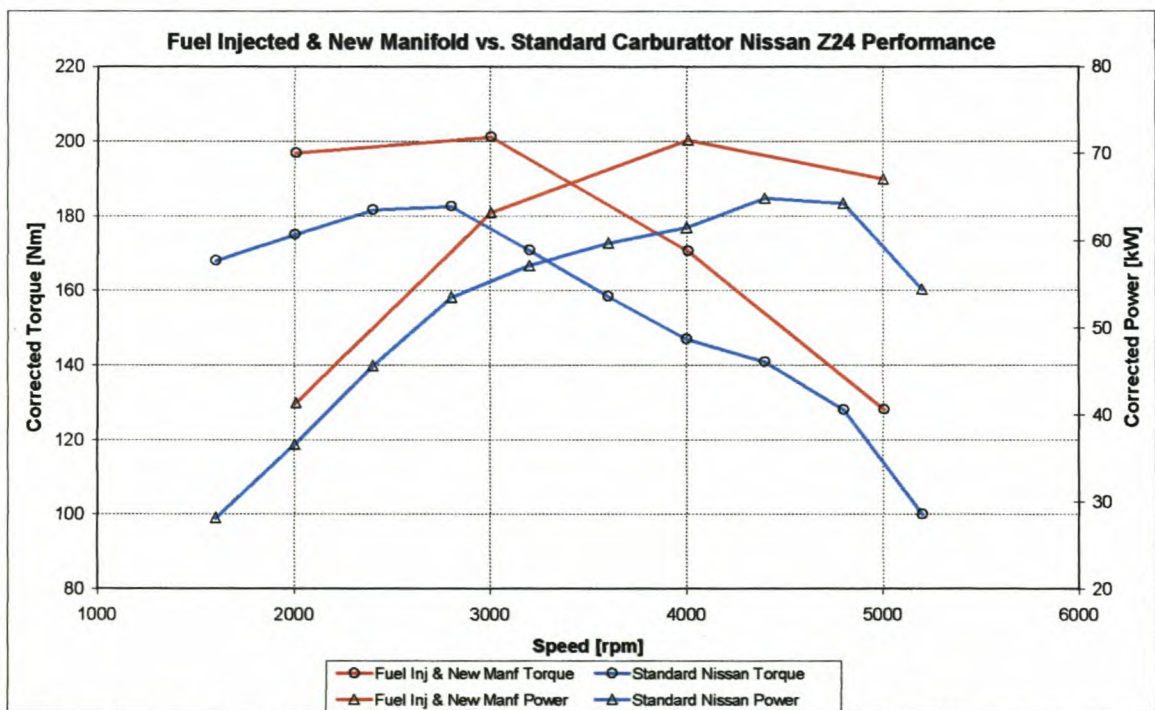


Figure 5-7: Fuel injected & new manifold vs. standard carburettor Nissan Z24 performance

clear from Figures H-1 and H-3 that with an increase in manifold length, the engine speed decreases at which that length performs to its optimum and vice versa. This means that for a specified inlet diameter, a longer length inlet manifold is better for low speed torque and a short length manifold is better for high speed power. This phenomenon is further explained in Chapter 6 with some more examples.

Chapter 5: Experimental Verification Testing

In Figure 5-8 the difference in tested and modelled engine performance is illustrated. It is clear from this graph that the software predicts the performance within 3% of the tested values. Figure 5-9 also shows good correspondence between tested and modelled data on the advancing camshaft performance. More information on camshaft timing and other engine parameters, and the influence on engine performance are presented in Chapter 6.

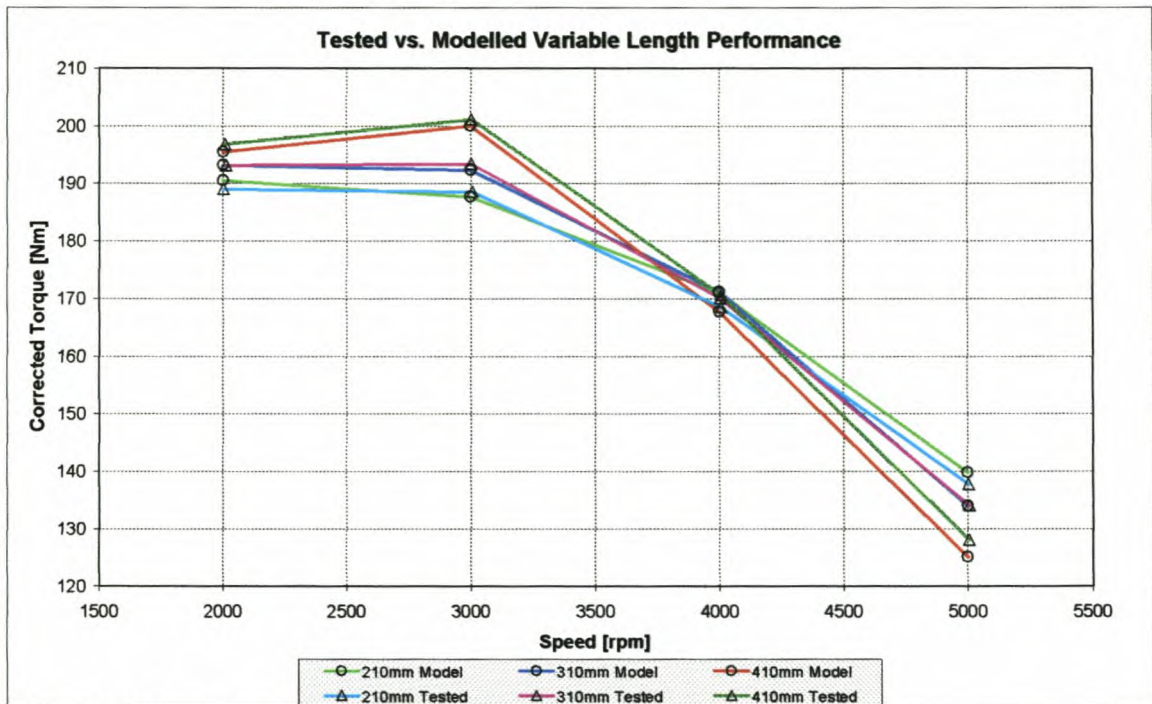


Figure 5-8: Tested vs. modelled variable length performance

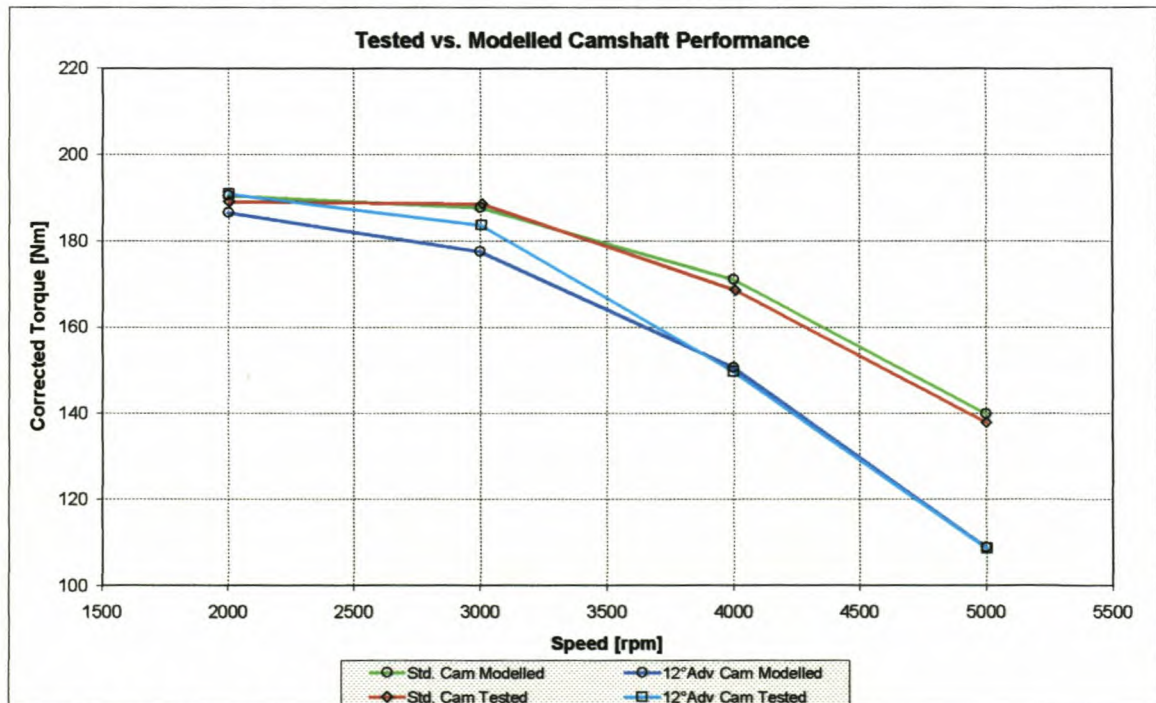


Figure 5-9: Tested vs. modelled camshaft performance

Chapter 5: Experimental Verification Testing

5.3.3. Inlet manifold pressure pulse trace results

In Appendix I all pressure trace data is presented. The results of Test 1 are presented in Figures I-1 to I-8. In Figure 5-10, the pressure trace data at point A is presented at the different engine speeds and in Figure 5-11, the pressure data at the three measurement points are illustrated at an engine speed of 3000rpm.

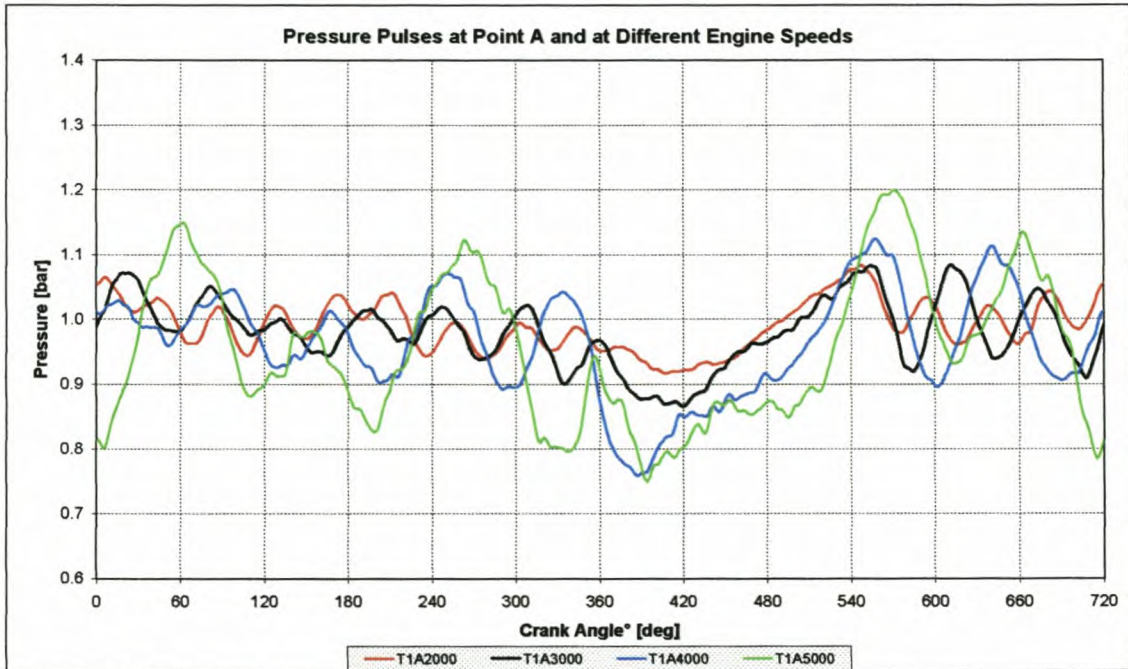


Figure 5-10: Pressure trace data measured at point A, Test 1

Figures 5-10 and 5-11 also illustrate the change in characteristic of the pressure waves while the inlet valve is open between $\pm 360^\circ$ and 540° crank angle.

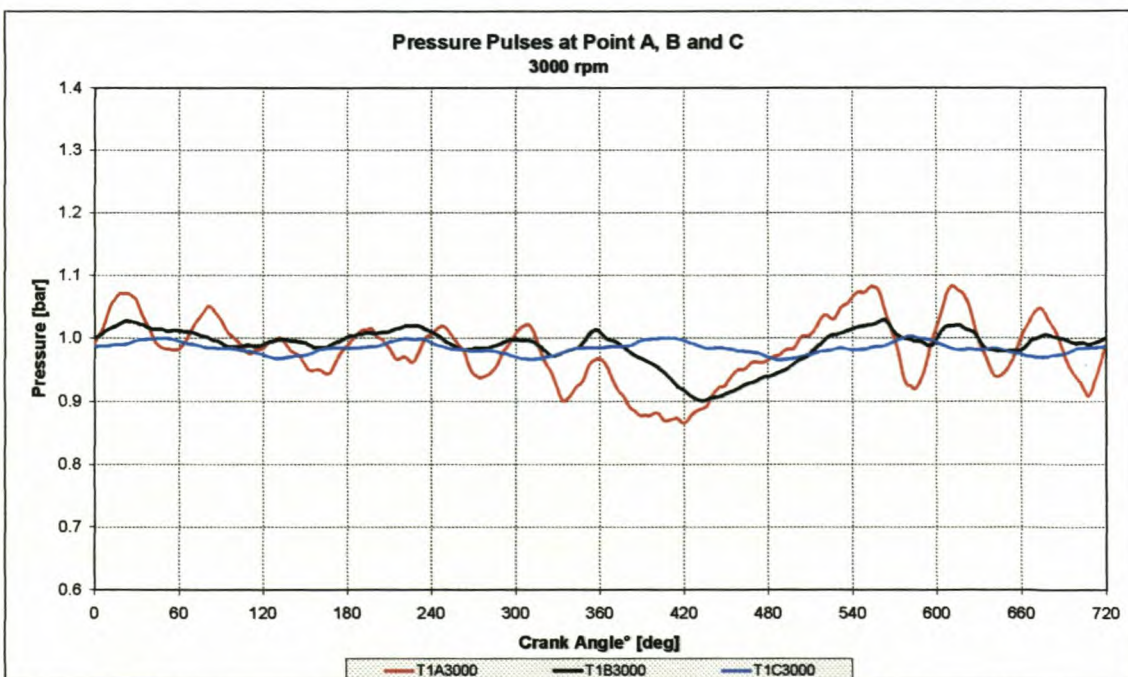


Figure 5-11: Pressure trace data measured at points A, B and C @ 3000rpm, Test 1

Chapter 5: Experimental Verification Testing

The results of Test 2 are presented in Figures 1-9 to 1-17. In Figure 5-12 the pressure trace data at point C is presented at the different engine speeds and in Figure 5-13 the pressure data at the three measurement points are shown at an engine speed of 5000rpm.

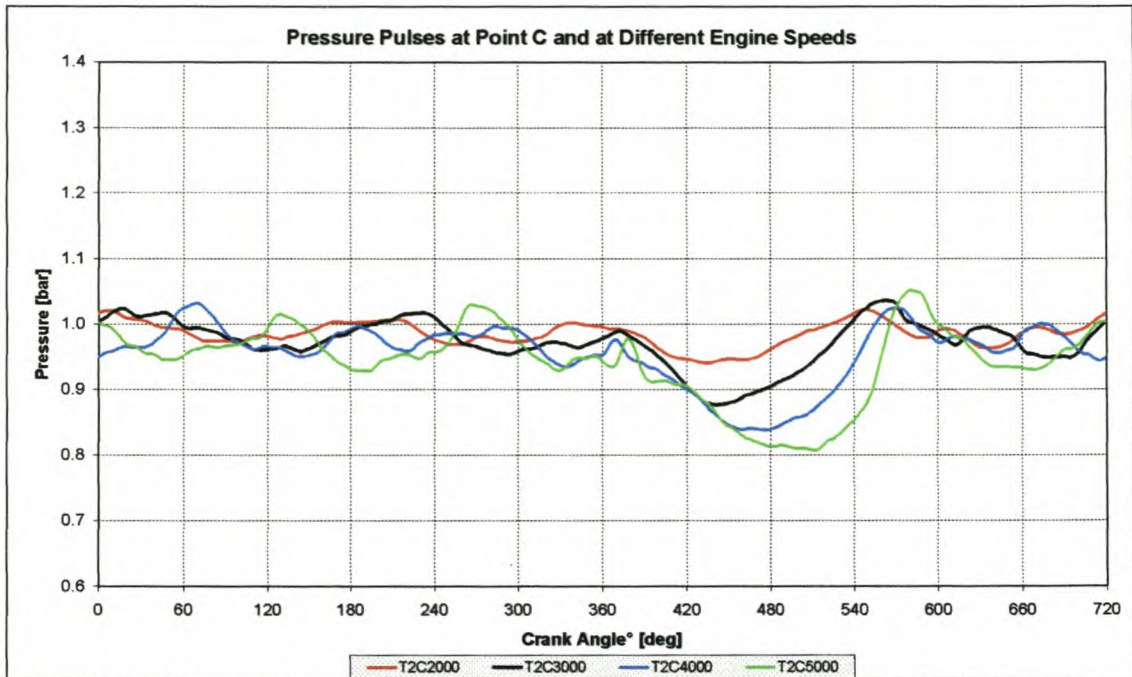


Figure 5-12: Pressure trace data measured at point C, Test 2

From Figures 5-10 and 5-13 it is clear how the pulse frequency changes at different engine speeds. Figures 5-12 and 5-14 also show the effect of friction and other losses on the pressure pulses, weakening towards the plenum end.

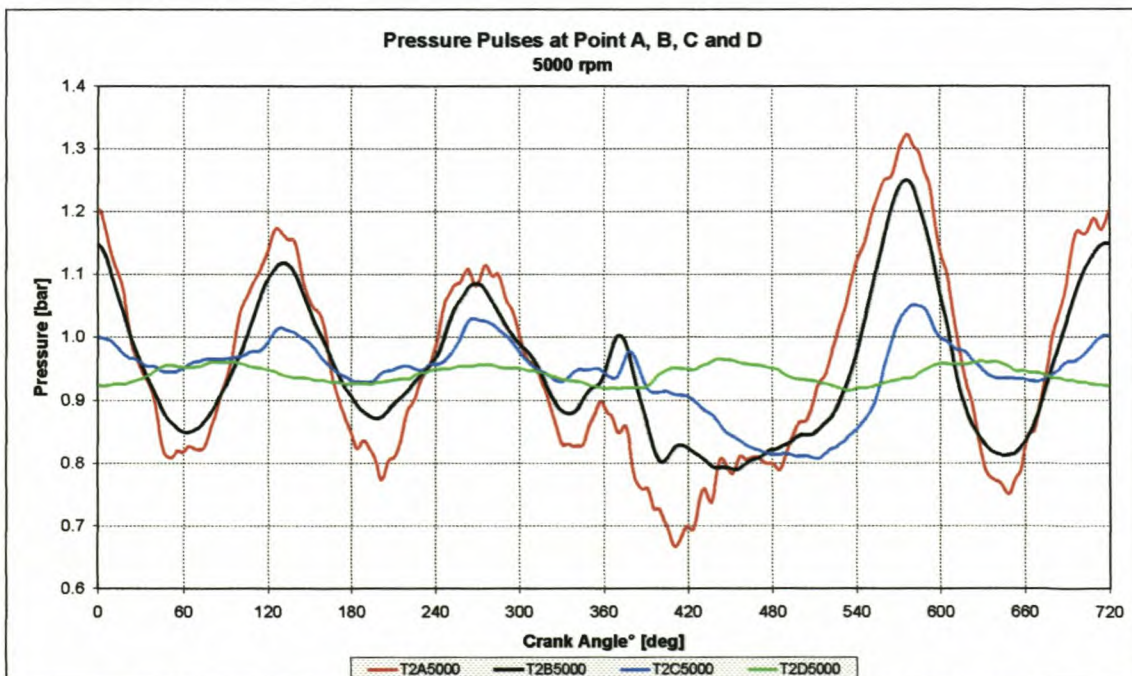


Figure 5-13: Pressure trace data measured at points A, B, C and D @ 5000rpm, Test 2

Chapter 5: Experimental Verification Testing

The engine performance data and pressure trace data of Test 3 are presented in Figures I-18 to I-23. These figures and Figure 5-14 show quite clearly that the new exhaust system used in these tests did not make a significant difference in the quality of the pressure traces. Either not much exhaust interference existed or the exhaust did not influence the inlet pulses significantly, more likely the latter.

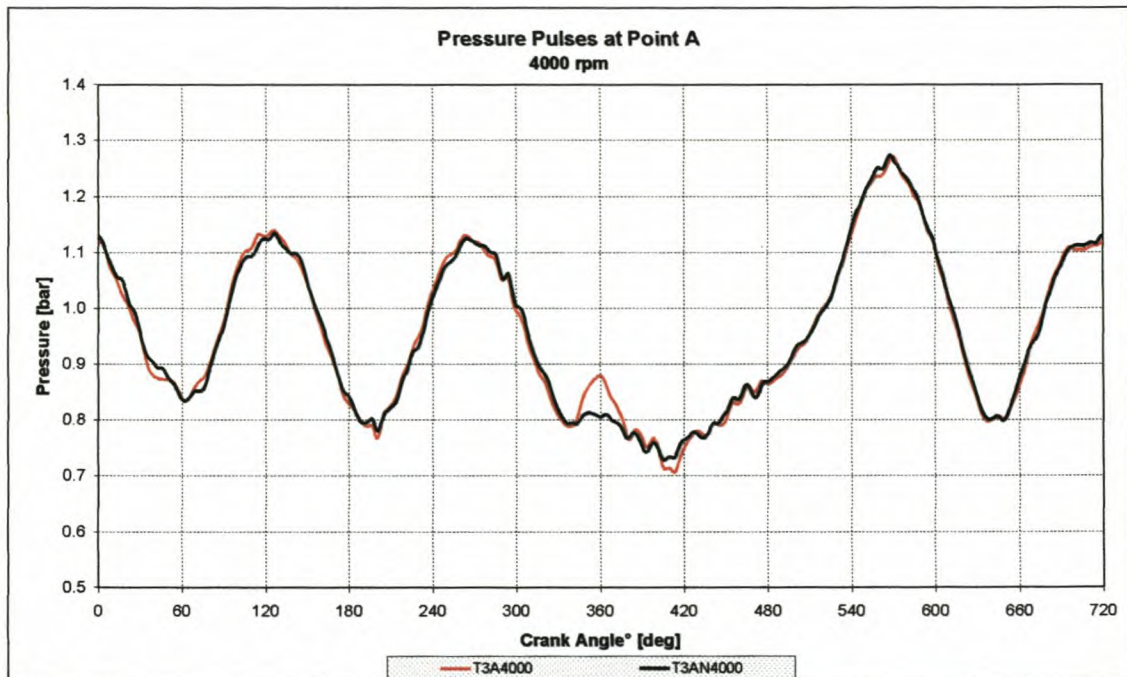


Figure 5-14: Pressure trace data at point A for the two exhaust systems, Test 3



Figure 5-15: Modelled and tested performance data on a 410mm inlet manifold, Test 4

The results of Test 4 are illustrated in Figures I-24 to I-42. In these graphs the results created by the ESA simulation software, are compared to measured

Chapter 5: Experimental Verification Testing

engine performance results and pressure data measured in the inlet manifold of the engine. From Figure 5-15 it is clear that a good correspondence was obtained between the modelled and tested data. In Figures 5-16 to 5-20 comparisons between modelled pressure pulse data and actual measured data is presented. In both cases, the correspondence is quite good. From the figures in Appendix I, it is evident that some inaccuracies do exist. The frequency

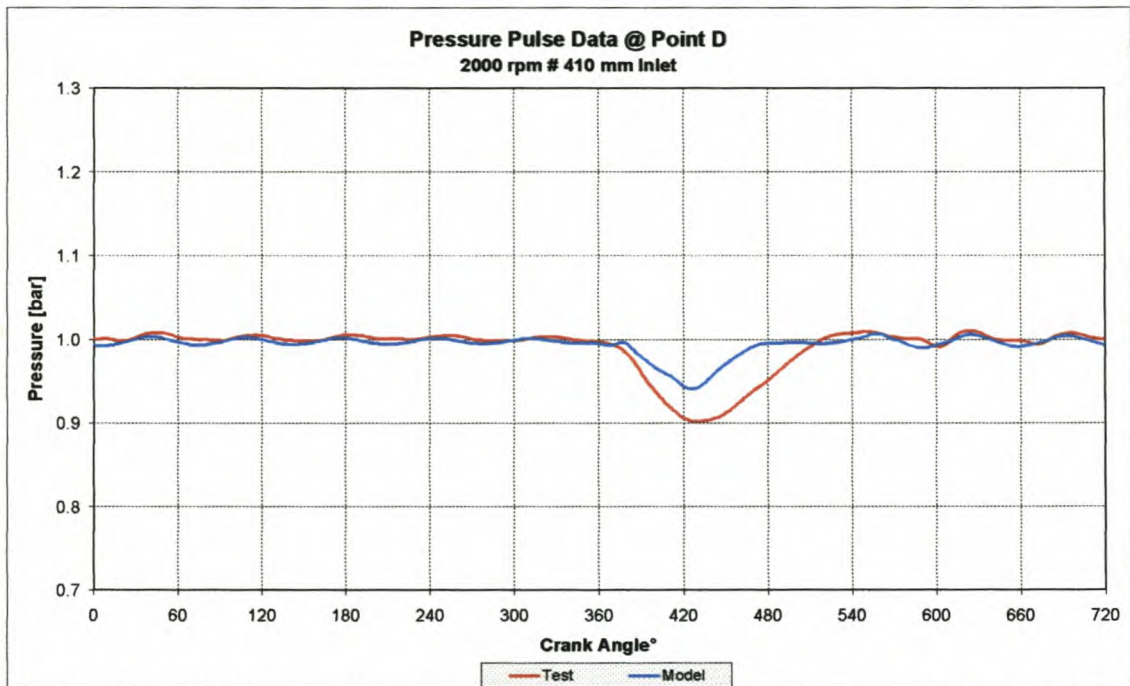


Figure 5-16: Modelled and tested pressure pulse data at point D @ 2000rpm, Test 4

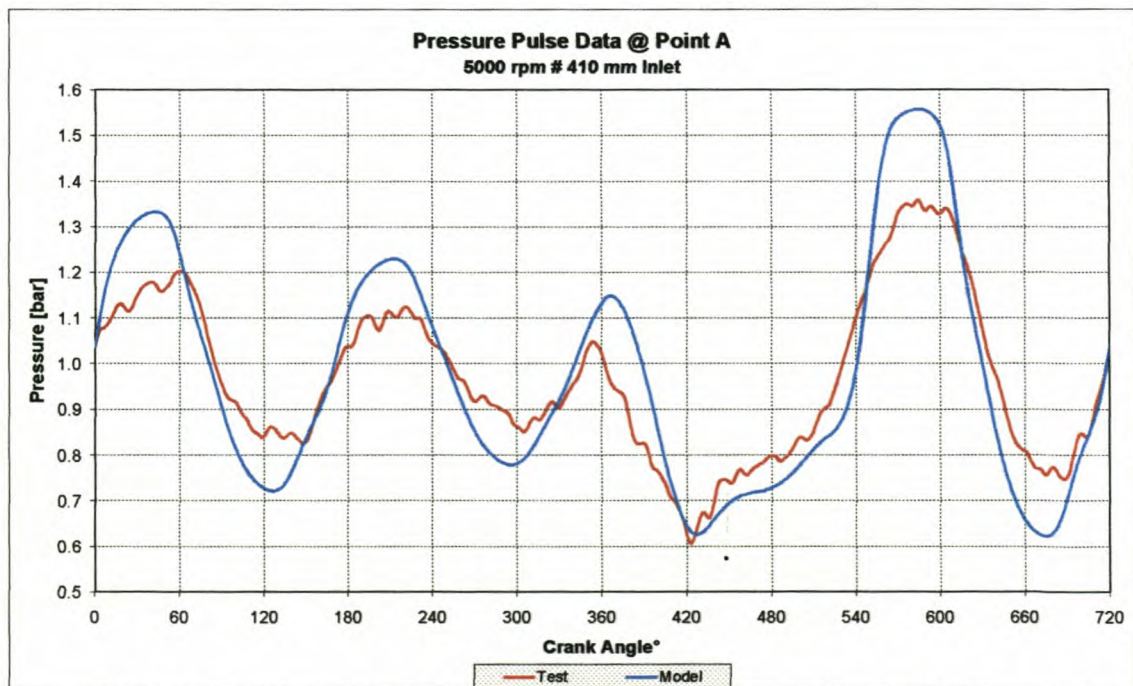


Figure 5-17: Modelled and tested pressure pulse data at point A @ 5000rpm, Test 4

Chapter 5: Experimental Verification Testing

of the pressure pulses correspond well, but the major differences are at the maximum and minimum values of the pulses. It is also clear from the graphs that at low engine speeds the modelled pressure pulses have smaller amplitudes than the measured ones, and vice versa at high engine speeds. A possible reason for this is that at low engine speeds the model has the problem of not having enough grid points in the inlet and exhaust tracts to predict the flow very accurately. This can cause the model to underpredict the maximum and minimum values of the pulses. At high engine speeds this is not the case, but here the inaccuracy is more due to the fact that the model under predicts the losses that exist in the inlet manifold. This can be loss due to friction, heat transfer and especially inaccurate discharge coefficients for the valves. Although there are some differences, the correspondence between the modelled and measured results is still satisfactory.

In Test 5 the performance results and pressure traces were created on a 310mm inlet manifold. These results are presented in Figures I-43 to I-48. Again good correspondence was obtained between the modelled and measured engine performance data. Good correspondence was also obtained between the modelled and measured pressure pulse results, with the same differences at low and high engine speeds as explained previously.

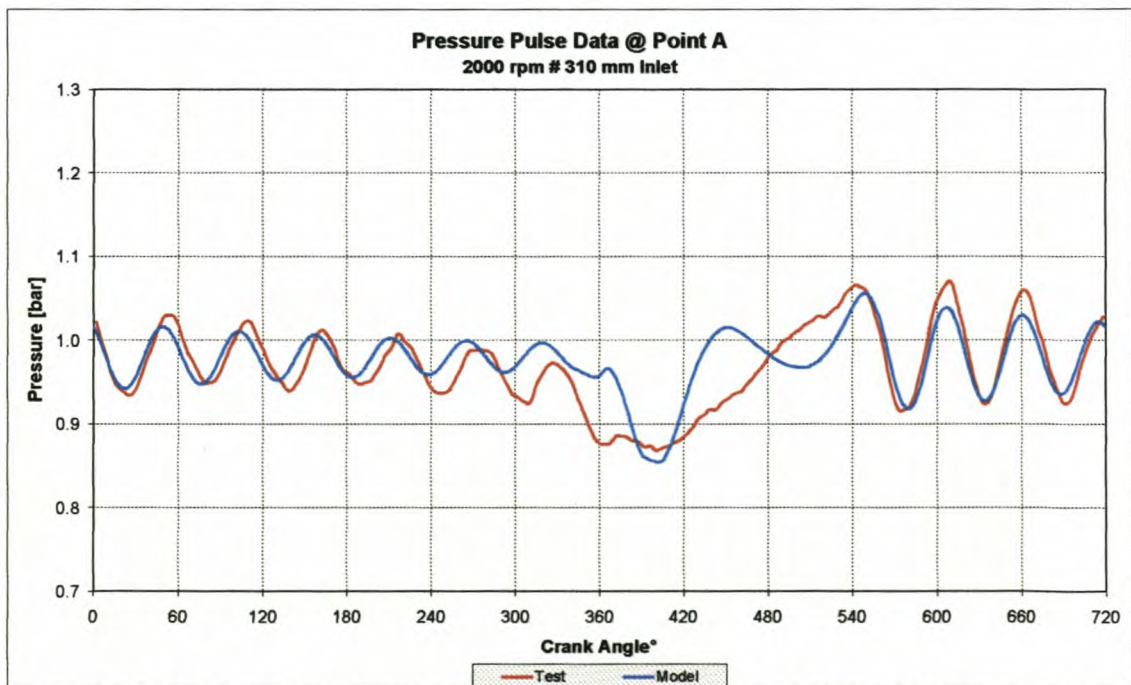


Figure 5-18: Modelled and tested pressure pulse data at point A @ 2000rpm, Test 5

Chapter 5: Experimental Verification Testing

The pulse frequency correspondence between the modelled and measured pressures were still found to be good (Figure 5-18).

The results for Test 6 are presented in Figures I-49 to I-54. Good correspondence was obtained between the modelled and tested engine performance as well as for the pressure frequency correspondence. Figure 5-19 illustrates the latter, but also illustrates the differences between the modelled and measured results.

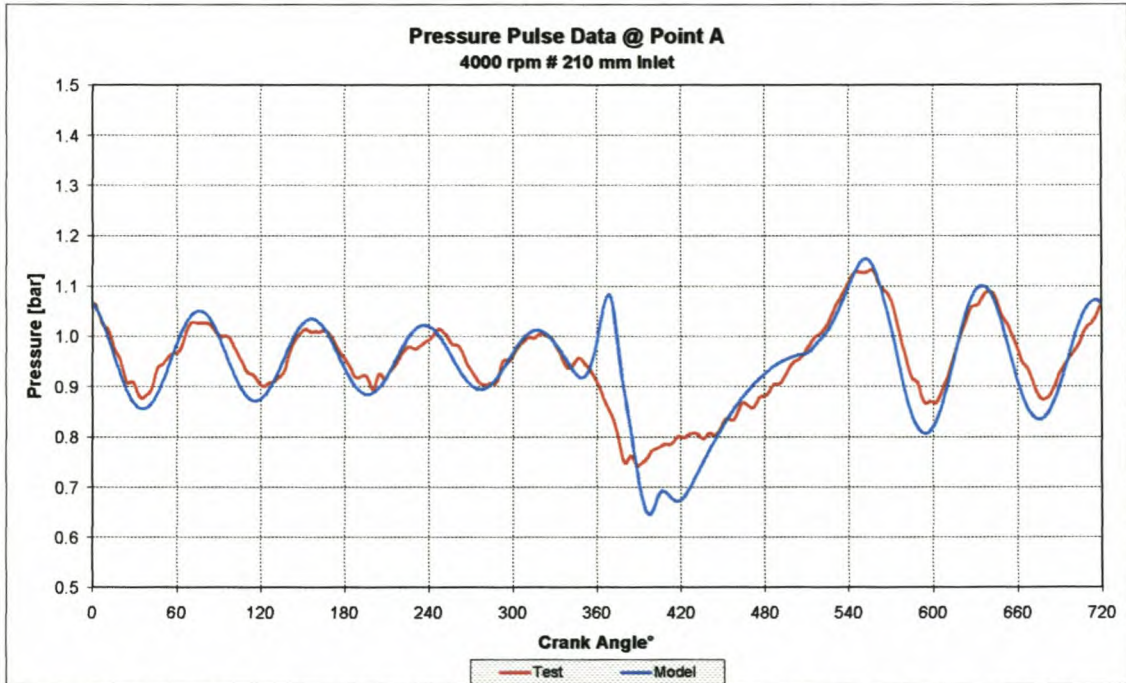


Figure 5-19: Modelled and tested pressure pulse data at point A @ 4000rpm, Test 6

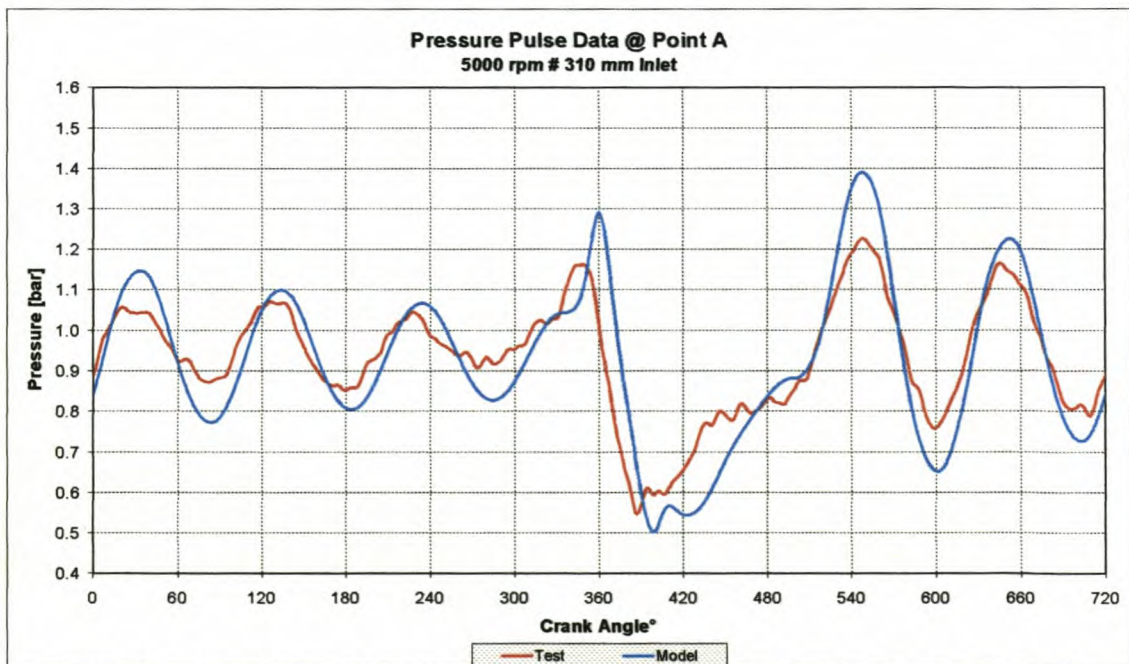


Figure 5-20: Modelled and tested pressure pulse data at point A @ 5000rpm, Test 7

Chapter 5: Experimental Verification Testing

In Test 7 the engine setup was kept the same as for Test 6, except for the change in camshaft timing. The camshaft was advanced with 12° crank angle. The measurements are presented in Figures I-55 to I-60. With this setup there is some differences at low engine speed between the modelled and tested engine performance, but the correspondence is still good. Even with this significant change, the pressure pulse correspondence is good (Figure 5-20).

The last few graphs in Appendix I, Figures I-61 to I-75, show the difference in pressure pulses in the inlet with all the pipes connected to the plenum chamber and with cylinder 1 isolated. From these graphs it is clear that pressure pulse interaction between inlet pipes, play a major role in the frequency and size of these pressure pulses (Figure 5-21).

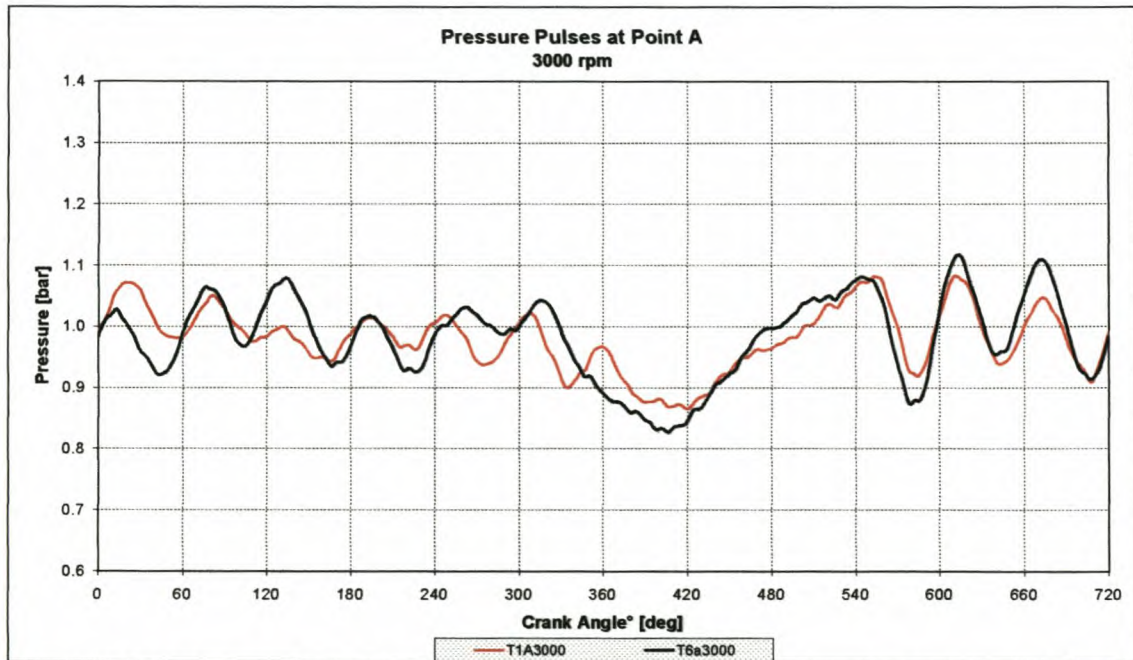


Figure 5-21: Measured pressure pulse data at point A @ 3000rpm for Tests 1 and 6

All the necessary information to run the above problems with the ESA software is supplied on the installation CD. The engine files are:

- Test 4: NissanTest4.eng
- Test 5: NissanTest5.eng
- Test 6: NissanTest6.eng
- Test 7: NissanTest7.eng

Chapter 5: Experimental Verification Testing

5.4. CONCLUSION

In this chapter it was shown that the ESA software could predict and model engine performance accurately. The program can also simulate pulsating flow fairly well.

In Chapter 6 the versatility of the ESA software, to simulate different engines and different engine configurations, is considered.

CHAPTER 6: EXPERIMENTAL VERSATILITY TESTING

In this chapter the use of the ESA software to investigate different engine design parameters and the effects of the changes to these parameters are described. The parameters covered are manifold length and diameter changes, trumpet sections on the inlet manifold, plenum volume sizes and valve timing changes. The applicability of the program as a design tool is demonstrated by means of two inlet manifold design projects that were done for Volkswagen South Africa and FAW-VW in China.

6.1. OPTIMUM INLET MANIFOLD DIMENSIONS

In the design of inlet manifolds, the length and the diameter are very important in achieving optimum performance. The performance of an inlet manifold is measured by the engine volumetric efficiency. The volumetric efficiency mainly depends on the inlet pressure during the short period, near bottom dead centre (BDC), before the intake valve is closed. The volumetric efficiency under wide open throttle conditions is also strongly influenced by the dynamic effects in the intake system. Peaks in volumetric efficiency occur when the natural frequencies of the intake system tune favourably with the engine induction period so that the pressure at the inlet valve is raised in the critical region around bottom dead centre of the induction stroke, before the valve closes. It was also found that the manifold length has a more significant influence on the volumetric efficiency than the manifold diameter.

Benson [4] and other designers (e.g. Stone and Etminan [35]) found that inlet manifold length not only changes the engine speed at which the manifold performs at its optimum, but can also increase the maximum torque of the engine as illustrated in Figure 6-1. The manifold diameter tends to only change the engine speed at which the manifold performs to its optimum, with the maximum torque only changing slightly as illustrated in Figure 6-2. This phenomenon is typical of all engines.

6.1.1. Inlet manifold length

The optimum inlet length depends on the performance targets set for a specific

Chapter 6: Experimental Versatility Testing

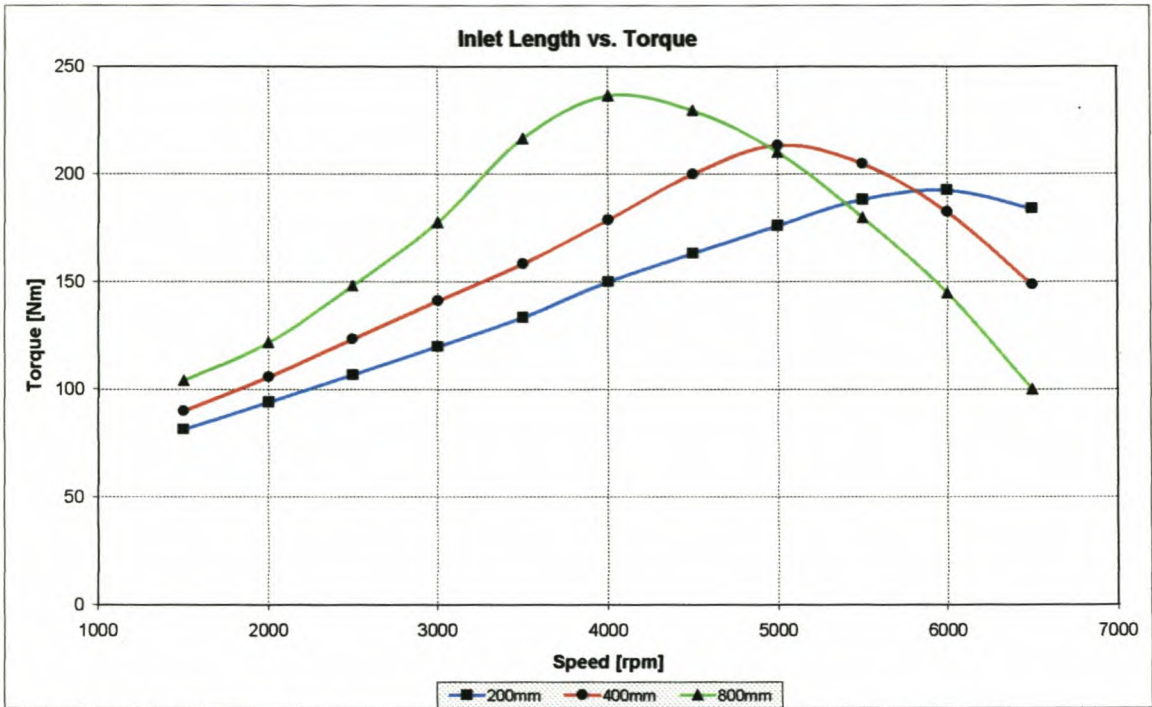


Figure 6-1: Influence of inlet length on maximum torque [35]

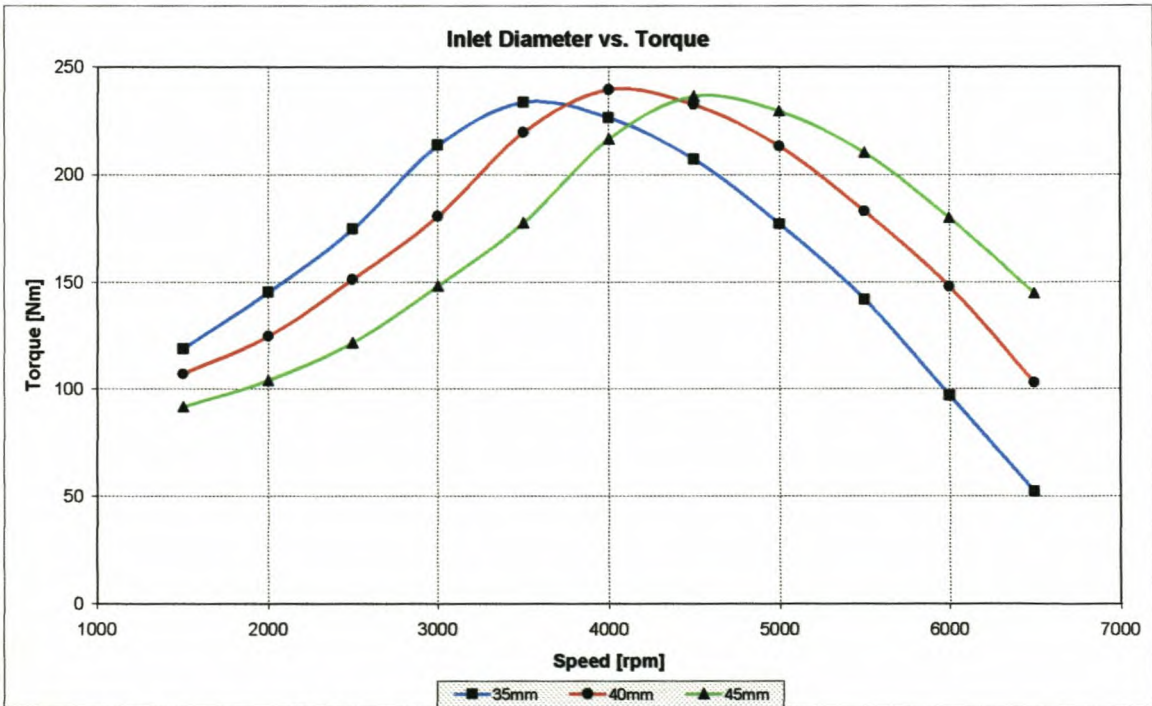


Figure 6-2: Influence of inlet diameter on maximum torque [35]

engine. Usually the customer wants emphasis on either low speed torque or high-speed power or often both. Because of the flow phenomena in inlet and exhaust systems it is very difficult to achieve low speed torque and high-speed power with a constant length and diameter inlet manifold. With more complex inlet and exhaust manifolds it is possible to achieve these targets, but not without added cost and complexity of the manifold. The optimum manifold length

Chapter 6: Experimental Versatility Testing

becomes shorter when the engine speed is increased, due to the increase in frequency of pressure waves [25] and decrease in flow friction. Increasing the length of a primary pipe lowers its natural frequency and benefits low speed torque. Long inlet lengths also have more available kinetic energy to assist in the ramming effect of the air while the inlet valve is open. At high speeds though, friction in the long length inlet pipes has a detrimental effect on performance. These effects are illustrated in Figure H-1 where the length of the inlet manifold was changed from 210mm to 410mm.

The ESA program was used to produce the data presented in Figure 6-3: a 3-dimensional map to investigate the effect of inlet length on engine torque at different engine speeds. The engine setup is described in section 6.6.2. From the graph it is clearly illustrated how the increase in length lowers the engine speed at which the optimum torque is obtained. It is also clear that some inlet lengths are better tuned for the engine configuration and enhances the ramming effect substantially. This map gives the user the opportunity to choose the right length for the prescribed engine performance targets.

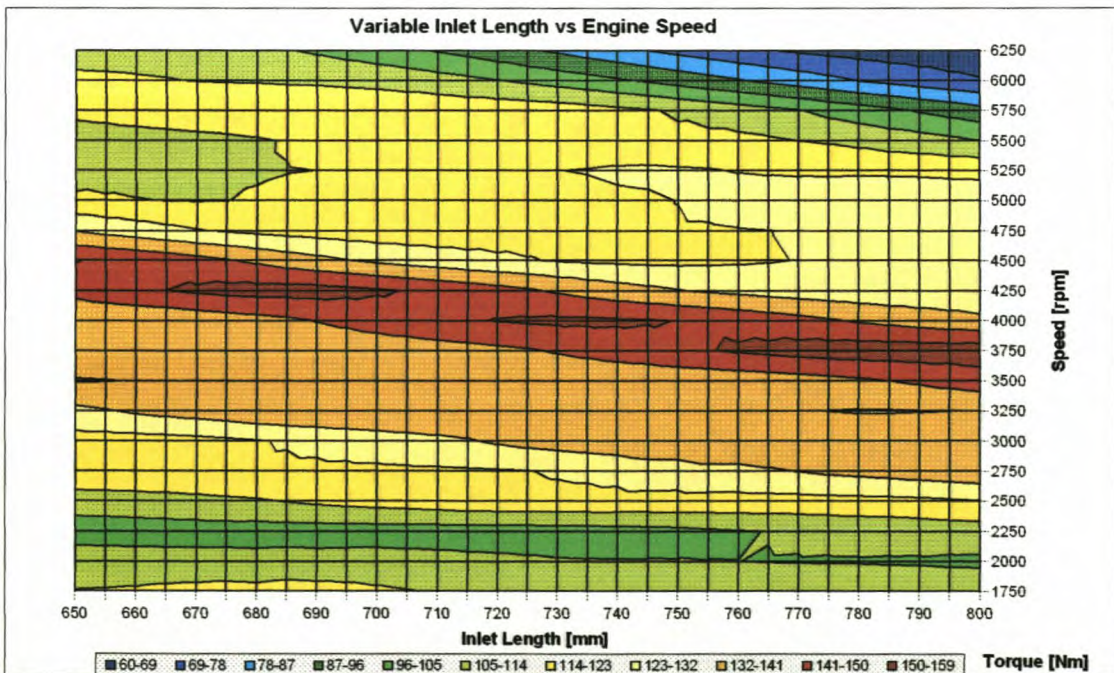


Figure 6-3: Variable inlet length modelled performance

6.1.2. Inlet manifold diameter

During the design process of inlet and exhaust manifolds it is not always possible to make the manifold length to the desired specification of the engineer, because

Chapter 6: Experimental Versatility Testing

of e.g. spatial constraints in the engine bay. It is then necessary to consider the manifold diameter to optimise the performance of the engine. The optimum manifold diameter gets larger when the engine speed is increased, due to the increase in frequency of pressure waves [25] and decrease in flow friction. Decreasing the diameter of a primary pipe lowers its natural frequency, but increases friction at high engine speeds.

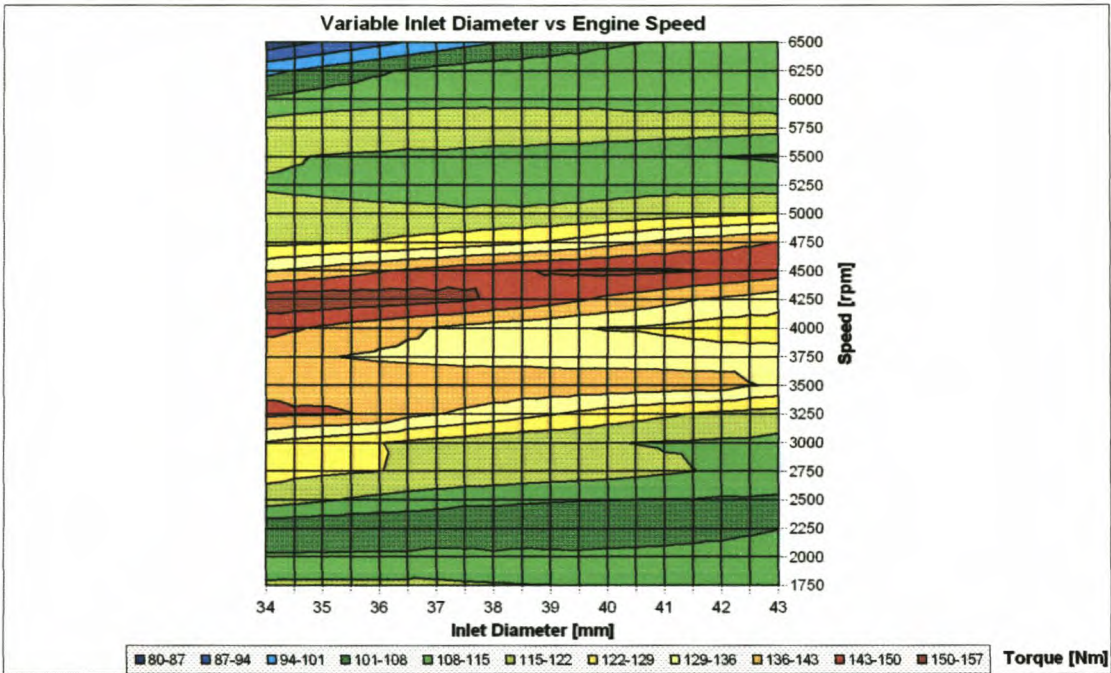


Figure 6-4: Modelled variable diameter performance

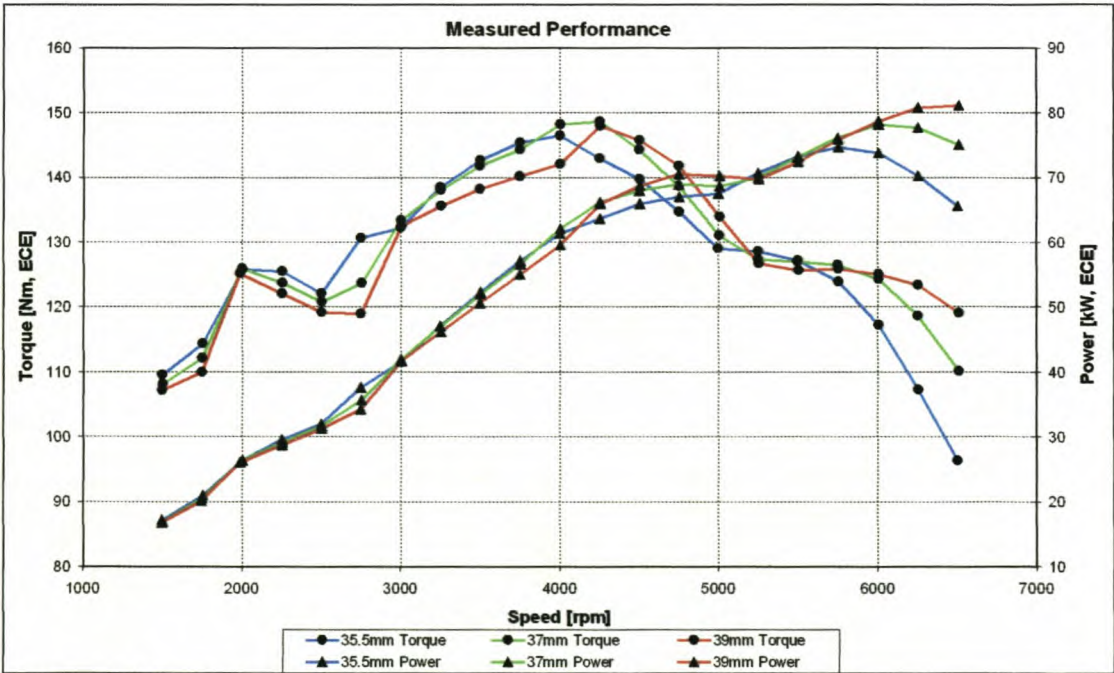


Figure 6-5: Tested variable diameter performance

The ESA program was used to produce the data presented in Figure 6-4: a 3-dimensional map to investigate the effect of inlet manifold diameter on engine torque at different engine speeds. The engine setup is presented in section 6.6.2. From the graph it is clear how the increase in diameter increases the engine speed at which optimum torque is achieved.

As described in the first part of section 6.1 and from Figures 6-2, 6-4 and 6-5 it is clear that the influence of manifold diameter is not as significant as the manifold length influence. Figure 6-5 shows the tests that were done on a Volkswagen engine that was part of one of the inlet manifold projects. The graph might be a bit confusing in that the maximum torque of the 35.5mm manifold is lower than the other two manifolds. On this engine though, knock or pre-ignition sensitivity was a problem; this is explained in section 6.6.2.

6.2. OPTIMUM VALVE TIMING CHARACTERISTICS

The valve timing of an engine can also have a significant influence on the performance of an engine [20]. It is important to note that for each engine configuration and each engine speed, a different optimum valve timing exists [15].

Advancing the intake valve opening (increasing the valve duration) decreases the volumetric efficiency slightly at low engine speeds. The increase in time that the inlet valve is open during this speed causes an increase in reverse flow just before the valve closes. Fresh air and fuel mixture is lost due to this as illustrated in Figures F-25 and F-26.

At higher engine speeds advancing the intake valve opening increases the volumetric efficiency (Figure 6-6). These changes do not cause an increase or decrease throughout, but an optimum opening and closing angle do exist for each engine and manifold set-up. The optimum intake valve closing angle coincides with the pressure in the intake valve and cylinder reaching equilibrium. If the valve is closed after this point, fresh air and fuel mixture in the cylinder will flow back into the intake system, losing available energy. If the valve is closed before this point, fresh air and fuel mixture that would have gone into the cylinder will then be cut off at the valve. This optimisation is an iterative process to get the right configuration for each engine and each engine speed. The opening

Chapter 6: Experimental Versatility Testing

and closing of the inlet valve do have a slightly smaller effect on optimum engine performance than that of inlet manifold length [25].

The operation of the exhaust valve is similar. If the exhaust valve opens too early the gas in the cylinder will escape through the valve and the pressure in the cylinder will drop, causing a decrease in positive work done on the piston. If the exhaust valve opens too late or closes too early, the decrease in valve opening duration can cause exhaust gas to be trapped inside the cylinder at exhaust valve closure, taking the space of fresh air and fuel mixture, decreasing the volumetric efficiency of the engine. If the exhaust valve closes too late, the increase in valve overlap can cause fresh air and fuel mixture to pass through the exhaust valve, losing potential energy; it can also cause exhaust backfire or very high temperatures at the exhaust valves.

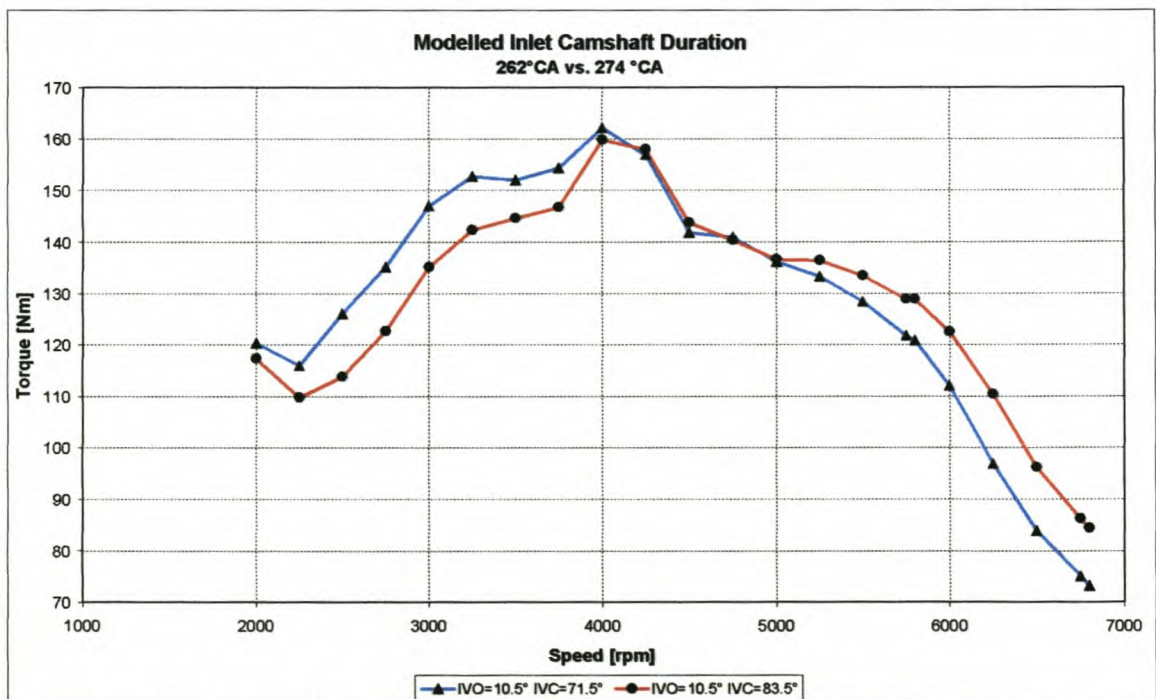


Figure 6-6: Inlet valve duration vs. engine torque

In modern engines the valve timing can sometimes be changed, either between two extremes, or continuously with changing engine speed. This is well known as Variable Valve Timing (VVT). This unfortunately leads to an increase in cost and complexity of the engine.

More information on camshafts, valves and the influence on engine performance, can be found in the thesis of Williams [15].

6.3. INLET PLENUM DESIGN

Plenum design is sometimes neglected and is usually designed to only fit nicely in the engine bay. Ohata and Ishida [22] found that a small inlet plenum has a positive effect on engine performance at lower engine speeds and a negative effect at higher engine speeds. They showed that the inlet pressure profile consists of a shorter and a longer periodic component, each of which is determined by the design factors of the intake system, and showed that the plenum volume has the main influence on the longer periodic component which influences the volumetric efficiency at lower engine speeds positively and at higher speeds slightly negatively. A smaller plenum would therefore enhance the longer periodic component, because of more effective energy transfer between the cylinders of a multi-cylinder engine.

This phenomenon is proved with engine testing on a prototype manifold. A full load power curve was done with a large and small plenum inlet manifold and the results, illustrated in Figure 6-7, proved the theory of Ohata and Ishida [22]. It is also interesting that there was no negative effect at high engine speeds.

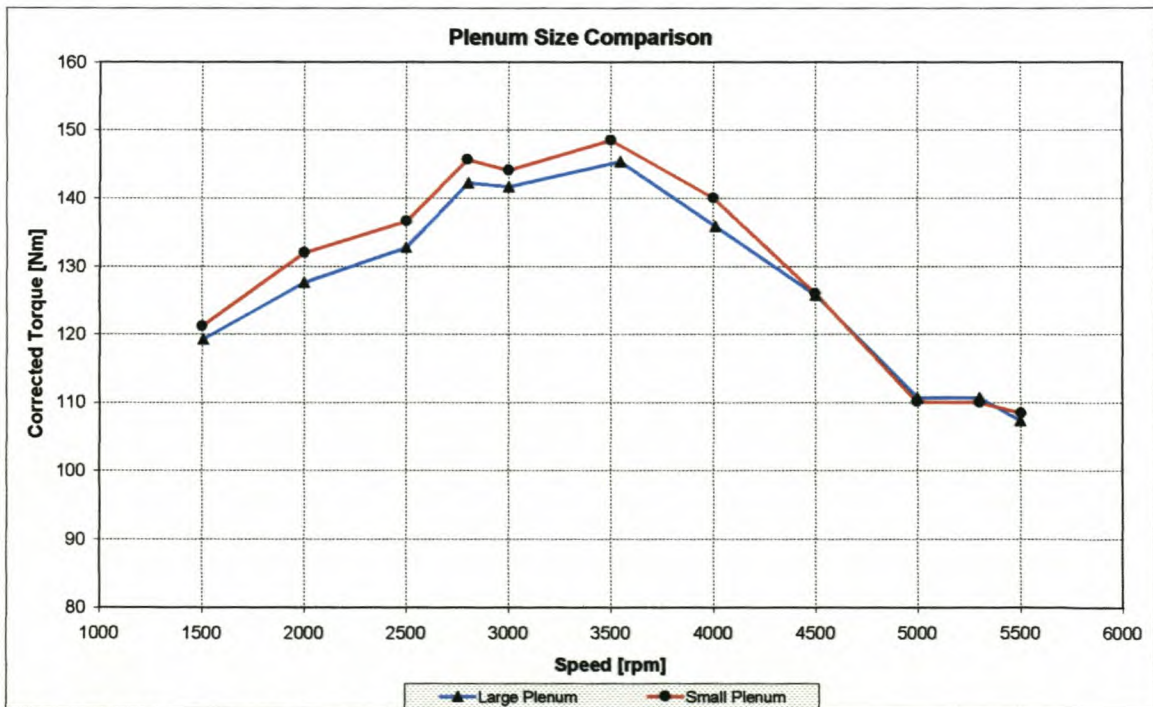


Figure 6-7: Small and large plenum investigation

At this moment the ESA program is unable to model plenum volumes. This shortcoming is discussed in Chapter 7.

6.4. INLET TRUMPET OR DIFFUSER DESIGN

The diffuser or trumpet design concept that originated with steady state flow is also used in unsteady flow with great success. A trumpet at the inlet side of an inlet manifold can have performance advantages at high engine speeds, without having any significant detrimental effects at low engine speeds.

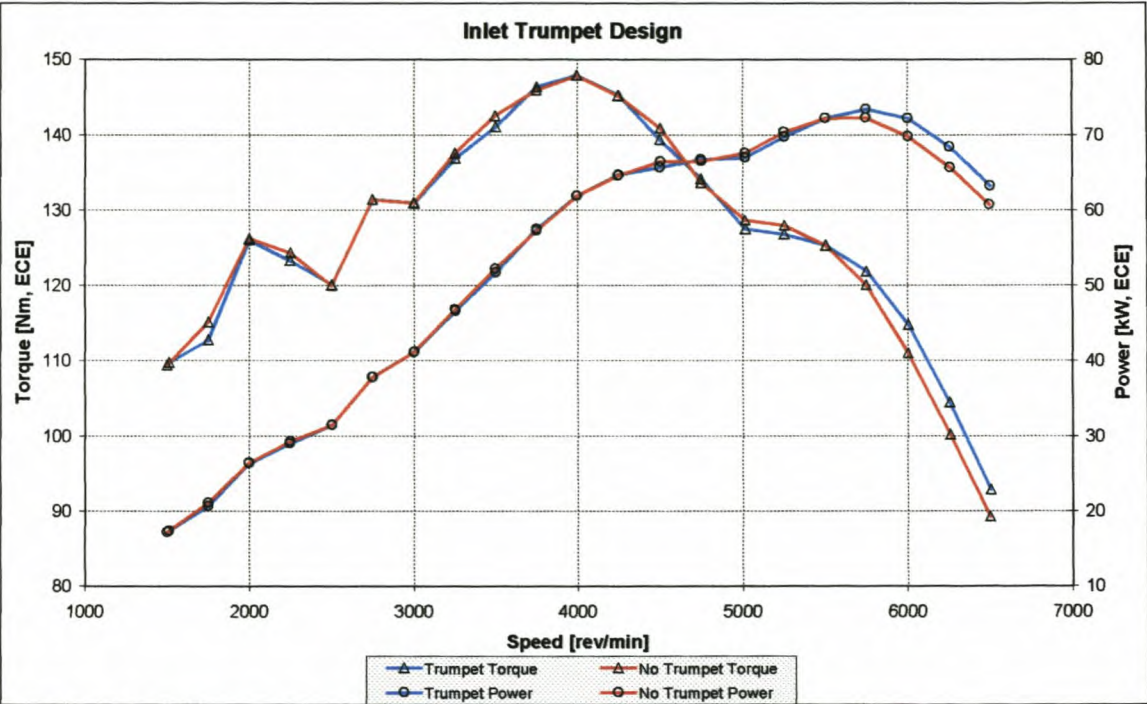


Figure 6-8: Influence of an inlet trumpet on engine performance

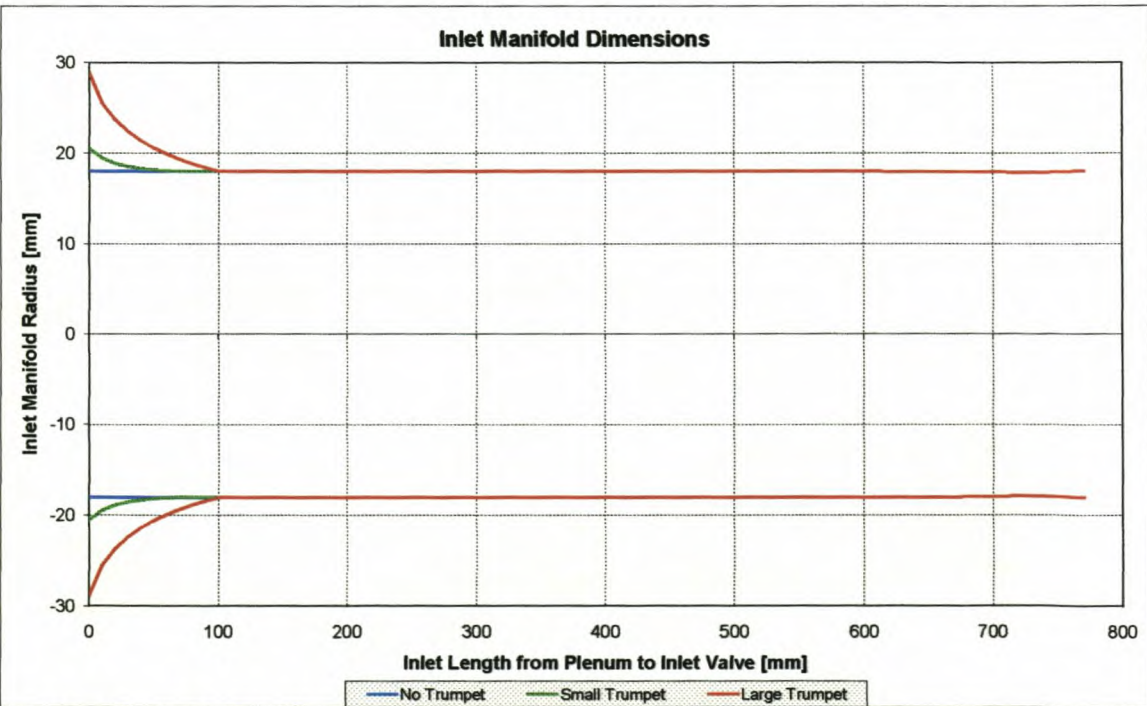


Figure 6-9: Inlet manifold dimensions for different trumpets

Chapter 6: Experimental Versatility Testing

The basic idea is to decrease the flow velocity at the manifold inlet so as to increase the average pressure there. In designing the trumpet, it is also important to remember that separation of the flow can occur if the area variation is too steep. This is achieved by making sure that the acceleration of the flow in the diffuser is constant throughout the length of the diffuser. The influence of the trumpet at high engine speeds was tested and is illustrated in Figure 6-8.

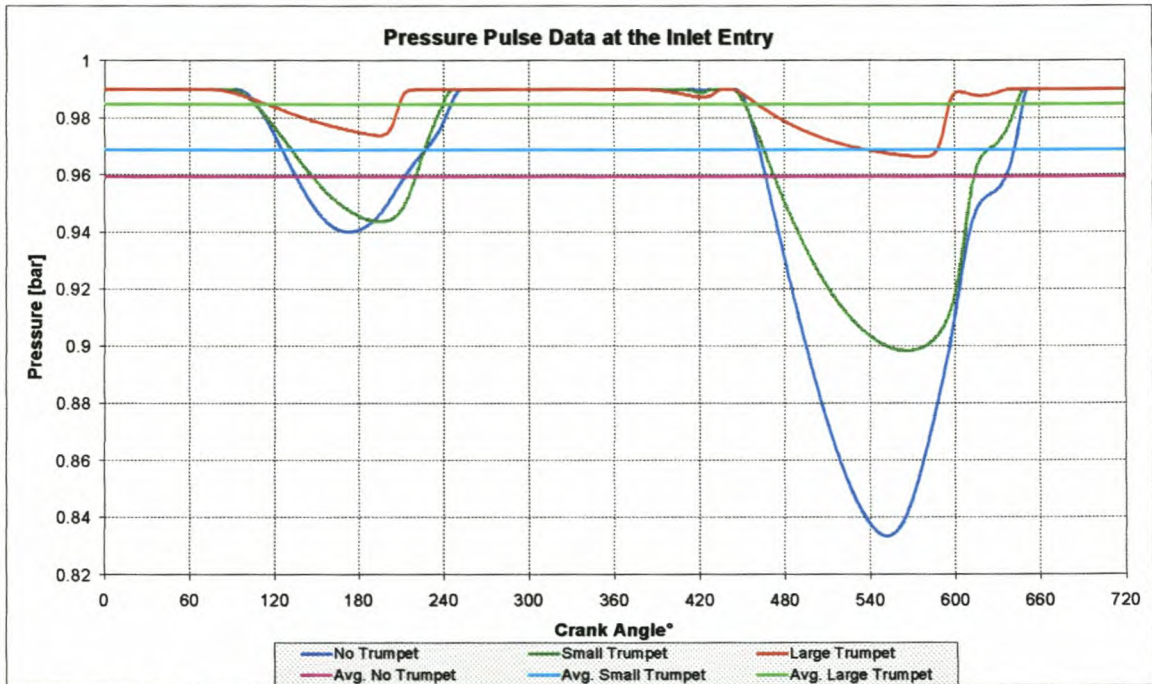


Figure 6-10: Pressure pulses and average pressure at inlet manifold entry

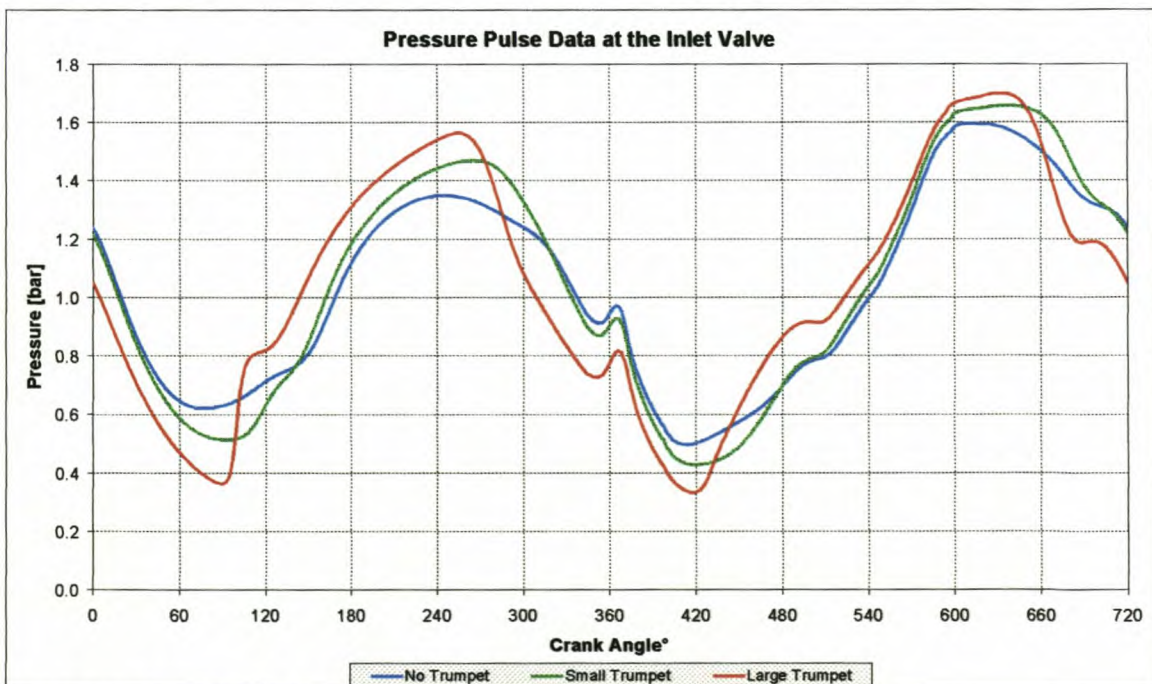


Figure 6-11: Pressure pulses at the inlet valve

In Figure 6-9 a manifold is shown with three different entry dimensions, called "No Trumpet", "Small Trumpet" and "Large Trumpet". These manifolds were modelled with ESA at a speed of 5750 rpm; the resulting pressures at the entry of the inlet manifold are presented in Figure 6-10. The trumpet sections not only improve the average pressure, but also enhances the pressure pulses at the inlet valve (Figure 6-11), which improves the volumetric efficiency of the engine.

6.5. EXHAUST MANIFOLD DESIGN

Under pulse operation, the exhaust gases from the different cylinders are discharged into single or properly paired small bore exhaust pipes. The release of high-pressure and high-temperature gas at high velocities (sonic at the beginning) into a narrow pipe causes the propagation of pressure pulses in the pipe which travels at approximately the speed of sound at the prevailing gas temperature. These pressure waves are distorted while travelling along the pipes by friction, heat transfer, pipe bends, junctions, silencers and to a smaller extent, by passing through the interface of different density gas layers.

The flow phenomenon in the exhaust system of an engine is very complex. Pulse interaction can be found in the exhaust, which influences the performance of the exhaust system. The ESA software cannot model branch flow and therefore no modelling was done changing exhaust manifold parameters. Until further development on the ESA program, it cannot be used with a great deal of accuracy on exhaust systems. This shortcoming of the program is further discussed in Chapter 7.

6.6. ENGINE DESIGN USING ESA SIMULATIONS

The competitiveness of the local and international automotive industry has provided a great stimulus for development in the design of internal combustion engines in the past century. The expansion of many of the larger international vehicle manufacturing companies into global development and marketing strategies has placed a large strain on the local automotive industry, while also creating new opportunities for involvement in international design and development projects.

Chapter 6: Experimental Versatility Testing

With the opening of South Africa to world markets, local vehicles have had to compete with, and match up to many different imported models. In order to stay competitive, the local industry must stay abreast of the developments in modern technology in the design of engines and be prepared to use this knowledge in an innovative way so as to produce cheap, reliable and efficient engines for the local market.

One of the ways in which the industry meets these requirements is in the upgrading and modernisation of older engine designs, the tooling for which is easily and cheaply available internationally. Often, small modifications can be made to these designs, increasing the competitiveness of these engines enough to not only survive on the local market, but also provide exports to other developing countries e.g. India, China, etc.

Traditionally, modifications to production engines have provided for an industry of after-market high performance specialists who have made use of mainly empirical data, hearsay and personal experience to upgrade these engines. These modifications are mainly to the exhausts, manifolds, valves, cams and ports of the engines in order to increase the breathing capacity, and thus the performance of the engines.

The ESA software research attempted to provide a tool for developers to reduce or eliminate both the guesswork and iterations needed for a design upgrade. The theoretical development and ESA computer program provided not only for a more educated design process, but also for the ability to analyse various designs before the manufacture of prototype manifolds, heads, valves and camshafts. Two recent projects involved the design of a new inlet manifold.

6.6.1. FAW-VW China Jetta inlet manifold development

An old generation engine used in China, a four cylinder 1.6ℓ 8-valve carburettor engine, had to be converted to a fuel injection unit and certain performance targets were set for the engine. The engine had to develop its maximum torque, $\pm 135\text{Nm}$, at $\pm 2800\text{rpm}$ or at low engine speeds with the emphasis on driveability. The engine also had to develop at least 64kW at an engine speed of $\pm 5300\text{rpm}$ or higher. The new upper inlet manifold had to fit on an existing lower

Chapter 6: Experimental Versatility Testing

inlet manifold with an inside diameter of 34.5mm. The manifold also had to fit neatly in the engine bay with the necessary clearance from the bonnet line. Using drawings from Volkswagen, the limits for the inlet manifold were calculated. The total head port, lower and upper inlet manifold length had to be between 600mm and 700mm long.

The initial approach was to design two manifolds on the basis of calculated results from the ESA software. Thereafter, 4 more manifolds were designed in which each of the critical parameters was varied about the predicted optimum value. The result was a set of 10 prototype manifolds, which allowed the optimum value for each of the critical parameters to be identified.

Initially, the existing manifold was studied in an attempt to identify specific performance features. A series of calculations using ESA were then carried out to investigate the airflow characteristics and resonant frequencies of the various components of the new inlet manifold. The following parameters were taken into account in the design process of the composite prototype manifolds:

- **General inlet manifold pipe shape.** The upper part of the inlet manifold was designed to fit on a small lower part with round ports. The spatial constraints forced the designers to curve the pipes of the upper manifold (Figure 6-12). This curvature forced the design to go to elliptical pipes for most of the manifold pipe length. Transitions from round to elliptical ports were therefore necessary and were achieved in 50mm of pipe length.



Figure 6-12: Curved pipes of new inlet manifold

Chapter 6: Experimental Versatility Testing

- **Inlet manifold pipe length and performance specifications.** Expected performance figures, for the designed engine, were specified by FAW-VW. The engine had to develop $\pm 135\text{Nm}$ of torque at $\pm 2800\text{rpm}$ and $\pm 64\text{kW}$ at $\pm 5300\text{rpm}$. Two main tract lengths, 700mm and 600mm, were then chosen to cover the spatial constraints in the car. These lengths, the 600mm tuned for high frequency and the 700mm tuned for low frequency, would also give the extremes of maximum power at high engine speeds and maximum torque at low engine speeds. After a detailed design and simulation of numerous variations on ESA, the results presented in Figures 6-13 and 6-14, it was decided to make another two lengths, 640mm and 680mm.

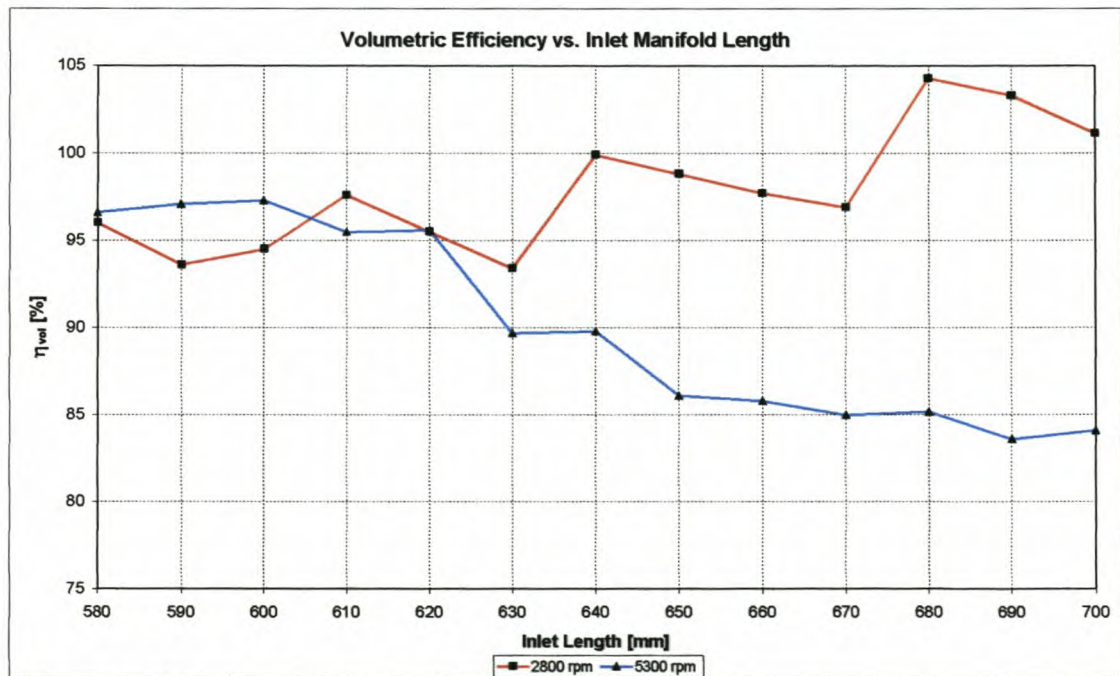


Figure 6-13: Inlet length changes at 2800rpm and 5300rpm

From Figure 6-14 it is clear that the increase in length decreases the engine speed at which the manifold will perform at its optimum. It is also clear from Figures 6-13 and 6-14 that certain lengths are tuned to the optimum, because of the ramming effect it has just before the inlet valve is closed.

From the spatial constraints and information gained from Figures 6-13 and 6-14, four prototype manifolds were made:

- Prototype 1: 700mm x 34.5mm
- Prototype 2: 600mm x 34.5mm
- Prototype 3: 640mm x 34.5mm
- Prototype 4: 680mm x 34.5mm

Chapter 6: Experimental Versatility Testing

The diameter of the prototypes were kept the same as the lower inlet manifold, 34.5mm, until further investigation was done on the effect of diameter changes, using ESA simulations. All four manifolds also had a trumpet section at the plenum end; this will be discussed later.

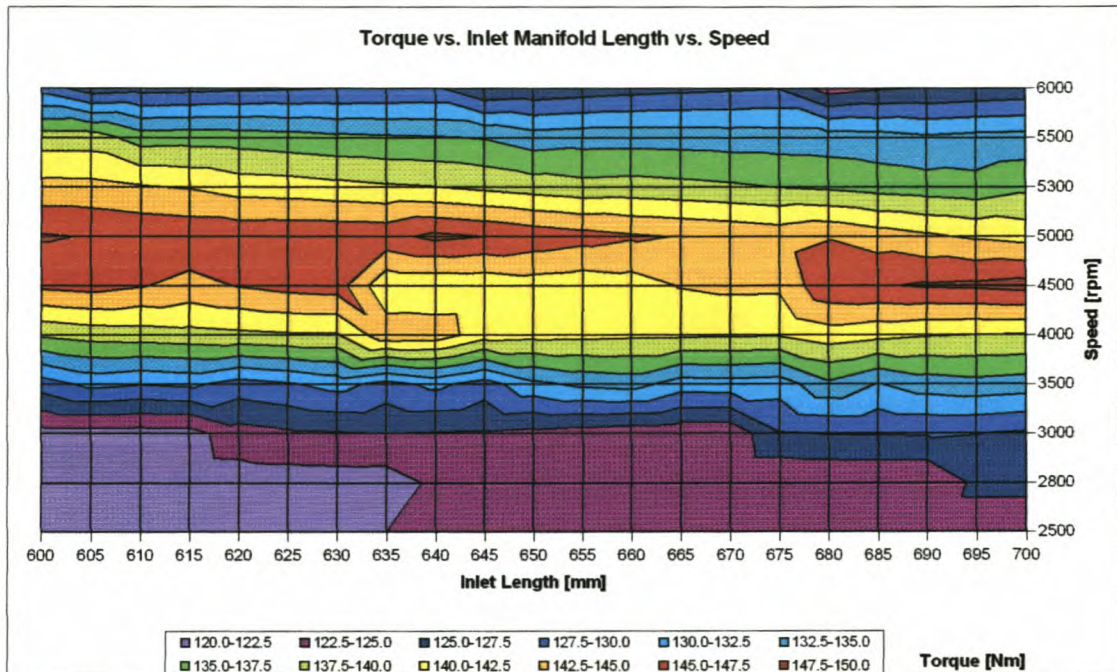


Figure 6-14: 3-Dimensional map of torque

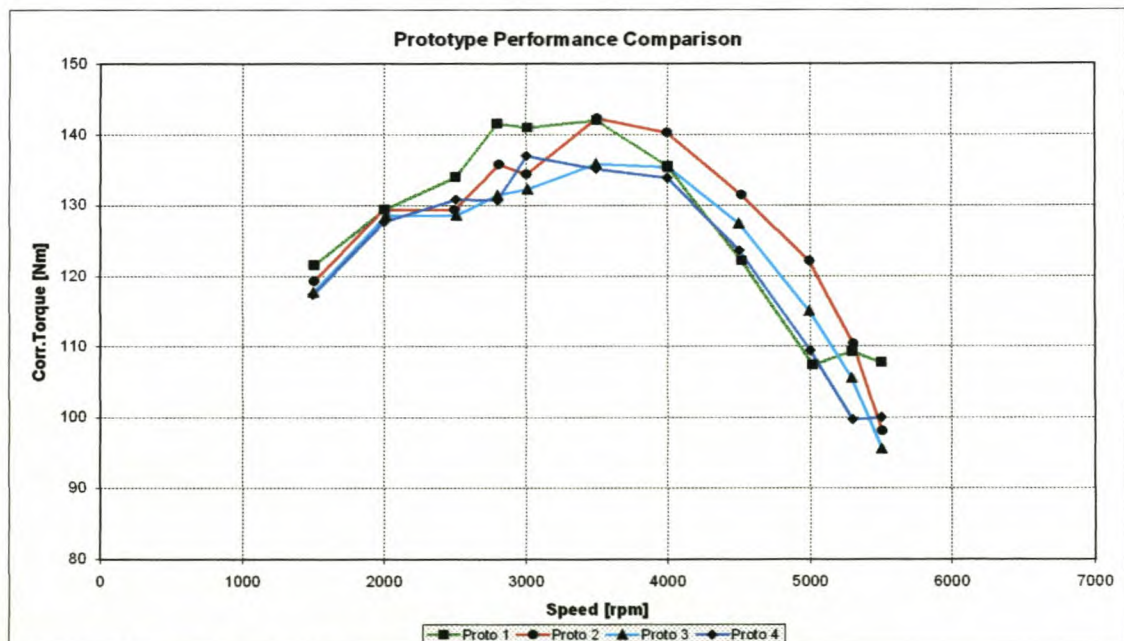


Figure 6-15: Engine performance on new prototypes

The performance curves of the four prototypes are presented in Figure 6-15. The torque benefits at low engine speeds of the 680mm manifold and the power benefits at high engine speeds of the 640mm manifold influenced the

Chapter 6: Experimental Versatility Testing

final decision to investigate these two prototypes further. The 700mm prototype was too long to give the high-speed power and the 600mm prototype was too short to give the low speed torque.

- **Inlet manifold diameter.** The diameter or effective flow area has a significant effect on the extent of the ramming effect achieved in the inlet manifold. The flow area must not be too small that the flow is restricted, but also not be too big that kinetic energy is not utilised. Optimum performance at

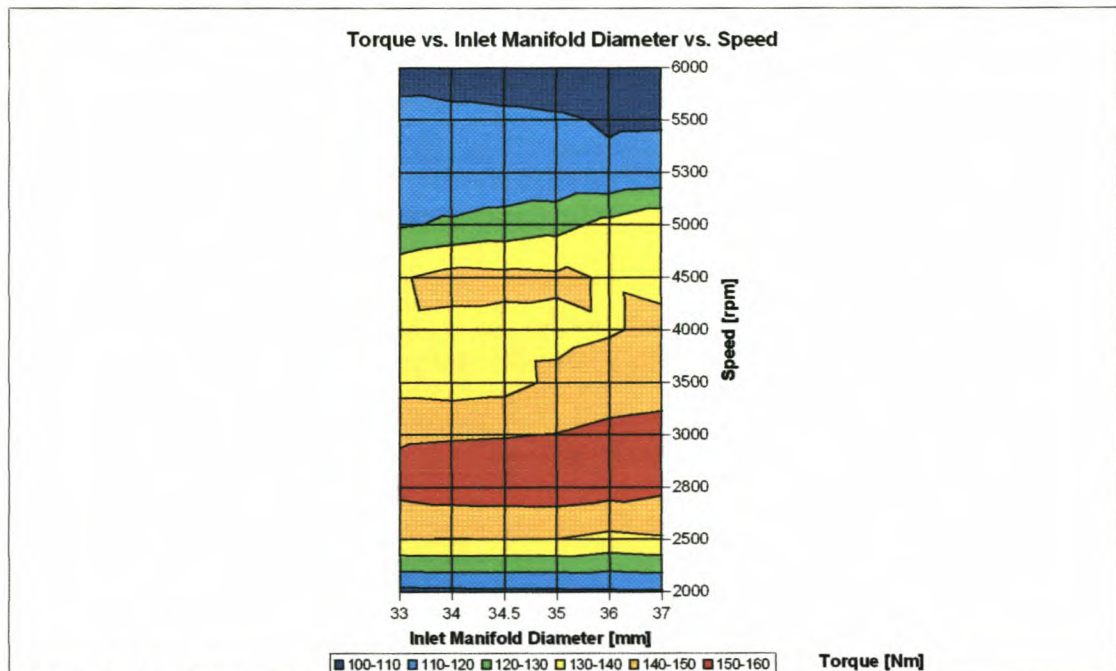


Figure 6-16: 3-Dimensional torque map for 680mm prototype

higher engine speeds normally requires a larger flow area than that required at lower engine speeds and vice versa. The existing diameter for the lower part of the manifold was 34.5mm and it was decided to keep this as the main diameter for the first four prototypes. Further tests were done on two inlet lengths, 680mm and 640mm as illustrated in Figures 6-16 and 6-17. From these graphs the following two prototypes were made:

- Prototype 5: 680mm x 37mm
- Prototype 6: 640mm x 36mm

After dynamometer tests on these prototypes, it was decided to go with 680mm manifold. The emphases on low speed torque and drive-ability turned the scale in favour of the longer length manifold. Further iterations were done on different diameters.

Chapter 6: Experimental Versatility Testing

The following prototypes were made:

- Prototype 7: 680mm x 33.3mm
- Prototype 8: 680mm x 34.5mm (improved plenum design)
- Prototype 9: 680mm x 35.6mm

The performance results on these prototypes are presented in Figure 6-18.

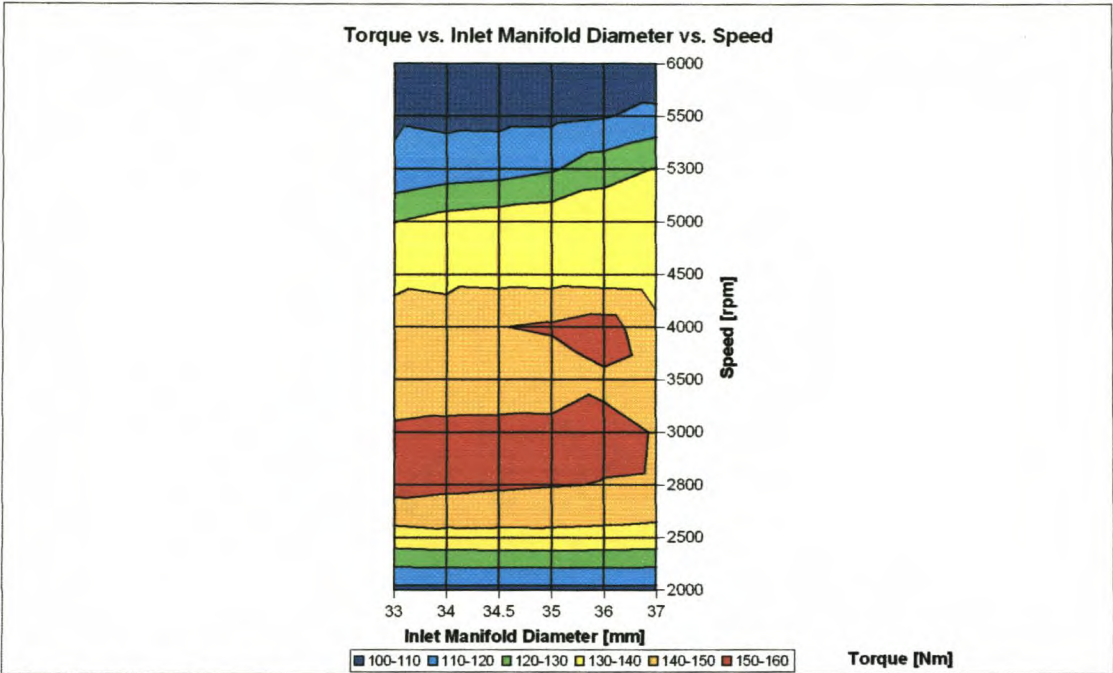


Figure 6-17: 3-Dimensional torque map for 640mm prototype

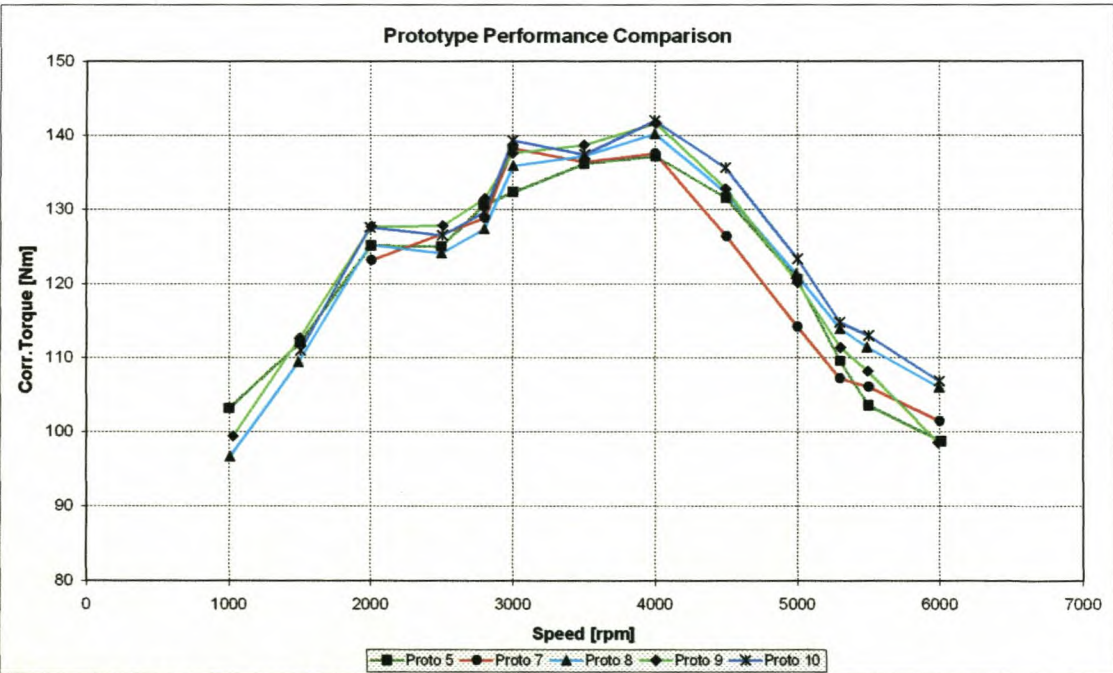


Figure 6-18: Engine performance on final prototypes

The last designed prototype, Prototype 10: 680mm x 34.5mm, the plenum volume of the manifold and trumpet were again redesigned and optimised.

Chapter 6: Experimental Versatility Testing

Photos of some of the glass fibre prototypes are presented in Appendix J.

- **Inlet trumpet shape.** The use of a trumpet or diffuser at the inlet to the manifold pipe is relatively common. Maximum pressure recovery at the inlet is vital to achieve good volumetric efficiency. To get pressure recovery at the inlet, the speed at the entrance of the inlet manifold must be kept as low as possible. This is achieved by keeping the particle acceleration in the trumpet constant. The optimum shape of the trumpet is a function of engine speed, engine displacement and manifold pipe length. This was also discussed in detail earlier in this chapter, section 6.4.
- **Plenum chamber.** It's been proved by Ohata and Ishida [22] that constructive resonance can take place in the plenum chamber of an inlet manifold. The frequency at which the plenum resonates is a function of its volume as well as the dimensions of the manifold pipes. The plenum must also be designed to have enough clearance around the trumpet section of the inlet, to ensure unrestricted airflow into each trumpet. The plenum design for this manifold was done to try and enhance low speed torque.

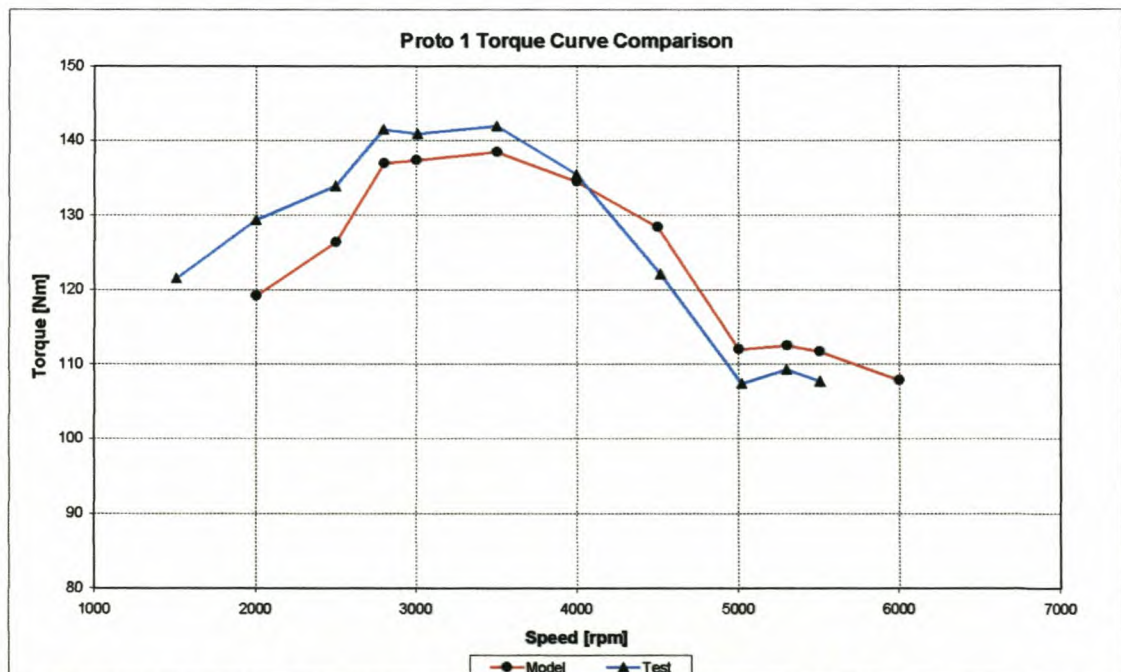


Figure 6-19: Initial torque comparison between modelled and tested data

In the development phase of the project, two different plenums were tested and it was found that the smaller plenum improved the torque over most of the engine speed range, but especially at low engine speeds. This showed that

Chapter 6: Experimental Versatility Testing

the minimum energy was lost in the plenum and energy was transferred through to the other inlet pipes, maximising the volumetric efficiency of the engine. This was also discussed earlier in the chapter, section 6.3.

The ESA simulation program used in the design process of the inlet manifold was very much in the development stage at the start of the project. During the development of the inlet manifold the program was running with a one-zone combustion model which is not as accurate as the final two-zone combustion model now in use. Good comparison was still found between the modelled and tested data as illustrated in Figures 6-19 and 6-20.

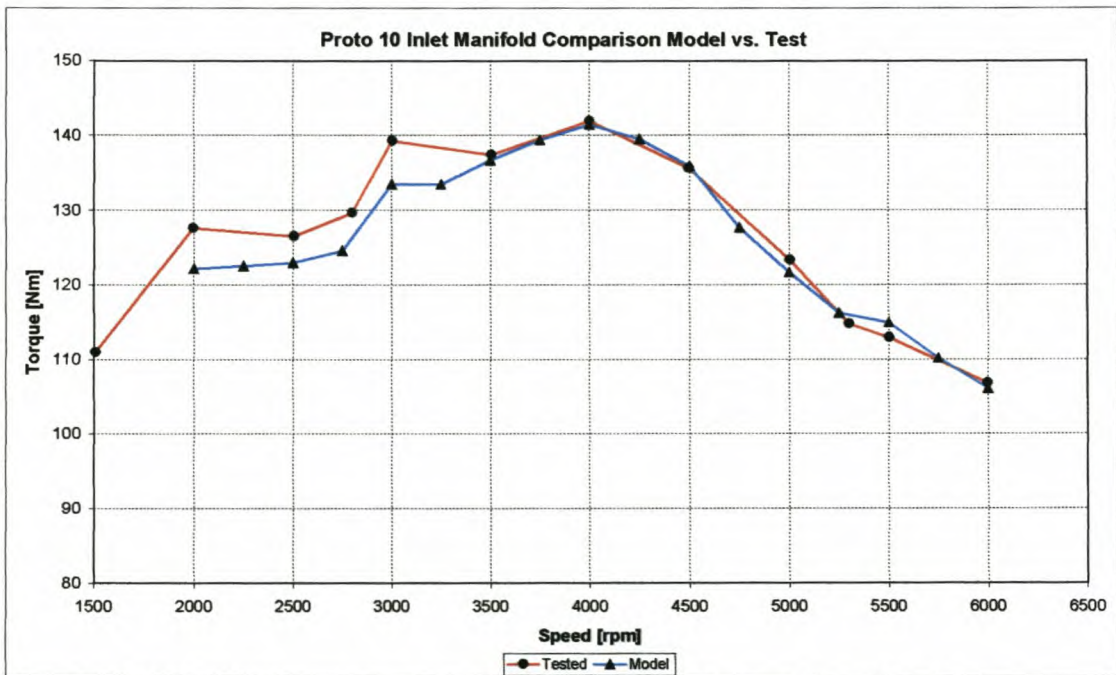


Figure 6-20: Final torque comparison between modelled and tested data

In Figure 6-19 the initial model is compared to the test results of Prototype 1. At this stage of the development only some of the engine information for e.g. exhaust back pressure and temperature, ignition timing and inlet plenum pressures were available. This caused some differences between the modelled and tested data. At the end of the project when all the final engine information was available, the simulation data illustrated in Figure 6-20 was created. Very good comparison between modelled and tested data is found. The only significant difference is at low engine speeds. This phenomenon is explained in Chapters 4 and 5.

Chapter 6: Experimental Versatility Testing

6.6.2. FAW-VW China Bora inlet manifold development

One of the emerging markets for international motor companies is China. Volkswagen AG, in Germany, decided to launch the new Jetta 4 in China in 2001 and that it will be called the Volkswagen Bora. It was decided that the top of the range Bora would have a four cylinder 1.6ℓ 20-valve engine. In the current A2 Jetta range in China such an engine does exist, but it does not fit into the engine bay of the Bora. The Chinese public also feels that the engine is low on performance. FAW-VW and Volkswagen AG then contracted Volkswagen South Africa and the University of Stellenbosch to develop a new inlet manifold, based on the current manifold used in the 1.8ℓ 20-valve Audi engine (Figure 6-21). The performance targets for the engine were specified as follows:

- Maximum torque of $\pm 150\text{Nm}$ @ 4000rpm or below.
- Maximum power of $\pm 78\text{kW}$ @ 5750rpm or higher.

Emphasis must also be on a smooth torque curve to enhance drive-ability. The new upper inlet manifold had to fit on an existing lower inlet manifold with an inside diameter of 37mm. The manifold also had to fit neatly in the engine bay with the necessary clearances from the bonnet line and other external parts. Using drawings supplied by Volkswagen, the limits for the inlet manifold



Figure 6-21: Inlet manifold for the Audi 1.8ℓ 20-valve engine

Chapter 6: Experimental Versatility Testing

were calculated. The drawings showed that it would be very difficult to change the length of the existing 1.8ℓ 20-valve manifold. Volkswagen AG also then prescribed that the length and overall appearance of the existing 1.8ℓ 20-valve engine inlet manifold had be the same, leaving only the diameter and trumpet of the inlet manifold as varying parameters.

The initial approach was to design two manifolds on the basis of calculated results from the ESA software. A further 3 manifolds were then designed, varying only slightly in design, in an attempt to obtain the optimum configuration. The result was a set of 5 glass fibre prototype manifolds.

Initially, the current 1.6ℓ 20-valve inlet manifold (Figure 6-22) and 1.8ℓ 20-valve manifold were studied in an attempt to identify specific performance features. The existing 1.6ℓ 20-valve engine and manifold setup was simulated by ESA. Some performance information on this engine was available and certain parts of the engine would stay the same for the new manifold development. A comparison of the base model and tested data are illustrated in Figure 6-23.

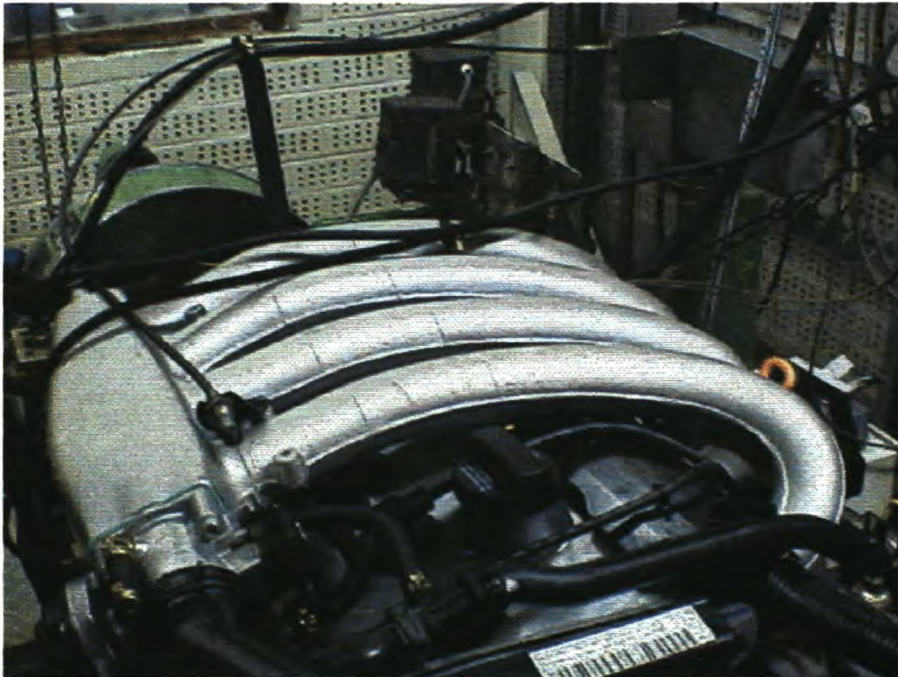


Figure 6-22: Standard A2 Jetta 1.6ℓ 20-valve inlet manifold

A series of calculations using ESA were then carried out to investigate the airflow characteristics and resonant frequencies of the new inlet manifold and engine configuration.

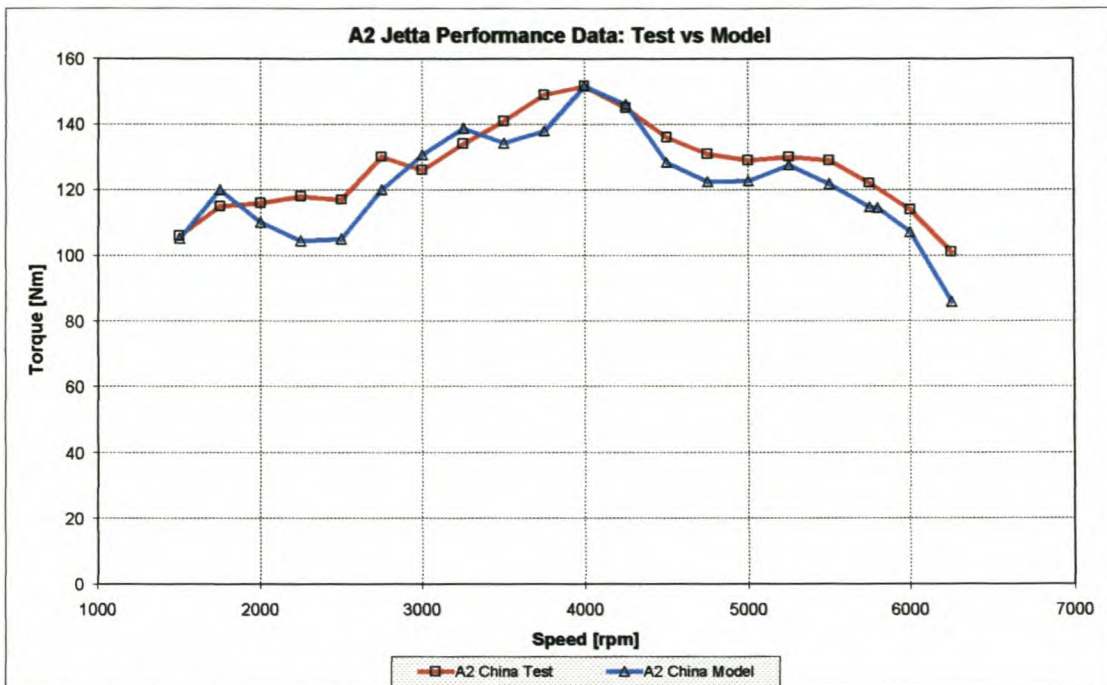


Figure 6-23: A2 Jetta base model comparison

The following parameters were taken into account in the design process of the composite prototype manifolds:

- General inlet manifold pipe shape.** The upper part of the inlet manifold was designed to fit on a small lower part with round ports. The spatial constraints forced the designers to keep the shape of the upper manifold the same as 1.8ℓ 20-valve Audi engine. The shape of the ports is round, except at the trumpet section where elliptical shape ports are used.
- Inlet manifold pipe length and performance specifications.** FAW-VW and Volkswagen AG specified the expected performance figures for the new engine. The engine has to develop $\pm 150\text{Nm}$ of torque at $\pm 4000\text{rpm}$ or below and $\pm 78\text{kW}$ at $\pm 5750\text{rpm}$ or higher. Due to the specification of the client, the designers were not allowed to change the length of the inlet manifold (total length = 686mm). Volkswagen South Africa wanted it investigated though, because it was felt that with the existing length the torque requirement might be difficult to obtain. With a longer length manifold this might have been possible. Numerous length variations on ESA were simulated and a 3-dimensional map was created to show the effect (Figure 6-24).

From Figure 6-24 it is clear that the increase in length decreases the engine speed at which the manifold will perform at its optimum. It is also clear from

Chapter 6: Experimental Versatility Testing

Figure 6-24 that certain lengths are tuned to its optimum, because of the ramming effect it has just before the inlet valve is closed. It was most interesting to see that with the existing length and a diameter 37mm (same as lower manifold) the maximum torque of the engine would be at 4250rpm. This proved the suspicion of the designers and this information was given to the client which replied that the length must stay the same and other means must be found to get the maximum torque at 4000rpm or below. The next step was therefore to investigate the effect of diameter on the torque characteristics of the engine.

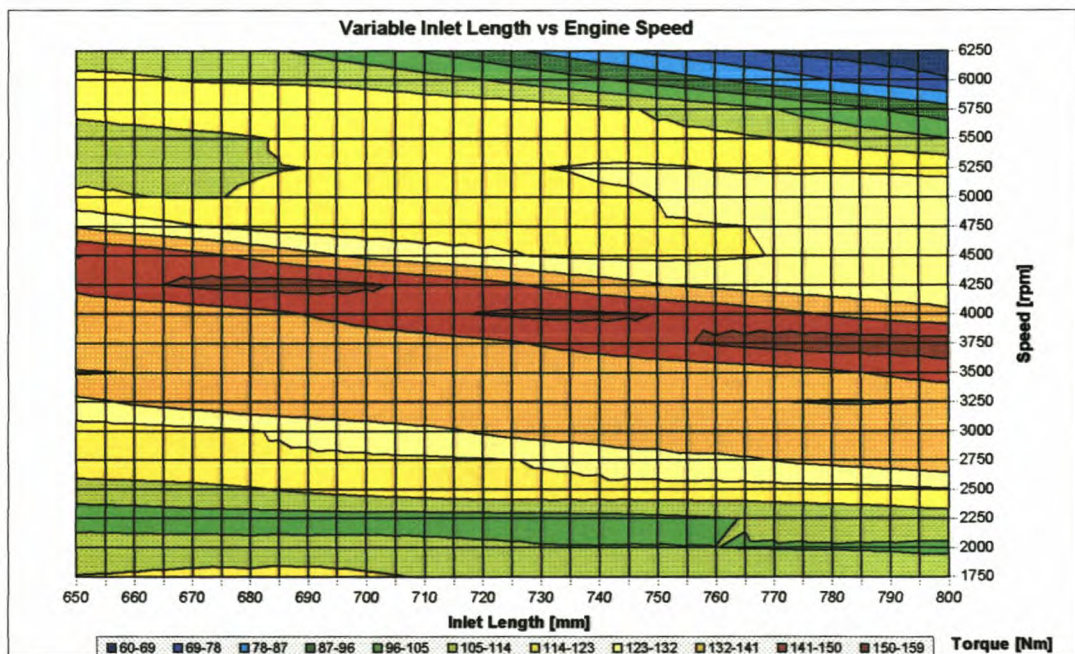


Figure 6-24: 3-Dimensional map of torque at different engine speeds and inlet lengths

- **Inlet manifold diameter.** The diameter or effective flow area has a significant effect on the extent of the ramming effect achieved in the inlet manifold. The flow area must not be too small that the flow is restricted, but also not too big that the kinetic energy is not utilised. The existing diameter for the lower part of the manifold is 37mm, but the model showed that this might cause the engine to not make the specification torque target at 4000rpm or below. Simulations using ESA were done to investigate the effect of diameter changes.

From Figure 6-25 the following two prototypes were made:

- Prototype 1: 686mm x 36mm (no trumpet)
- Prototype 2: 686mm x 36mm (with trumpet)

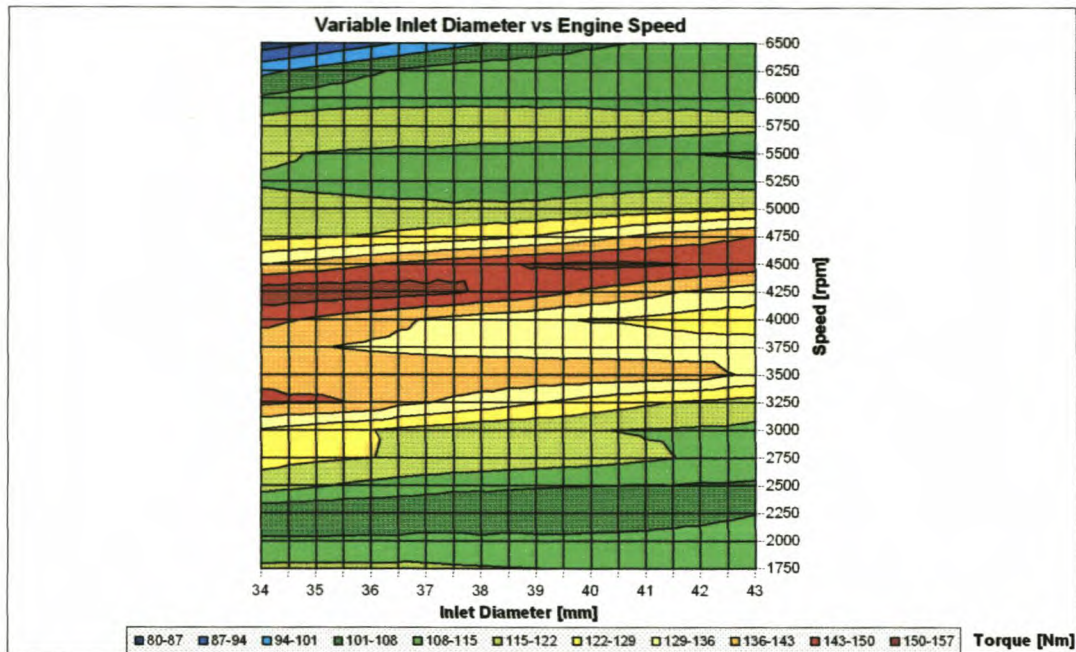


Figure 6-25: 3-Dimensional torque map for diameter change

In the manufacturing process of the cores, the cores unfortunately shrunk to a diameter of 35.5mm, which meant that the engine would probably develop its maximum torque at ± 4000 rpm. These two manifolds were then tested on an engine; the performance curves are presented in Figure 6-26.

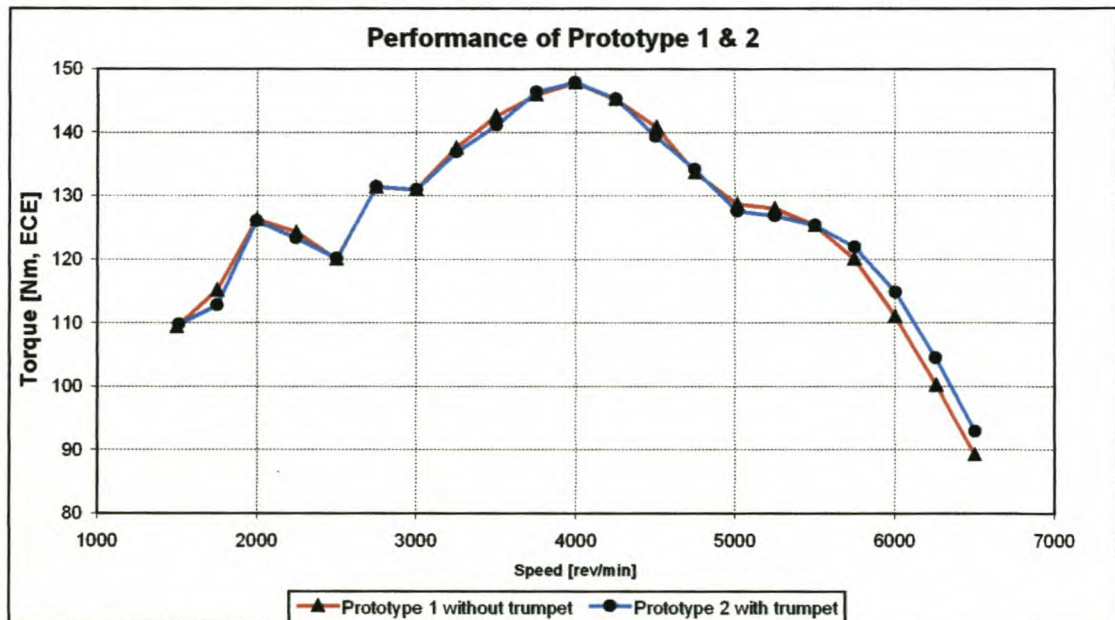


Figure 6-26: Performance of prototypes 1 & 2

With these two prototypes it was possible to get the peak torque at 4000rpm and the peak power at 5750rpm, but the maximum values were below the requirement. It was especially the maximum power of 73kW that fell well short of the specified 78kW.

Chapter 6: Experimental Versatility Testing

Meanwhile Volkswagen South Africa got some aluminium prototypes that were used for the 1.8ℓ 20-valve Audi development. The following aluminium prototypes were available for testing:

- Aluminium 1: 686mm x 37mm
- Aluminium 2: 686mm x 39mm
- Aluminium 3: 686mm x 41mm

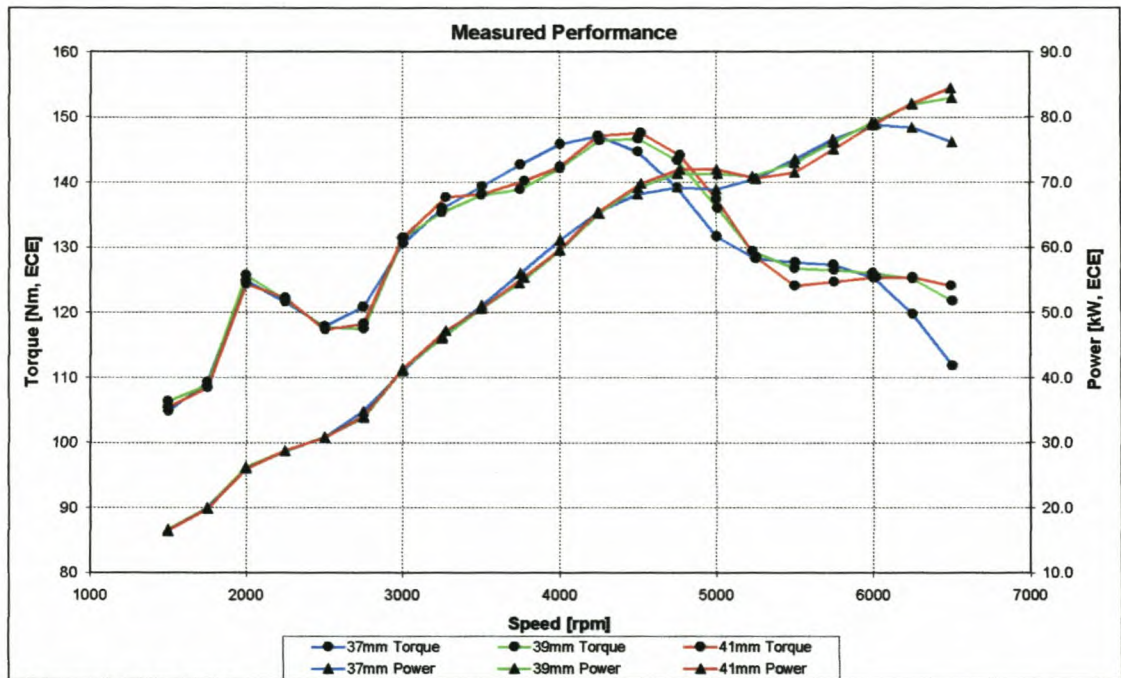


Figure 6-27: Performance data on aluminium prototypes

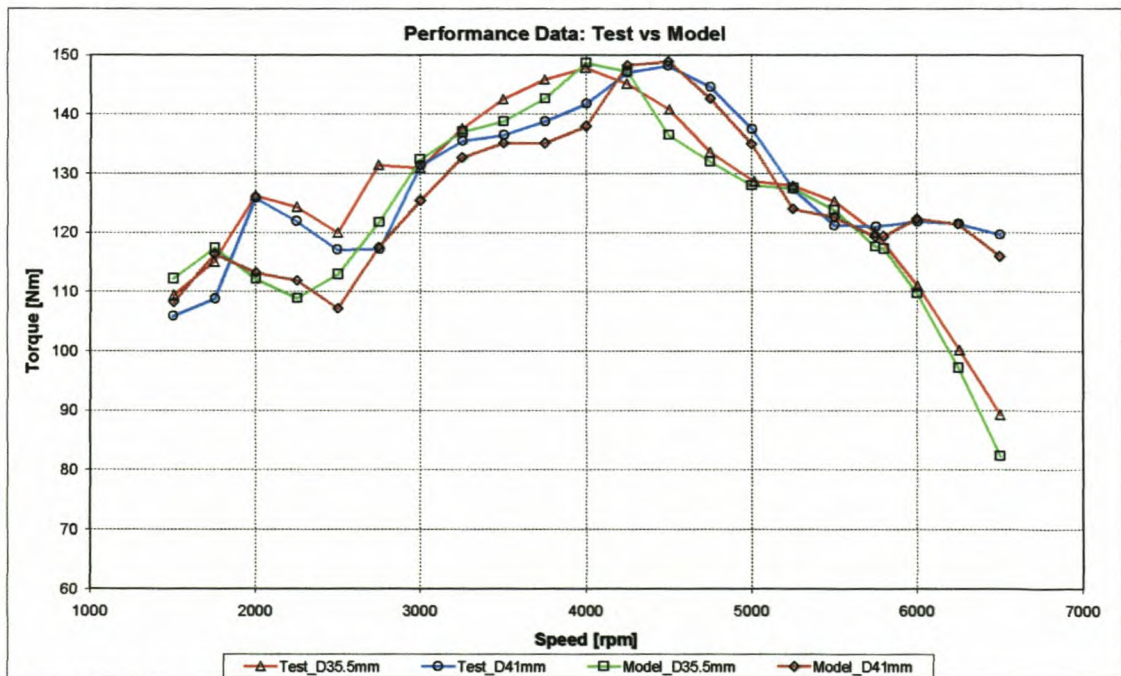


Figure 6-28: Model and test data comparison

Chapter 6: Experimental Versatility Testing

These manifolds were then tested on the engine (Figure 6-27). The ESA model was then evaluated by simulating the two extreme diameters tested up to that point. Simulations were done on the 35.5mm composite manifold and 41mm aluminium manifold (Figure 6-28). Extremely good agreement was obtained between the tested and simulated data.

Due to pressure from Volkswagen AG, a decision had to be made on the final dimensions of the inlet manifold. All test data and simulated data were investigated and the final decision was to make a 37mm inside diameter manifold. The emphases on low speed torque, a smooth torque curve and drive-ability turned the scale in favour of the 37mm diameter inlet manifold. A final glass fibre inlet manifold was then made to get performance data. Two other prototypes were also made to further investigate the influence of trumpets and diameters. The following prototypes were made, all with a new redesigned inlet trumpet:

- Prototype 3: 686mm x 37mm
- Prototype 4: 686mm x 35.5mm
- Prototype 5: 686mm x 36.5mm

The performance results on prototype 3 are presented in Figure 6-29. Unfortunately prototype 4 & 5 have not been tested up to date, due to time constraints in the project and availability of engines.



Figure 6-29: Engine performance on final prototypes

Chapter 6: Experimental Versatility Testing

Images of some of the glass fibre composite prototypes, CAD models and final aluminium prototype can be seen in Appendix J.

- **Inlet trumpet shape.** Maximum pressure recovery at the inlet is vital to achieve good volumetric efficiency. The optimum shape of the trumpet is a function of engine speed, engine displacement and manifold pipe length. On this manifold the trumpet design was changed twice, from a small very conservative trumpet, to a trumpet that just fitted into the plenum volume. The larger of the two trumpets proved to work the best with this manifold and engine setup.

Good agreement was obtained between the ESA software modelled and tested data (Figure 6-30). This simulation model, *Bora.eng*, can be found on the supplied installation CD. More pressure and velocity trace data can be found in Appendix K.

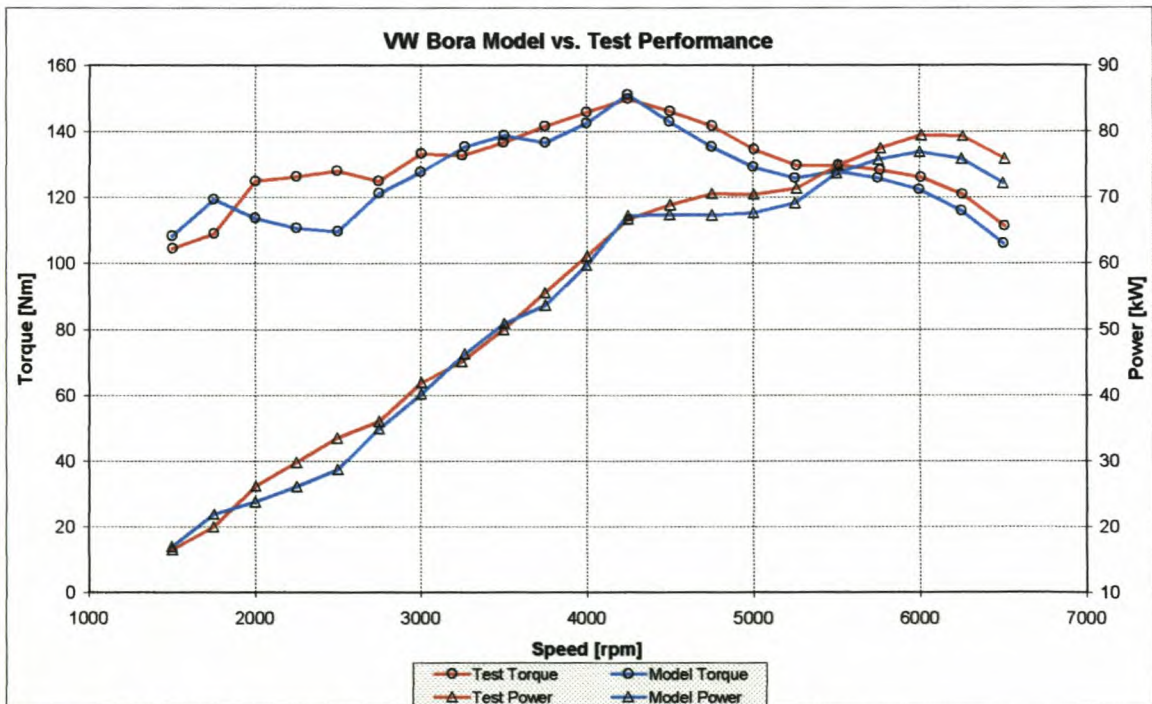


Figure 6-30: Final comparison between modelled and tested data

The development project was a great success. The clients, FAW-VW and Volkswagen AG, approved the final performance of the engine although the maximum torque was not reached at or below 4000rpm. The limitation of not being able to change the length of the manifold is accepted as the reason for this. The engine also struggled to get the 150Nm maximum torque value, because it was found to be extremely knock sensitive. By running a slightly richer

Chapter 6: Experimental Versatility Testing

air/fuel mixture this problem was solved and the engine managed to deliver 150Nm of torque. The maximum power of 78kW was also exceeded and some of the engines have delivered up to 83kW after a long run-in process. At the end of the project FAW-VW also decided to go for an additional option on the existing engine. Variable Valve Timing (VVT) could be added to the engine with little additional cost. The VVT system is a two-stage valve timing system that advances the inlet camshaft with 19° crank angle at speeds below 3250rpm. The difference in performance between the old and new 1.6l 20-valve engine is illustrated in Figure 6-31. This figure shows that the performance of the engine improved significantly.

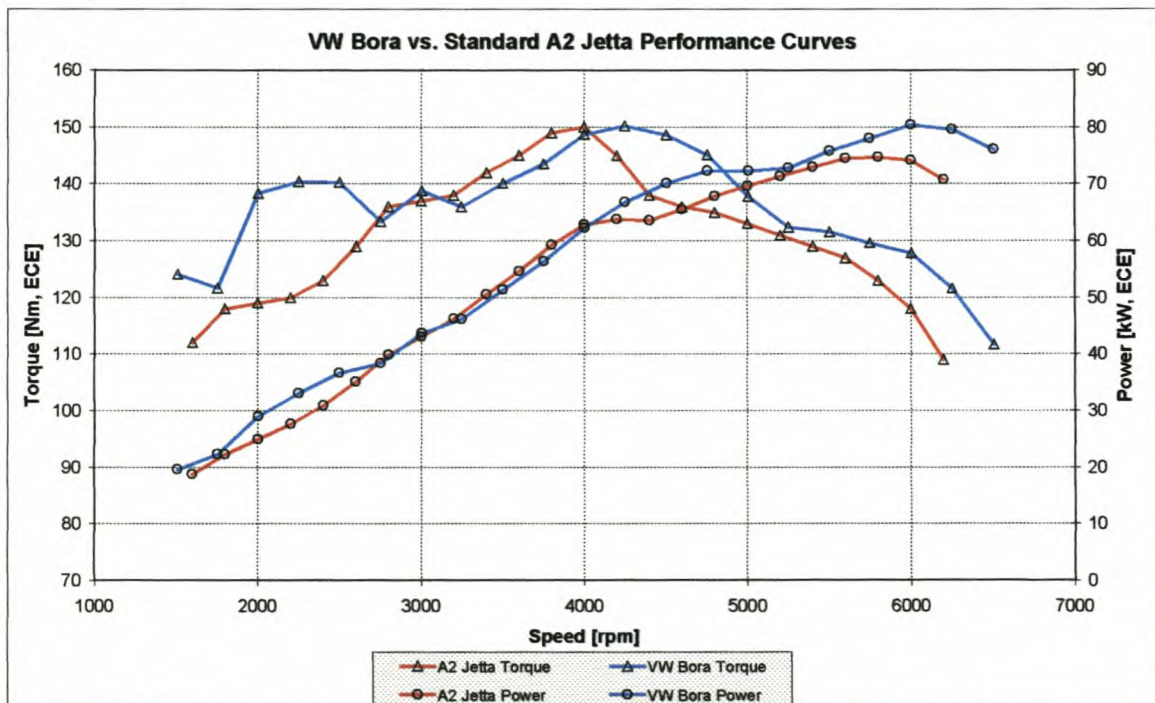


Figure 6-31: Performance comparison between standard A2 Jetta and VW Bora

6.7. CONCLUSION

In Chapters 5 and 6 it was shown that the ESA simulation program does very well in predicting actual engine performance. In Chapter 6 the versatility of the ESA program was illustrated by simulating different engines and different engine configurations.

In Chapter 7 the problems, shortcomings and recommendations for the ESA software and this thesis in general are discussed.

CHAPTER 7: CONCLUSIONS AND RECOMMENDATIONS

The primary objective of this thesis was to get a better understanding of gas flow through IC engines by means of numerical and experimental modelling. This was obtained in this thesis and can best be evaluated with the results of the ESA simulation program as presented in Chapters 5 and 6.

The objective of the simulation program is to enable a design engineer to test his proposed design on an interactive computer and to arrive at an optimum condition for the engine, designed to meet certain requirements. This computer simulation saved time and money in the engine development stage, by spending less time doing physical engine tests on a dynamometer test bed.

Performance data and pressure traces in the inlet manifold were recorded for comparison with the ESA software. Good correspondence was found between tested and modelled data and the differences varied between $\pm 5\%$ on engine performance data and pressure wave frequency predictions, and $\pm 10\%$ on pressure pulse amplitudes.

To conclude, the project undertaken made a significant contribution to the development tools available to the University of Stellenbosch and its design engineers. To the author's knowledge, a similar simulation package has never been developed in South Africa and the codes that do exist in other parts of the world are extremely expensive and need powerful computer computing power. Although the simulation program is not fully developed and perfected yet, it forms a very good design tool and basis for further studies and development.

No masters thesis will ever be without some obstacles and difficulties. In the following sections recommendations for future research on the ESA software and modelling of IC engines are given.

7.1. MULTI-CYLINDER BRANCH TYPE FLOW

Experimental studies of single cylinder engines have been numerous, but multi-cylinder engines have been the subject of only a few studies so far world-wide. This leaves a number of uncertainties, such as the effect of interference from other cylinders on the inlet and exhaust, the relationship between the inlet

Chapter 7: Conclusions and Recommendations

pressure variation in the plenum volume and the volumetric efficiency, and the natural frequency of a complicated full intake and exhaust system.

In a multi-cylinder engine, which has many branch pipes in the intake system, the generated pressure waves interfere with each other and the dynamic behaviour of the flow in an intake manifold by pressure waves can be utilised to increase the volumetric efficiency of a multi-cylinder engine [24, 25].

For this thesis most of the testing was done on multi-cylinder engines. Some measurements on pressure waves in the inlet manifold were recorded and discussed in Chapter 6. Unfortunately no modelling could be done on multi-cylinder engines. The program does not have the capability of modelling branch type flow and the interference effects between different cylinders on the inlet and exhaust side. This must be the primary aim for future developments of the ESA software.

7.2. OTHER COMPLEX BOUNDARY CONDITIONS, VOLUMES AND COMBUSTION MODELS

Modelling of other complex elements e.g. sudden contractions, sudden expansions, pipe junctions and plenum volumes will be necessary to make the model complete and more representative of an actual engine [28, 31]. The effect of different size plenum volumes on the inlet was explained in Chapter 6. This effect cannot be simulated at present and further development on this will be a great attribute to a more complete simulation program. The full clean air system must also be included in future work to enable the simulation of complete inlet systems.

Modelling of turbo-charged engines is also not possible at the moment. The implementation of a turbo-charger element in the inlet and exhaust systems will make it possible for the design engineer to investigate the effects of turbo-conversions on petrol engines and the effect different turbos have on engine performance [29].

Exhaust gas re-circulation is another advanced technology used by engine developers during the last few years. Such a mass addition element should also be considered as a future development into ESA.

Chapter 7: Conclusions and Recommendations

Design engineers would also benefit from a full diesel combustion model. The only diesel engine simulation software available at the University of Stellenbosch is SPICE II, which unfortunately is quite old and does not consider pulsating flow.

7.3. OTHER NUMERICAL SCHEMES AND SOLUTION METHODS

In this thesis the method of characteristics was used to solve the one-dimensional, non-steady flow equations. There are other numerical methods that can be used to solve these equations. Various finite difference schemes like the Lax-Wendroff (central difference scheme) [33, 35] and Harten-Lax-Leer (upstream difference scheme) methods [18, 34] are well known and should be compared with MOC. The Random-Choice method has also been used to simulate flow through nozzles, elbows and junctions and is especially good to simulate flow with shock waves [35, 37]. The 2-step Lax-Wendroff method seems to be the best method to use for unsteady flow in the intake and exhaust systems of engines [18, 30, 34]. The merit of this method is in improved stability, convergence and applicability in branch type flow systems [32].

The iterative solution method, i.e. the Euler-Predictor-Corrector method, used in this thesis should also be reconsidered and the fourth-order Runge Kutta method would be a good replacement. This will also show the difference and sensitivity to stability of the different mathematical solutions.

7.4. EXHAUST SYSTEM DESIGN

The exhaust manifold, downpipe and silencer all influence the final performance characteristic of an engine. Many researchers throughout the world have proved that a properly designed exhaust system can enhance the performance of an engine.

It is particularly branching type flows that influence the design of the exhaust system. The ESA program is unable to simulate this flow system and more development in this field will be a great contribution to a more complete simulation program.

7.5. VALVE FRICTION MODELS

Friction in the inlet and exhaust system of an engine and the total engine friction can be modelled quite accurately. Friction in valves is unfortunately not as

simple and some uncertainty exists regarding this type of loss. The best way of quantifying valve friction is by using a discharge coefficient as explained in Chapter 3 of this thesis.

Discharge coefficients can unfortunately only be recorded on a steady state flow bench or modelled by means of 3-dimensional CFD packages like STAR-CD. Some uncertainties do exist regarding the measurement of discharge coefficients under pulsating flow conditions. This imposes a question mark over the applicability of this data in engine simulations. More research will have to be done to determine the effect of pulsating flow on valve friction [22].

7.6. INLET VELOCITY & EXHAUST PRESSURE MEASUREMENTS

Modelling of flow through inlet manifolds is possible with the ESA software. The model can create pressure and velocity data that exists in the manifold. Unfortunately it was only possible to compare pressure data with recorded experimental results. The reason, as explained in Chapter 5, is that the available velocity measuring equipment, a hot-wire anemometer, could not withstand the pulsating flow in the inlet manifold and the heating element kept on breaking. Another means of velocity measurement in the inlet and exhaust system will have to be developed. This will make available another variable for comparison with ESA simulations.

Modelling of complete exhaust systems is a possibility, but to record pressure data for full evaluation purposes is a problem. Even for this thesis pressure measurements in the exhaust system had to be done away with, due to the high surface temperatures there. The pressure sensors that were used for the measurements in the inlet manifold can only withstand a maximum temperature of 120°C and the temperature in the exhaust can easily exceed 900°C. Not even in-cylinder pressure transducers can withstand these constantly high temperatures. A small heat exchanger will have to be developed that can be installed on the exhaust without influencing the transfer of pressure pulses to the pressure sensor.

7.7. GENERAL ESA LIMITATIONS

Some general limitations do exist in the current ESA simulation. The grid size is a variable that is recalculated at each engine speed, because the program uses a constant time step of 1° crank angle. This has the detrimental effect that it is difficult to compare grid point data at different engine speeds. It also causes a small grid size at low engine speeds and large grid size at high engine speeds. This is detrimental to the accuracy of results at low engine speeds due to the small number of grid points available to simulate the pulsating flow. It also makes it difficult to simulate trumpet sections at the inlet entry and inlet ports with big area variations.

The modelling of the transition from forward to reverse flow at the inlet and exhaust valves was also found to be quite difficult. Due to the “large” time step at low engine speeds, it was difficult to get a smooth transition between forward and reverse flow. The numerical solution method tended to oscillate between the two flow types for a few crank-angle degrees before finally going to the opposite flow type.

Incorporating the recommendations discussed in sections 7.1, 7.2, 7.3 and 7.5 will make the ESA software an extremely powerful tool without the high cost of commercial programs such as WAVE [44] developed by Ricardo in England. This would be a very good follow-up subject for another masters student or even at PhD level.

Appendix A

Case Study 1:

Reservoir and pipe configuration

Appendix A

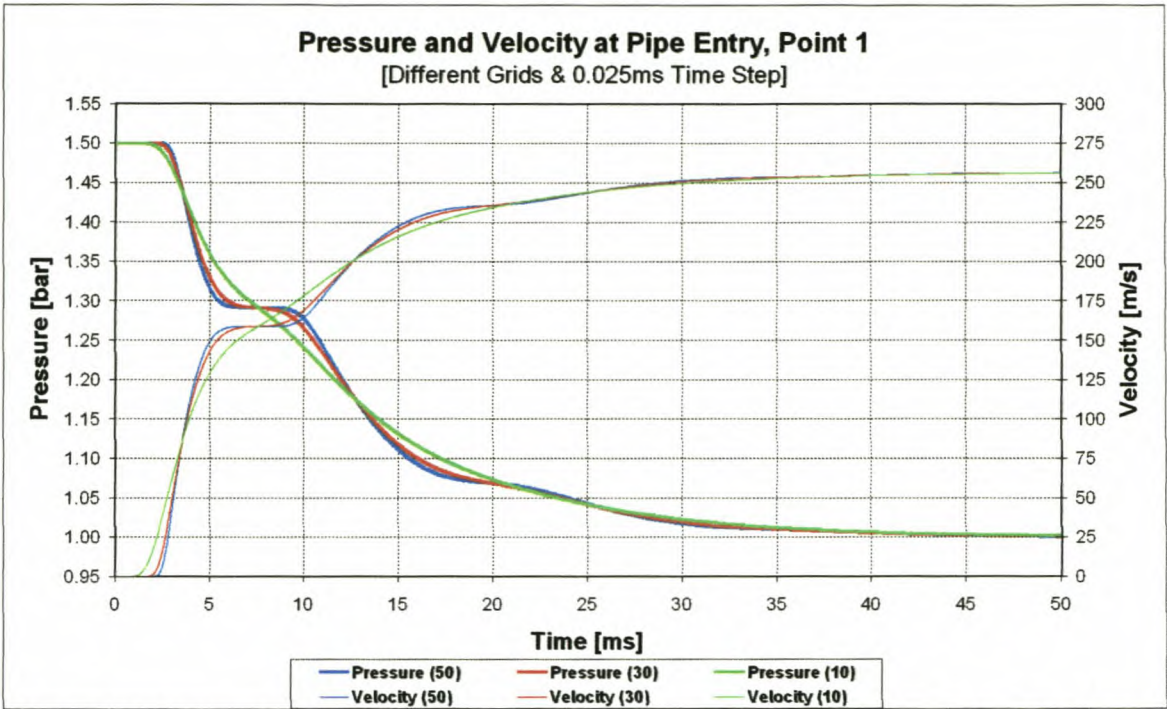


Figure A-1: Pressure and velocity at pipe entry [different grids & 0.025 ms time step]

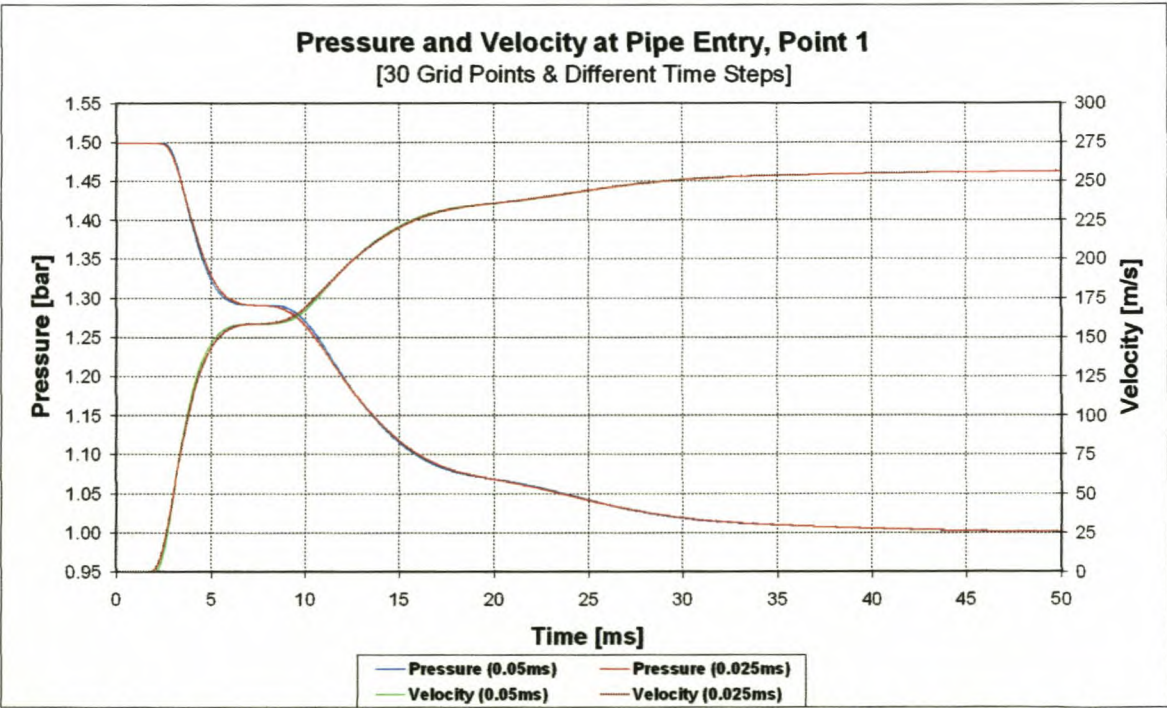


Figure A-2: Pressure and velocity at pipe entry [30 grid points & different time steps]

Appendix A

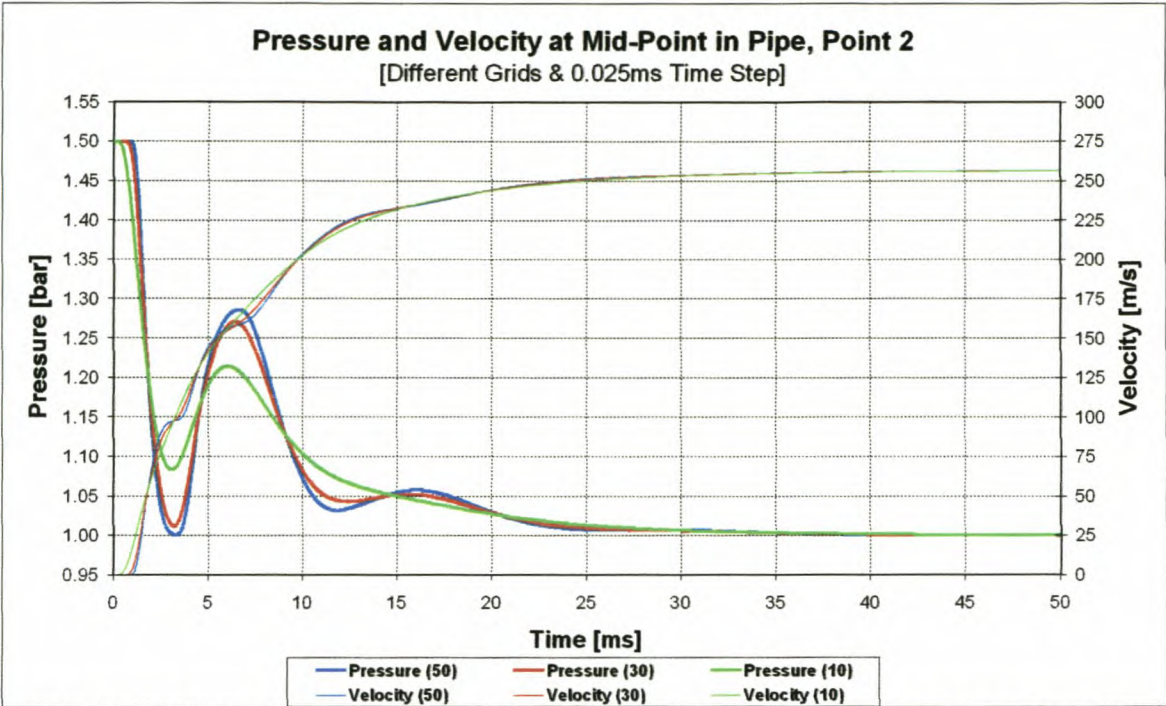


Figure A-3: Pressure and velocity at pipe mid-point [different grids & 0.025 ms time step]

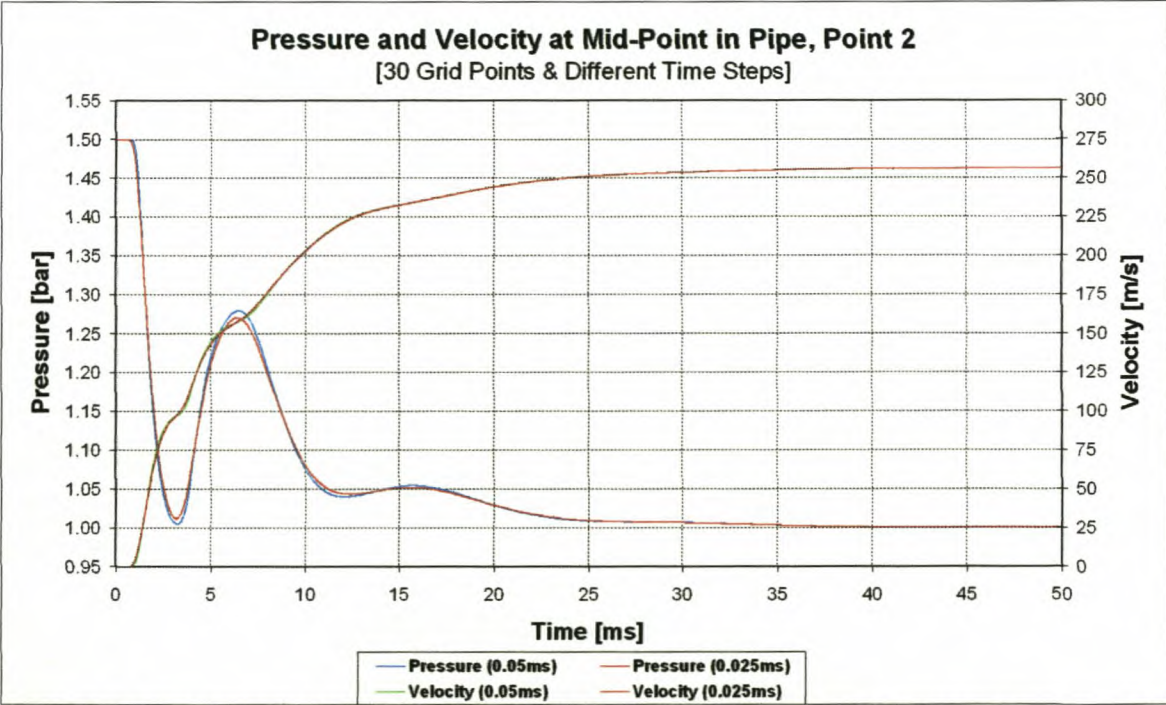


Figure A-4: Pressure and velocity at pipe mid-point [30 grid points & different time steps]

Appendix A

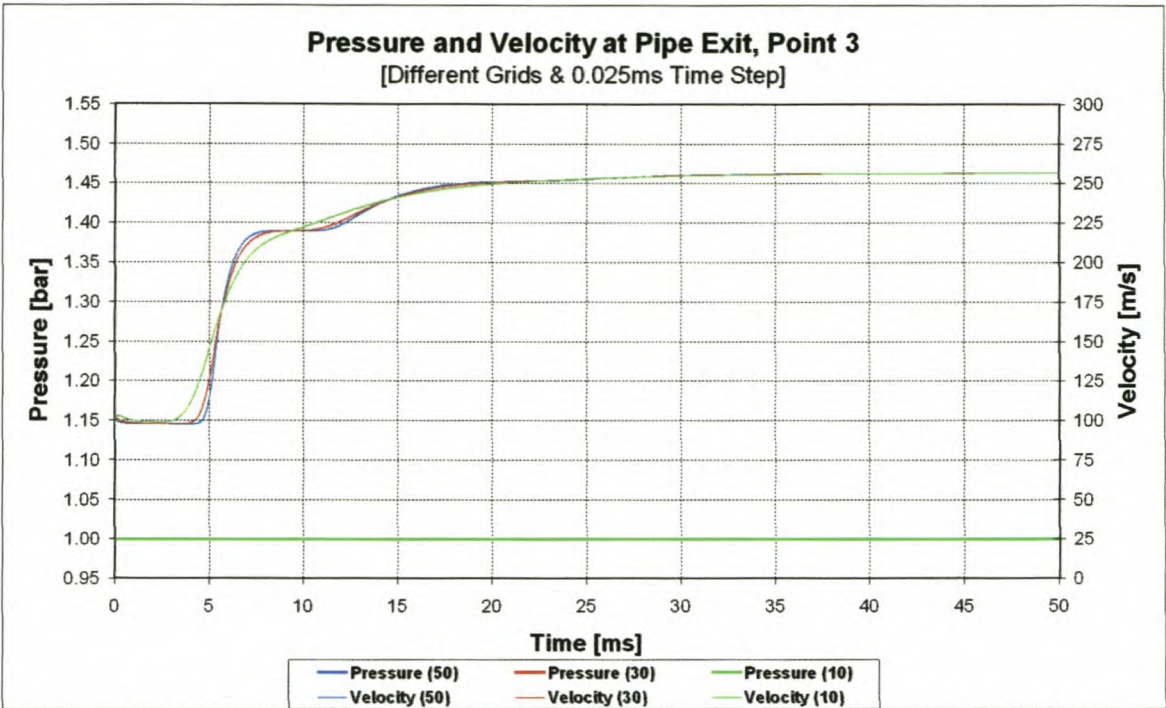


Figure A-5: Pressure and velocity at pipe exit [different grids & 0.025 ms time step]

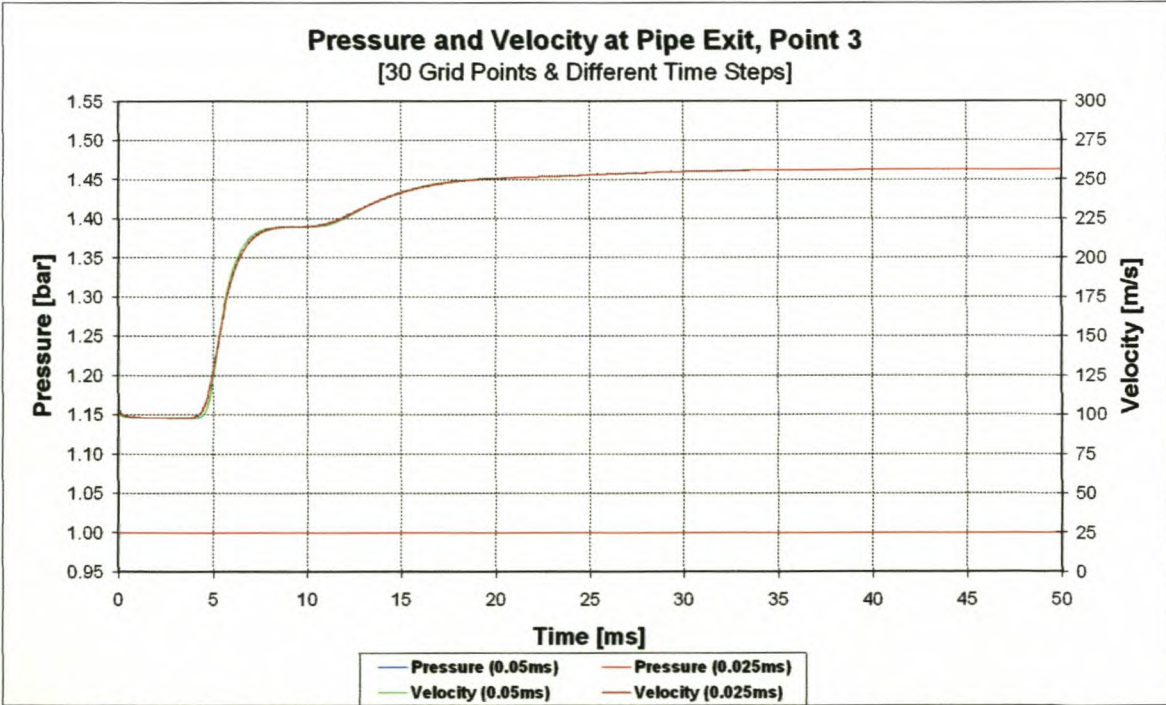


Figure A-6: Pressure and velocity at pipe exit [30 grid points & different time steps]

Appendix A

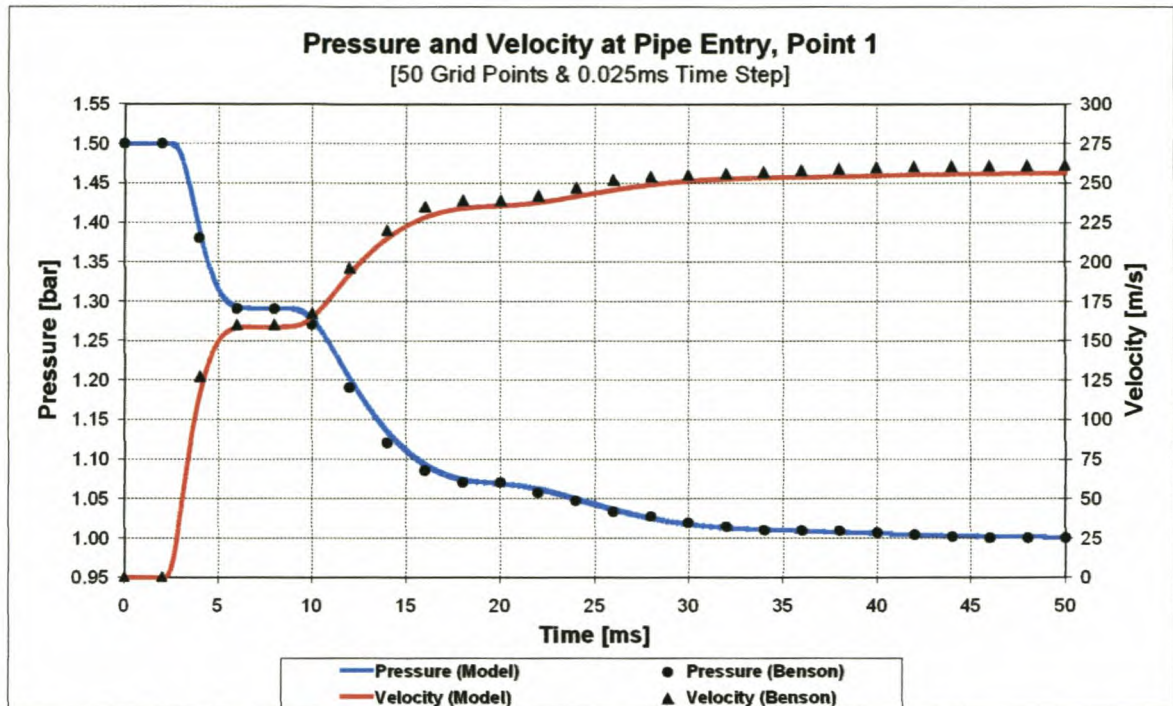


Figure A-7: Comparison of modelled data vs. Benson [4] data at pipe exit
[50 grid points & 0.025 ms time step]

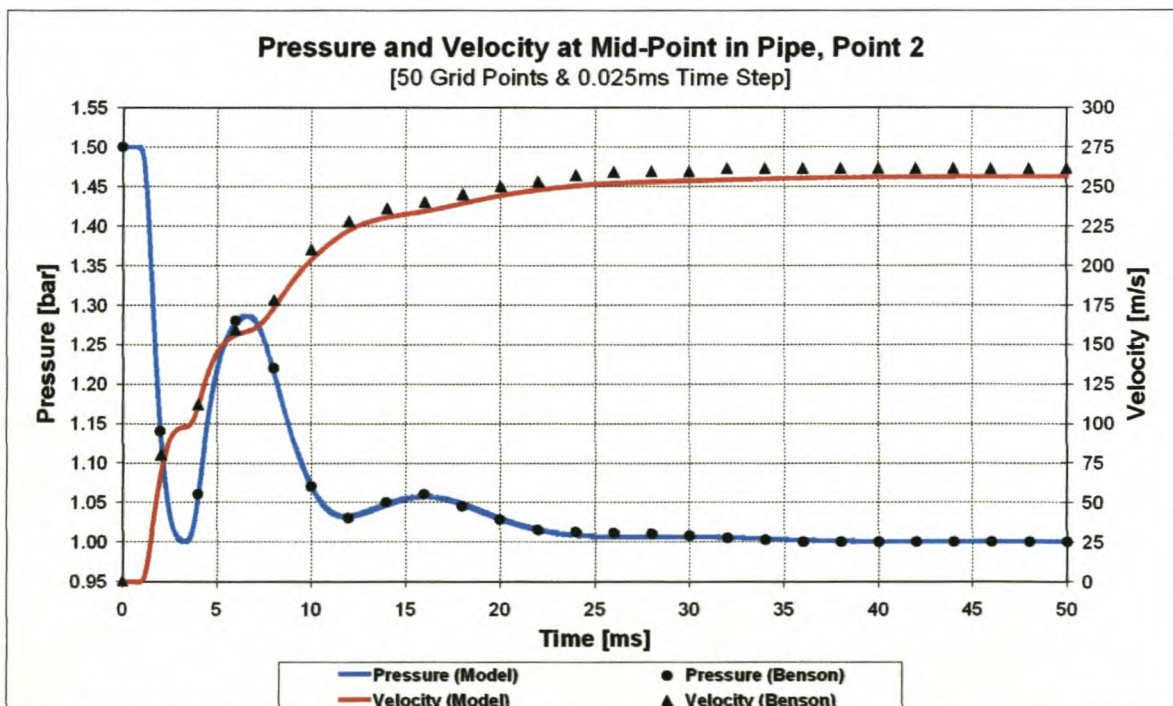


Figure A-8: Comparison of modelled data vs. Benson [4] data at mid-point in pipe
[50 grid points & 0.025 ms time step]

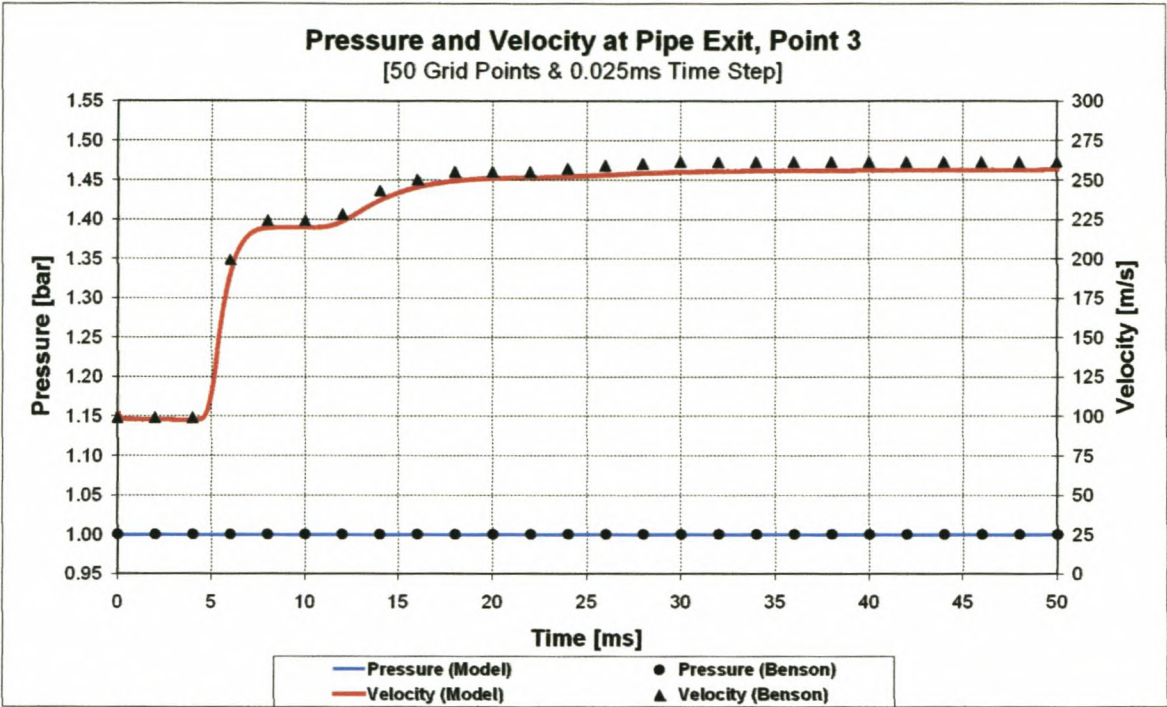


Figure A-9: Comparison of modelled data vs. Benson [4] data at pipe exit
[50 grid points & 0.025 ms time step]

Appendix B

Case Study 2:

Sudden discharge from a cylinder

Appendix B

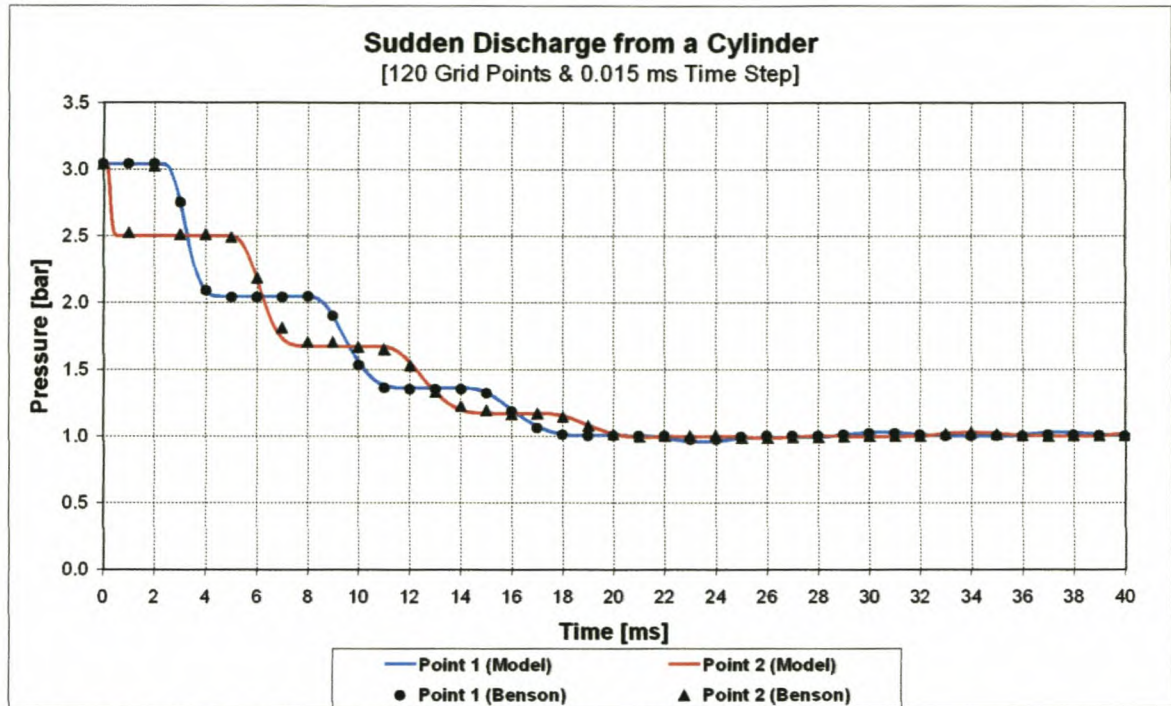


Figure B-1: Pressure in sudden discharge of a cylinder
[120 grid points & 0.015 ms time step]

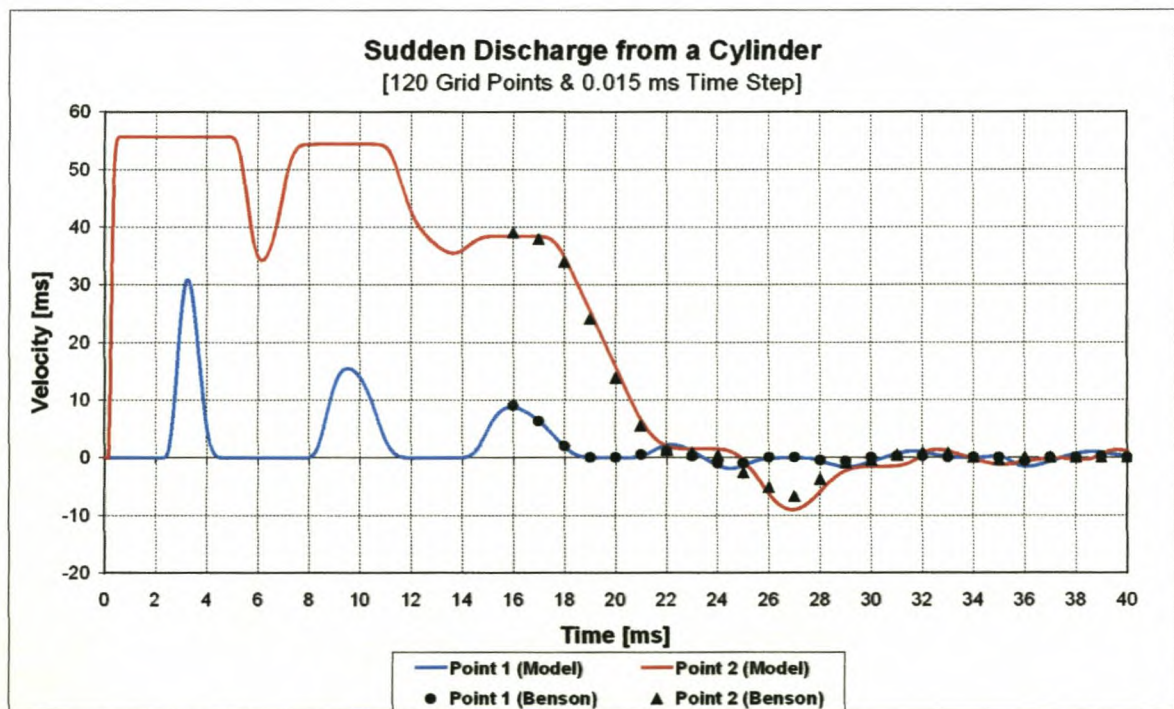


Figure B-2: Velocity in sudden discharge of a cylinder
[120 grid points & 0.015 ms time step]

Appendix B

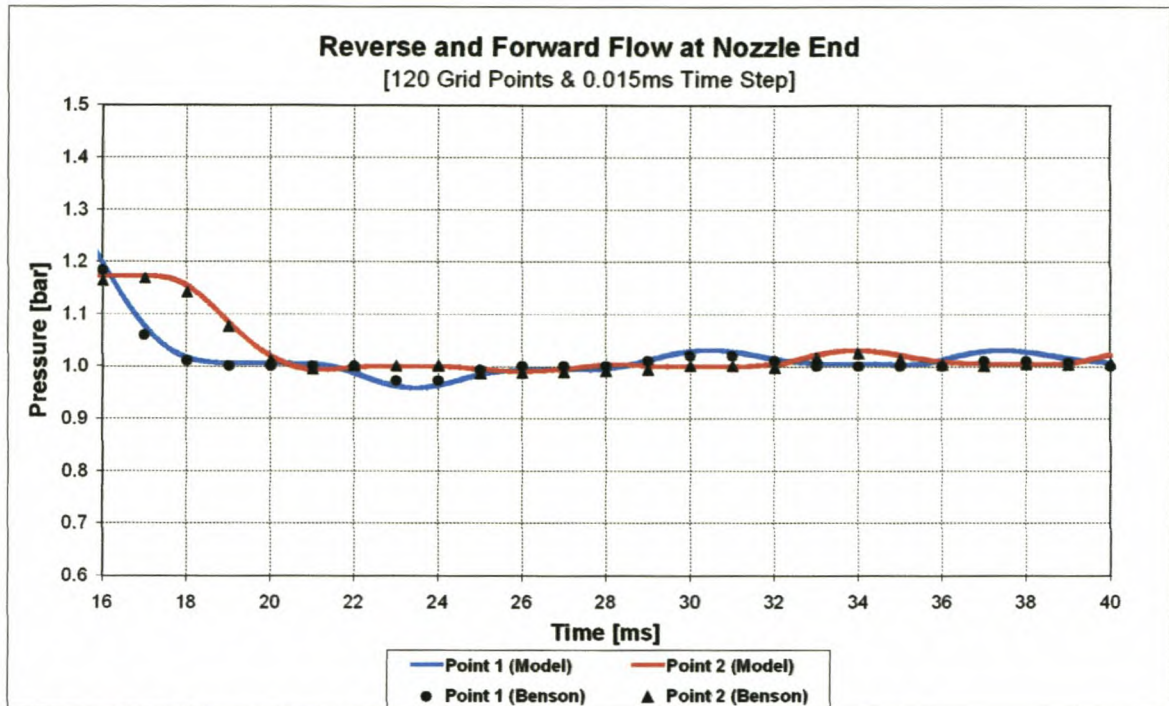


Figure B-3: Pressure trace for reverse and forward flow at nozzle end
[120 grid points & 0.015 ms time step]

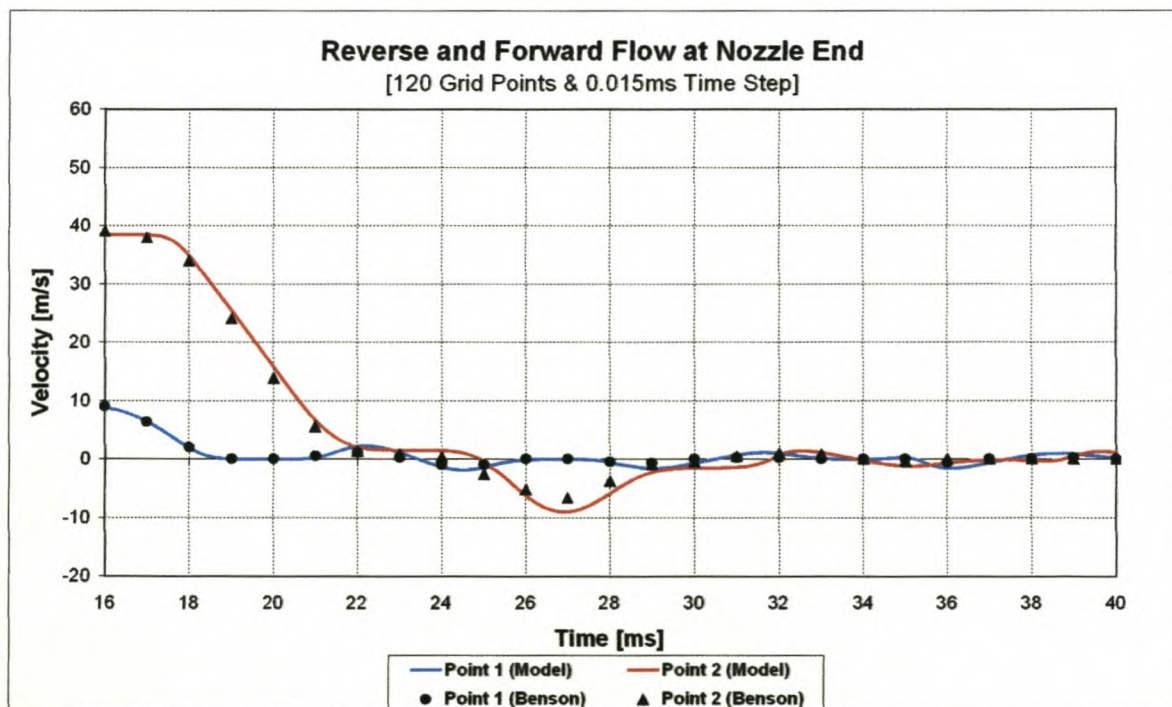


Figure B-4: Velocity trace for reverse and forward flow at nozzle end
[120 grid points & 0.015 ms time step]

Appendix C

Case Study 3:

Gradual discharge from a cylinder

Appendix C

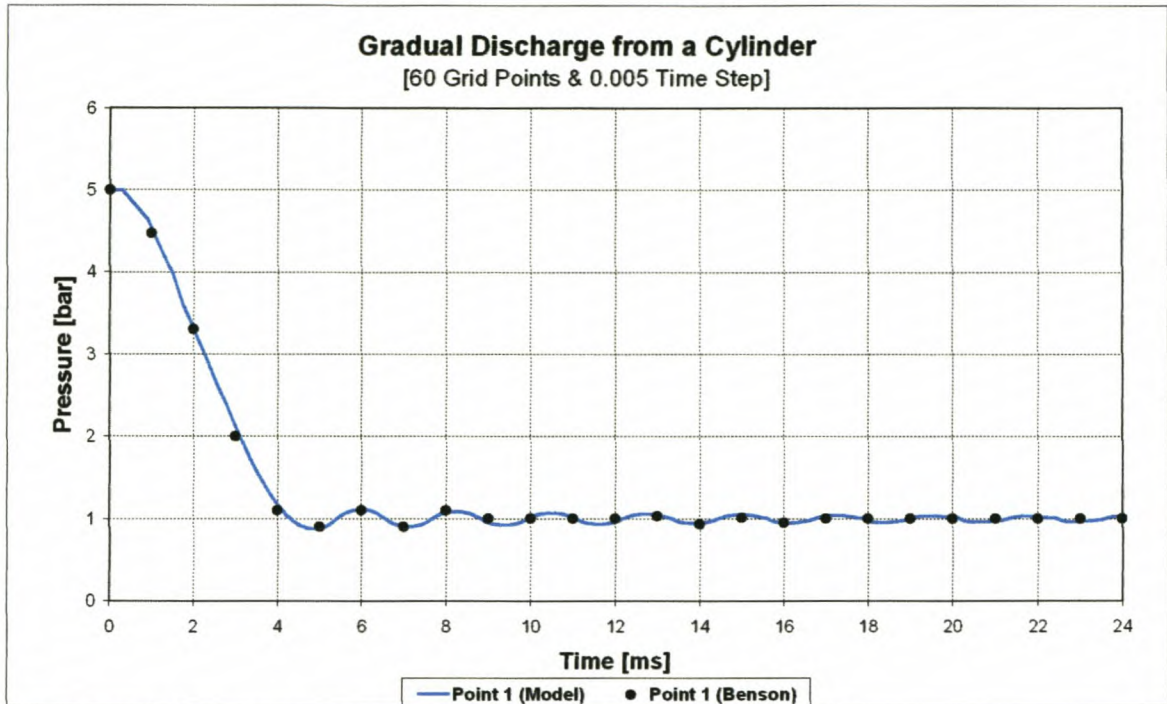


Figure C-1: Pressure at point 1 in gradual discharge of a cylinder
[60 grid points & 0.005 ms time step]

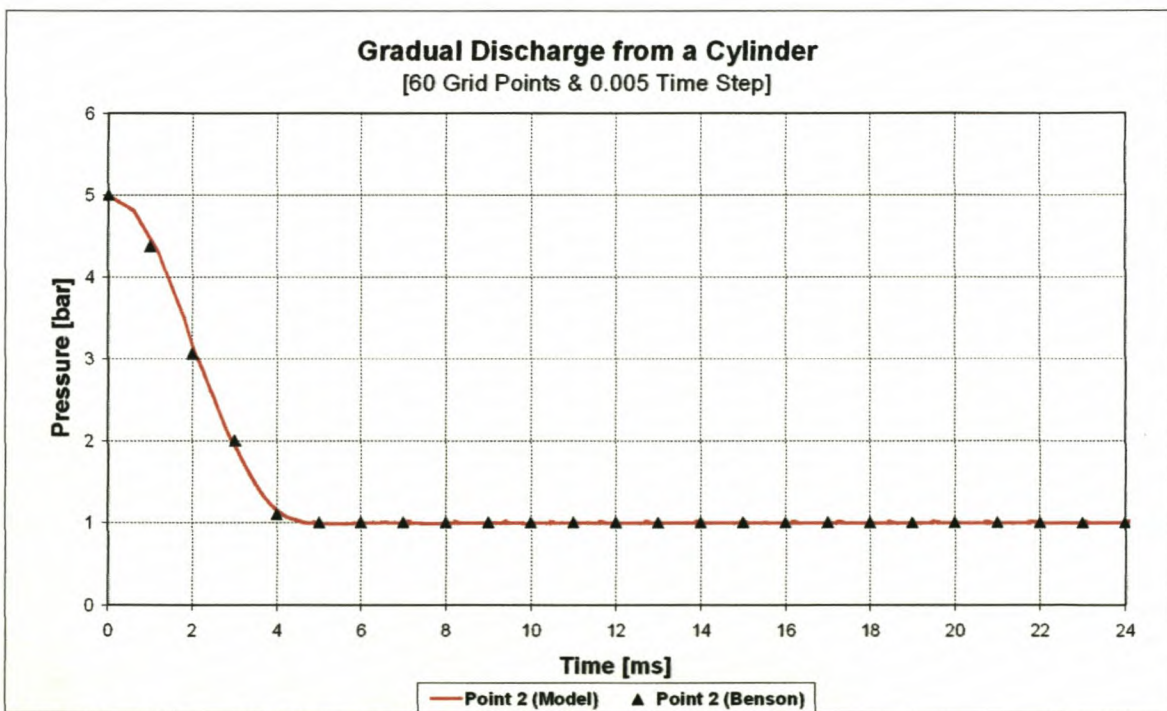


Figure C-2: Pressure at point 2 in gradual discharge of a cylinder
[60 grid points & 0.005 ms time step]

Appendix D

Case Study 1:

Simulation of an induction process

Appendix D

Test 1 [0.5 bar; 293 K]

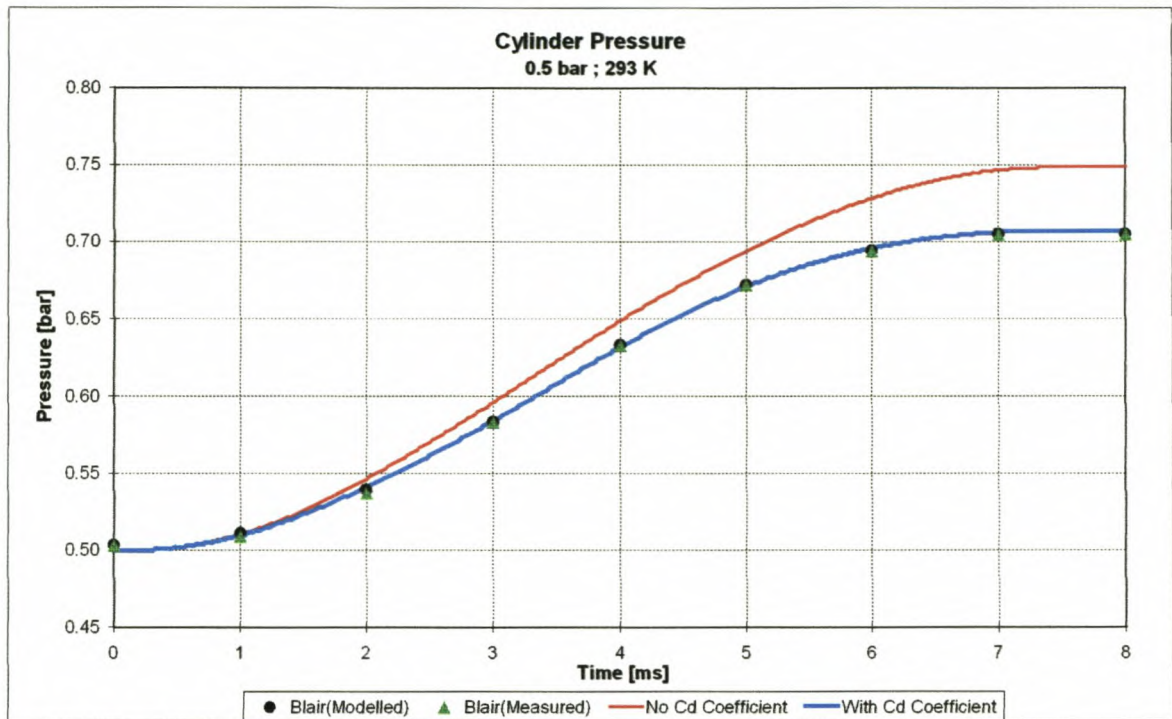


Figure D-1: Pressure data in the cylinder

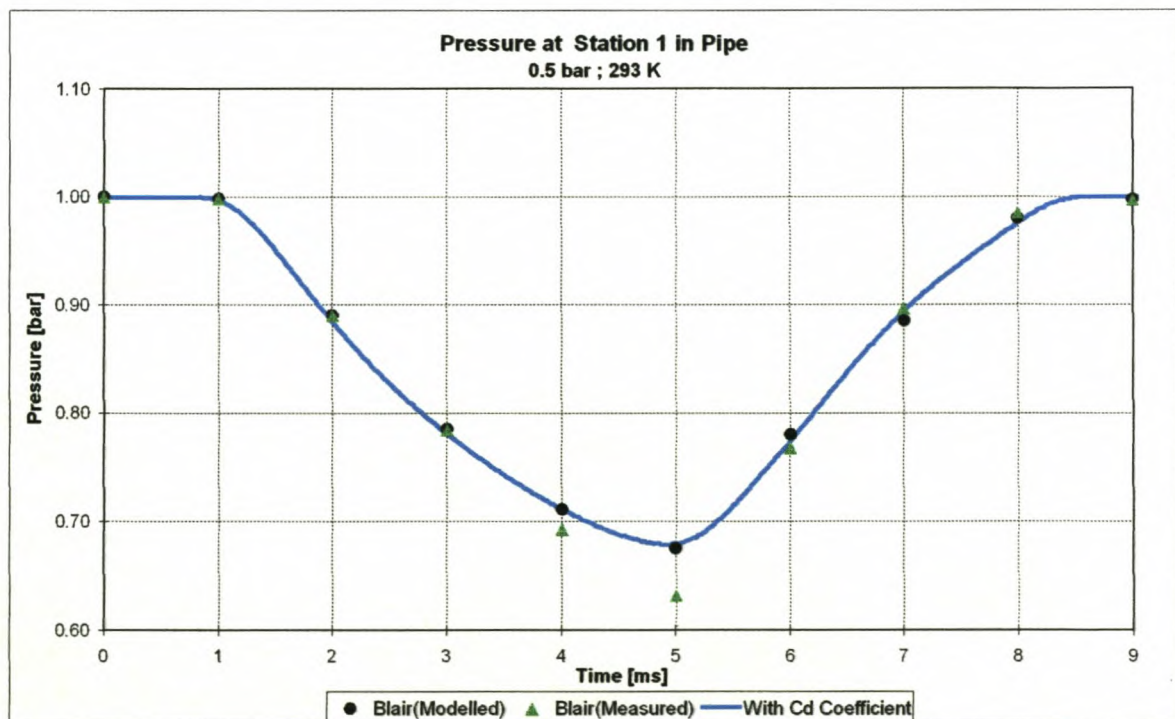


Figure D-2: Pressure data at point 1 in the pipe

Appendix D

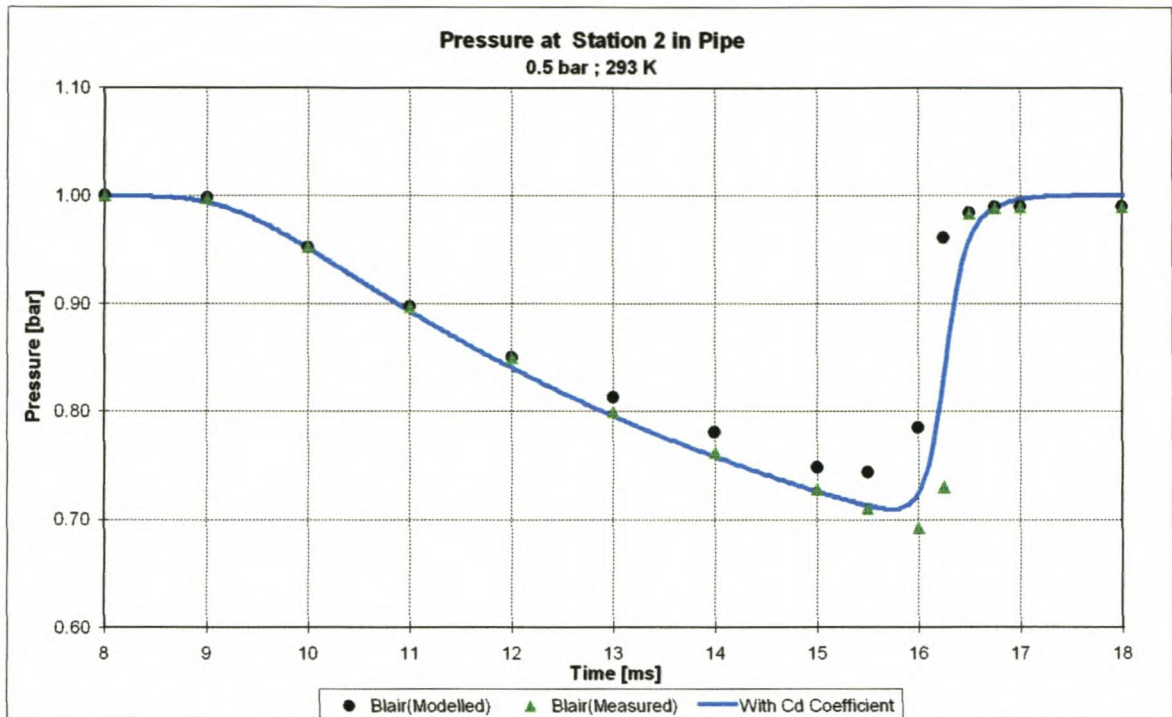


Figure D-3: Pressure data at point 2 in the pipe

Test 2 [0.8 bar; 293 K]

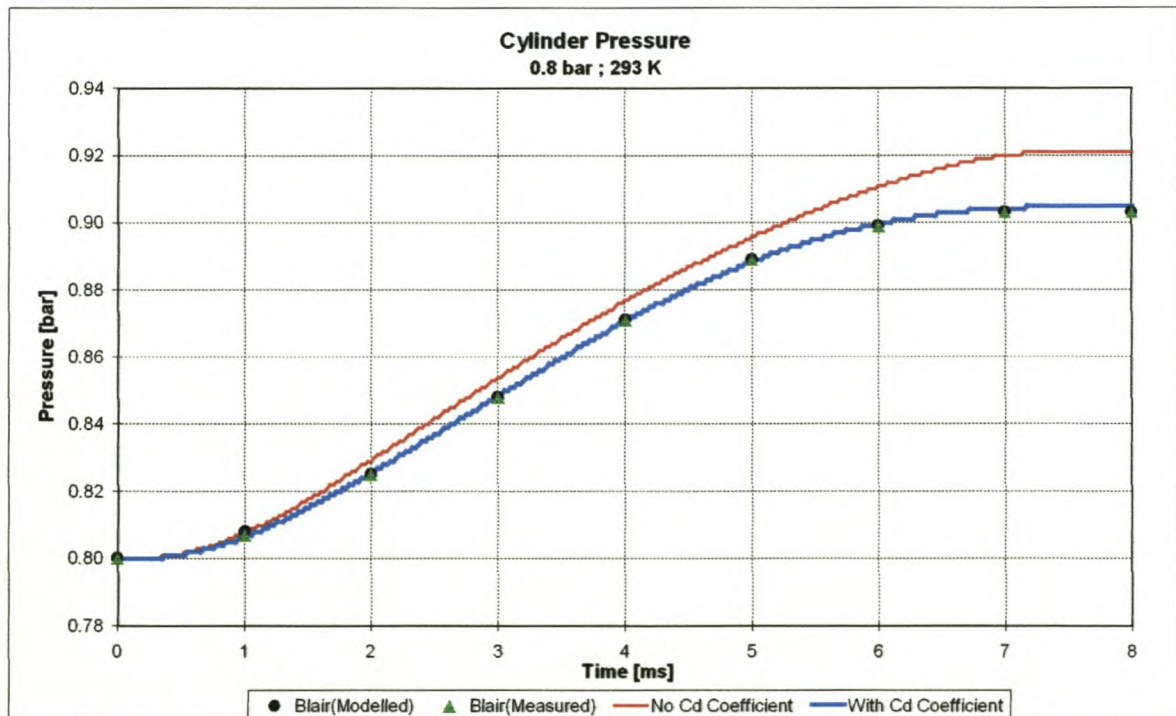


Figure D-4: Pressure data in the cylinder

Appendix D

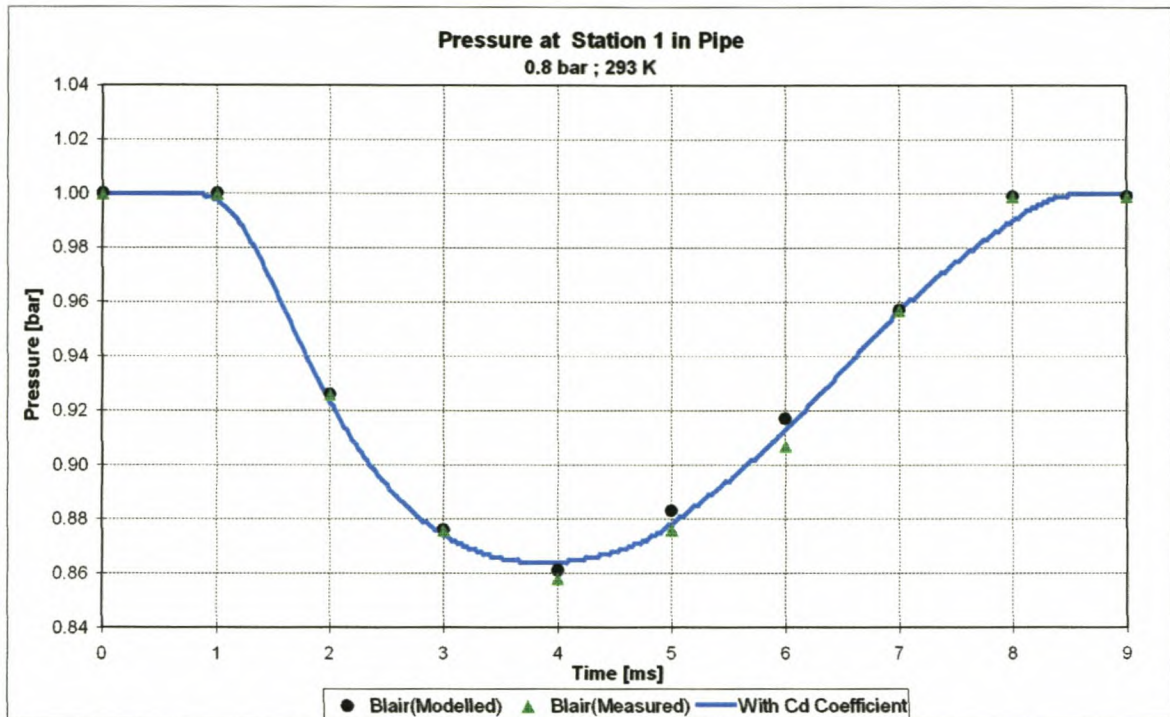


Figure D-5: Pressure data at point 1 in the pipe

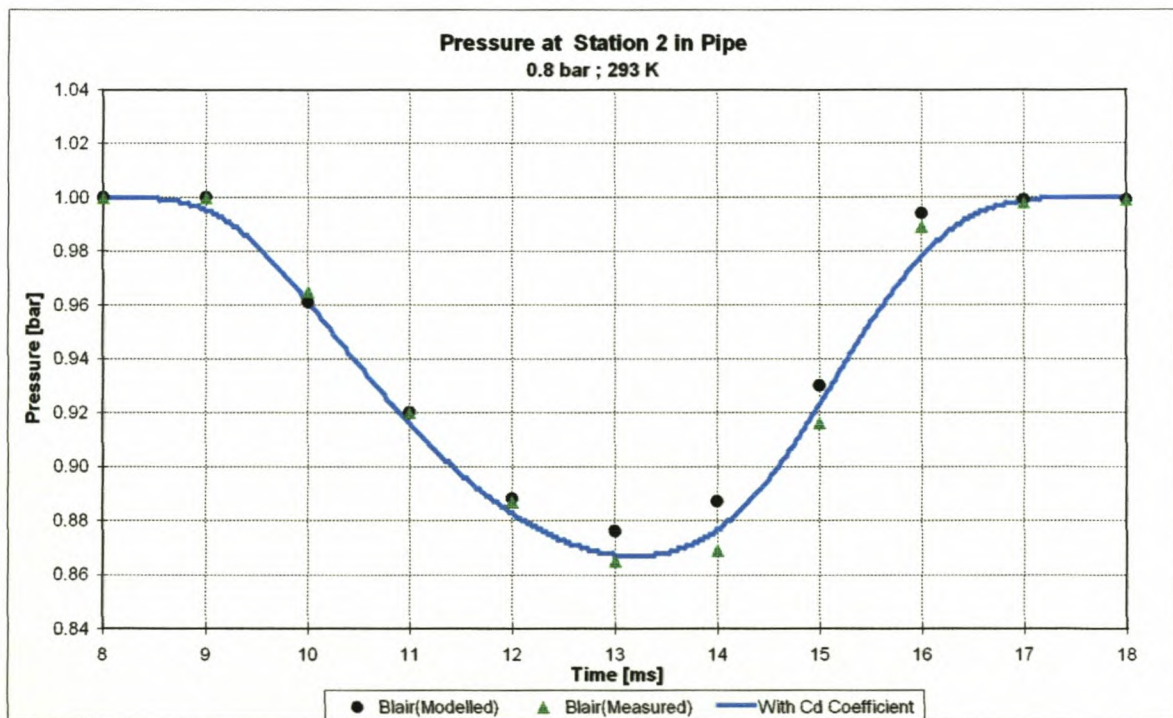


Figure D-6: Pressure data at point 2 in the pipe

Appendix E

Case Study 2:

Simulation of an exhaust process

Appendix E

Test 1 [1.5 bar; 293 K]

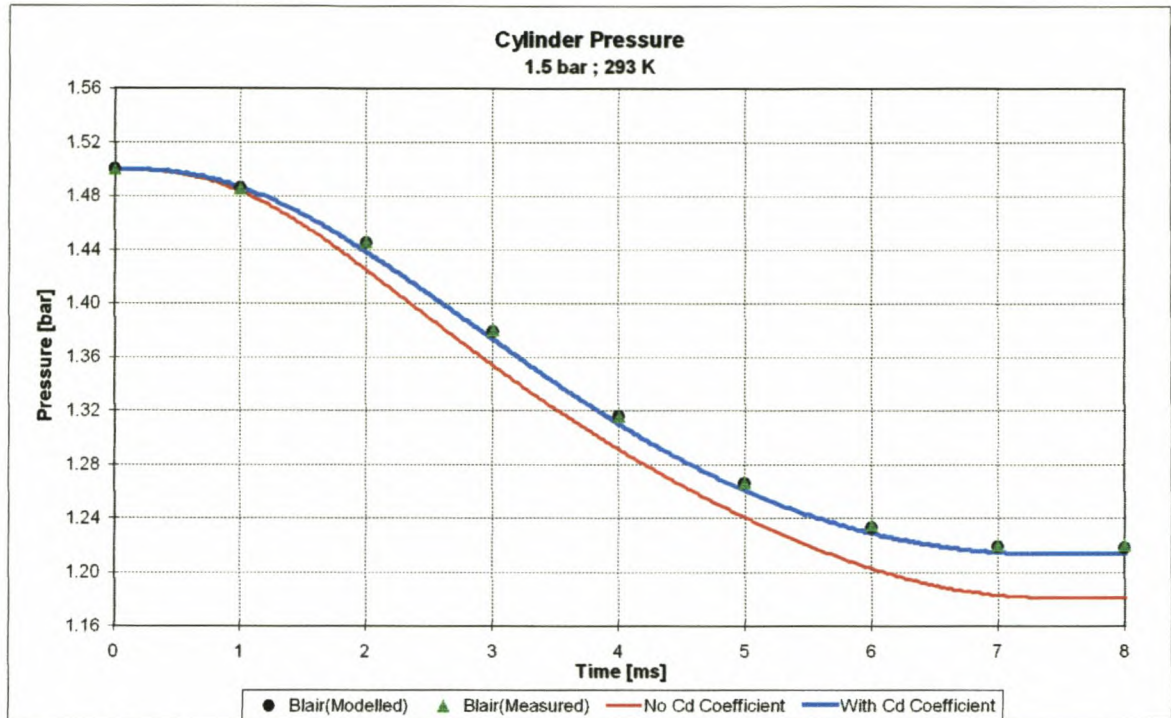


Figure E-1: Pressure data in the cylinder

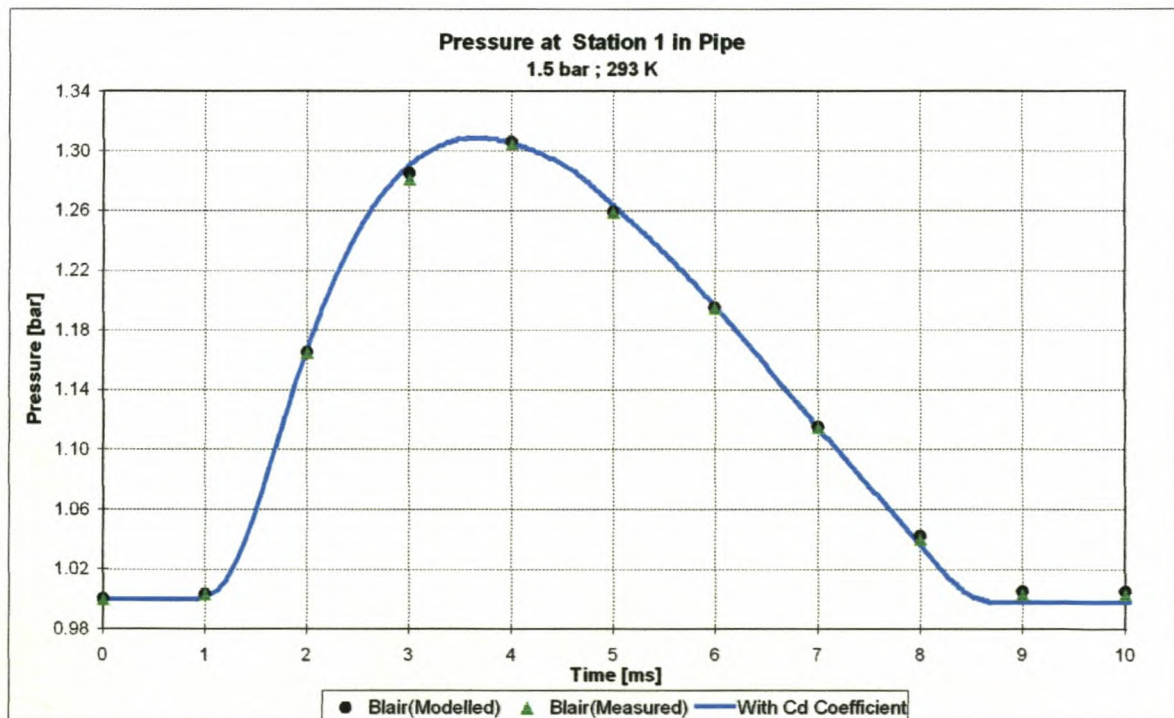


Figure E-2: Pressure data at point 1 in the pipe

Appendix E

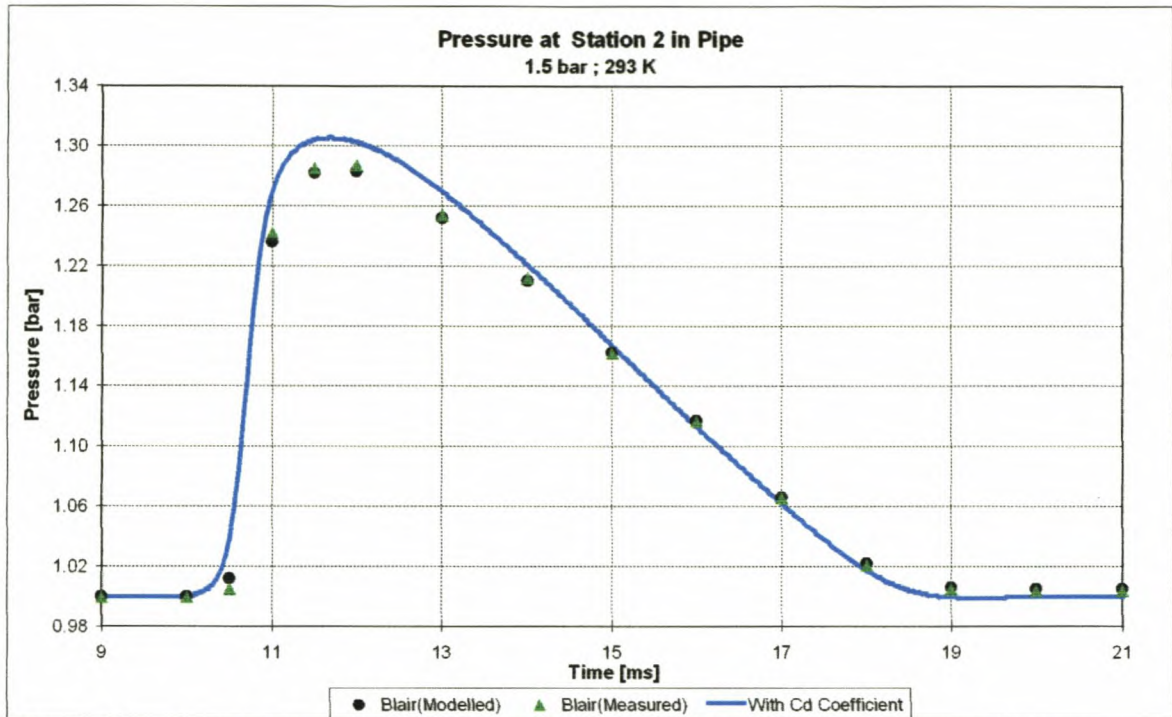


Figure E-3: Pressure data at point 2 in the pipe

Test 2 [2.4 bar; 293 K]

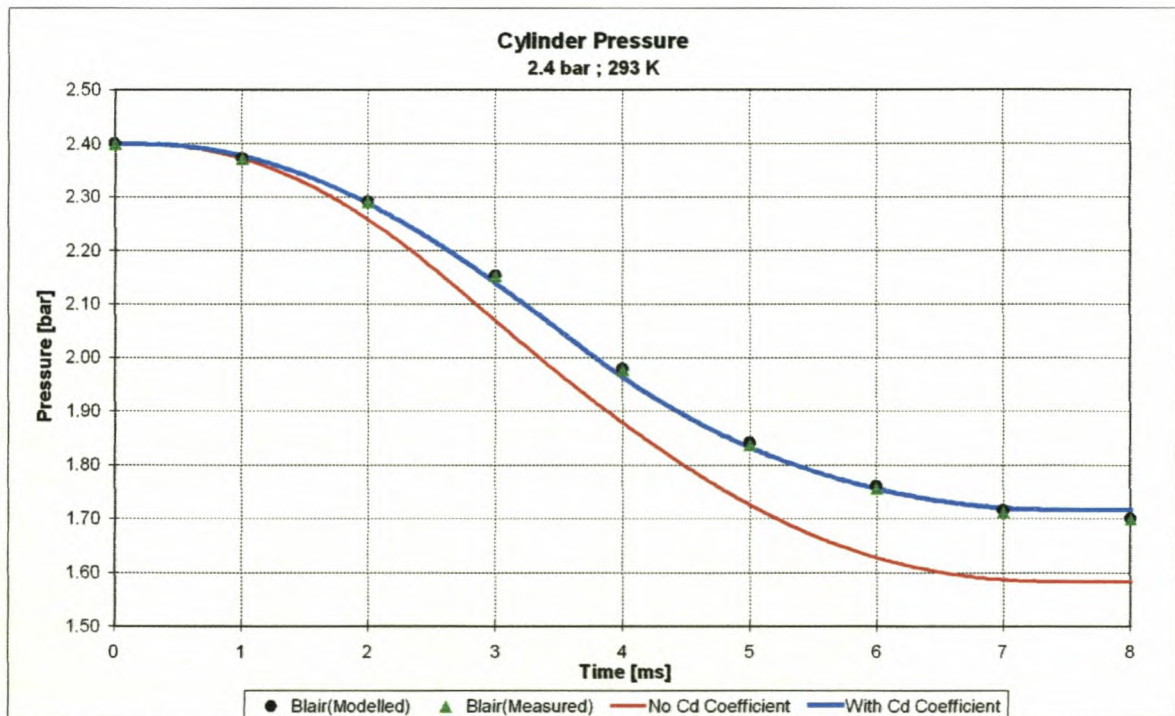


Figure E-4: Pressure data in the cylinder

Appendix E

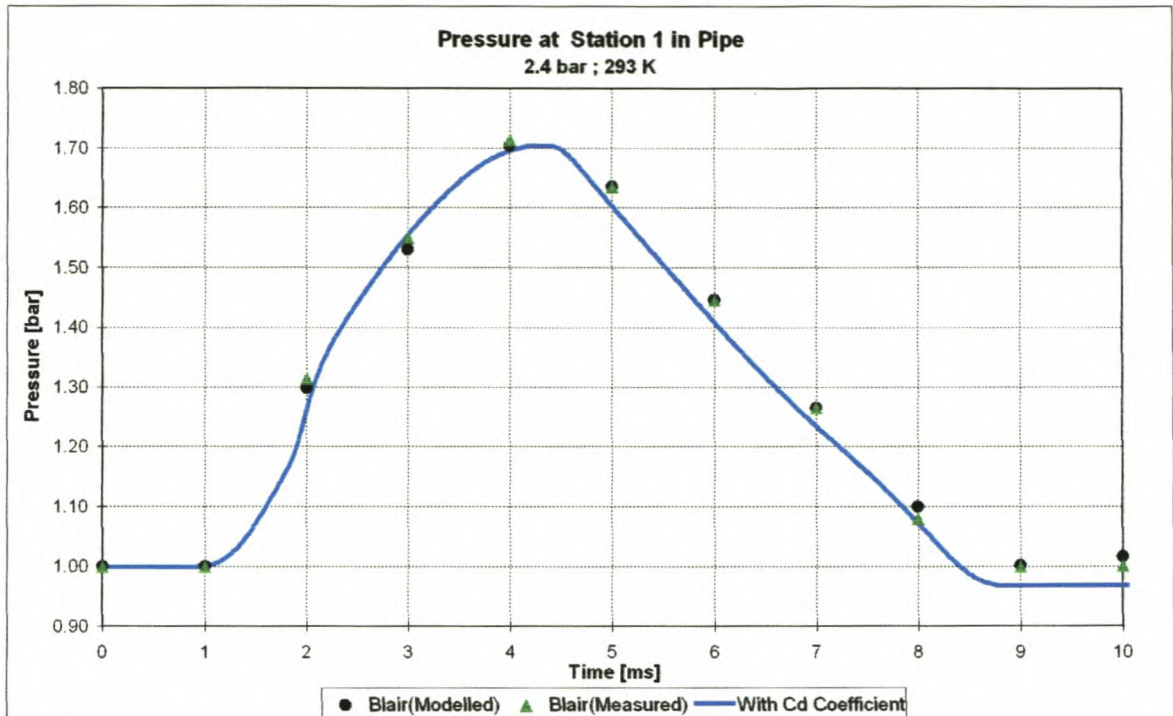


Figure E-5: Pressure data at point 1 in the pipe

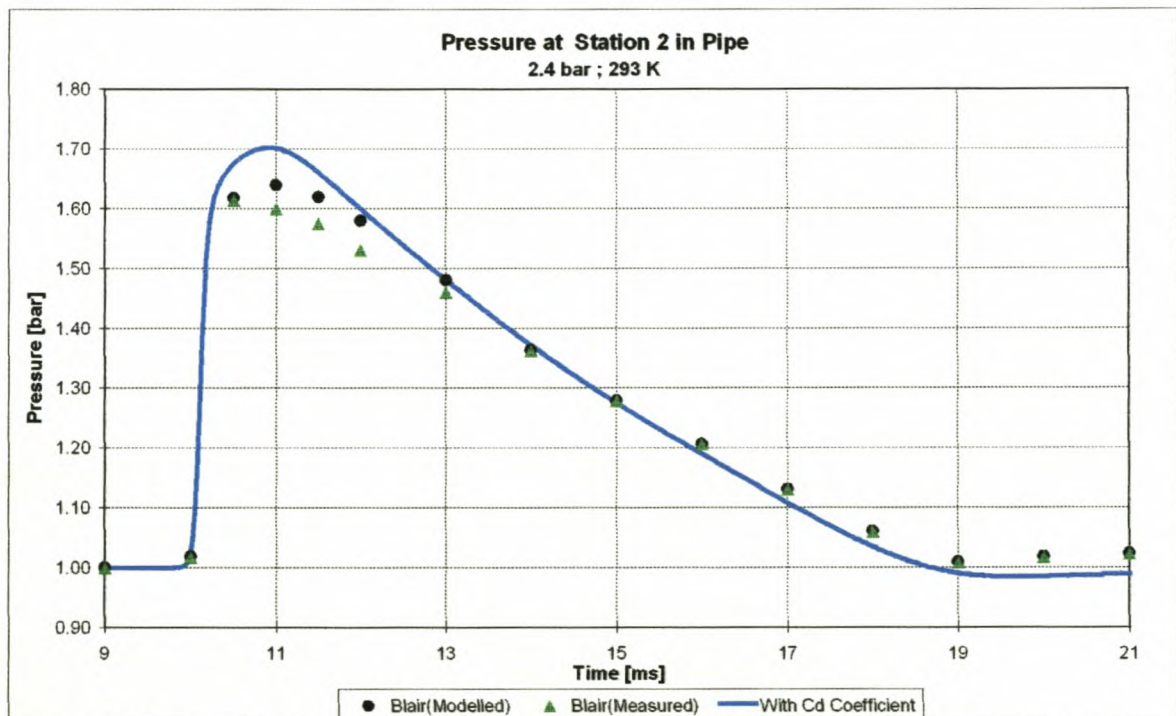


Figure E-6: Pressure data at point 2 in the pipe

Appendix E

Test 3 [2.0 bar; 473 K]

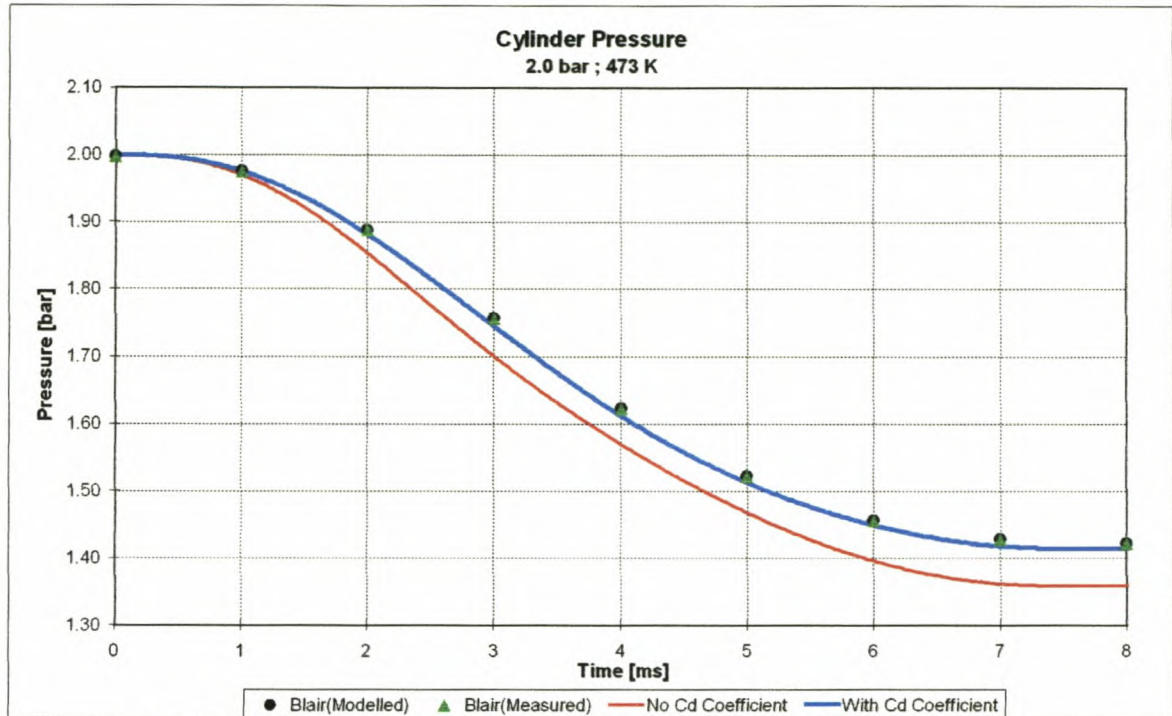


Figure E-7: Pressure data in the cylinder

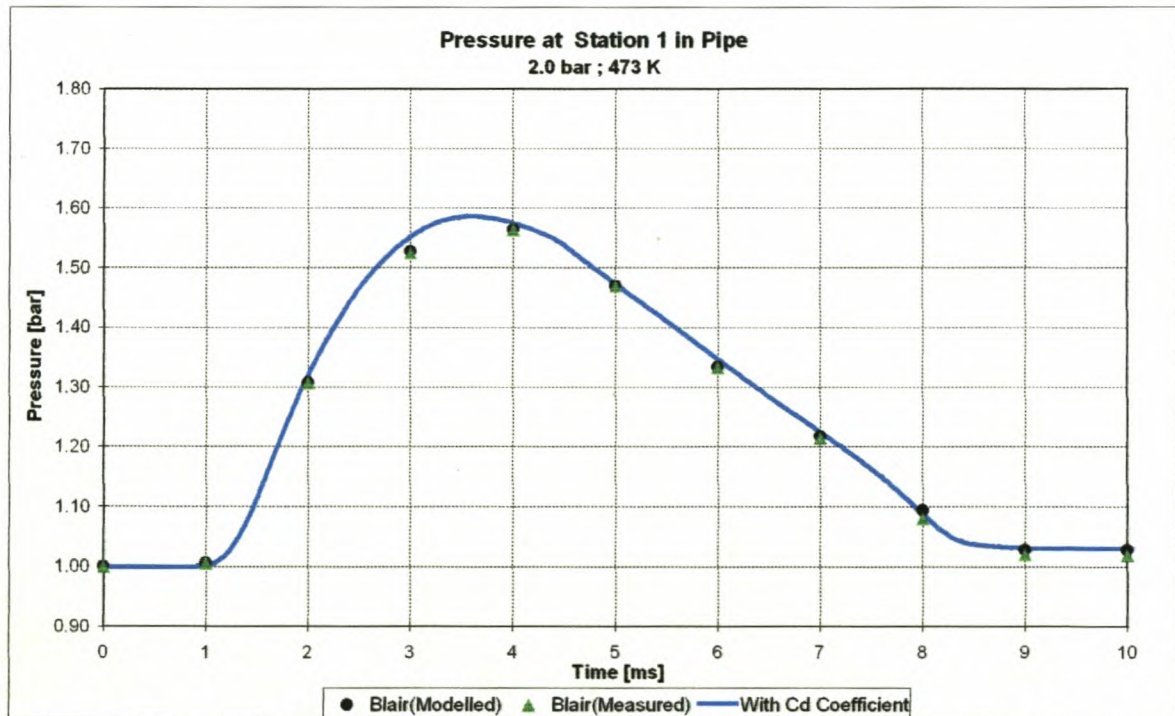


Figure E-8: Pressure data at point 1 in the pipe

Appendix F

User manual for Engine Simulation and Analysis (ESA) software

F-1. Introduction

ESA is an internal combustion engine simulation package written by post-graduate students of the University of Stellenbosch as part of their studies. The simulation package consists of a two-zone thermodynamic combustion model linked to a computation fluid dynamics (CFD) manifold and pipe flow model and integrated with a camshaft analysis model. The combination of these three models allows accurate simulation of all the effects of variation of cam profiles, manifold and exhaust pipe dimensions as well as geometric, fuel and other properties of the engine and its environment. The program was written in Borland Delphi 4 and compiled to a user friendly, full 32 bit Windows 95/98 and NT application.

F-2. Disclaimer

The authors, the CAE and the University of Stellenbosch, make no warranty of any kind, expressed or implied, including without limitation any warranties of merchantability and/or fitness for a particular purpose. The authors do not assume any liability for the use of ESA, as will be displayed on initialising the program.

In no event will the authors be liable for any additional damages. This include any lost profits, lost savings, or other incidental or consequential damages arising from the use of, or inability to use, this software and its accompanying documentation, even if the authors have been advised of the possibility of such damages.

Please note that the software is still in the developmental phase. The software has been extensively tested for bugs and other irregularities, but please feel free to report any further errors or suggestions to the author of this thesis or the CAE at email address cae@ing.sun.ac.za.

For quick assistance, please feel free to contact the CAE at (+27 21) 808 2497.

F-3. Installation and Setup

The computer installation code is supplied on a CD-ROM disc. The program can be installed on the computer of the user by the standard Windows method of

Appendix F

running SETUP.EXE on the CD. This is accomplished either by selecting **Start, Settings, Control Panel, Add/Remove Programs** and then clicking **Install** or by selecting **Start, Run** typing X:\ESA\SETUP.EXE in the open box and then clicking **Ok** (X is the letter of the appropriate disk drive, normally D for the CD-ROM drive). Once the Install Wizard is running, the user should follow the instructions as given, remembering to type the user details and serial number supplied with the program in the required dialog. ESA installs by default into the C:\ESA directory, but this can be changed by the user if so desired.

The Install Wizard installs the following files into the selected folder of the user. A description of the exact nature of the user adjustable files is given later in this document.

- *ESA.exe* - the executable file to run the program
- *Default.eng* - a default engine setup file
- *Default.cwt* - a default head, piston and liner temperature vs. speed file
- *Default.spk* - a default ignition timing vs. speed file
- *Default_Inl.maf* - a default inlet manifold and pipe geometric profile file
- *Default_Exh.maf* - a default exhaust manifold and pipe geometric profile file
- *Default.exh* - a default exhaust gas temperature and pressure vs. speed file
- *Default_Inl.cam* - a default inlet valve lift profile file
- *Default_Exh.cam* - a default exhaust valve lift profile file
- *Default_IV.vcd* - a default inlet valve C_d map (forward flow) file
- *Default_IVRev.vcd* - a default inlet valve C_d map (reverse flow) file
- *Default_EV.vcd* - a default exhaust valve C_d map (forward flow) file
- *Default_EVRev.vcd* - a default exhaust valve C_d map (reverse flow) file
- *Errorlog.err* - a file used to log errors that may occur in the simulation
- *ESA.ini* - a program setup file installed into the C:\Windows directory.

Once the installation has been completed, the user can run the program by clicking on the ESA icon under the **Start Menu / Programs** folder. No further user setup is required at this time. The program runs best in a screen resolution of 800x600 or 1024x768 with at least 256 colours.

F-4. Program and Menu Overview

A short description of the menu items and functions as well as basic operation of the program is given in this section.

On program start-up, the displayed user interface consists of a menu bar, a status bar and four display areas (Figure F-1).

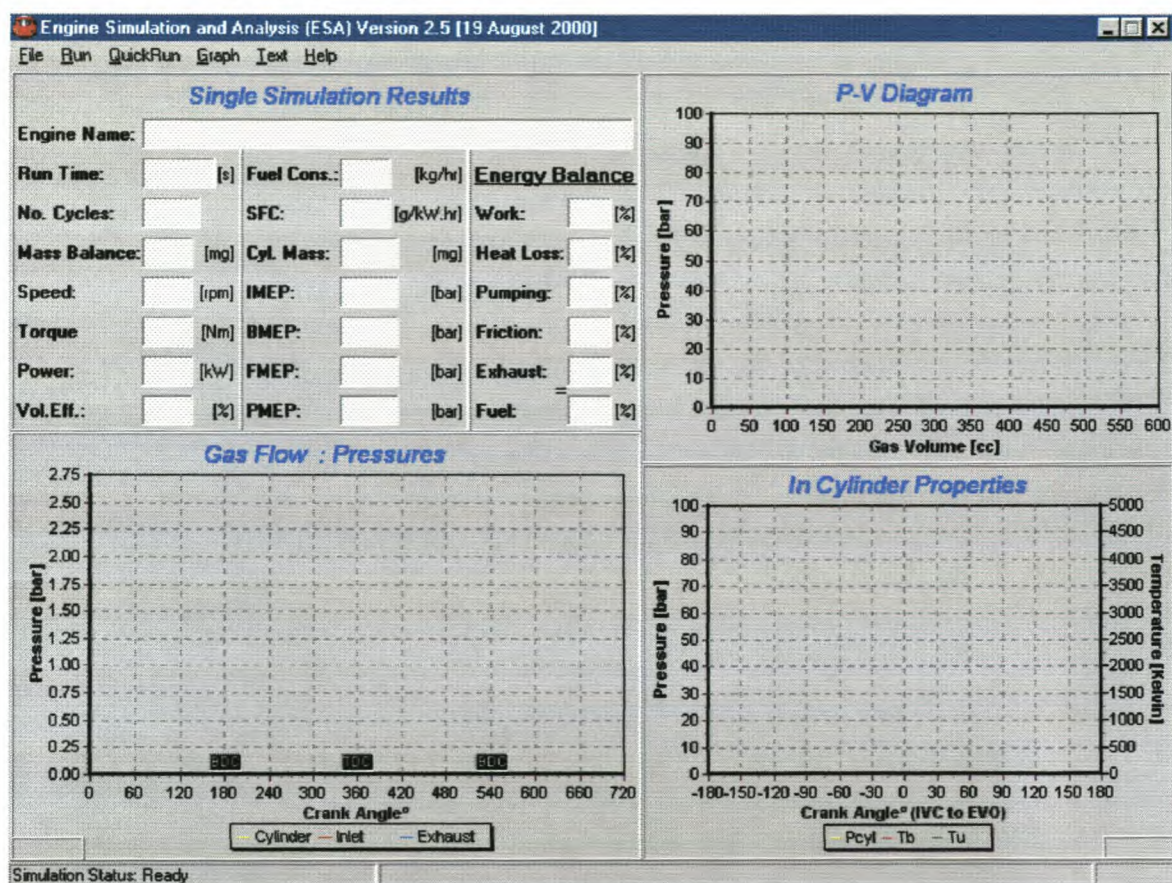


Figure F-1: User interface during program start-up

In the top left corner is a multiple text box area where the program reports the results of a single simulation run. Some of the reporting is online while the program is running. Other information is only displayed, as it becomes available at the completion of the simulation.

In the top right corner is a graph that displays an online indicator PV-diagram, cylinder pressure vs. volume for one cylinder. This graph scales automatically unless the user performs a manual scaling as described later in this manual.

In the bottom right corner is a graph providing a trace of in-cylinder properties vs. crank angle. The properties displayed are cylinder pressure (P_{cyl}), mixture burned temperature (T_b) and mixture unburned temperature (T_u).

Appendix F

In the bottom left corner is a graph that can display the following:

- Cylinder conditions: pressure, total trapped mass, unburned mass and burned mass vs. crank angle
- Inlet valve conditions: pressure, velocity and mass transfer vs. crank angle
- Exhaust valve conditions: pressure, velocity and mass transfer vs. crank angle.

The status bar display information regarding the files loaded or saved by the user as well as the simulation status including crank angle and simulation time elapsed.

The initial available menu items are the following (Figure F-1):

File | Run | QuickRun | Graph | Text | Help.

Under the **File** menu, the user elects to **Load**, **Save** and **Edit** the geometrical and operational details of a desired simulation as well as **Exit** the program.

The **Run** menu is used to initialise or **Pause** and **Stop** the various simulation modes. Selecting the **Single Point Simulation** option initialises the simplest simulation mode. To run multiple point simulation runs, choose **Multi Point Simulation**. These options are executed after an engine file has been loaded.

The **QuickRun** menu is used to initialise the **Single Point Simulation** option by loading the default engine data file and configuration.

The **Graph** menu is used to alter the various parameters that are displayed on the graphs during and after completion of the simulation. Some of the options are only available after an engine file has been loaded. The options are changing **Run-Time Graph Options**, viewing a **Torque Curve**, **Valve Opening** and the **Energy Balance** during the last engine cycle.

The **Text** menu is used to view and save (default to *Lastcyc.text*) the results of a completed simulation. The text format is suitable for use in a spreadsheet e.g. Excel. This provides accurate data for all simulated parameters at each crank angle degree.

The **Help** menu provides access to this **User Manual** that serves as a help document and the **About** box, giving some detail on the software and its creators.

F-5. Creating an Engine Data File

This section describes the basic use of the program and creating an engine data file. For the purposes of this tutorial, the user will load the default engine file; modify a few operating parameters and then run a simple simulation.

On initialising the program, the user interface becomes visible (Figure F-1). To load the engine data files, the user clicks **File, Load**. The *Open Engine Data File* dialog box is displayed (Figure F-2). The user can select the desired *.eng files using the standard windows dialog box. Select the file and then click **Open**.

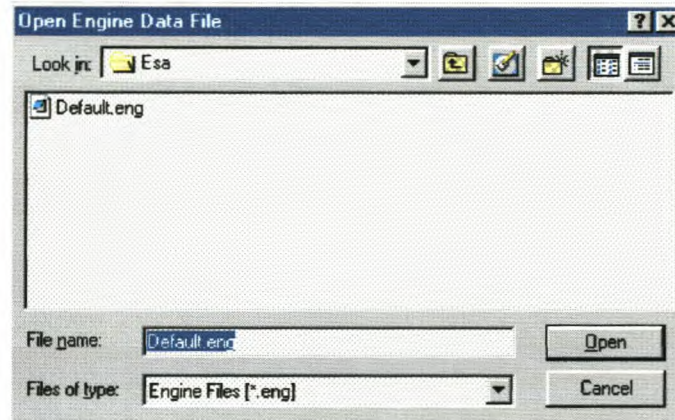


Figure F-2: Load engine data file

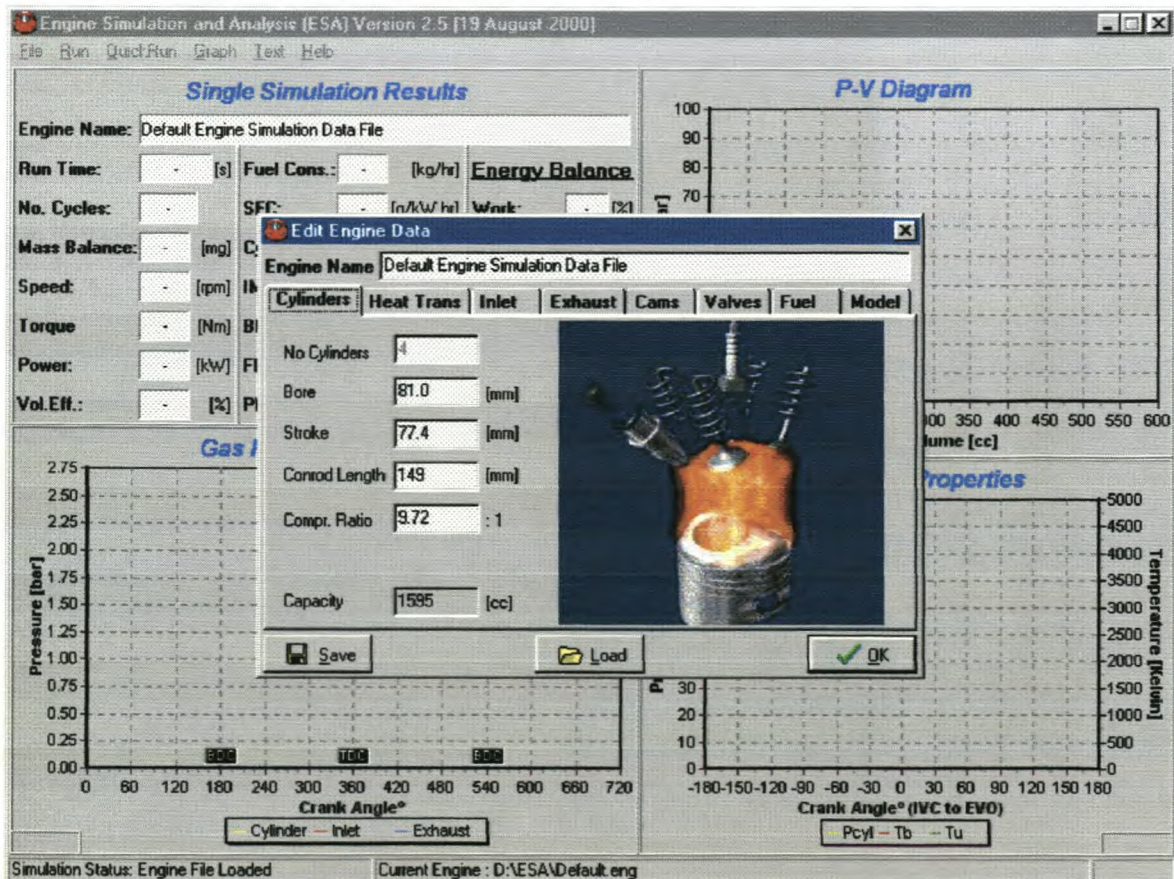


Figure F-3: Edit engine data file

Appendix F

The loaded filename is displayed in the lower status bar. To load the default engine file automatically, the user clicks **File, Load Default**.

To modify the engine model input data, click **File, Edit**. The *Edit Engine Data* dialog box will be displayed (Figure F-3).

To modify any parameter, change the text or value in the edit boxes (Figure F-4). **Cylinders** is the first edit tab to be displayed (Figure F-4). The following geometric information on the engine can be changed here:

- Number of cylinders
- Bore, stroke and conrod length
- Compression ratio

The capacity of the engine is then calculated and displayed as in Figure F-4.



Figure F-4: Cylinder data

Heat Trans (heat transfer) is the next edit tab (Figure F-5). Here information on the heat transfer of the engine, burn angle and ignition timing of the engine can be changed. The surface temperatures of the head, piston, upper and lower liners are given as an input file to the program via a text file, *.cwt (Figure F-6). Different input files are selected by clicking the *Browse* button. In this file surface temperatures at different engine speeds are given. The format of the text file is the same for all the other input files to the program. The value in the first text line sets the number of data lines in the text file. The second line has headings for all the data sets. The remaining lines, as specified by the value in the first text line, have all the necessary input data for the program.

Appendix F

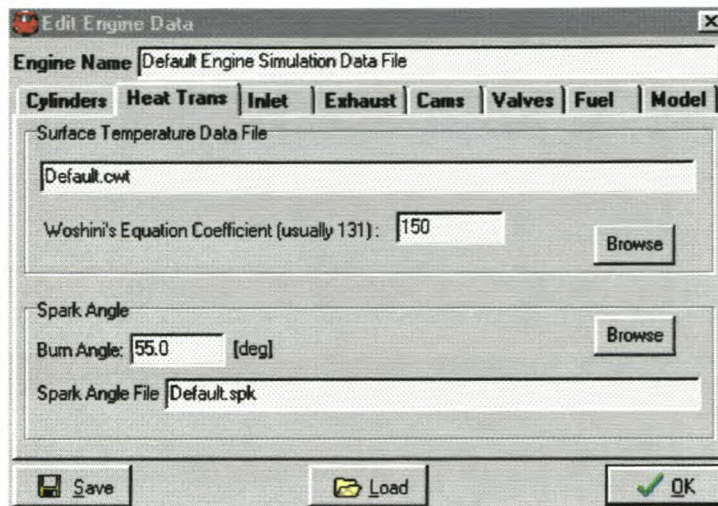


Figure F-5: Heat transfer and ignition timing data

	SPEED	THEAD	TPISTON	TULINER	TLLINER
7	1000	350	440	495	350
	2000	365	450	405	365
	3000	380	470	425	380
	4000	400	490	445	400
	5000	415	510	460	415
	6000	435	530	480	435
	7000	460	550	505	460

Figure F-6: Temperature data for the head, piston and liners

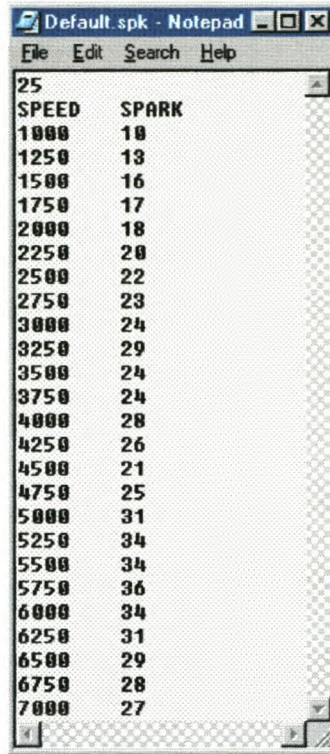
The *Woshini's Equation Coefficient* [2] exists to fine-tune the heat transfer in the model. The model is not accurate enough to calculate the heat transfer exactly as in the physical engine. Because of limited information, the model needs to be fine-tuned to get the heat transfer equalling the right percentage loss of the total available energy of the engine. This percentage value can be obtained by doing physical engine tests or by assuming a value of $30 \pm 5\%$ [2].

The *Burn Angle* of the fuel also depends very much on the combustion chamber design of the engine. By doing a full combustion analysis on the engine, the burn angle can be obtained at each engine speed. If this information is not available, a good estimate is a value between 40° - 60° crank angle [2].

The information needed for the *Spark Angle File* (Figure F-7) is usually only obtained after doing physical engine tests. If this is not possible, experience and other similar data from other engines are used to create such a file. The most beneficial timing (MBT) can also be estimated by doing variable ignition timings with the model at the same speed and with the same burn angle. The ignition

Appendix F

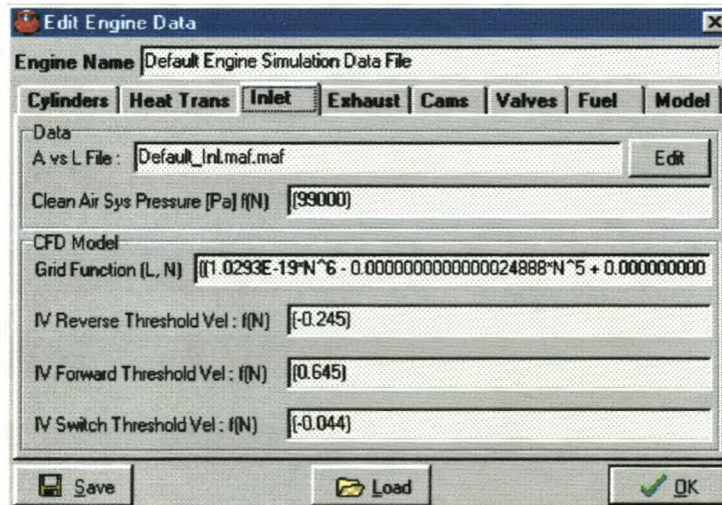
timing that gives the maximum torque will then be used, until further engine data is available.



SPEED	SPARK
25	
1000	10
1250	13
1500	16
1750	17
2000	18
2250	20
2500	22
2750	23
3000	24
3250	29
3500	24
3750	24
4000	28
4250	26
4500	21
4750	25
5000	31
5250	34
5500	34
5750	36
6000	34
6250	31
6500	29
6750	28
7000	27

Figure F-7: Ignition timing information

Inlet is the next edit tab (Figure F-8). In the edit boxes of this tab, all the information on the inlet manifold is displayed. The first information needed is the geometrical detail on the inlet manifold. For this information the program uses an input file that is created by clicking on the *Edit* button. A new window is displayed that has length and area as input (Figure F-9). This data is also displayed as a graph and saved as a text file, *.maf.



Engine Name: Default Engine Simulation Data File

Cylinders: Heat Trans: **Inlet**: Exhaust: Cams: Valves: Fuel: Model:

Data

A vs L File: Default_Inl.maf [Edit]

Clean Air Sys Pressure [Pa] f(N): 99000

CFD Model

Grid Function (L, N): $f(1.0293E-19 \cdot N^6 - 0.00000000000000024888 \cdot N^5 + 0.00000000000000000000 \cdot N^4 - 0.00000000000000000000 \cdot N^3 + 0.00000000000000000000 \cdot N^2 - 0.00000000000000000000 \cdot N + 0.00000000000000000000)$

IV Reverse Threshold Vel : f(N): -0.245

IV Forward Threshold Vel : f(N): 0.645

IV Switch Threshold Vel : f(N): -0.044

Save Load OK

Figure F-8: Inlet manifold data

Appendix F

The length of the manifold is taken from the entrance of the plenum (zero point) up to where the inlet valve ports end. The area along this length is then given in small length steps.

Sometimes it is necessary to simplify the area variation in the inlet port. Big area changes can be found in this region, which can lead to simulation instabilities. The simulation program is using a grid to solve the flow in the inlet. If the area change is very big, the grid might not be small enough to take it into account. The grid also changes with engine speed, meaning that sometimes this area change is taken into account and other times not. It is therefore better to keep area variation smooth, as illustrated in Figure F-9.

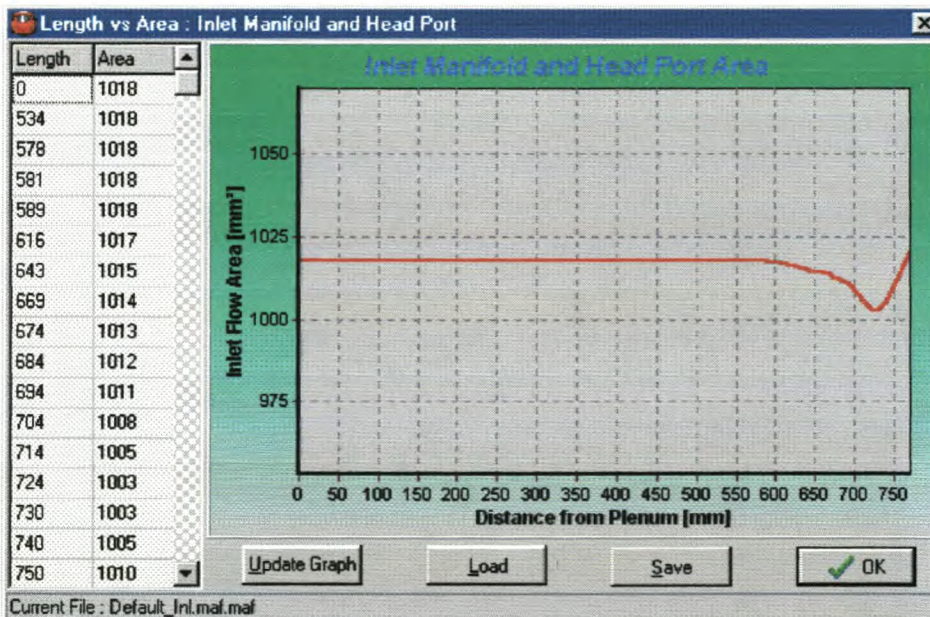


Figure F-9: Inlet manifold area vs. length

The next information needed is the *Clean Air Sys Pressure*. This pressure is part of the boundary condition at the open end to the manifold plenum. In a well-designed inlet manifold this pressure is almost constant, but it will drop slightly as the engine speed increases. This data is usually obtained from engine tests. The pressure is given to the program as an equation, which is a function of engine speed for e.g. $(E-10*N^3 - 1E-06*N^2 - 0.0009*N + 1014.4)$.

The information needed to ensure mathematical stability and smooth transition between forward and reverse flow is displayed in the last four edit boxes, as displayed in Figure F-8. The first edit box, *Grid Function*, is the inlet grid size equation, which is a function of engine speed and inlet length. For each engine

Appendix F

model this needs to be fine-tuned by first calculating the grid size using the CFL stability criterion. The grid size is then tested and corrected by running simulations with a grid size just above and below the CFL calculated grid to correct for velocity changes.

Getting smooth transition between forward and reverse flow at the inlet valves can be very difficult. The pressures at the inlet valve and in the combustion chamber can sometimes be very close together; for example just before the inlet valve closes (described in Chapter 2). To help in the smoother transition between forward and reverse flow, a minimum velocity (trial-and-error based) at the valve is given before the flow will change from forward to reverse, or reverse to forward flow.

Edit Engine Data

Engine Name: Default Engine Simulation Data File

Cylinders | **Heat Trans** | **Inlet** | **Exhaust** | **Cams** | **Valves** | **Fuel** | **Model**

Data

A vs L File: Default_Exh.maf.maf

Exh Back Pres and Temp File: Default.exh

CFD Model

Grid Function [L,N]: $[[1.0533E-16 \cdot N^5 - 0.0000000000020345 \cdot N^4 + 0.000000014859$

EV Reverse Threshold Vel: f(N) [-0.6]

EV Forward Threshold Vel: f(N) [0.41]

EV Switch Threshold Vel: f(N) [-0.715]

Figure F-10: Exhaust manifold data

Exhaust is the next edit tab (Figure F-10). In the edit boxes of this tab, all the information on the exhaust manifold and pipe is displayed. The first information needed is the geometrical detail on the exhaust manifold and pipe. For this information the program uses an input file that is created by clicking on the *Edit* button. A new window is displayed that has length and area as input (similar to inlet Figure F-9). This data is also displayed as a graph and saved as a text file, *.maf (Figure F-11).

The length of the manifold and pipe is taken from the entrance of the exhaust valve ports (zero point) up to the first sudden expansion, usually a silencer box or catalyst.

Appendix F

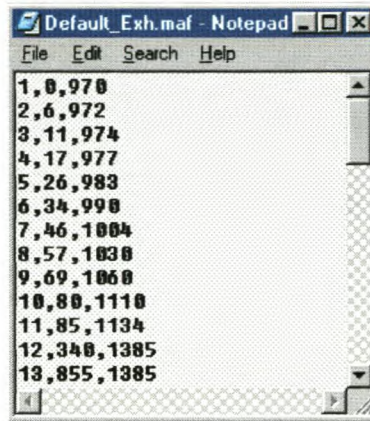


Figure F-11: Exhaust manifold area vs. length

The next information the program will need is the exhaust back pressure and temperature boundary data. This information is given to the program as an input file, *.exh (Figure F-12). The pressure and temperature data is given at each engine speed. This information can be obtained from engine tests or just using experience and other similar engine data. The back pressure of the exhaust system has a big influence on the gas flow through the engine and should therefore be obtained as early as possible in the design process of an engine or its manifolds.

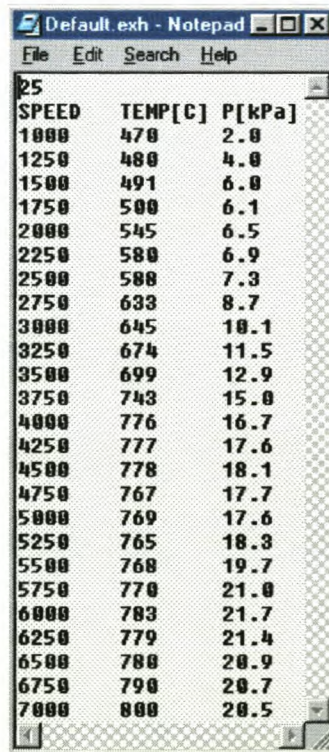


Figure F-12: Exhaust gas temperature and pressure

The grid size information and velocities at the exhaust valve that will ensure smooth transition between forward and reverse flow, will not be discussed again

Appendix F

for the exhaust. The same principles as discussed for the inlet valve, apply at the exhaust valve. It is a bit easier though, because of the larger pressure differences at the exhaust valve between the exhaust and the cylinder.

All the camshaft information can be entered in the **Cams** edit tab (Figure F-13). The inlet and exhaust valve lift profiles are given to the program as an input file, *.cam. The camshaft model creates the data in this file. The model creates unit duration of zero to one and unit lift of zero to one. This makes it possible to fit the camshaft profile to any opening and closing angle or valve lift value.

The screenshot shows the 'Edit Engine Data' dialog box with the 'Cams' tab selected. The 'Engine Name' is 'Default Engine Simulation Data File'. The tabs are 'Cylinders', 'Heat Trans', 'Inlet', 'Exhaust', 'Cams', 'Valves', 'Fuel', and 'Model'. The 'Inlet Valve Cam' section has a 'Profile' of 'Default_Inl.cam' and a 'Browse' button. Below it are input fields: 'IVD [°BTDC]' with value 19, 'IVC [°ABDC]' with value 80, 'Total Valve Lift (mm)' with value 8.62, and 'Duration [°CA]' with value 279. The 'Exhaust Valve Cam' section has a 'Profile' of 'Default_Exh.cam' and a 'Browse' button. Below it are input fields: 'EVD [°BBDC]' with value 64, 'EVC [°ATDC]' with value 37, 'Total Valve Lift (mm)' with value 10.4, and 'Duration [°CA]' with value 281. At the bottom are 'Save', 'Load', and 'OK' buttons.

Figure F-13: Camshaft information

The inlet and exhaust valve lift, opening and closing angles are all entered in this edit tab. The duration of each camshaft is then calculated from its opening and closing angles.

The screenshot shows the 'Edit Engine Data' dialog box with the 'Valves' tab selected. The 'Engine Name' is 'Default Engine Simulation Data File'. The tabs are 'Cylinders', 'Heat Trans', 'Inlet', 'Exhaust', 'Cams', 'Valves', 'Fuel', and 'Model'. The 'Inlet' section has input fields: 'No Valves' with value 3, 'Diam (mm)' with value 27, 'Forward Flow Cd' with value 'Default_IV.vcd', and 'Reverse Flow Cd' with value 'Default_IVRev.vcd'. Each of the last two has an 'Edit' button. The 'Exhaust' section has input fields: 'No Valves' with value 2, 'Diam (mm)' with value 30, 'Forward Flow Cd' with value 'Default_EV.vcd', and 'Reverse Flow Cd' with value 'Default_EVRev.vcd'. Each of the last two has an 'Edit' button. At the bottom are 'Save', 'Load', and 'OK' buttons.

Figure F-14: Inlet and exhaust valve data

Appendix F

Information on the valves of the engine is displayed in the **Valves** tab. In these edit boxes the following needs to be entered (Figure F-14):

- Number of inlet and exhaust valves for one cylinder
- Diameter of a single inlet and exhaust valve
- Input files containing the discharge coefficient (C_d) map data for each valve and for each flow direction, forward or reverse.

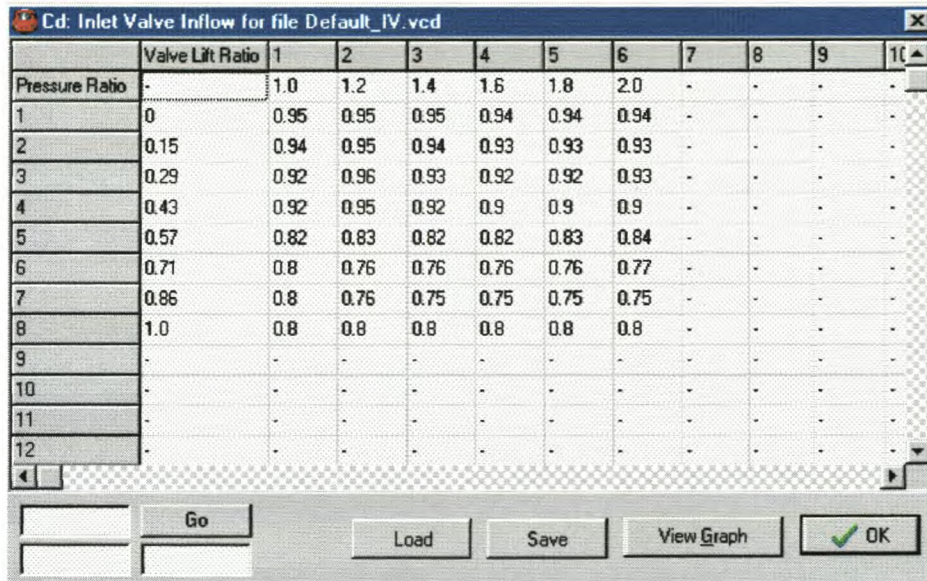


Figure F-15: Discharge coefficient map

Clicking *Edit* displays Figure F-15, the C_d map data. The information is stored in a text file, *.vcd. The discharge coefficient is a function of the pressure ratio over the valve (row 1 in Figure F-15) and the lift ratio (column 1 in Figure F-15). These C_d values for valves are measured on a steady state flow bench as explained in Chapter 3 of this thesis. The C_d map can also be viewed as a 3-dimensional graph in Figure F-16 (click *View Graph* button). These 3 dimensional maps are created for inlet and exhaust valves, and for forward and reverse flow.

The second last edit tab, **Fuel**, has data on the atmospheric conditions, oil and properties of the fuel (Figure F-17). The atmospheric temperature and pressure must be entered in the top left corner. These values are important for the initial values in the manifolds. The viscosity of the oil is used to calculate engine friction.

The following fuel properties are needed:

- *Stoichiometric A/F Ratio* is the amount of air units needed to burn one unit of fuel. Stoichiometric A/F Ratio is also known as the *Equivalence Ratio*.

Appendix F

- *Lambda* is an indication of the amount of fuel or air left in the exhaust after combustion. In the model it is assumed that all the fuel and air were used for combustion. In a real engine it is quite common for an engine to run with excess fuel, $\lambda = 0.9$, or it is said that the engine is running rich. An engine can also run lean with $\lambda > 1$ and therefore with excess air.
- *Fuel Energy* is a property of the fuel. Petrol usually has a value of 43 MJ/kg.
- *Fuel Temperature* is usually the same as the atmospheric temperature, but can be different when running a physical engine.

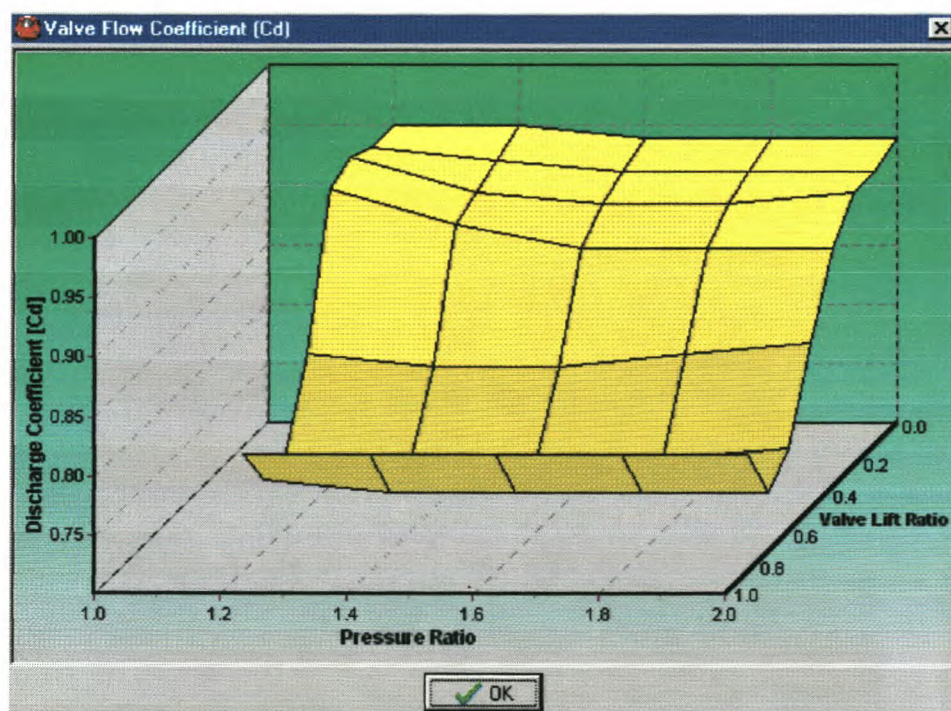


Figure F-16: Inlet valve C_d map graph

A dialog box titled "Edit Engine Data" with a tabbed interface. The "Fuel" tab is selected. The "Engine Name" field contains "Default Engine Simulation Data File". The tabs are: Cylinders, Heat Trans, Inlet, Exhaust, Cams, Valves, Fuel, Model.

Atmospheric Conditions		Fueling	
Temperature	25 [°C]	Stoich A/F Ratio	14.5 [-1]
Pressure	101.325 [kPa]	Lambda	1
		Fuel Energy	43 [MJ/kg]
		Fuel Temp	25.0 [°C]

Oil Viscosity: 100

Fuel Composition: C₇ H₁₇ O₀ N₀

Buttons: Save, Load, OK

Figure F-17: Atmospheric, oil and fuel information

Appendix F

At the moment the fuel composition is not used in the program. It is possible with the 2-zone combustion model though, to predict emissions and for this purpose the composition is necessary.

The last edit tab is called **Model** (Figure F-18). Here the user can make changes to some of the general program options. The program is now only running with the 2-zone combustion model and the 1-zone model is therefore not available anymore. The integration method will default to the *Runga Kutte Felberg* method, because of the accuracy benefit, but it is also possible to run with the faster *Euler* integration method. These integration methods are only applicable to the combustion model. Manifold data can also be saved for each grid point at each crank angle degree. The performance data filename can also be changed.

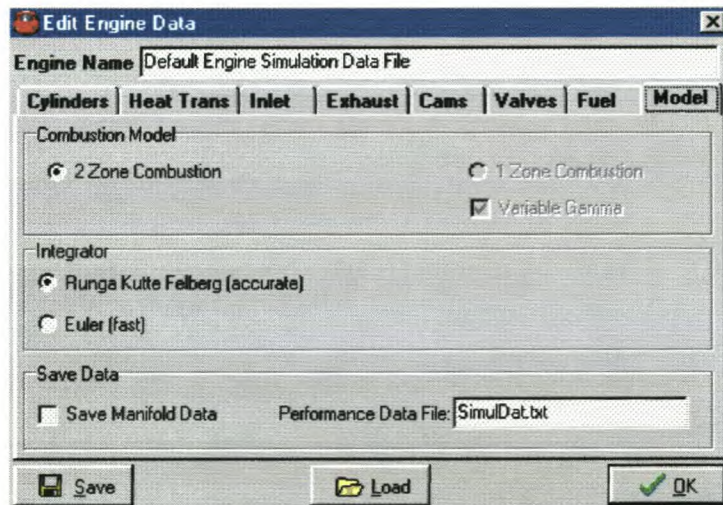


Figure F-18: General modelling information

Clicking the *Save* button saves engine data files. Other engine files are loaded by clicking the *Load* button. Engine information can also be entered at the top of the *Edit Engine Data* box. Click the *OK* button to continue with the simulation.

F-6. Single Point Simulation

In Section F-5 it was described how the user creates the necessary engine data file to run a simulation successfully. In this section it is explained how to run a single speed *Single Point Simulation*.

In the main menu, click **Run** and then **Single Point Simulation**. The user sees a small box appear on the display window (Figure F-19). This small box gives the user the necessary information to run a single speed simulation. Enter the

Appendix F

simulated engine speed as well as the number of iteration cycles (at least 5) and the maximum mass balance value. The program monitors the total iteration cycles and the mass balance values to check when to stop the simulation. Whichever criteria occur first, will stop the simulation. No more than 10 cycles are usually needed to get a reliable answer from the simulation.

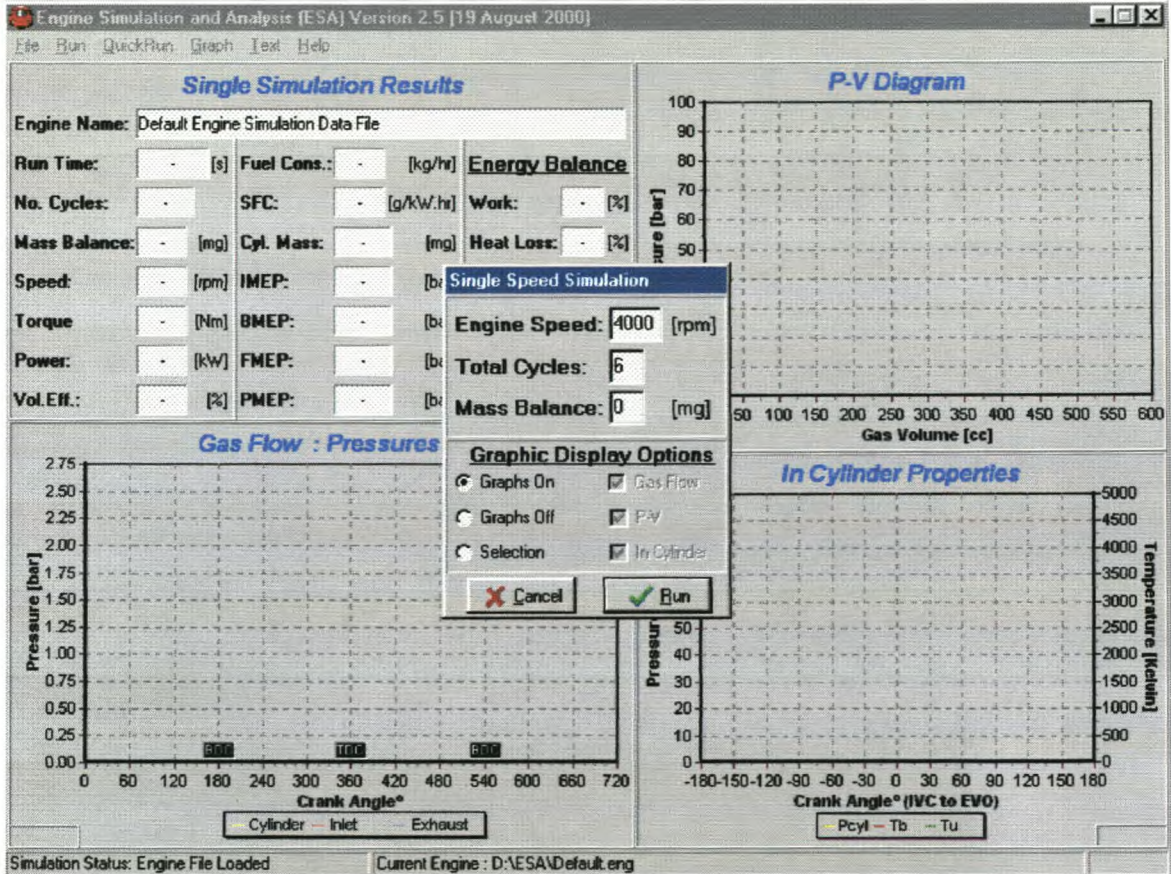


Figure F-19: Single speed simulation run

During the runtime of the simulation the user have different options on what must be displayed on the three graphs of the main window. The user has three main options on what the graphs display during run-time (Figure F-20).

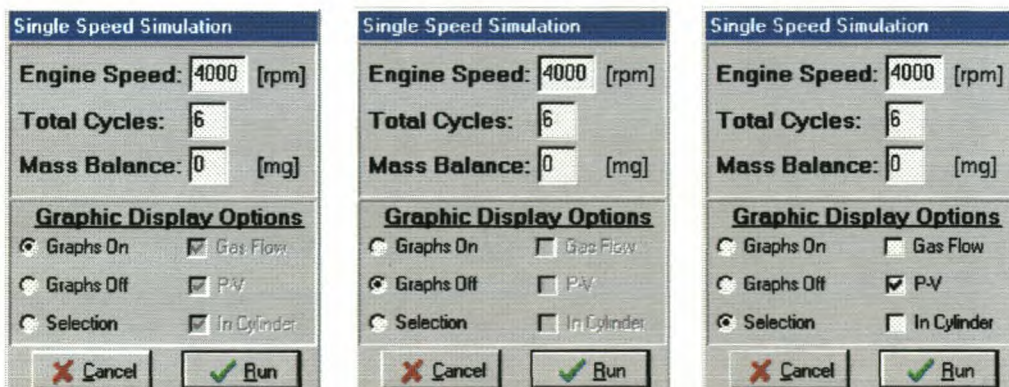


Figure F-20: Runtime graphic display options

Appendix F

Checking the **Graphs On** option causes the simulation to show all the graphs displayed in the main window. Checking **Graphs Off** causes the simulation to show no online graphics. The **Graphs Off** simulations run considerably faster, because of the slow speeds of graphic cards compared to computer processors. The last graphic display option is **Selection**, where the user can specify which graphs to show.

Graphical options can also be changed while the simulation is running or at completion of the simulation. The user can access this option by either going to **Graph, Run-Time Graph Options** or by right clicking with the mouse on the display window and choosing **Options** (Figure F-21), which displays Figure F-22.

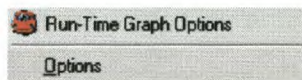


Figure F-21: Graph options

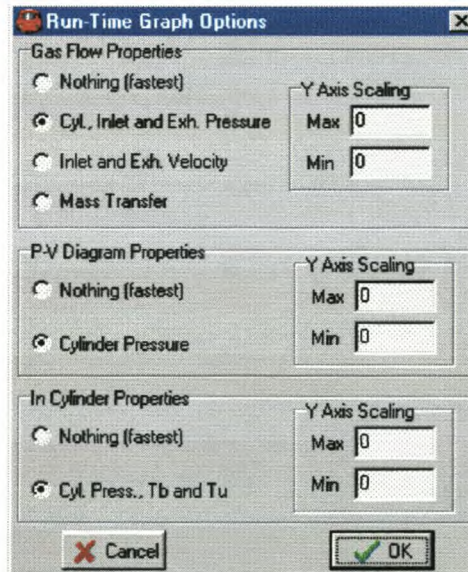


Figure F-22: Run-time graph options

Using the edit boxes in Figure F-22, the Y-axis scaling of the graphs can be changed. During the simulation the display window will look like Figure F-23 (if the **Graphs On** option is taken). In the top left corner the *Run Time* will update online and the *No. Cycles* and *Mass Balance* will update after each cycle. The other display boxes will only update at the completion of the simulation.

At completion of the simulation, the results are displayed in the rest of the open edit boxes in the upper left corner. The three graphs will also update and display

Appendix F

the final answer of the simulation, even if the **Graphs Off** option was taken during run-time (Figure F-24).

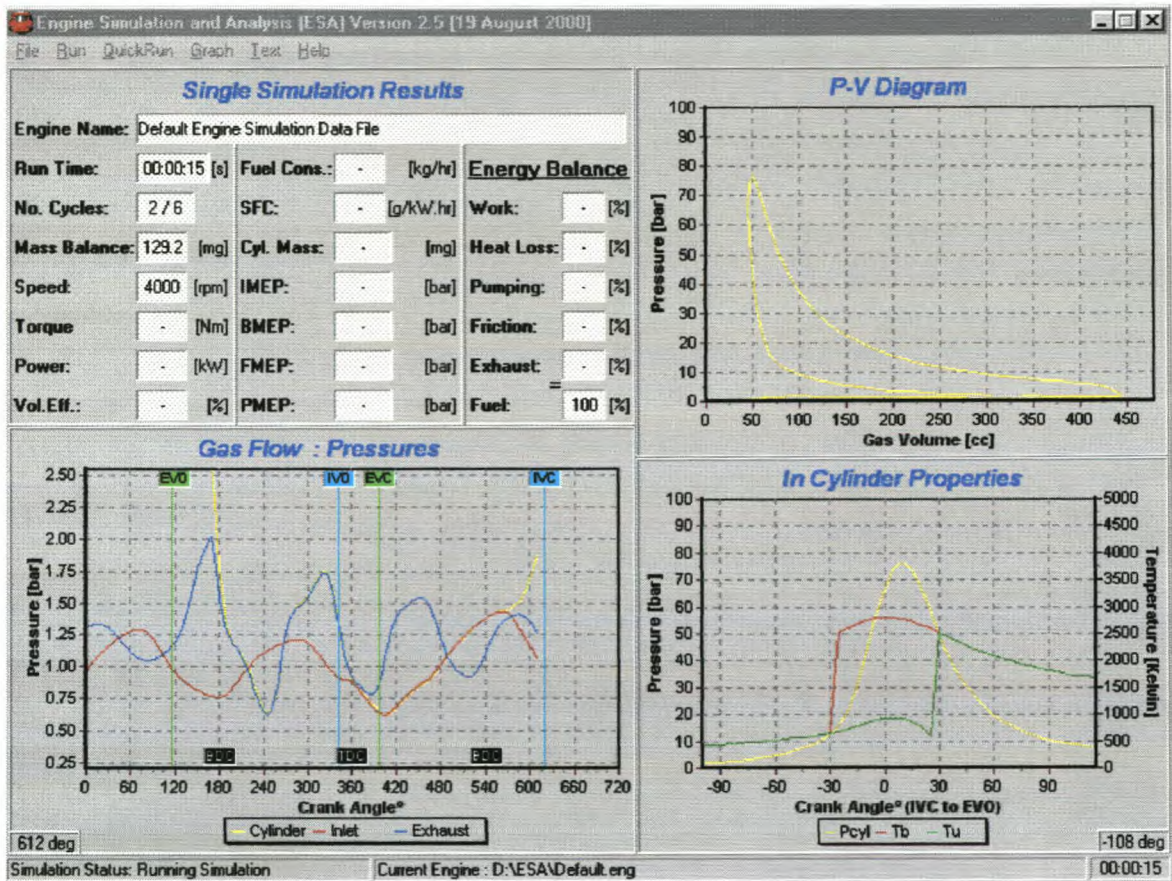


Figure F-23: Running simulation

The way in which the simulation results are calculated will not be discussed in this manual. Some of the parameters are discussed in Chapter 4 of this thesis, but more information can be obtained in Ferguson [1], Heywood [2], Heisler [3] and Benson [4].

The display of the graph in the bottom left corner can be changed as discussed earlier. In Figure F-24 the default view displays the pressure in the cylinder and at the inlet and exhaust valve. Figure F-25 displays the velocity at the inlet and exhaust valve during exhaust blow-down, valve overlap and inlet induction. Figure F-25 displays clearly the reverse flow at the exhaust valve and inlet valve. Figure F-26 displays the mass transfer at the valves and the trapped mass in the cylinder. The graph also shows how the mass in the cylinder decreases (just after BDC, 540° CA) during reverse flow at the inlet valve. The graph also displays the change in mass from unburned mass to burned mass. These three graphs can be

Appendix F

viewed alternatively online during the simulation by using the **Run-Time Graph Options**.

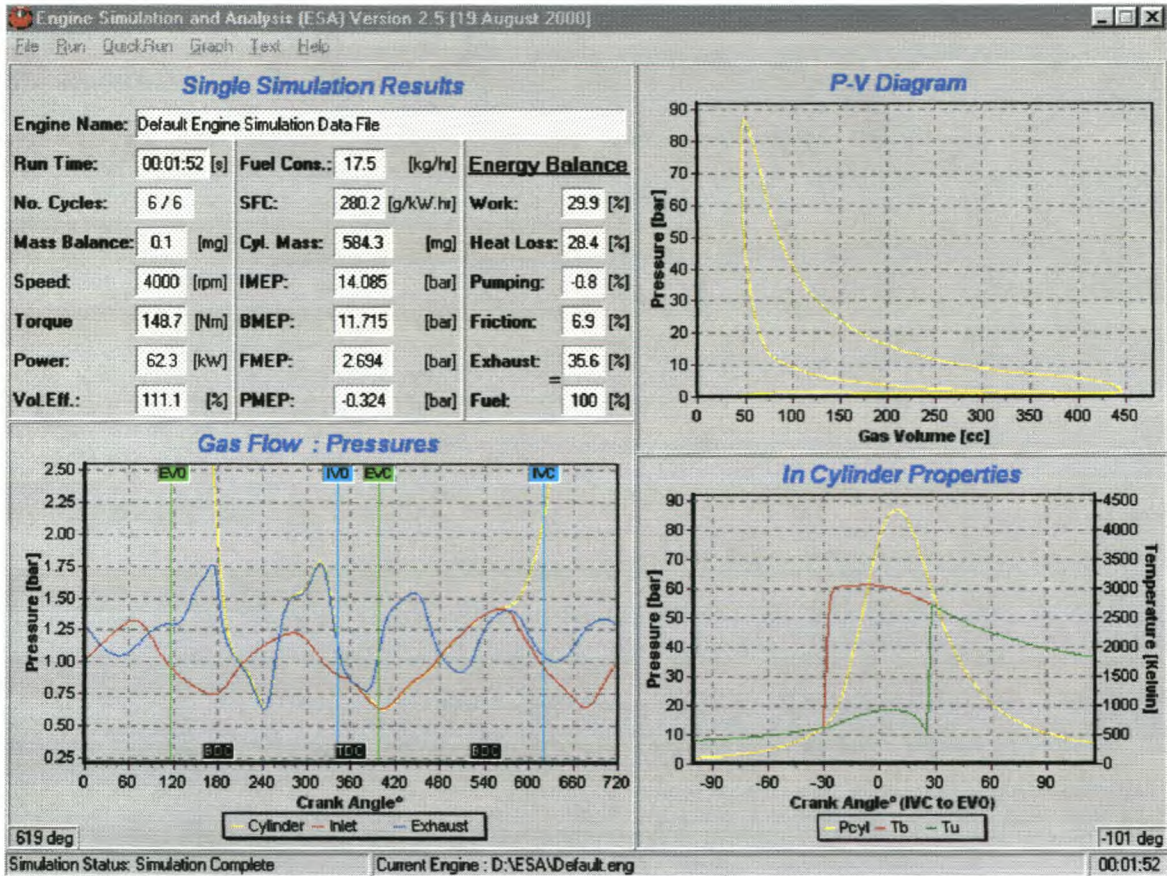


Figure F-24: Completed simulation

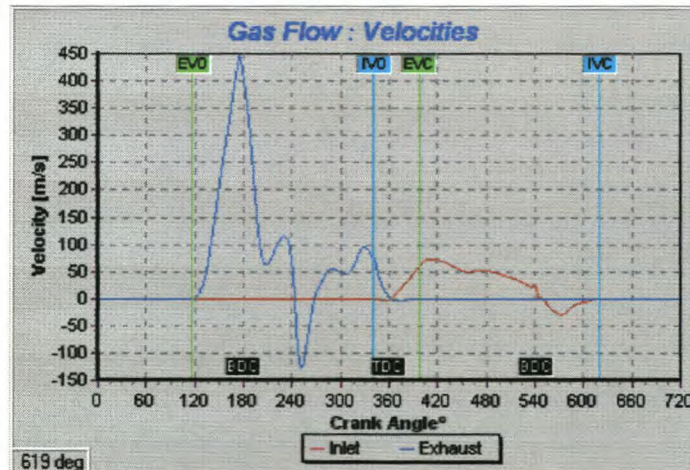


Figure F-25: Velocity at the inlet and exhaust valve

The user can also zoom into the **PV-Diagram** in the top right corner (Figure F-27) by clicking with the mouse on the graph and dragging a block, from left too right, around the desired view area. This enables the user to see for example the *Pumping Loop* of the engine (Figure F-27). The original view can again be obtained by dragging a small block, from right too left, with the mouse.

Appendix F

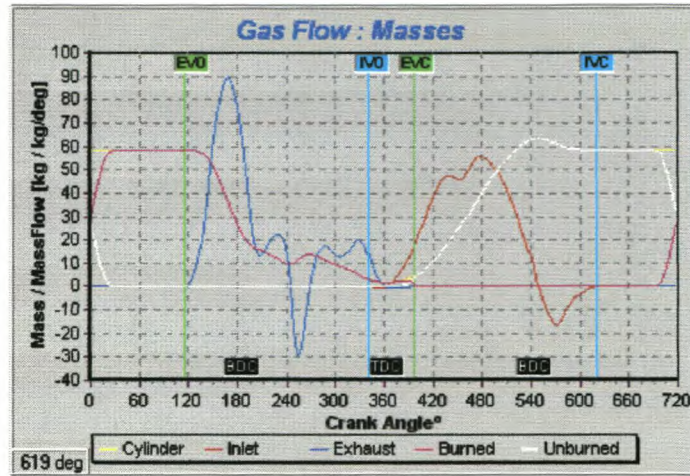


Figure F-26: Mass and mass flow

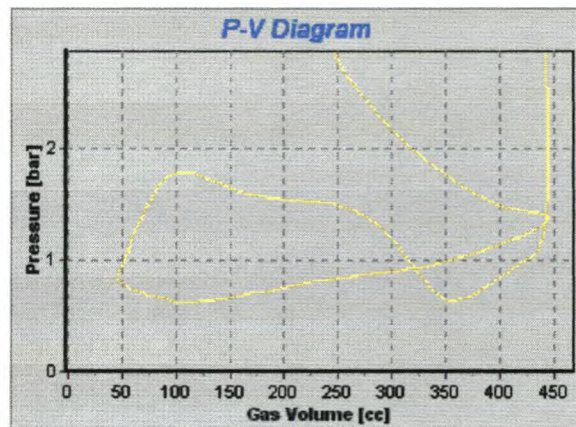


Figure F-27: Zoom into PV-diagram

To view or save the results for each crank angle degree, click the **Text, PVT Trace** menu item. A table (Figure F-28) is displayed with the state of each of the simulation variables for each 1° of crank angle. The full 720° (-360° to 360°) of the simulation (4-stroke) for the final cycle of the simulation is displayed. This data can be saved to a text file (default to *Lastcyc.txt*) using the **Save As** button and following the standard windows method of file saving. This saves a comma delimited text file (*.txt) with a user defined filename. This data can then be loaded into a spreadsheet program e.g. Excel, and the user can create graphs. It is important to note that this does not include manifold grid information. This information is available in separate text files as explained in Section F-5.

Some of these results can also be displayed graphically using the **Graph** menu option. Below the **Run-Time Graph Options** menu item, three available graph types are listed:

Appendix F

- *Torque Curve* displays the resulting torque, power and volumetric efficiency points. This graph is active when different speed points have been simulated with the **Multi Point Simulation**. More on this graph is shown in the next section on **Multi Point Simulation** runs.
- *Valve Opening* displays the valve lift profile for the inlet and exhaust valve (Figure F-29).
- *Energy Balance* displays the heat loss, work done and pump work of the last simulation cycle (Figure F-30).

CA	Vcyl	PCyl	Mcyl	Mb	Mu	Min	Mout	Vb	Vu	Tb	Tu	Qb	Q
-359	45.78	84890	18.57	18.57	0.00	-0.02	-0.01	0.00	0.00	766.4	762.1	-0.025	-0
-358	45.89	84371	18.60	18.60	0.00	0.00	-0.03	0.00	0.00	762.1	758.0	-0.025	-0
-357	46.08	83932	18.68	18.68	0.00	0.03	-0.04	0.00	0.00	758.0	754.3	-0.024	-0
-356	46.35	83443	18.77	18.77	0.00	0.05	-0.05	0.00	0.00	754.3	750.4	-0.024	-0
-355	46.69	82905	18.89	18.89	0.00	0.07	-0.05	0.00	0.00	750.4	746.5	-0.024	-0
-354	47.11	82336	19.03	19.03	0.00	0.09	-0.05	0.00	0.00	746.5	742.5	-0.024	-0
-353	47.61	81745	19.19	19.19	0.00	0.11	-0.05	0.00	0.00	742.5	738.5	-0.023	-0
-352	48.18	81134	19.39	19.39	0.00	0.14	-0.05	0.00	0.00	738.5	734.3	-0.023	-0
-351	48.83	80507	19.61	19.61	0.00	0.17	-0.05	0.00	0.00	734.3	730.1	-0.023	-0
-350	49.55	79872	19.86	19.86	0.12	0.20	-0.05	0.00	0.00	730.1	725.7	-0.023	-0
-349	50.35	79229	20.15	19.92	0.36	0.23	-0.05	0.00	0.00	725.7	721.1	-0.022	-0
-348	51.22	78581	20.46	19.97	0.62	0.27	-0.05	0.00	0.00	721.1	716.3	-0.022	-0
-347	52.16	77931	20.82	20.02	0.92	0.30	-0.05	0.00	0.00	716.3	711.2	-0.022	-0
-346	53.18	77279	21.21	20.07	1.27	0.34	-0.05	0.00	0.00	711.2	705.7	-0.022	-0
-345	54.27	76627	21.64	20.11	1.65	0.38	-0.05	0.00	0.00	705.7	699.9	-0.021	-0
-344	55.43	75978	22.11	20.16	2.08	0.43	-0.04	0.00	0.00	699.9	693.8	-0.021	-0
-343	56.67	75333	22.63	20.20	2.55	0.47	-0.04	0.00	0.00	693.8	687.2	-0.021	-0

Figure F-28: Table with simulation results

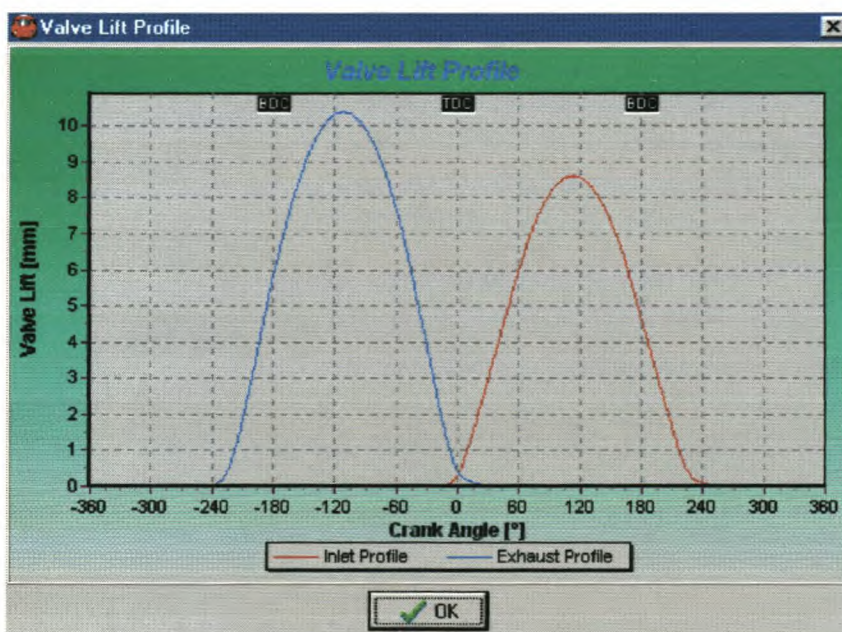


Figure F-29: Valve lift profile

Appendix F

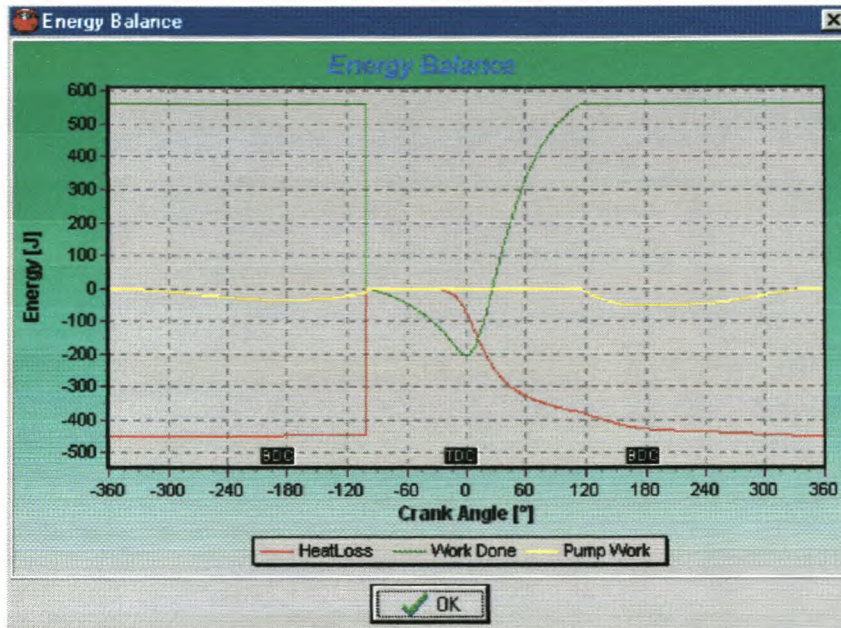


Figure F-30: Energy balance

Single Point Simulation runs are very useful when the user is in the process of creating a reliable engine model. It gives the user a quick, but sufficient indication of engine performance and other characteristics to further fine-tune the engine model.

F-7. Multi Point Simulation

In Section F-6 it was described how to run a single speed *Single Point Simulation*. In this section it is described how to do a *Multi Point Simulation*. This type of simulation gives the user the opportunity to do for example a torque curve at different engine speeds, without running the engine speed points separately using the *Single Point Simulation* option.

In the main menu, click **Run** and then **Multi Point Simulation**. A user box appears on the display window (Figure F-31). In the top left corner the engine file in use is displayed. In the table the following can be changed:

- *Speed* can vary for a torque curve or stay constant when testing other engine parameters.
- *Iters* is the amount of iterations or cycles to run for each simulation point.
- *IManfFile* and *EManfFile* give the option to enter any *.maf text file for the inlet and exhaust manifold. This is used for running manifolds with different lengths and diameters.

Appendix F

- *ICamFile* and *ECamFile* give the option to load any other camshaft lift profile by specifying a *.cam text file.
- *IVO*, *IVC*, *EVO* and *EVC* can be changed to let the inlet and exhaust valve open or close at different crank angle degrees. It gives the user the opportunity to change the overlap between the inlet and exhaust valve as well as the duration of the inlet and exhaust valve.
- *IValveLift* and *EValveLift* are used to change the maximum lift of the inlet and exhaust valve.
- *Spark°BTDC* gives the user the opportunity to change the ignition timing of the engine at different engine speeds. It is therefore possible to run a torque curve at different engine speeds and with a specific set of ignition timings.
- *Burn Angle°* gives the option to change the burn angle duration, in crank angle degrees, of the burning fuel.

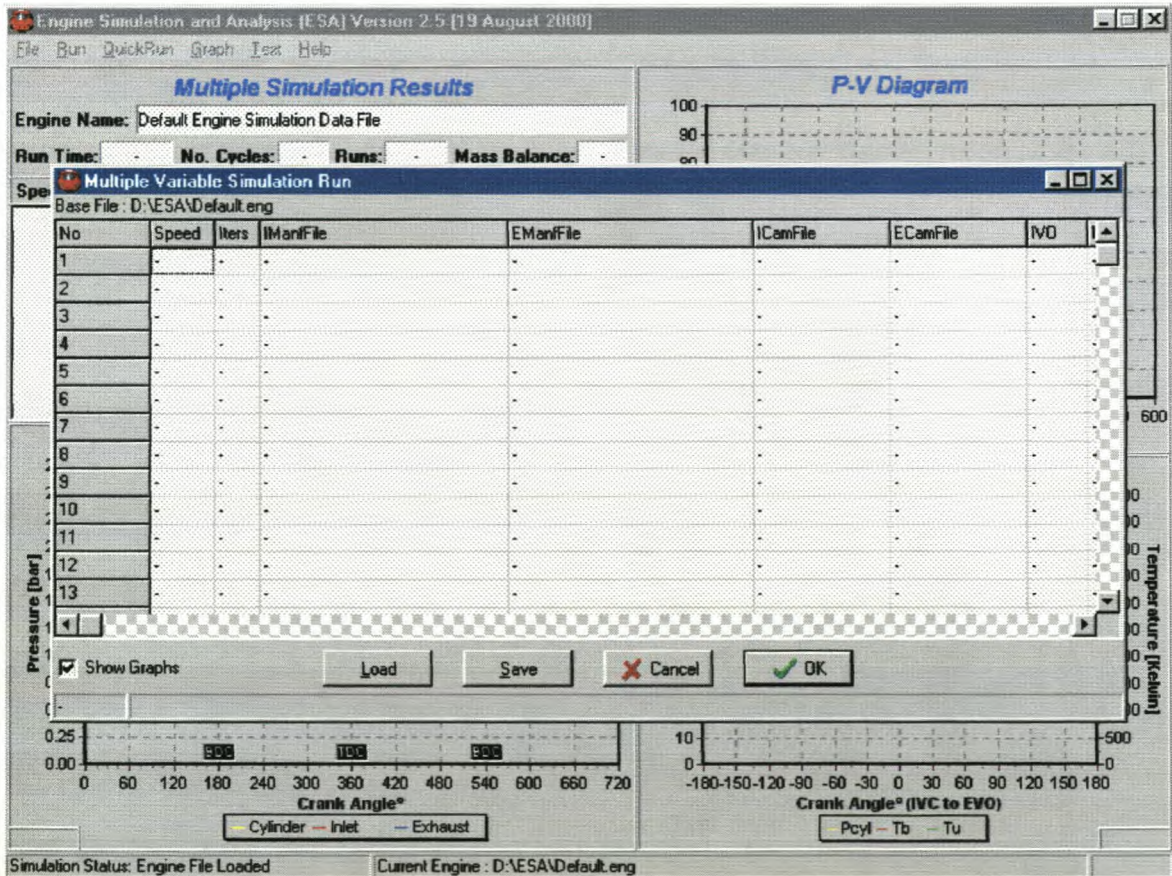


Figure F-31: Multiple simulation runs

All this information can be stored, using the *Save* button, in a user defined text file *.msr. Saved text files can also be loaded by clicking the *Load* button.

Appendix F

The user now has the option to run the **Multi Point Simulation**. In Figure F-32 a text file is displayed that was created to do a torque curve from a 1500 rpm to 6500 rpm in 250 rpm steps. The user also has the option to keep all the graphics on or to have it all off by making a selection in the bottom left corner. The simulation runs faster when the **Show Graphs** option is not selected.

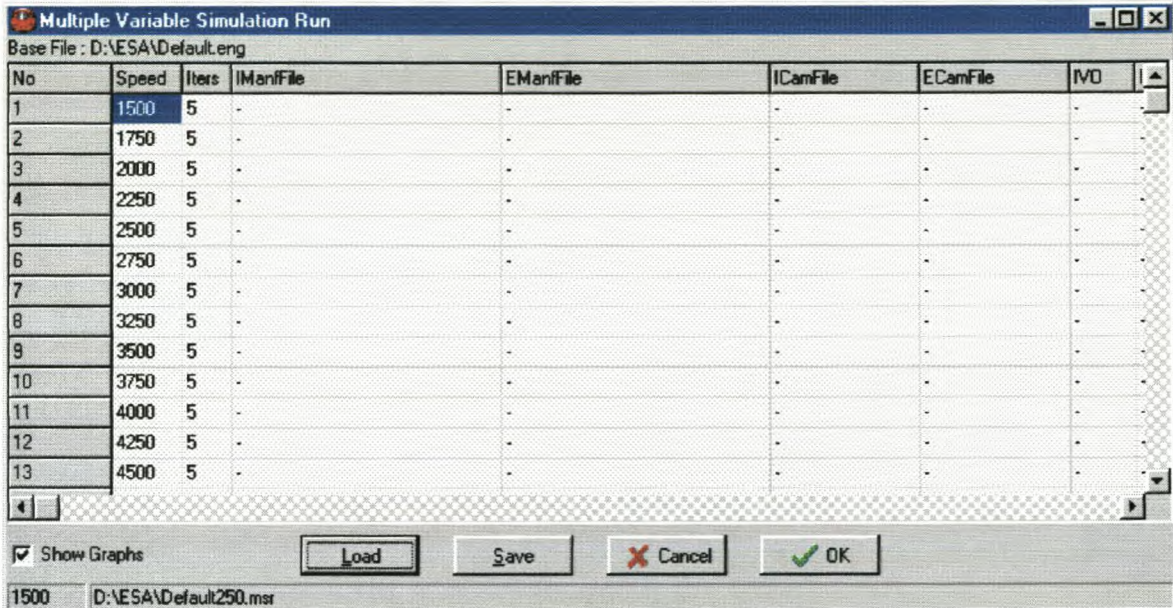


Figure F-32: Multiple simulation setup for a torque curve

During run-time the user is able to see the following (Figure F-33):

- Total run-time of the simulation.
- Number of cycles at the simulated point.
- Total number of simulated points and the current simulated point.
- Mass balance at the simulated point.
- Performance results of the completed simulation points. The results that are displayed are only a few of the more important engine parameters. More extensive results are illustrated in the **Text, PVT Trace** menu table.

During the run-time of the program and at completion of the simulation, the same graph options, as for a single simulation point, are available. At the completion of the simulation, the displayed data is of the last cycle of the last simulation point. All other menu options as for a single simulation point are still available.

The user might be interested to see the torque curve graphically when running such a **Multi Point Simulation**. This graph is selected under the **Run-Time Graph Options** menu item, **Torque Curve** (Figure F-34).

Appendix F

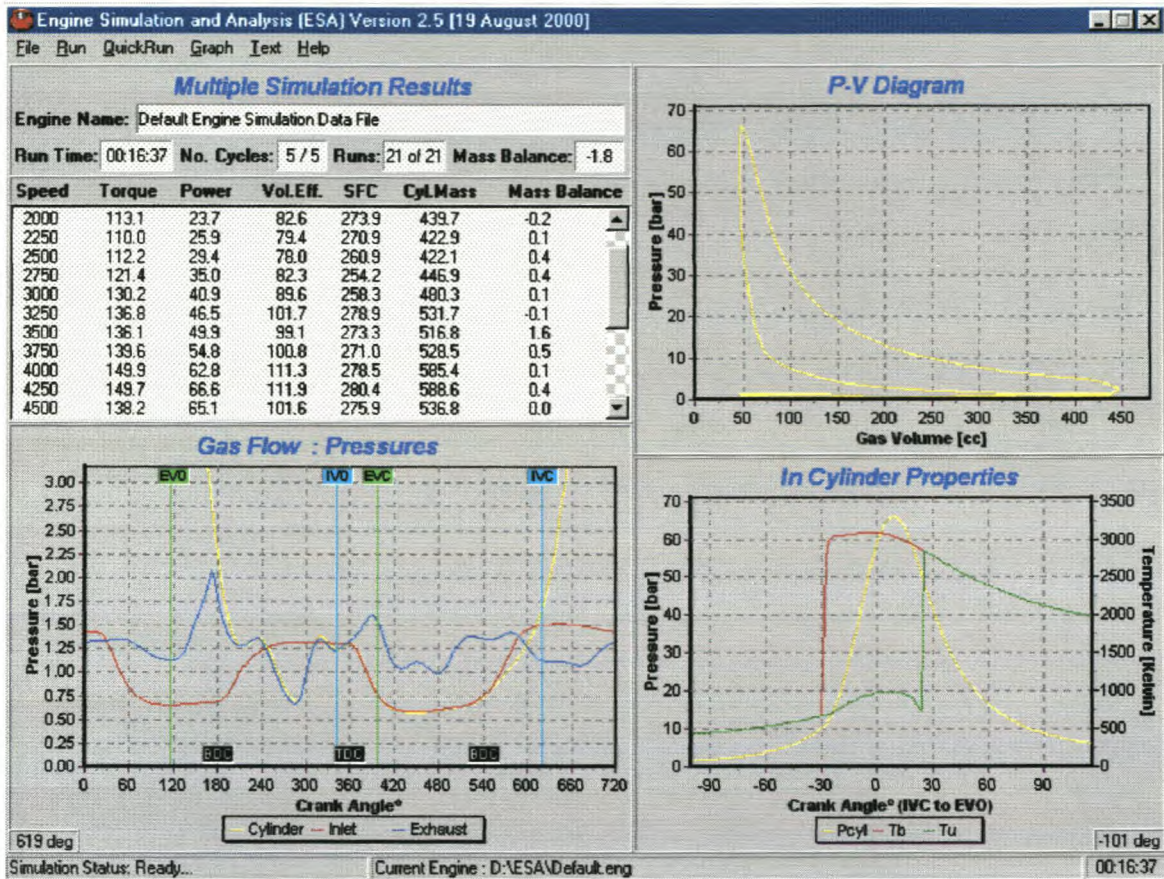


Figure F-33: Completion of Multi Point Simulation

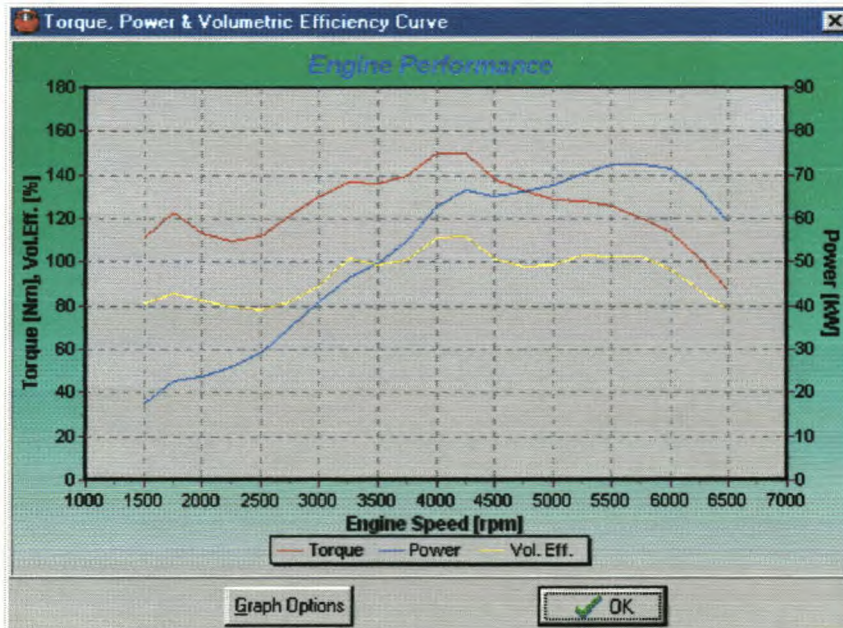


Figure F-34: Torque, power and volumetric efficiency curve

Graph options for Figure F-34 are available to the user by clicking the *Graph Options* button. Figure F-35 then displays edit boxes to change the maximum and minimum values for the graph axes.

Appendix F

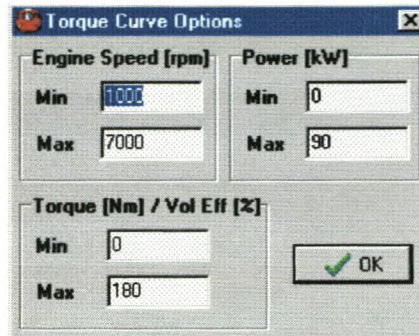


Figure F-35: Torque graph options

The *Multi Point Simulation* option in the ESA program is one of the most powerful and convenient options. It allows the user to do up to 100 simulation points at a time and can therefore gather a substantial amount of data in a relative short space of time. An accurate engine data file will contribute to the accuracy of these results.

F-8. General Information

An online user manual is available by clicking the **Help, User Manual** menu item. More about this program and its creators are displayed in the **Help, About** menu item (Figure F-36).

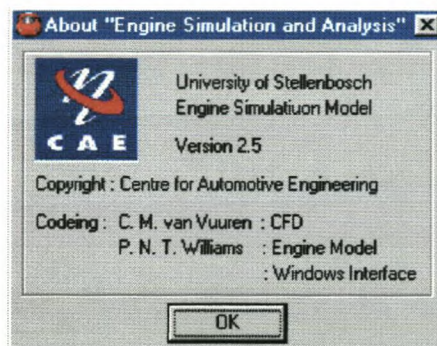


Figure F-36: About ESA

Appendix G

New fuel injected inlet manifold drawings

Appendix G

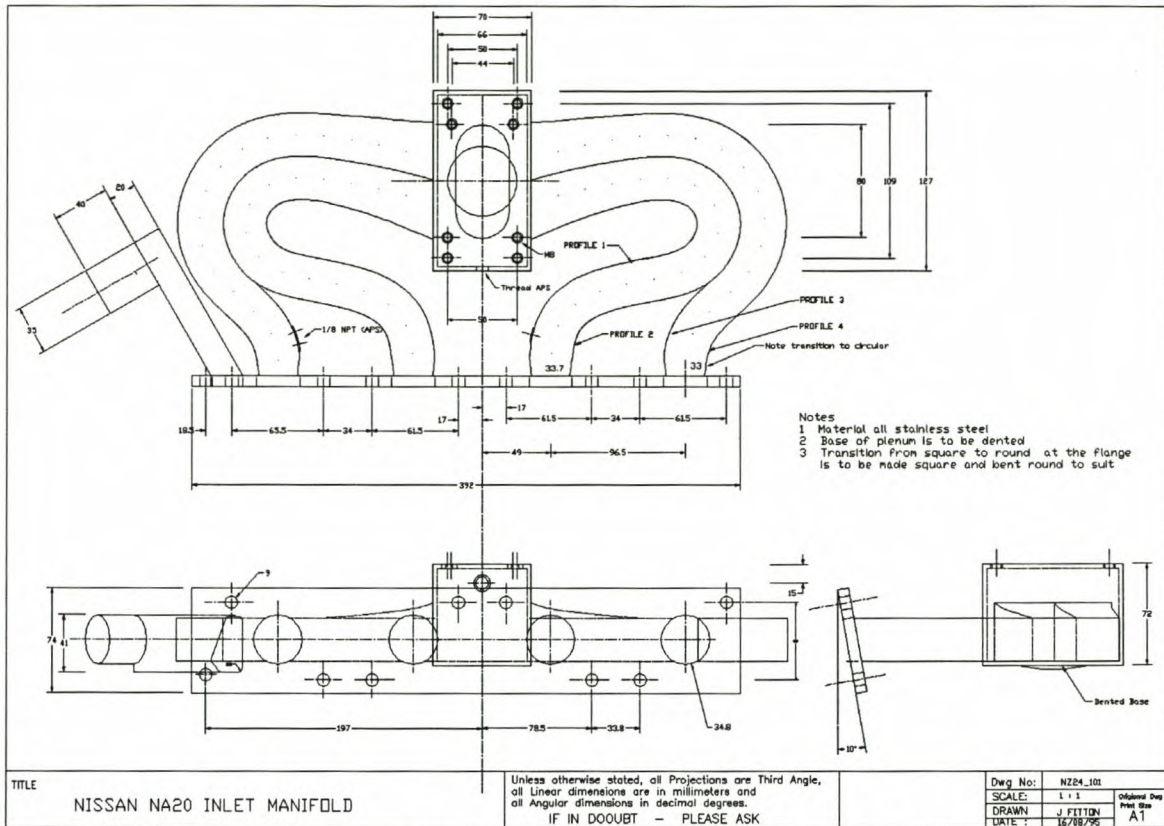


Figure G-1: Standard carburettor NA20 inlet manifold for use on Nissan Z24

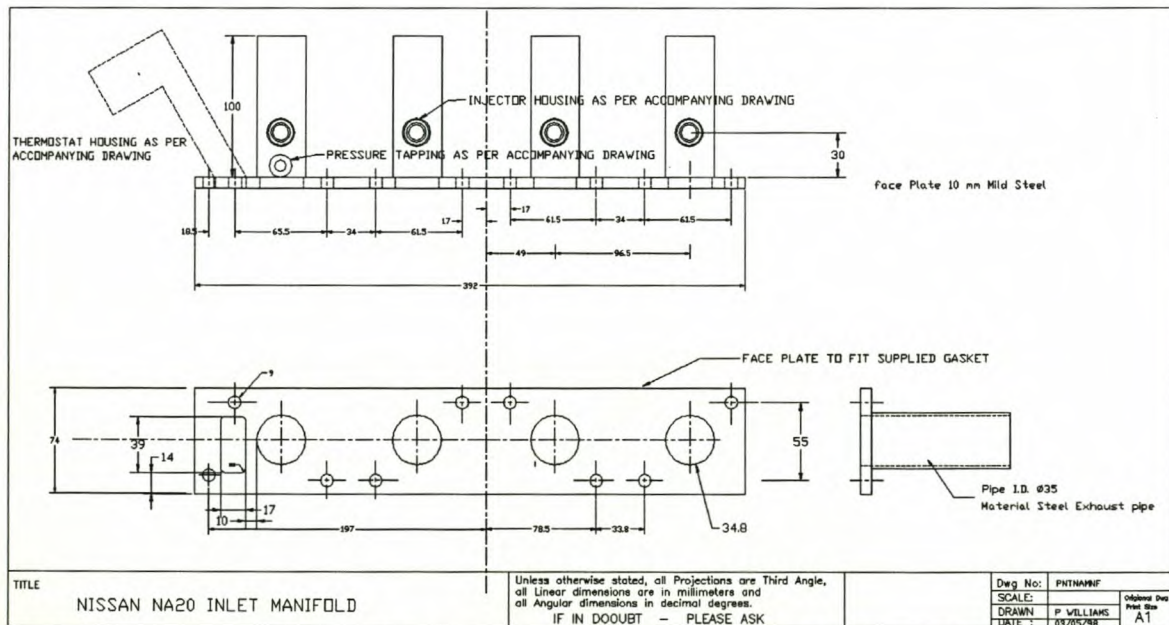


Figure G-2: Part 1 of new fuel injected inlet manifold for Nissan Z24 test engine

Appendix G

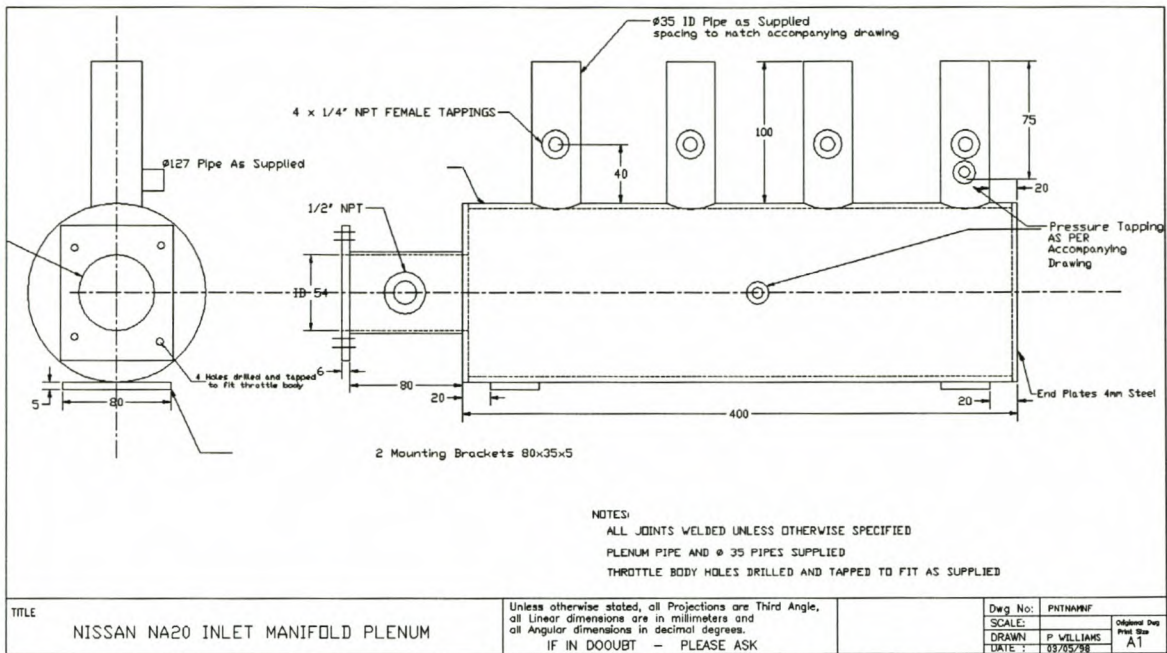


Figure G-3: Part 2 of new fuel injected inlet manifold for Nissan Z24 test engine

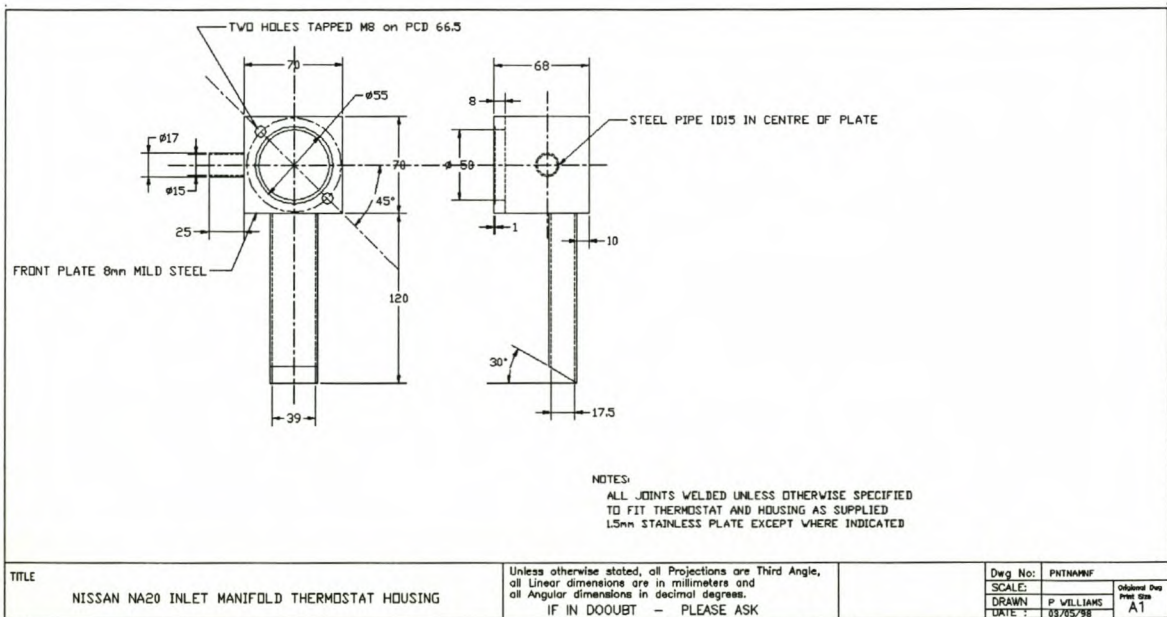


Figure G-4: Thermostat housing for new fuel injected inlet manifold

Appendix G

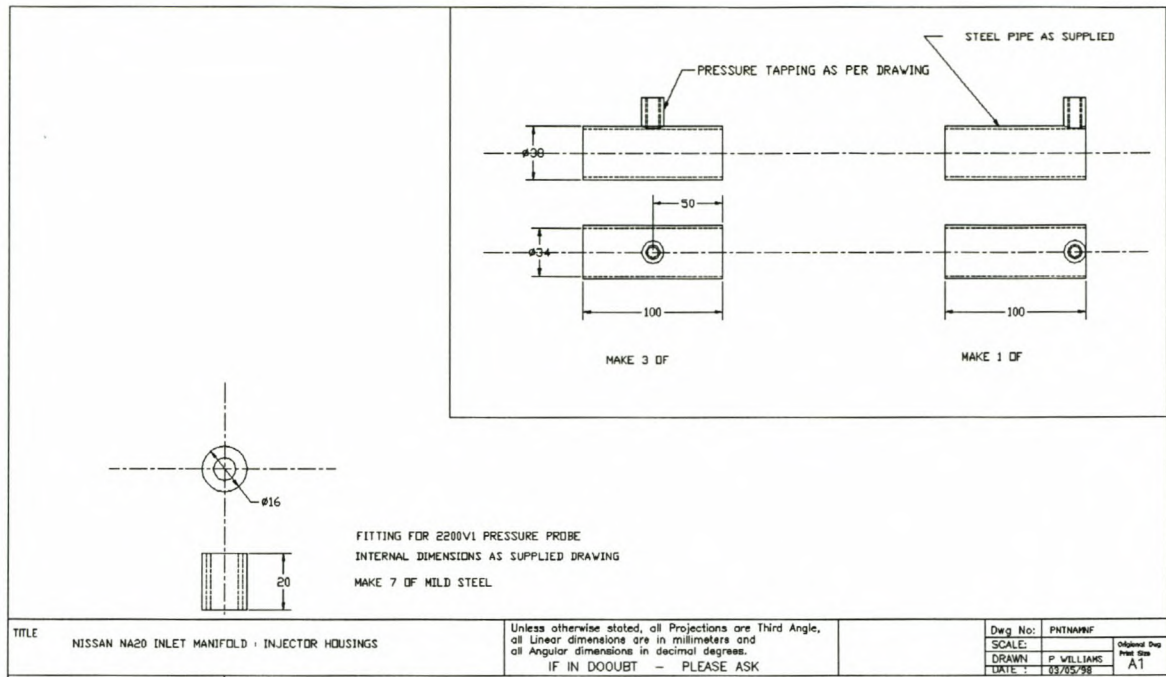


Figure G-5: Pressure transducer fittings for new fuel injected inlet manifold

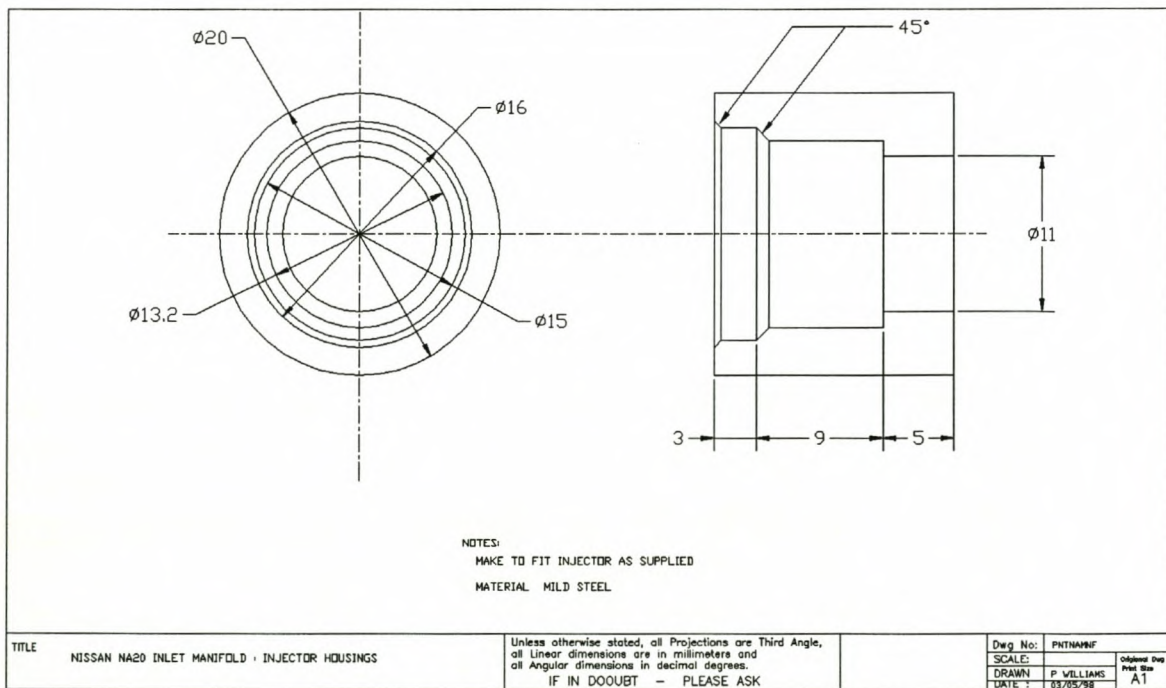


Figure G-6: Injector housing for new fuel injected inlet manifold

Appendix G

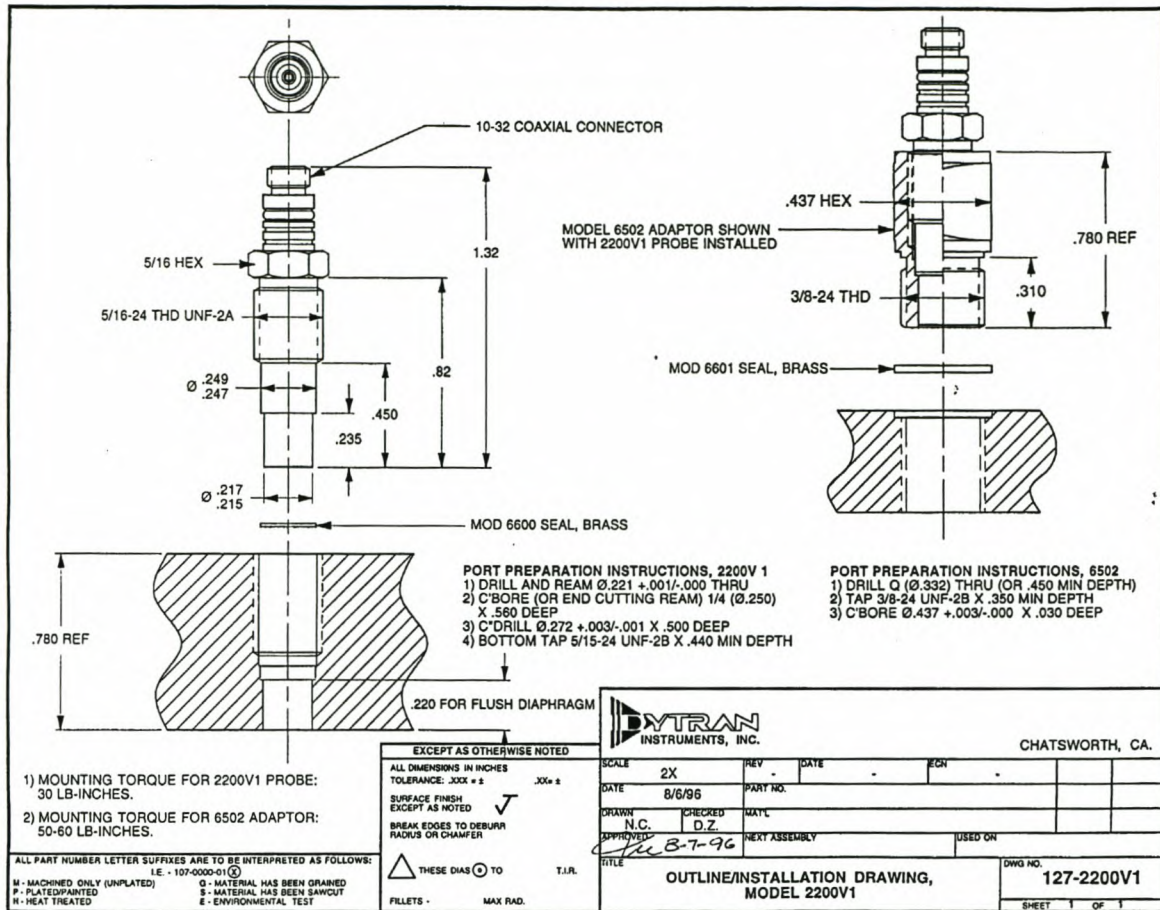


Figure G-7: DYTRAN dynamic pressure sensor for installation in new inlet manifold

Appendix H

Tested and modelled performance data on Nissan test engine

Appendix H

H-1: Testing performance data on Nissan test engine

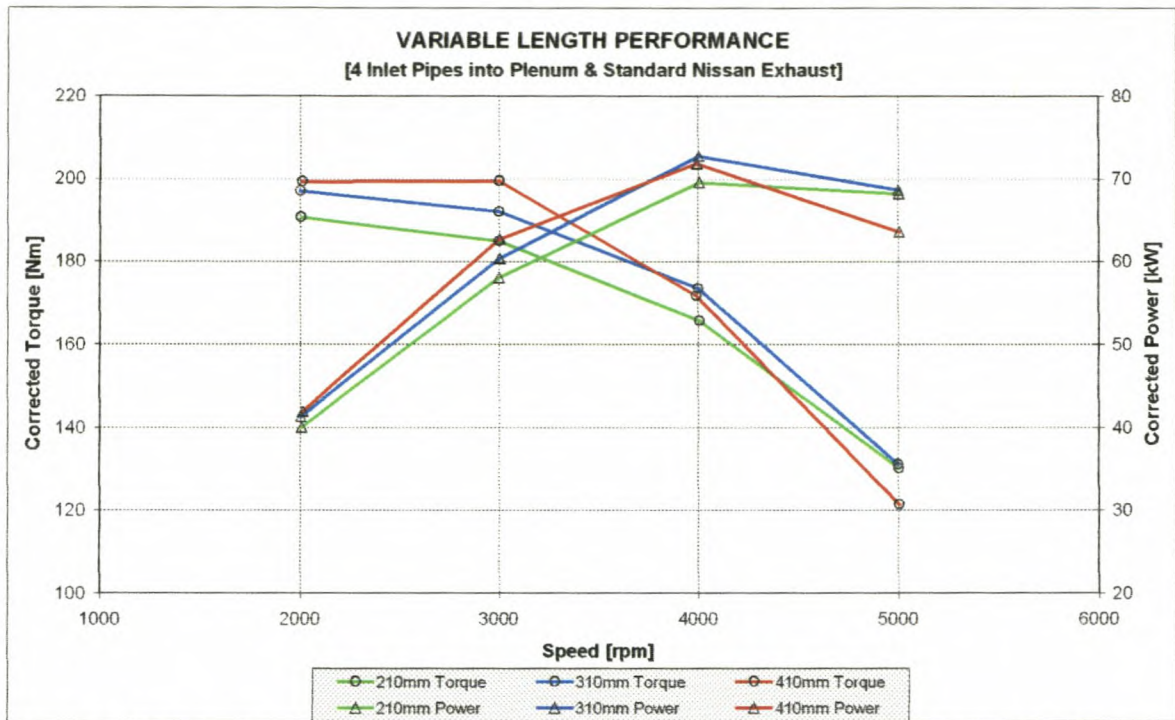


Figure H-1: Variable inlet manifold length performance with standard exhaust system

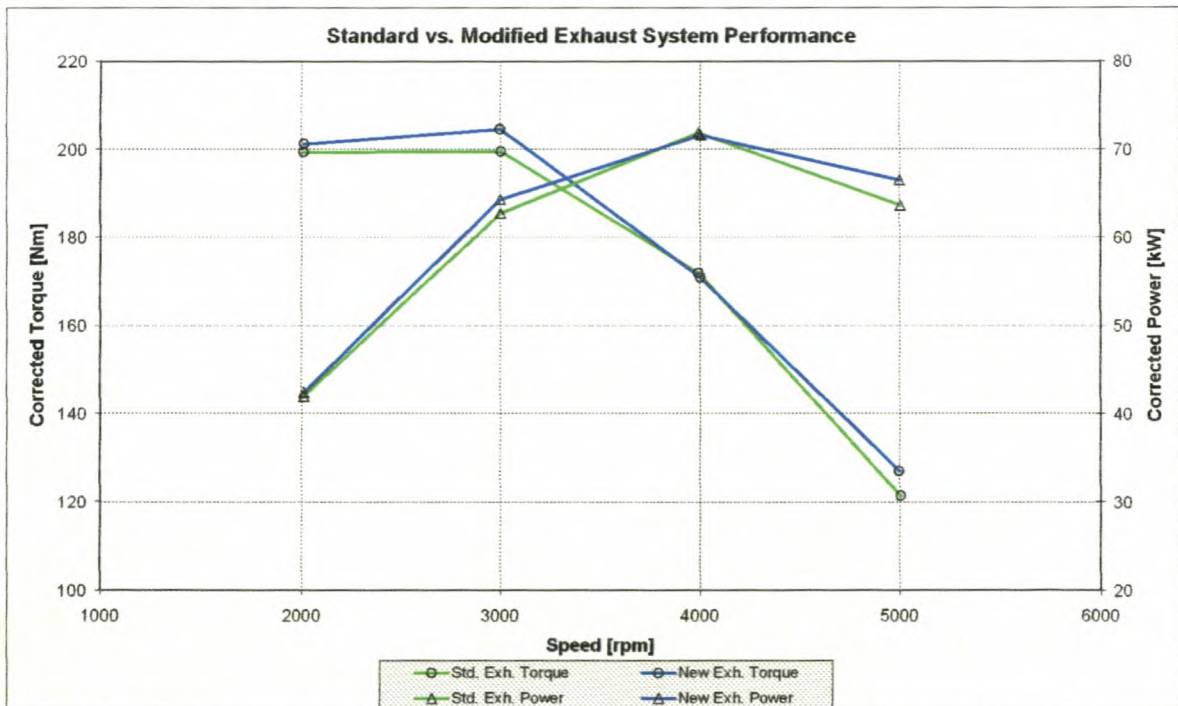


Figure H-2: Standard vs. modified exhaust system performance (410mm inlet manifold)

Appendix H

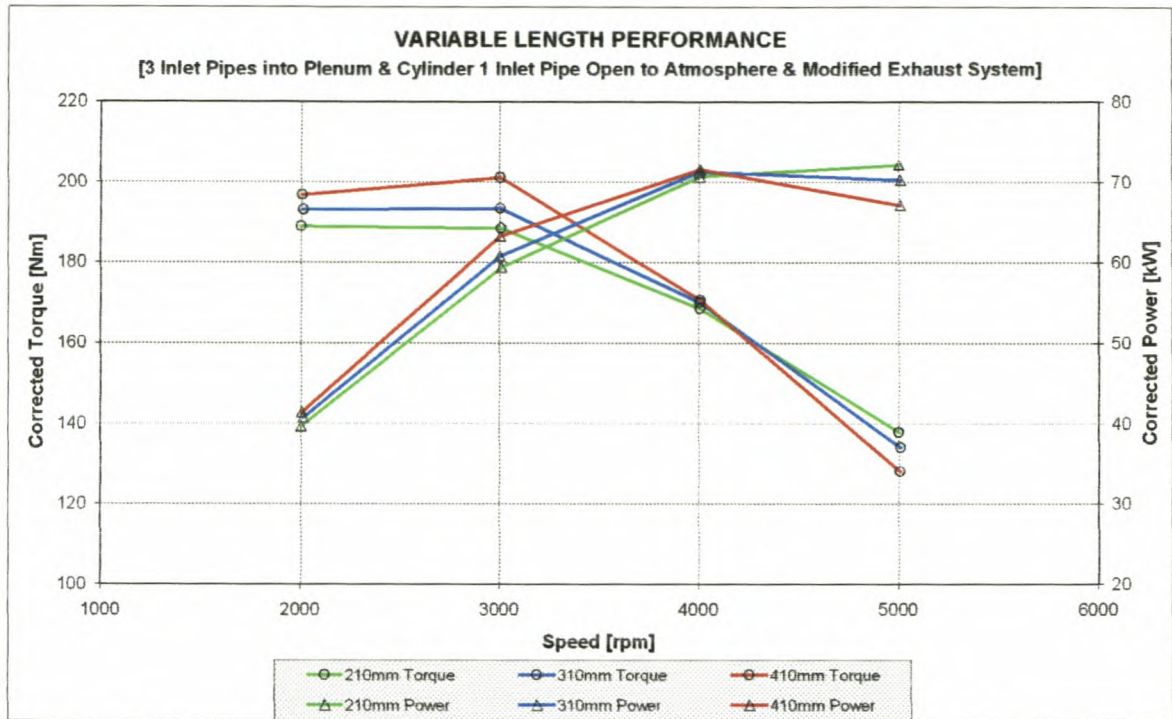


Figure H-3: Variable inlet manifold length performance on modified exhaust system

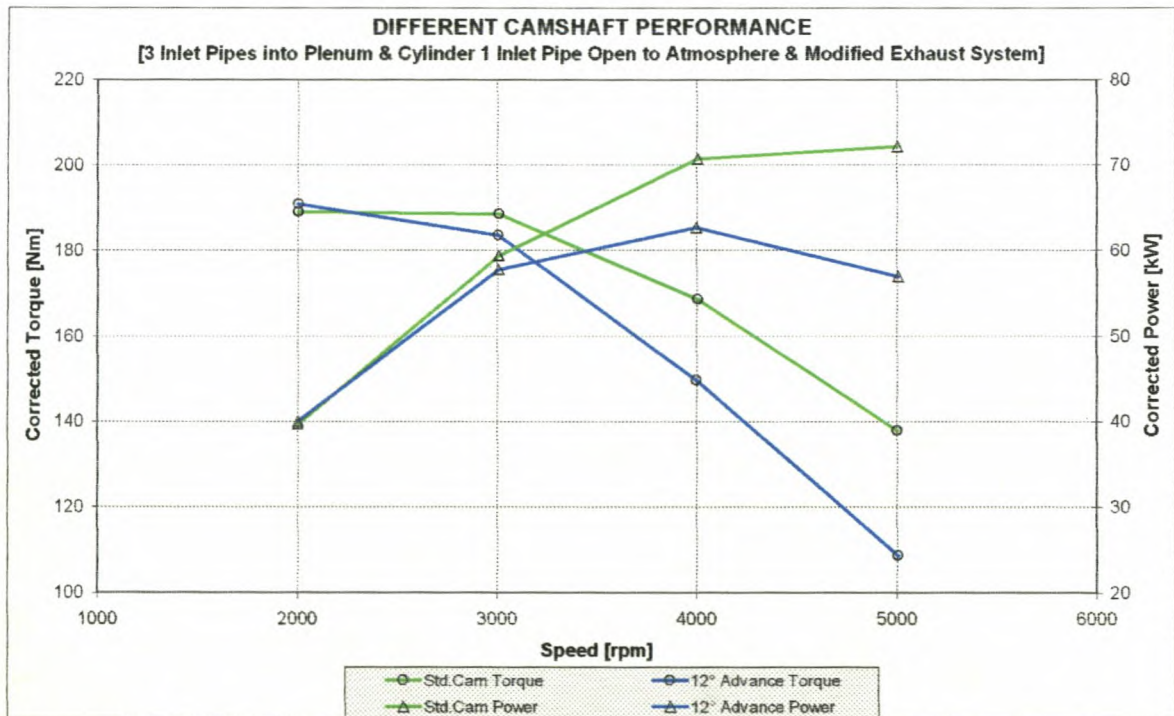


Figure H-4: Advancing camshaft performance with a 210mm inlet manifold

Appendix H

H-2: Modelled performance data on Nissan test engine

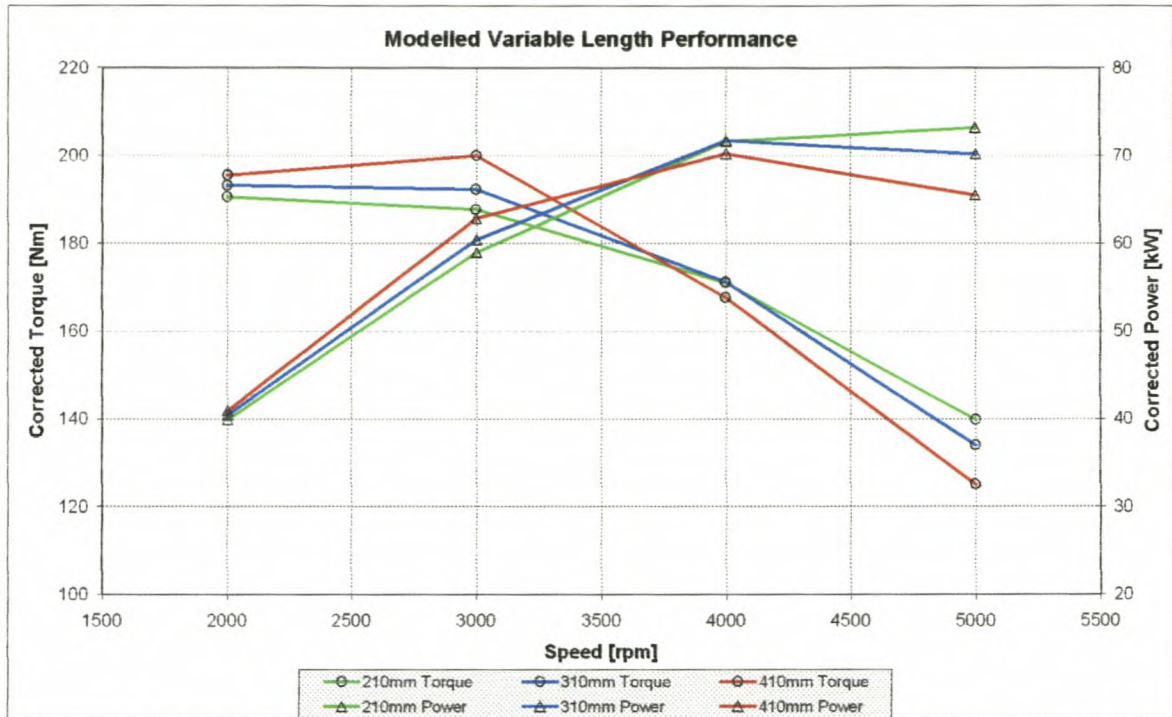


Figure H-5: Modelled variable length performance

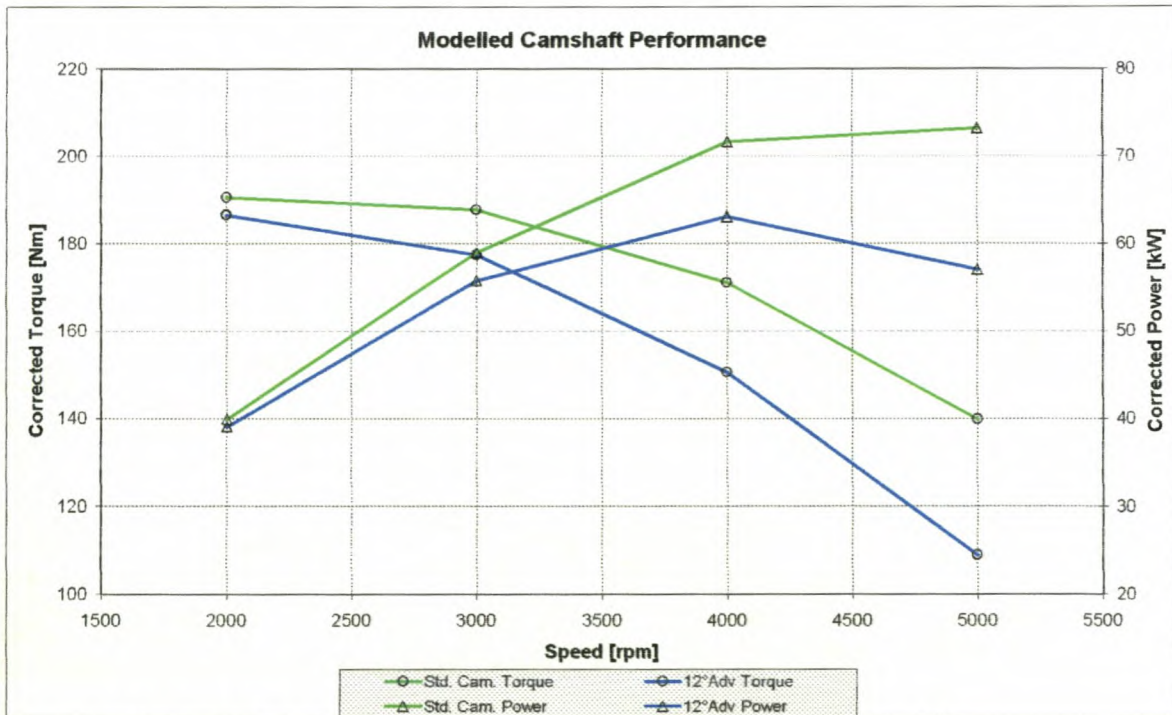


Figure H-6: Modelled camshaft performance with a 210mm inlet manifold

Appendix I

Tested and modelled pressure data on Nissan test engine

I-1: Test 1 engine performance and pressure data

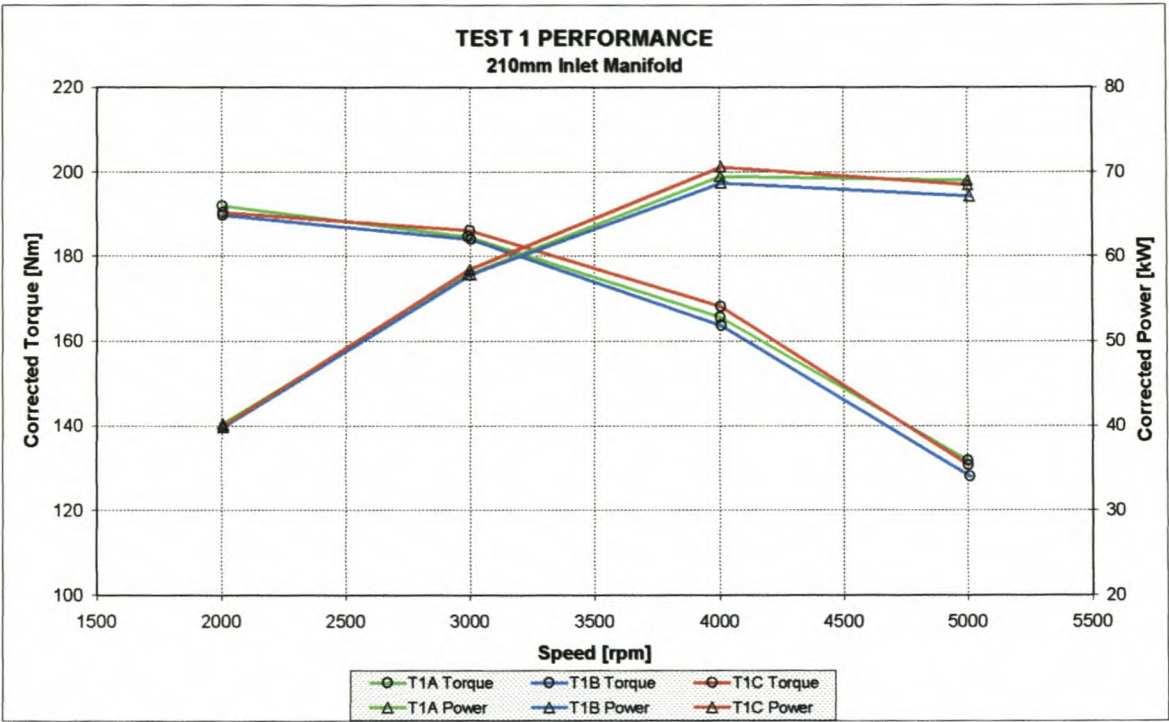


Figure I-1: Test 1 performance on a 210mm inlet manifold

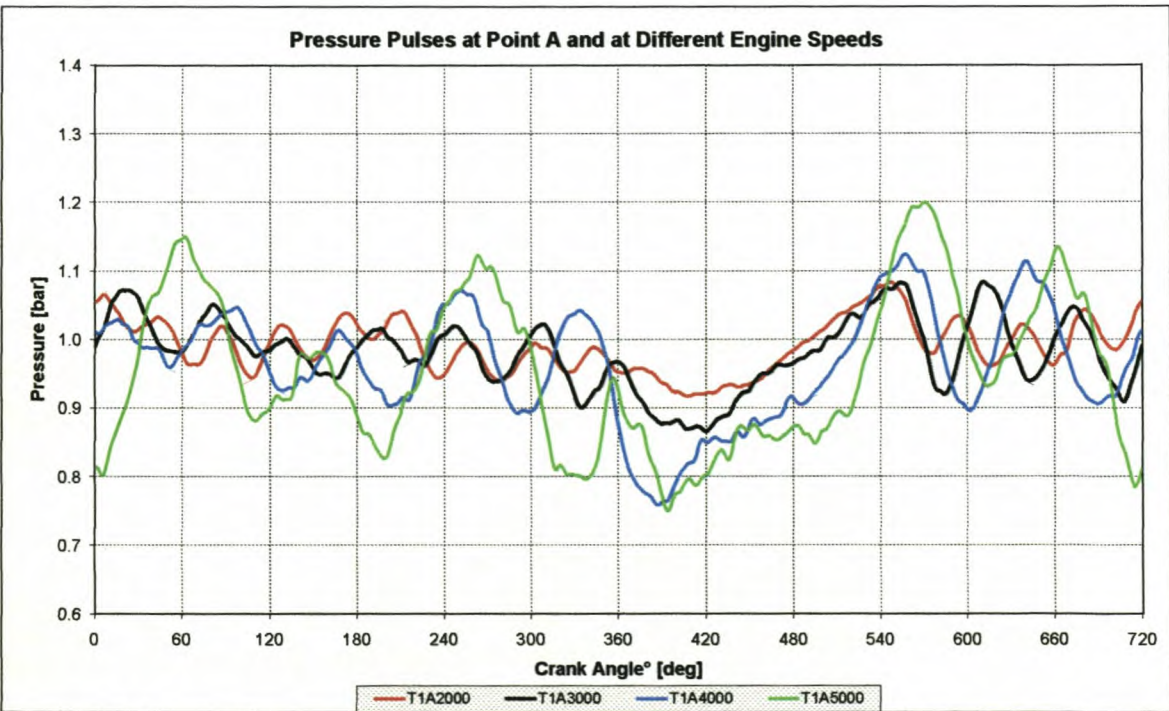


Figure I-2: Pressure pulse data measured at point A at different engine speeds

Appendix I

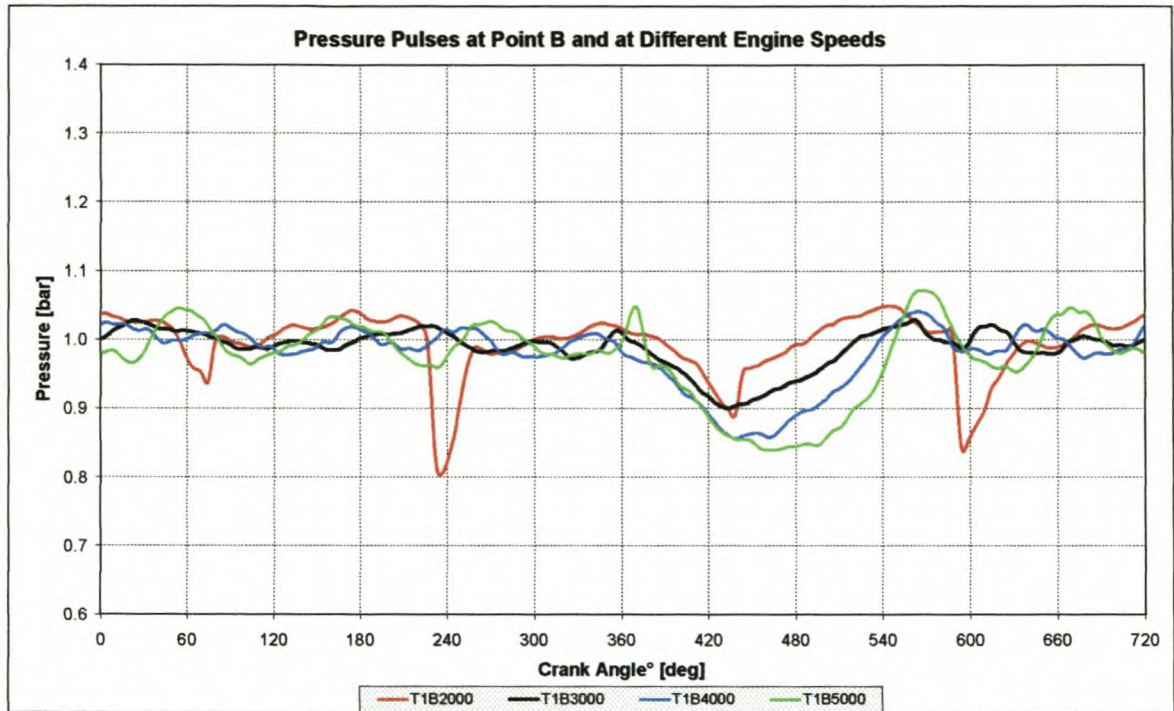


Figure I-3: Pressure pulse data measured at point B at different engine speeds

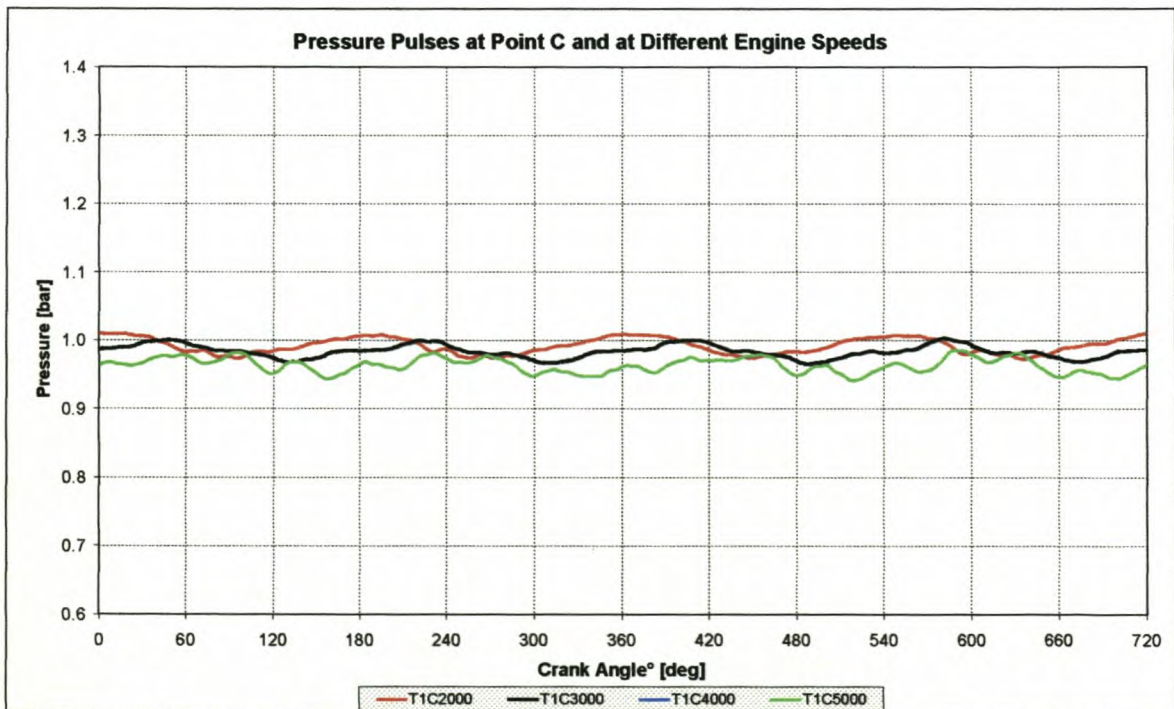


Figure I-4: Pressure pulse data measured at point C at different engine speeds

Appendix I

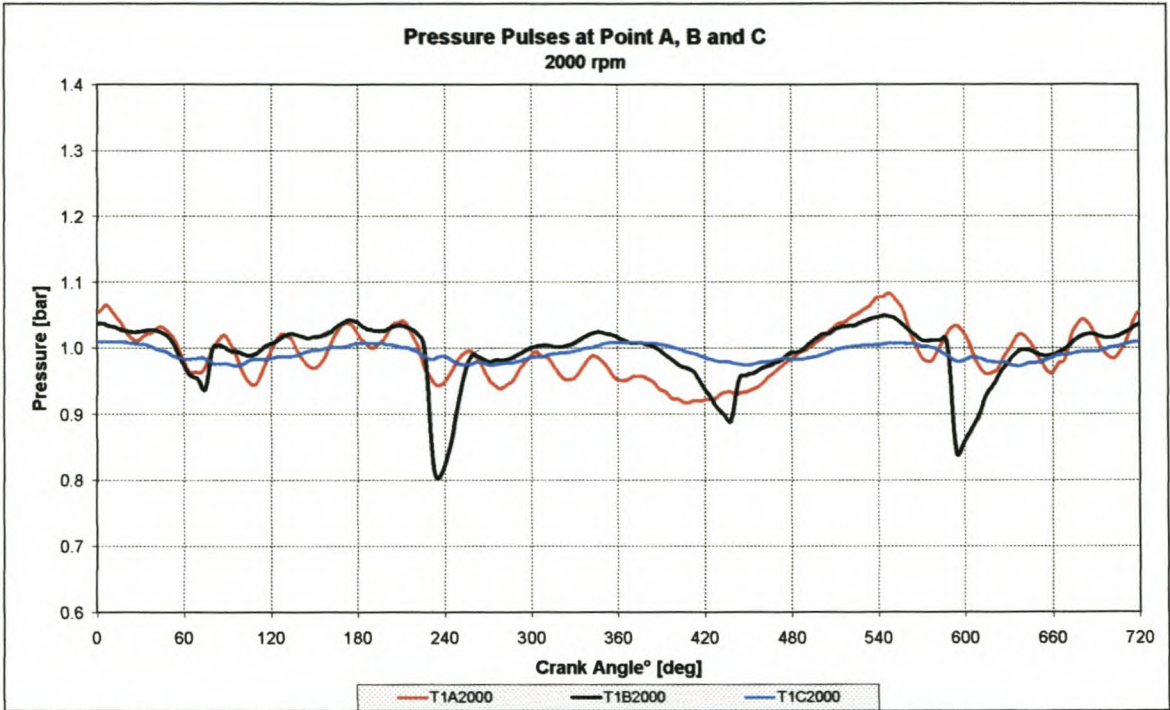


Figure I-5: Pressure pulse data measured at points A, B and C @ 2000rpm

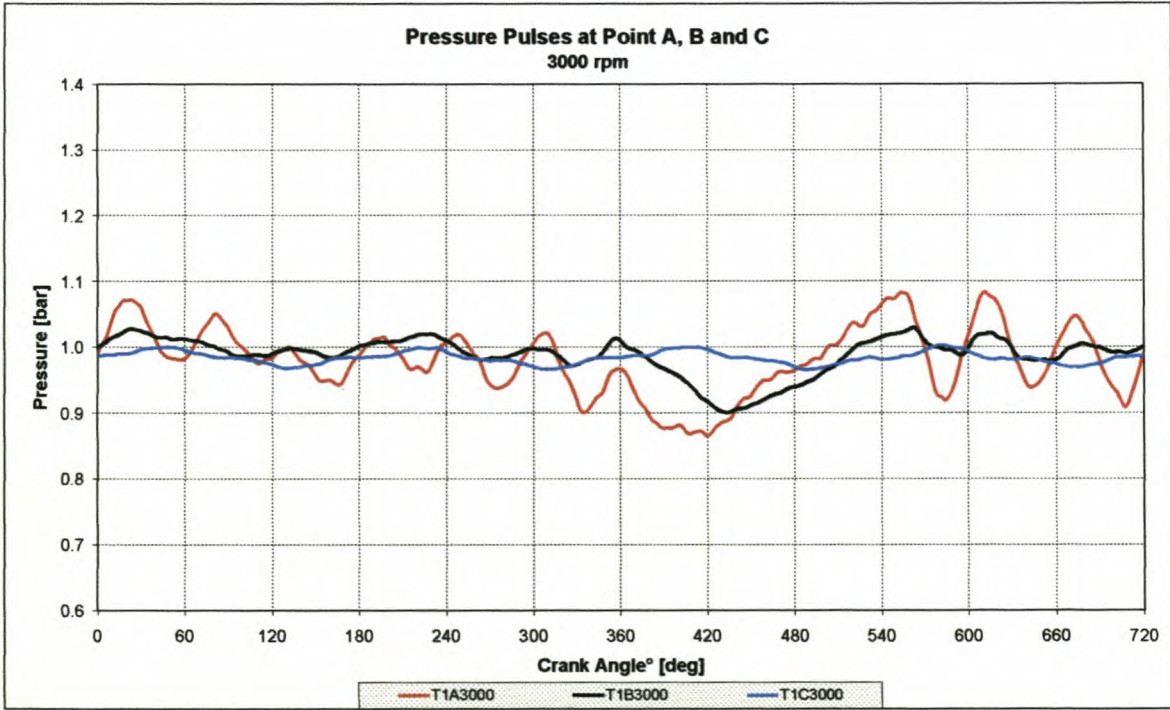


Figure I-6: Pressure pulse data measured at points A, B and C @ 3000rpm

Appendix I

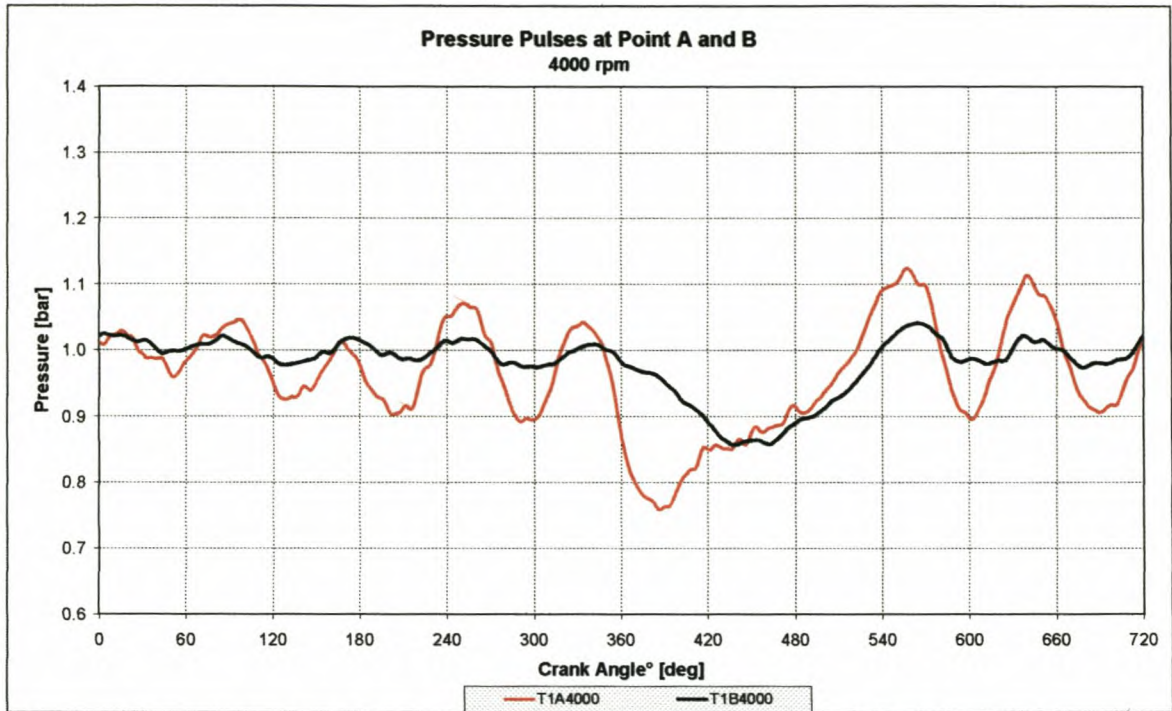


Figure I-7: Pressure pulse data measured at points A and B @ 4000rpm

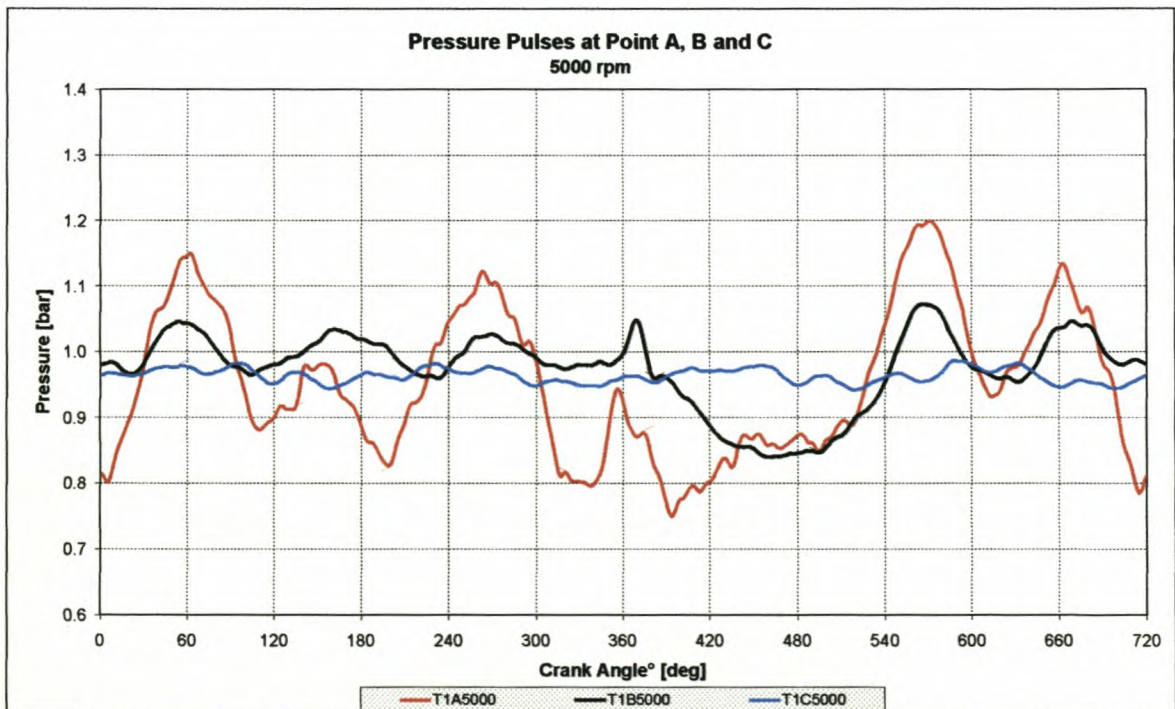


Figure I-8: Pressure pulse data measured at points A, B and C @ 5000rpm

I-2: Test 2 engine performance and pressure data

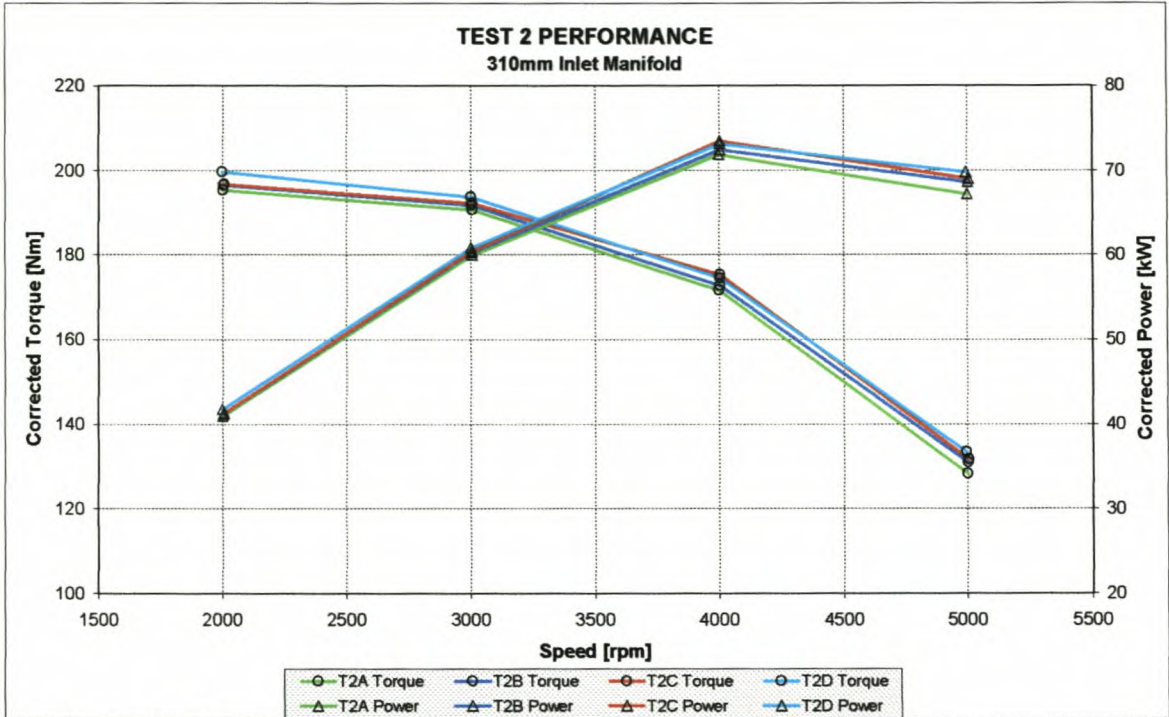


Figure I-9: Test 2 performance on a 310mm inlet manifold

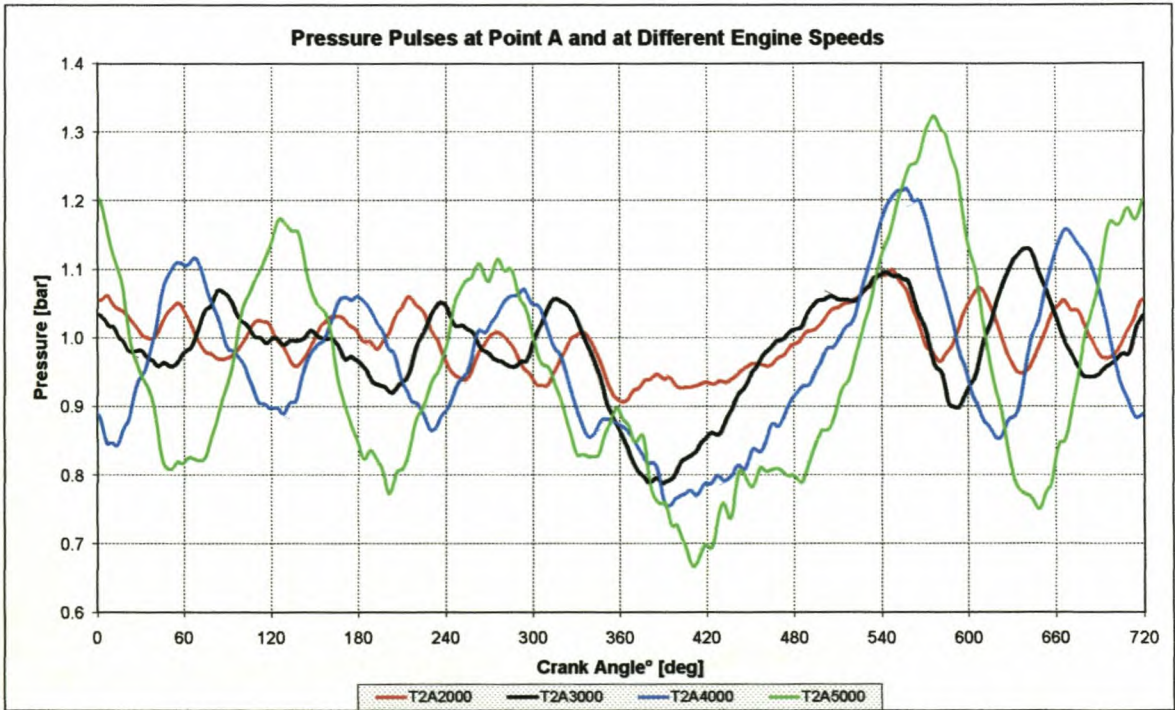


Figure I-10: Pressure pulse data measured at point A at different engine speeds

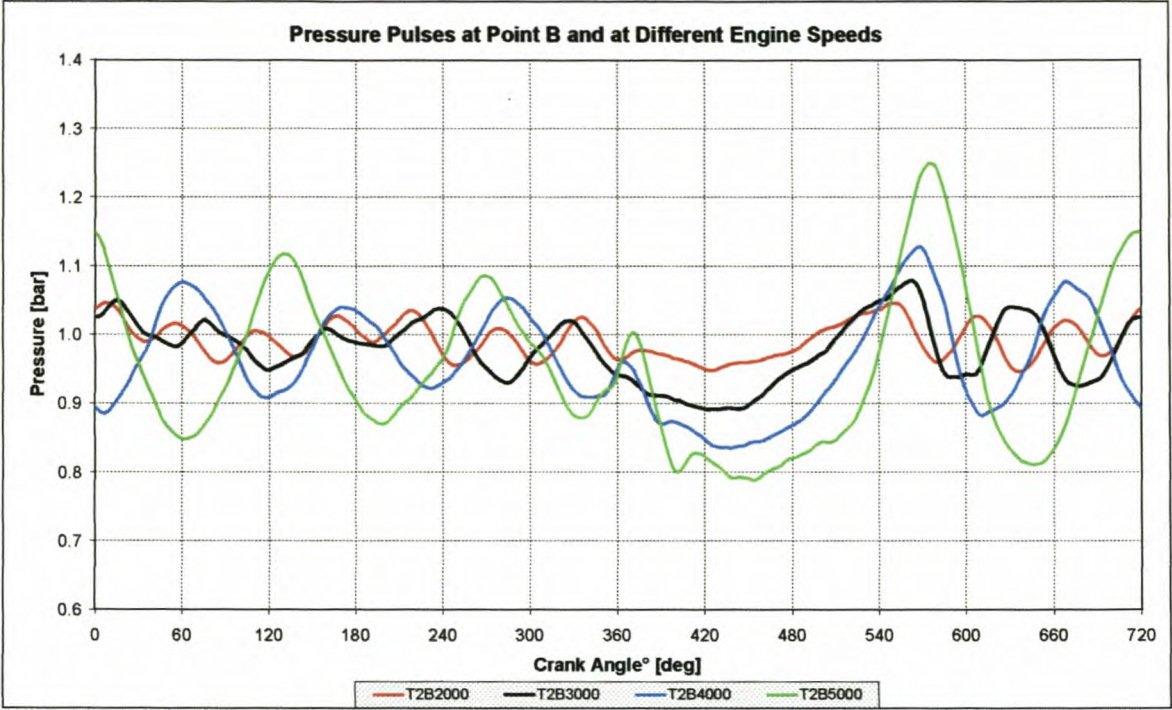


Figure I-11: Pressure pulse data measured at point B at different engine speeds

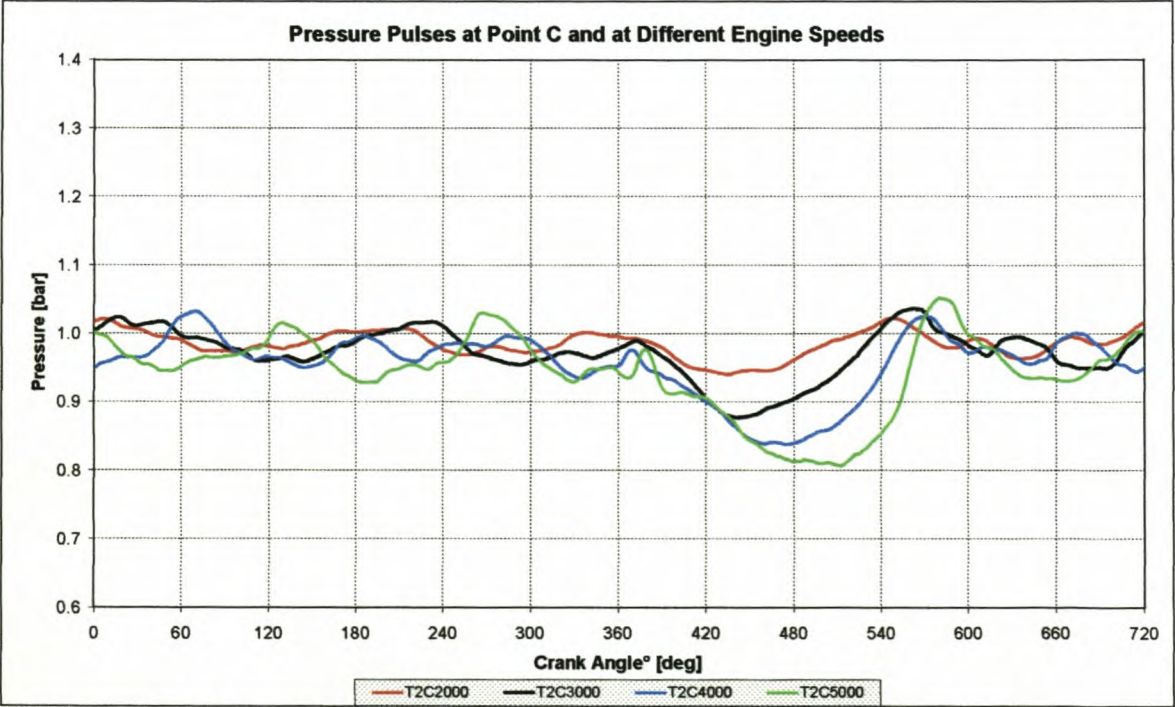


Figure I-12: Pressure pulse data measured at point C at different engine speeds

Appendix I

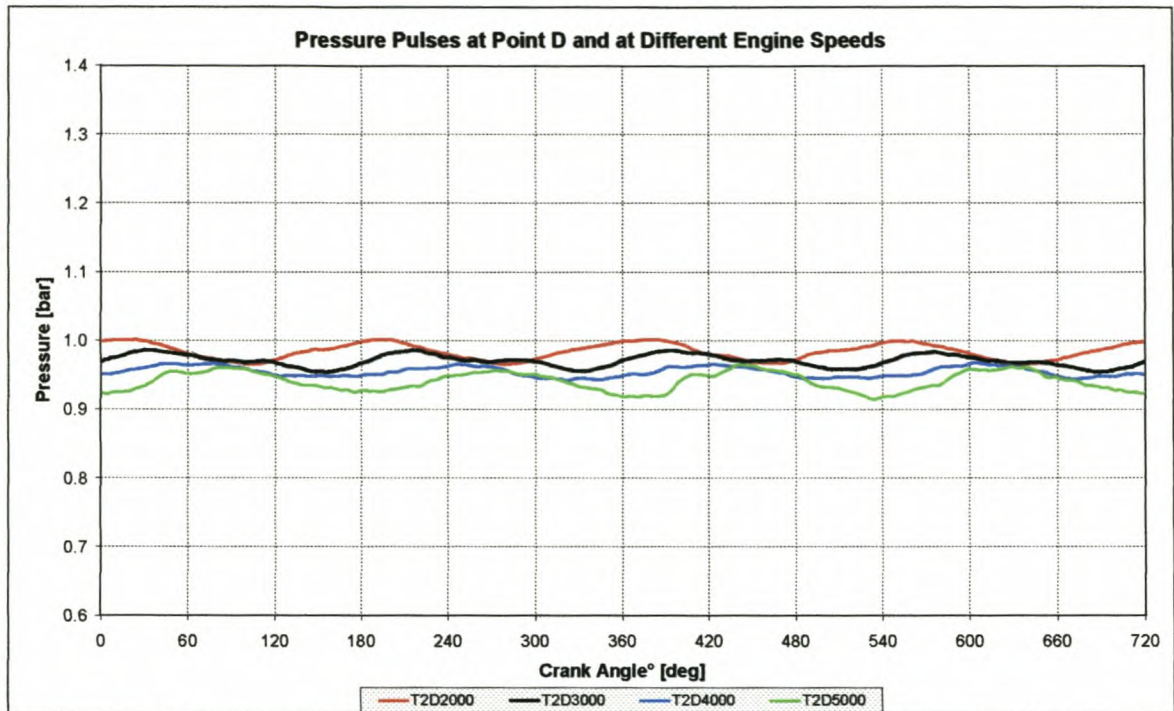


Figure I-13: Pressure pulse data measured at point D at different engine speeds

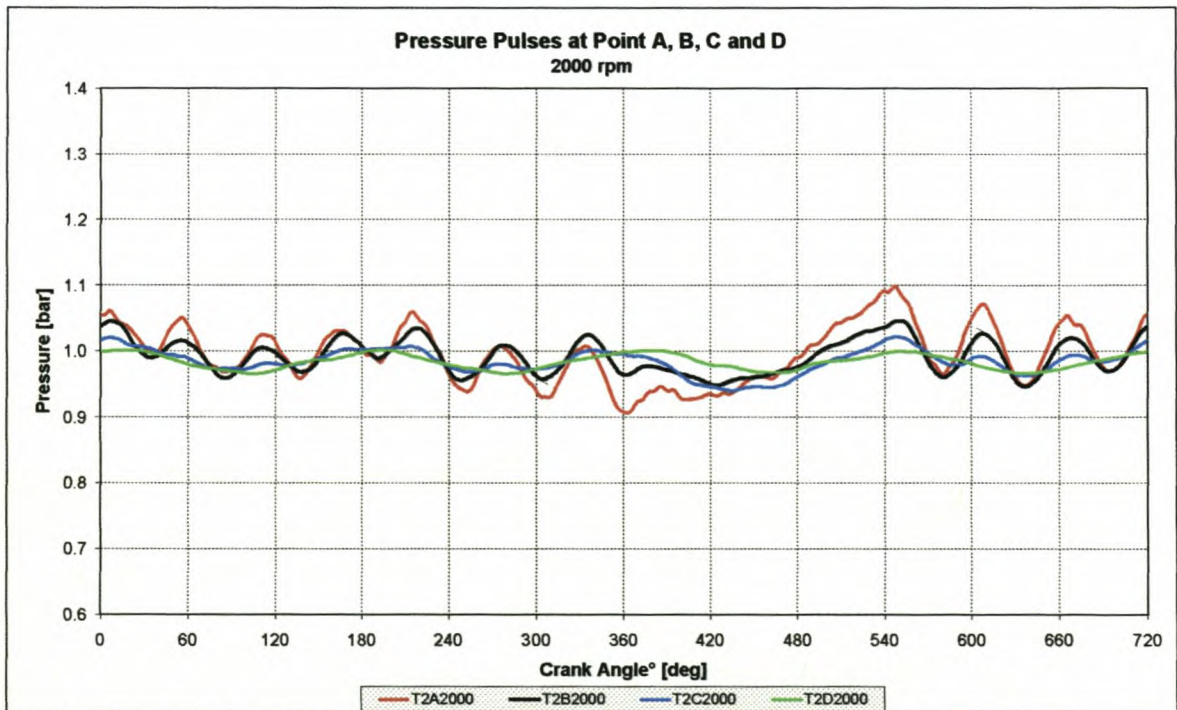


Figure I-14: Pressure pulse data measured at points A, B, C and D @ 2000rpm

Appendix I

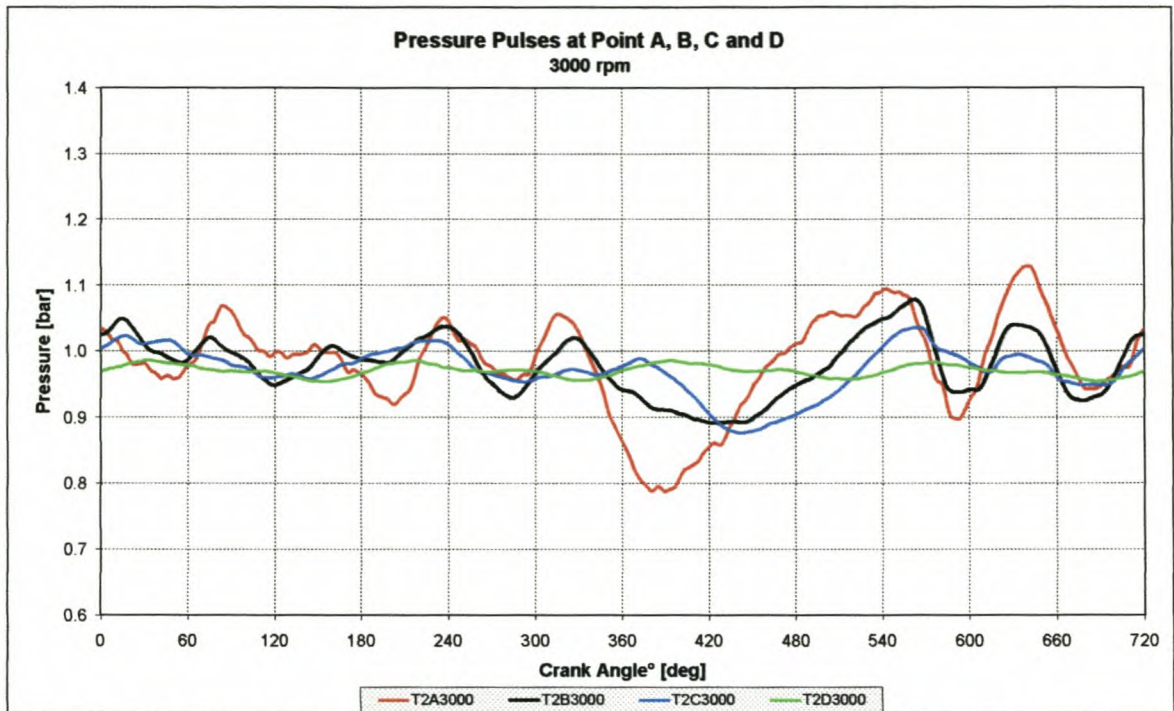


Figure I-15: Pressure pulse data measured at points A, B, C and D @ 3000rpm

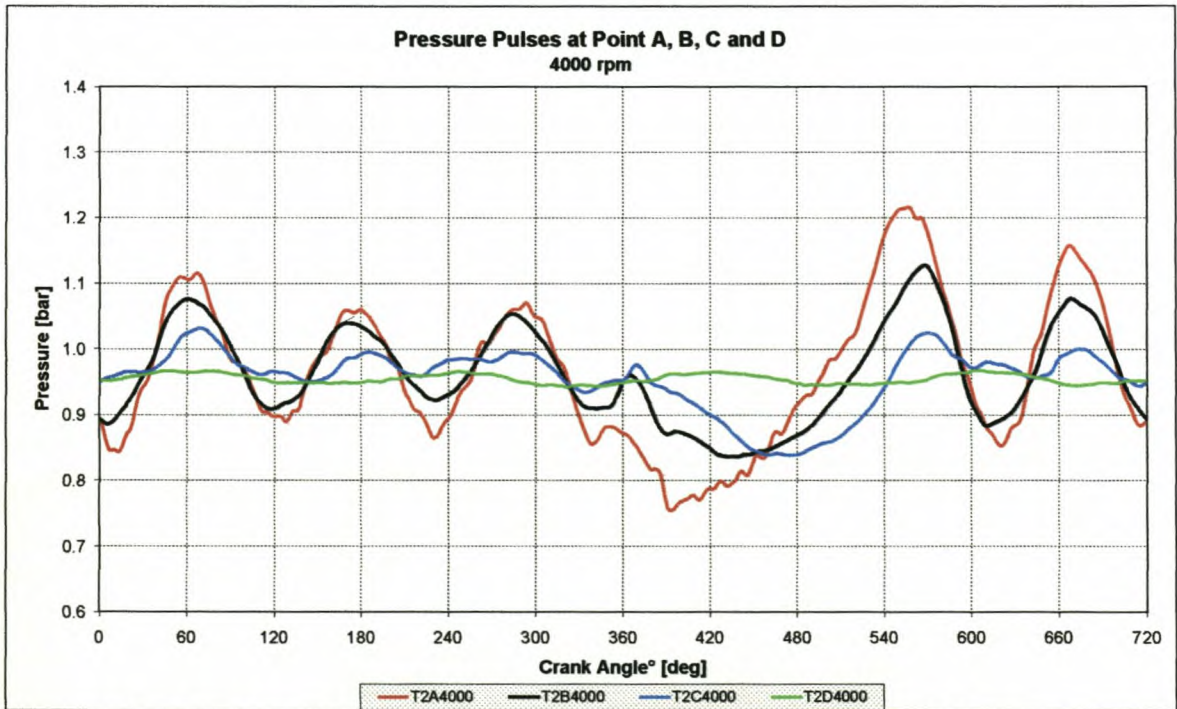


Figure I-16: Pressure pulse data measured at points A, B, C and D @ 4000rpm

Appendix I

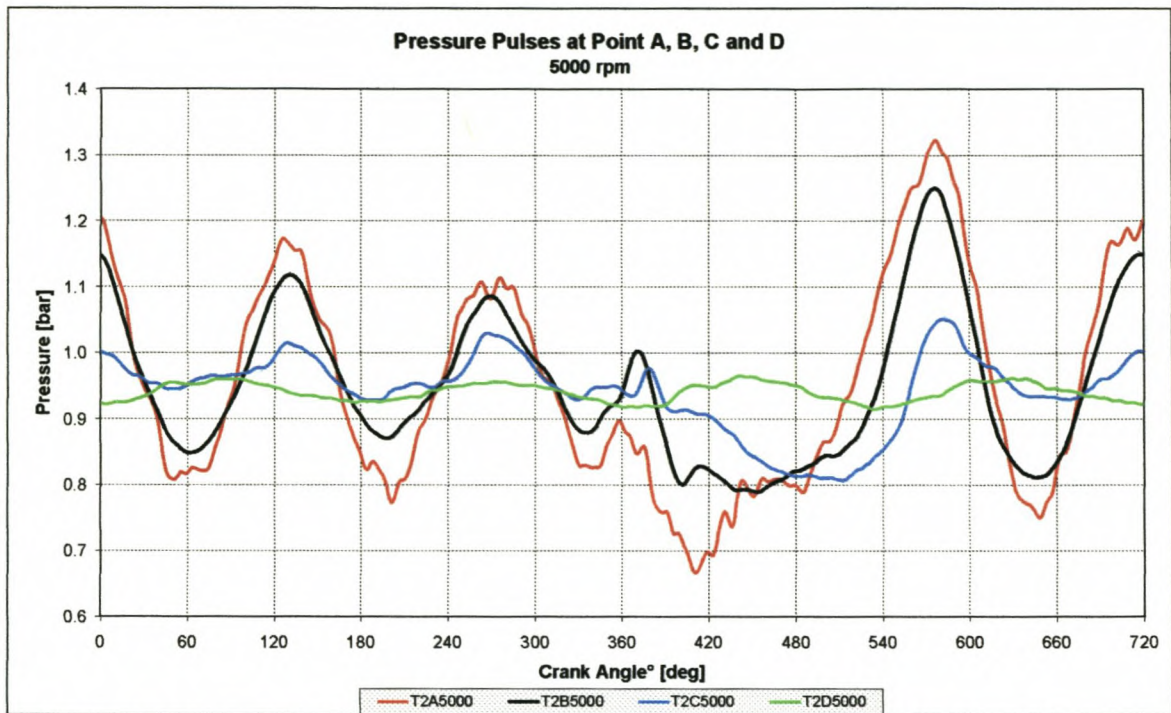


Figure I-17: Pressure pulse data measured at points A, B, C and D @ 5000rpm

I-3: Test 3 engine performance and pressure data

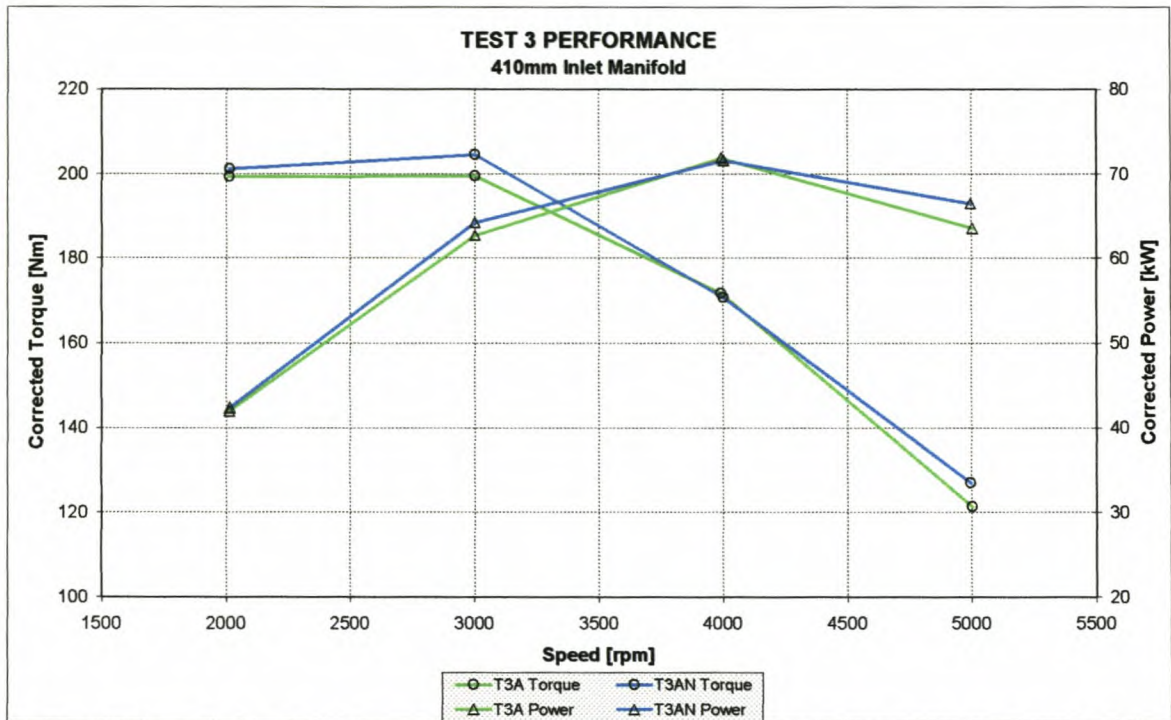


Figure I-18: Test 3 performance on a 410mm inlet manifold with the standard Nissan exhaust (T3A) and modified exhaust system (T3AN)

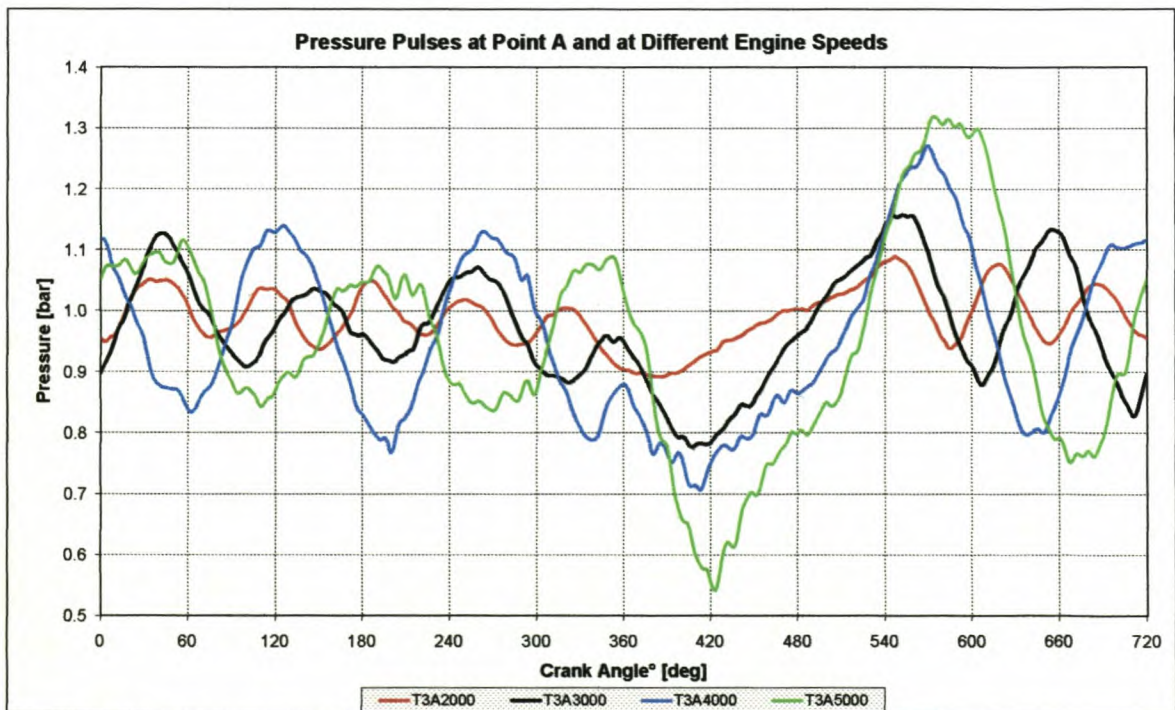


Figure I-19: Pressure pulse data measured at point A at different engine speeds

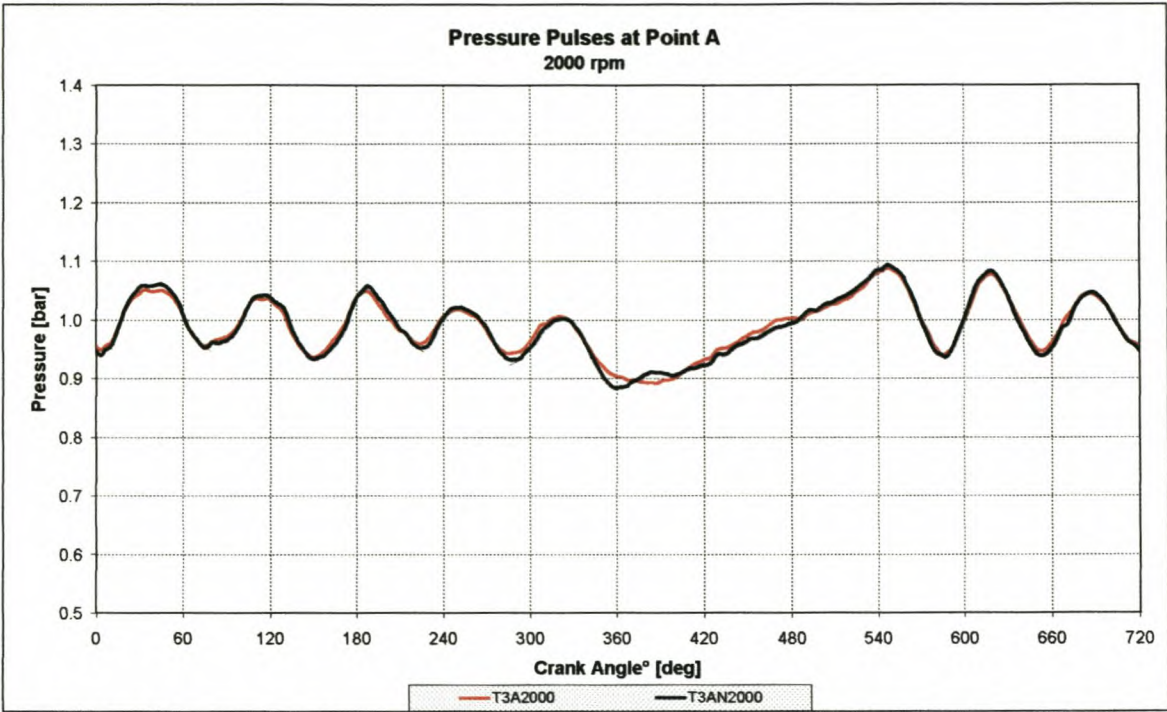


Figure I-20: Pressure pulse data measured at point A on the standard and modified exhaust system @ 2000rpm

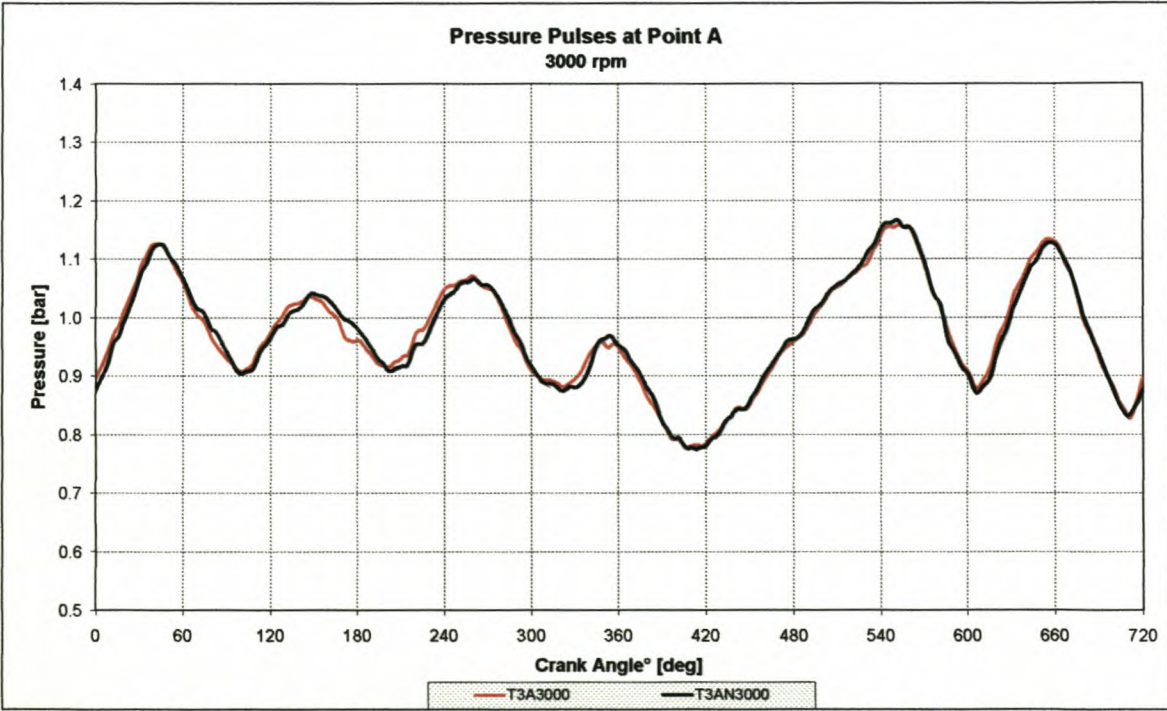


Figure I-21: Pressure pulse data measured at point A on the standard and modified exhaust system @ 3000rpm

Appendix I

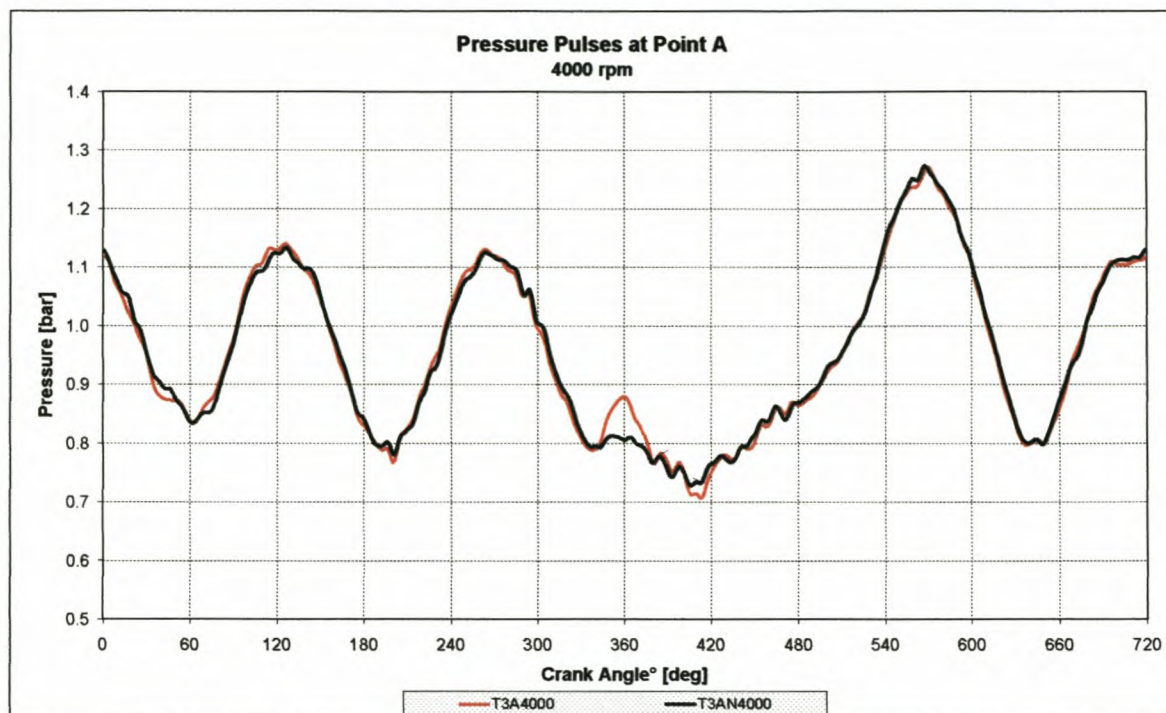


Figure I-22: Pressure pulse data measured at point A on the standard and modified exhaust system @ 4000rpm

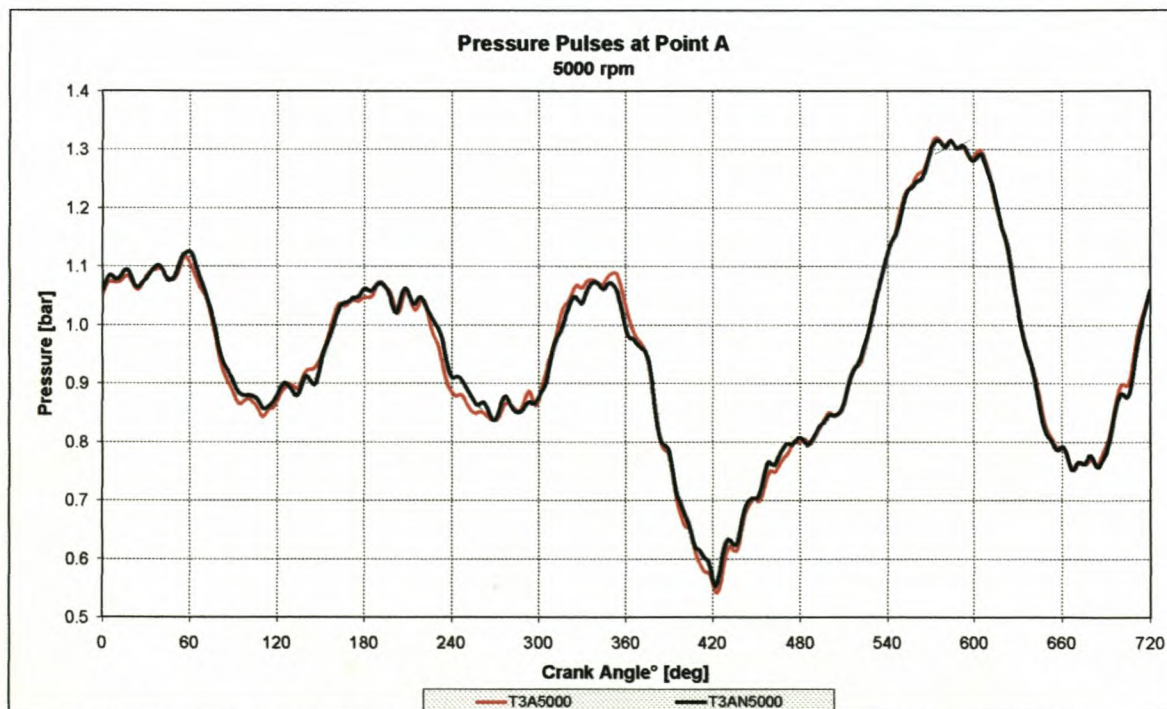


Figure I-23: Pressure pulse data measured at point A on the standard and modified exhaust system @ 5000rpm

I-4: Test 4 engine performance and pressure data, tested vs. modelled

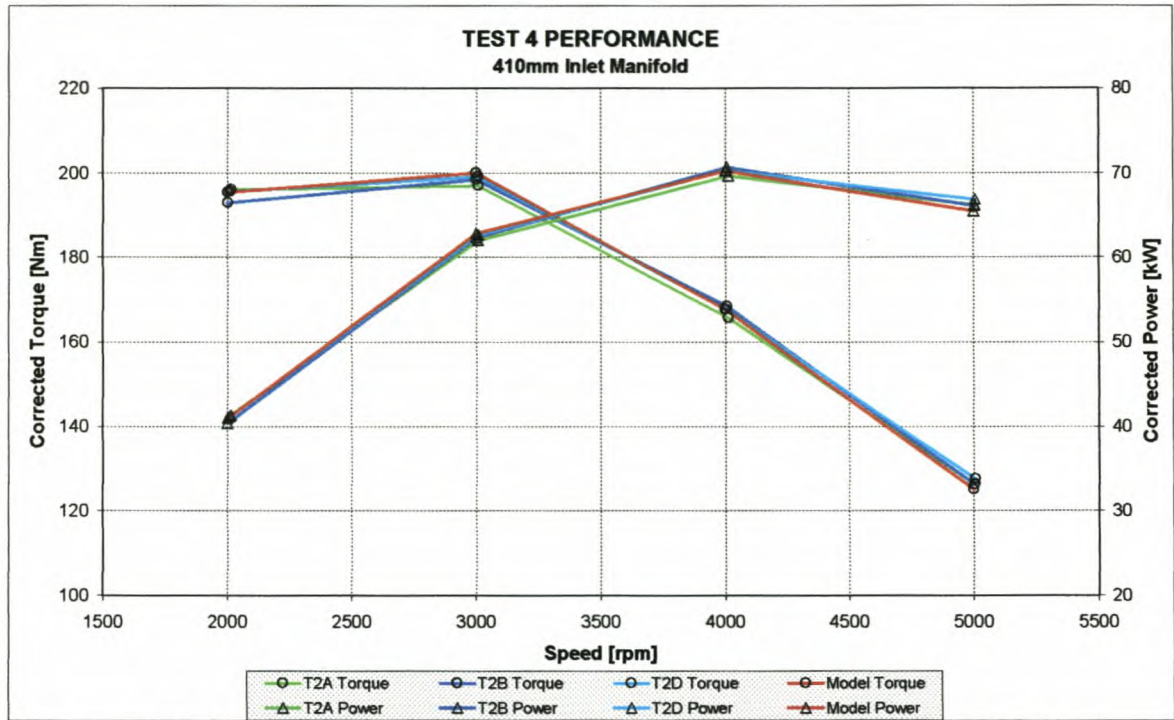


Figure I-24: Test 4 performance on a 410mm inlet manifold, tested vs. modelled

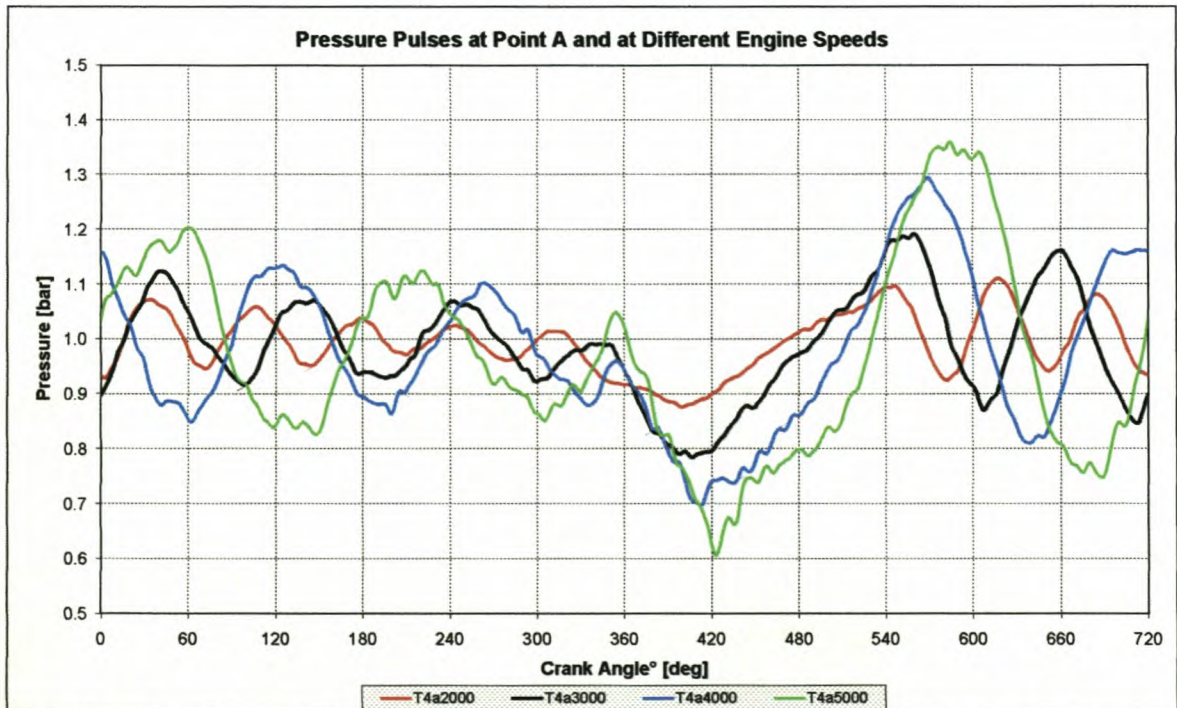


Figure I-25: Pressure pulse data measured at point A at different engine speeds

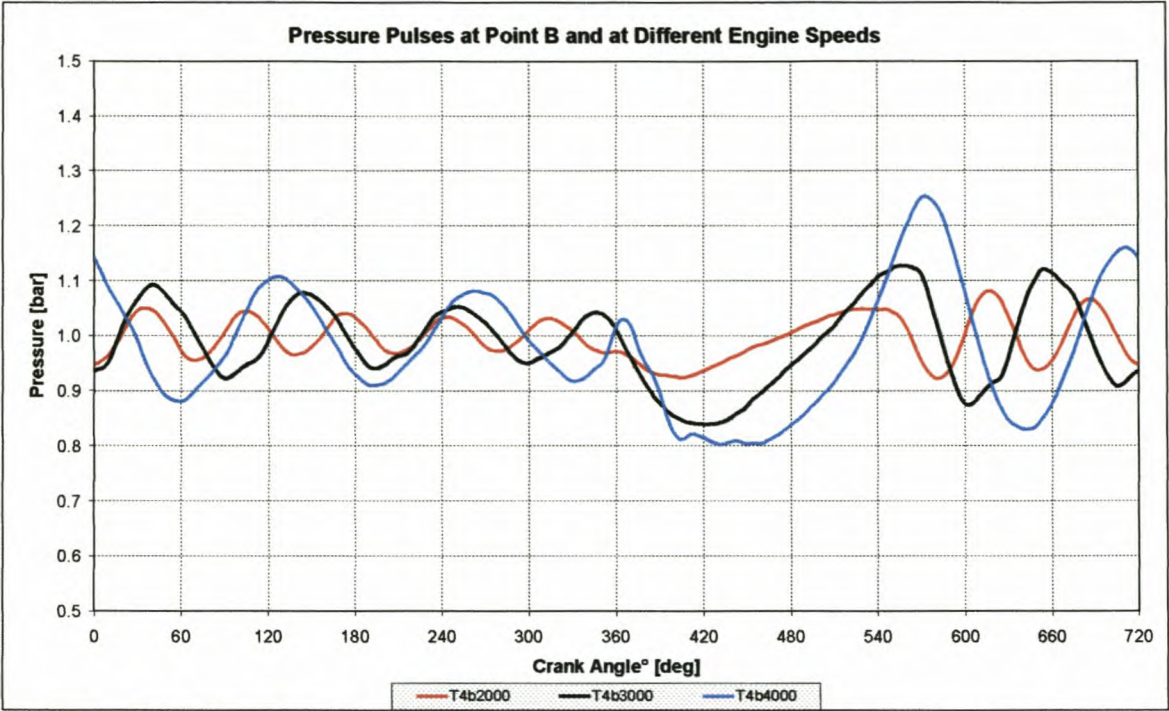


Figure I-26: Pressure pulse data measured at point B at different engine speeds

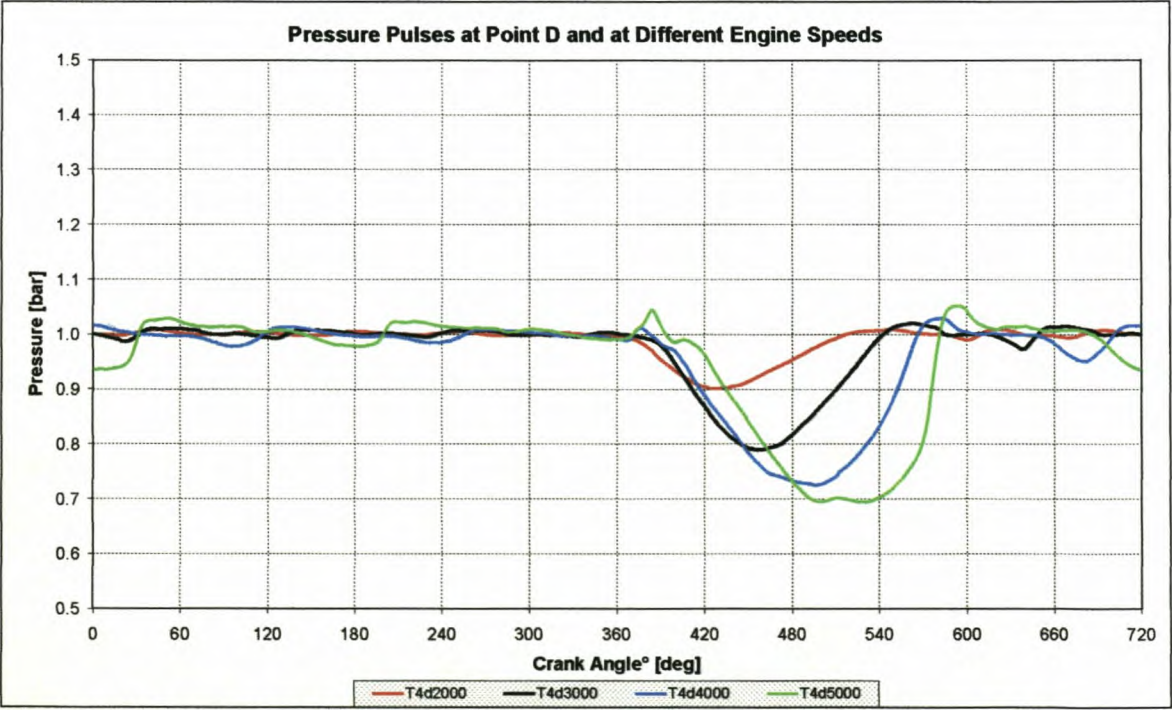


Figure I-27: Pressure pulse data measured at point D at different engine speeds

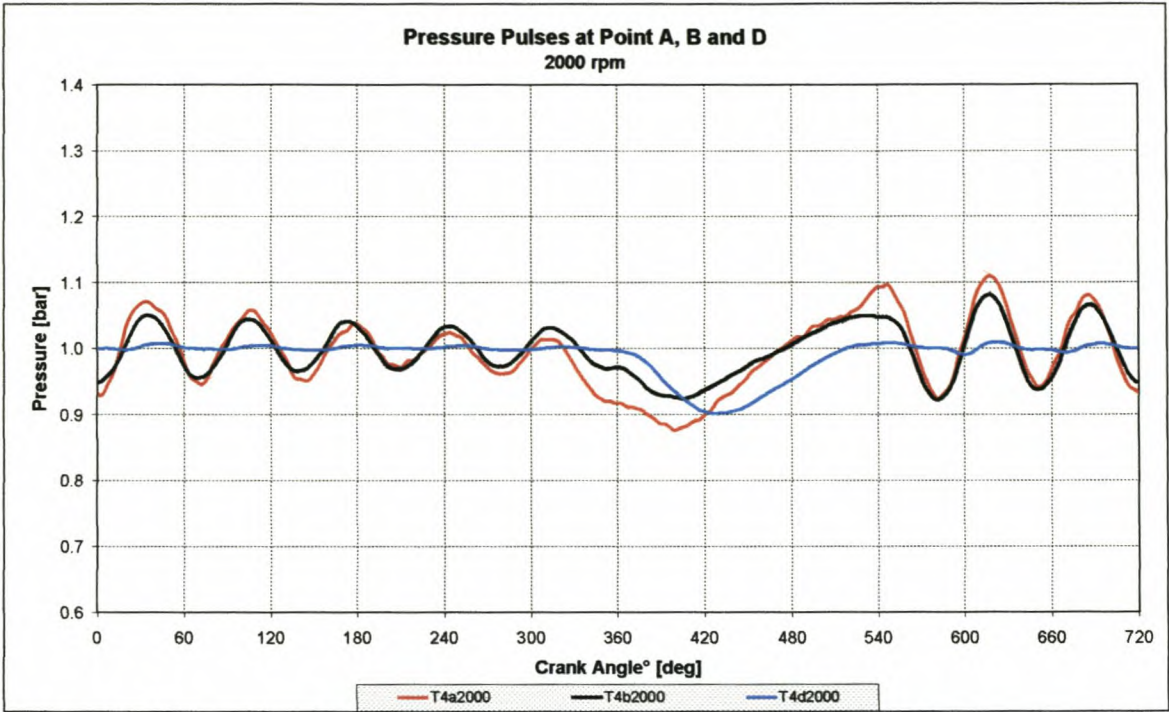


Figure I-28: Pressure pulse data measured at points A, B and D @ 2000rpm

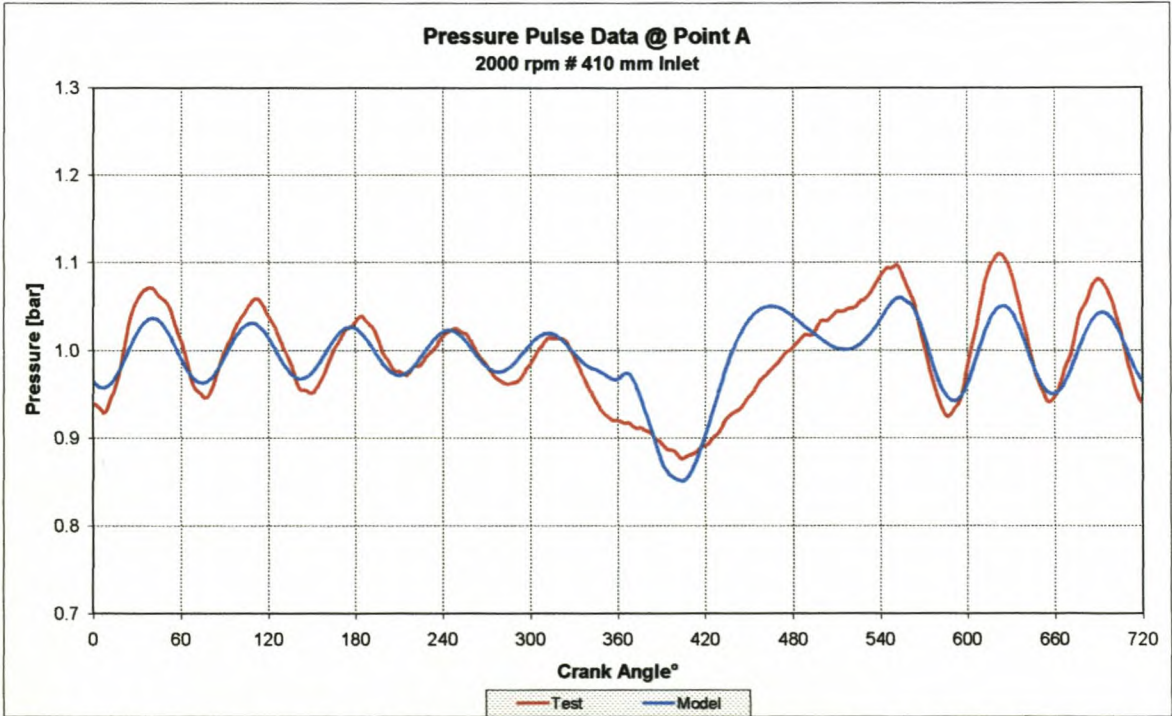


Figure I-29: Measured and modelled pressure pulse data at point A @ 2000rpm

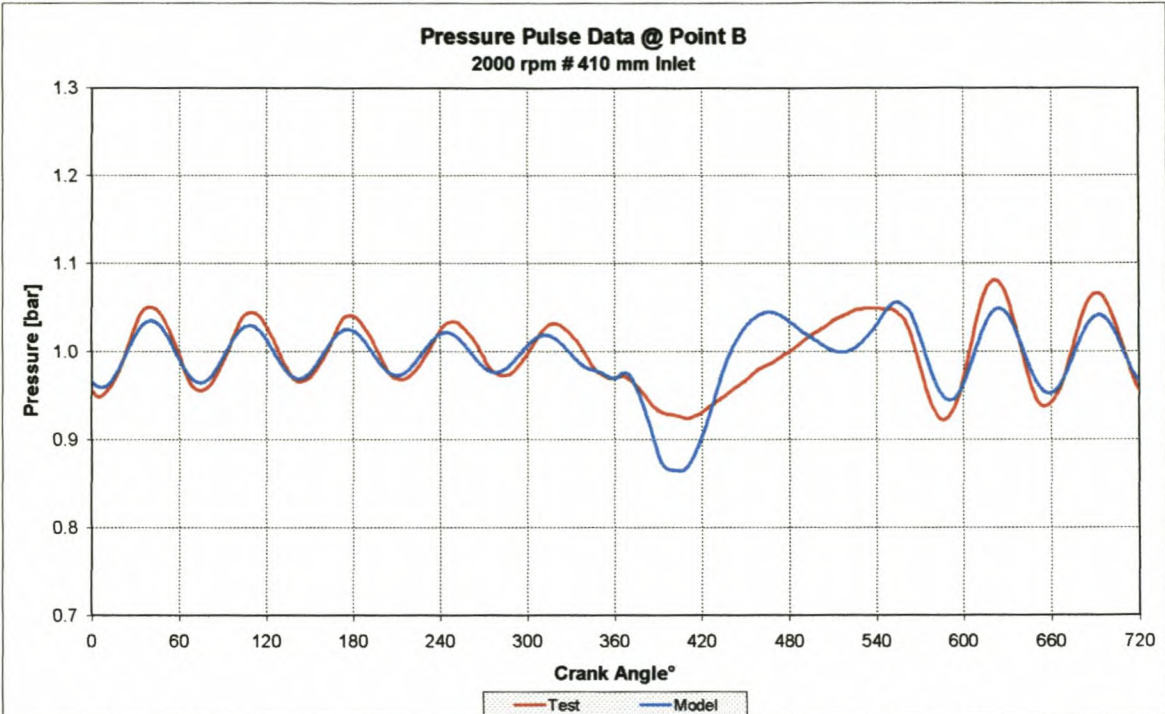


Figure I-30: Measured and modelled pressure pulse data at point B @ 2000rpm

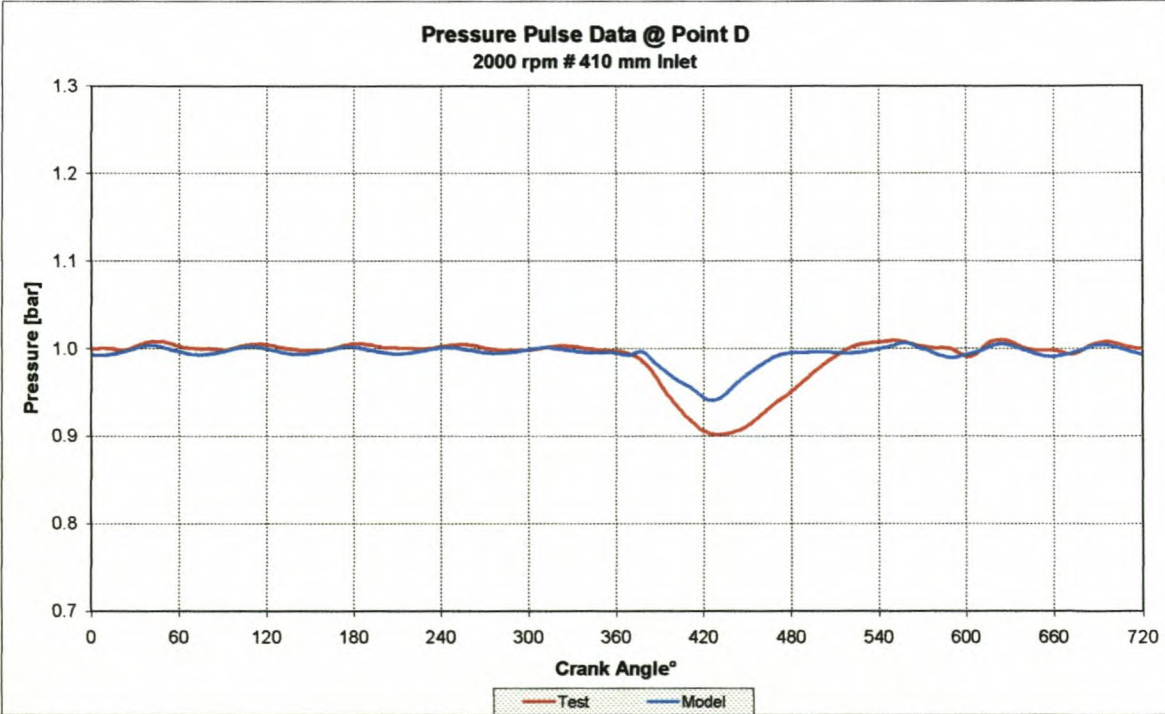


Figure I-31: Measured and modelled pressure pulse data at point D @ 2000rpm

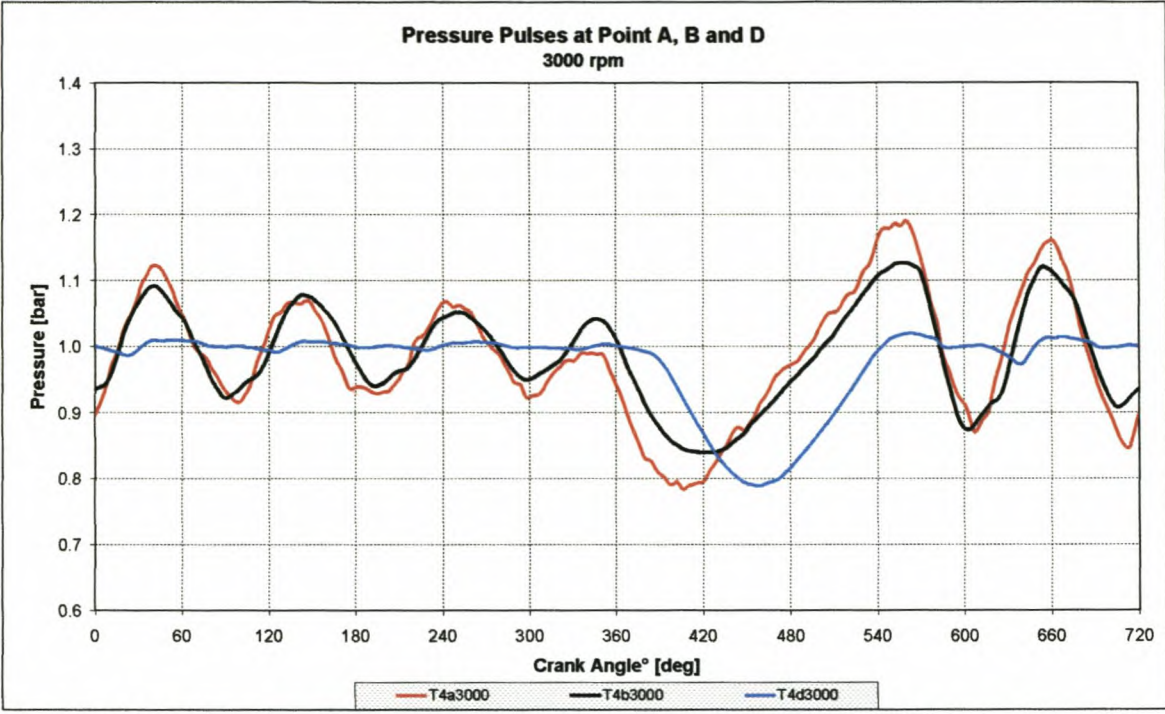


Figure I-32: Pressure pulse data measured at points A, B and D @ 3000rpm

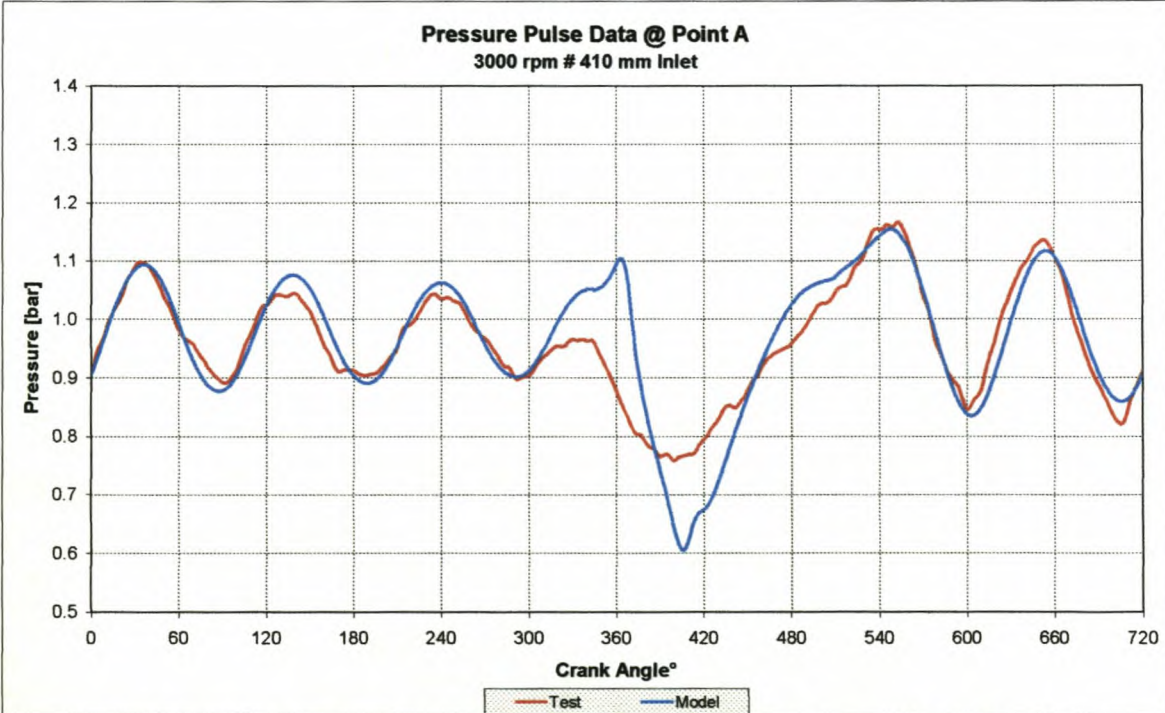


Figure I-33: Measured and modelled pressure pulse data at point A @ 3000rpm

Appendix I

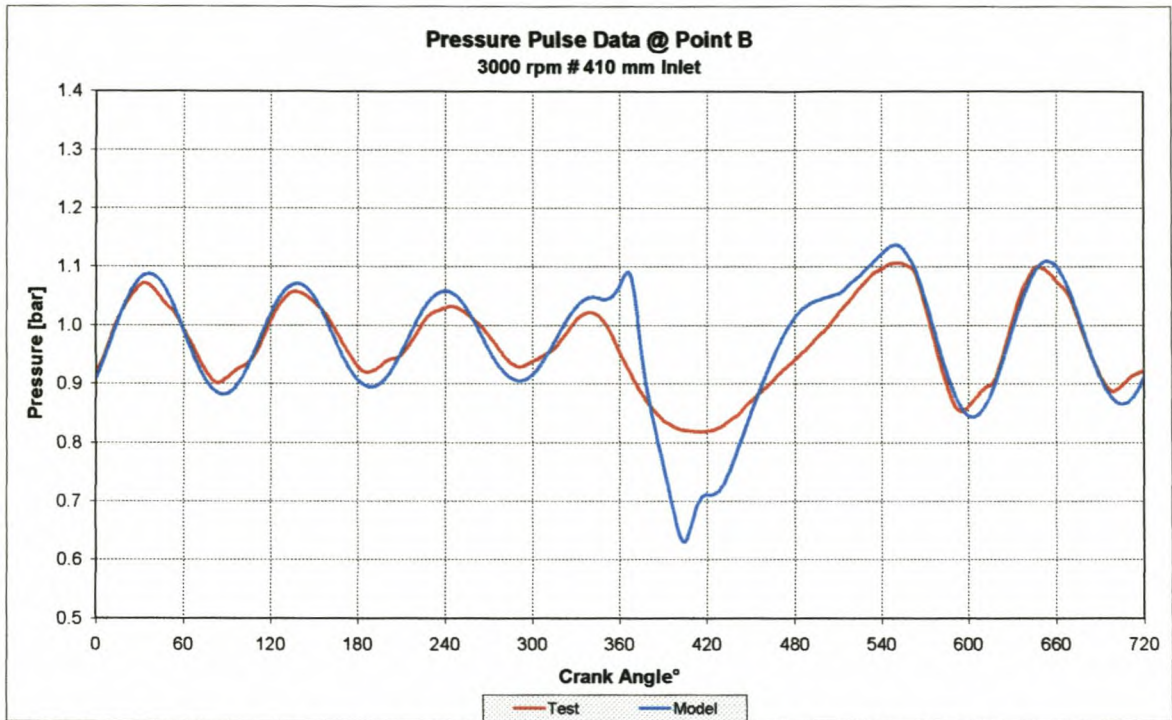


Figure I-34: Measured and modelled pressure pulse data at point B @ 3000rpm

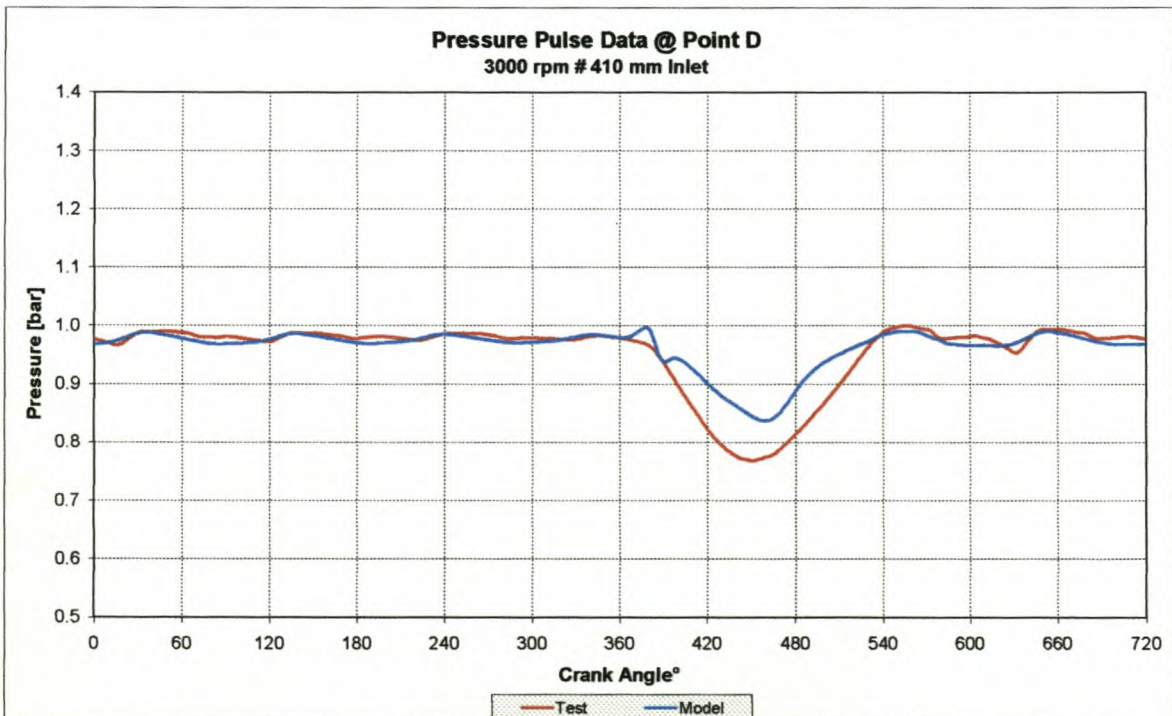


Figure I-35: Measured and modelled pressure pulse data at point D @ 3000rpm

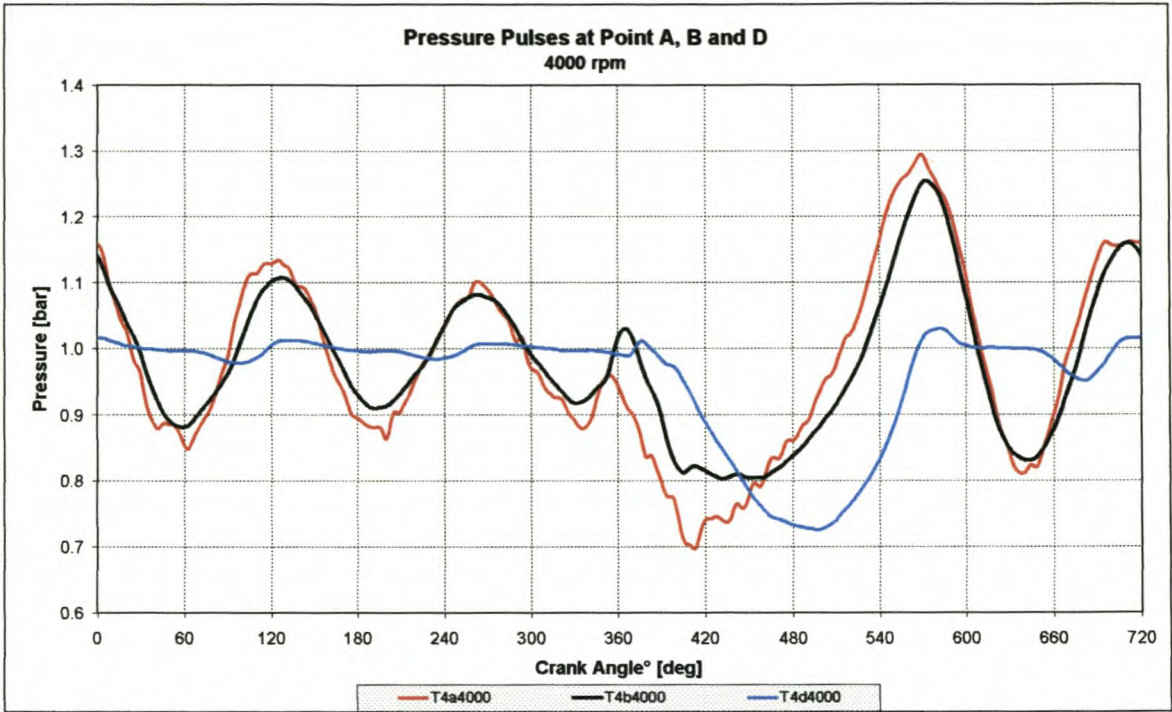


Figure I-36: Pressure pulse data measured at points A, B and D @ 4000rpm

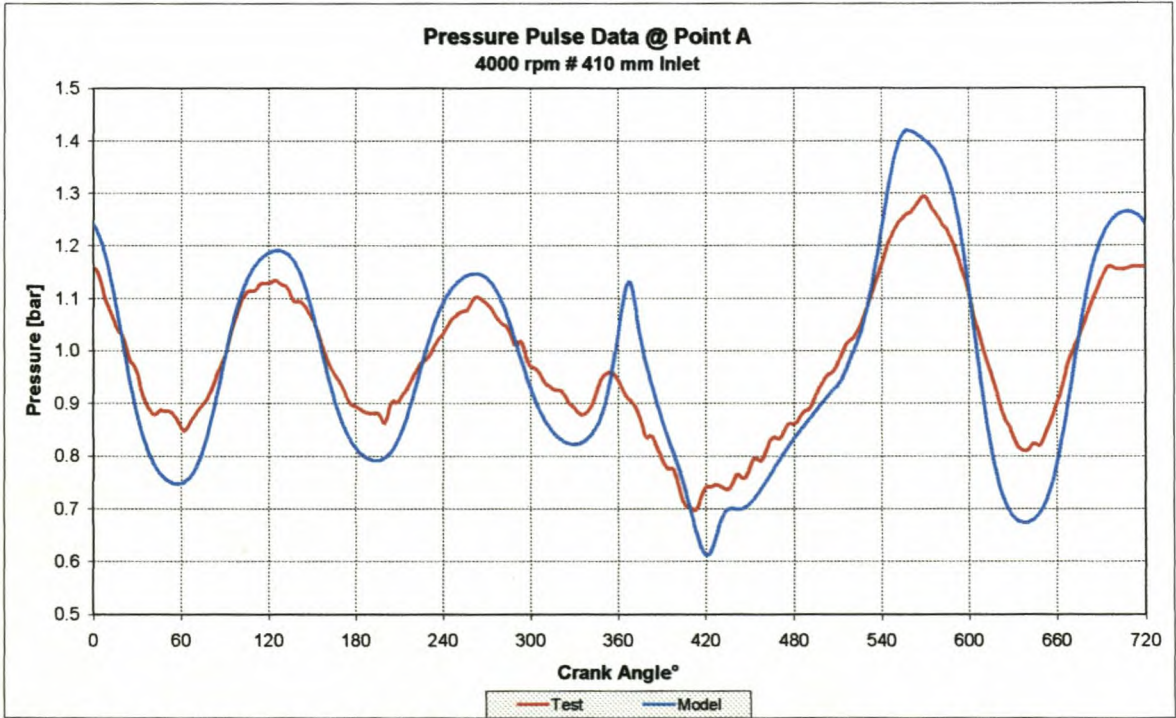


Figure I-37: Measured and modelled pressure pulse data at point A @ 4000rpm

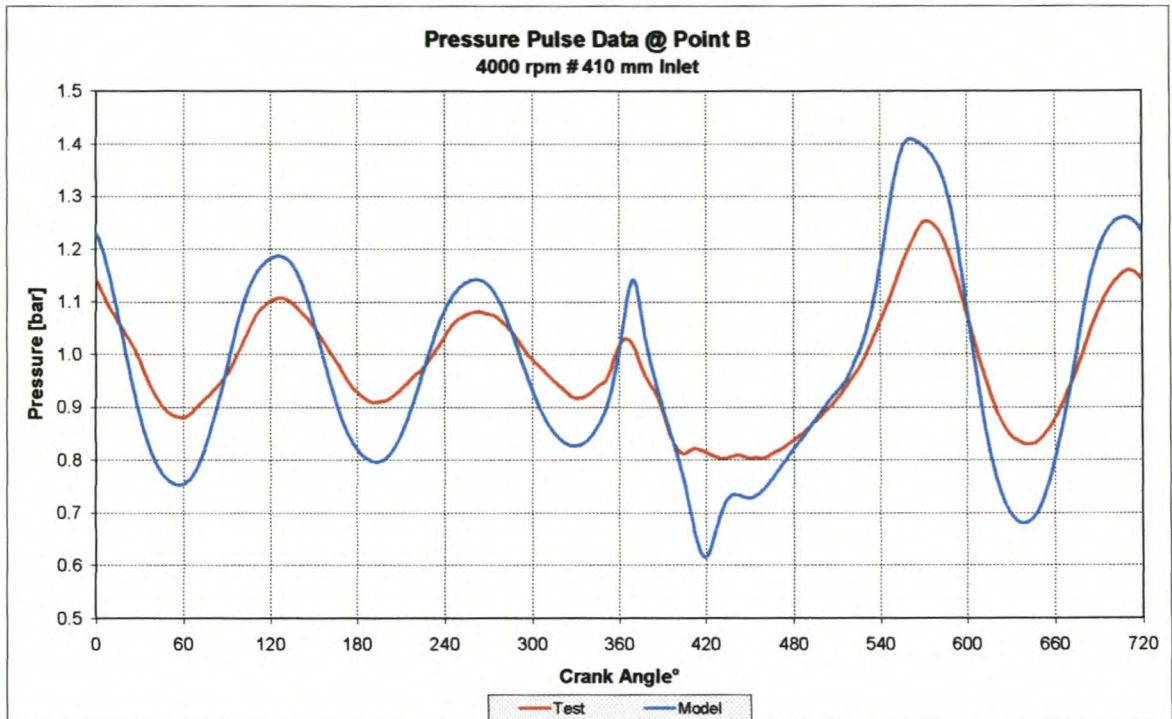


Figure I-38: Measured and modelled pressure pulse data at point B @ 4000rpm

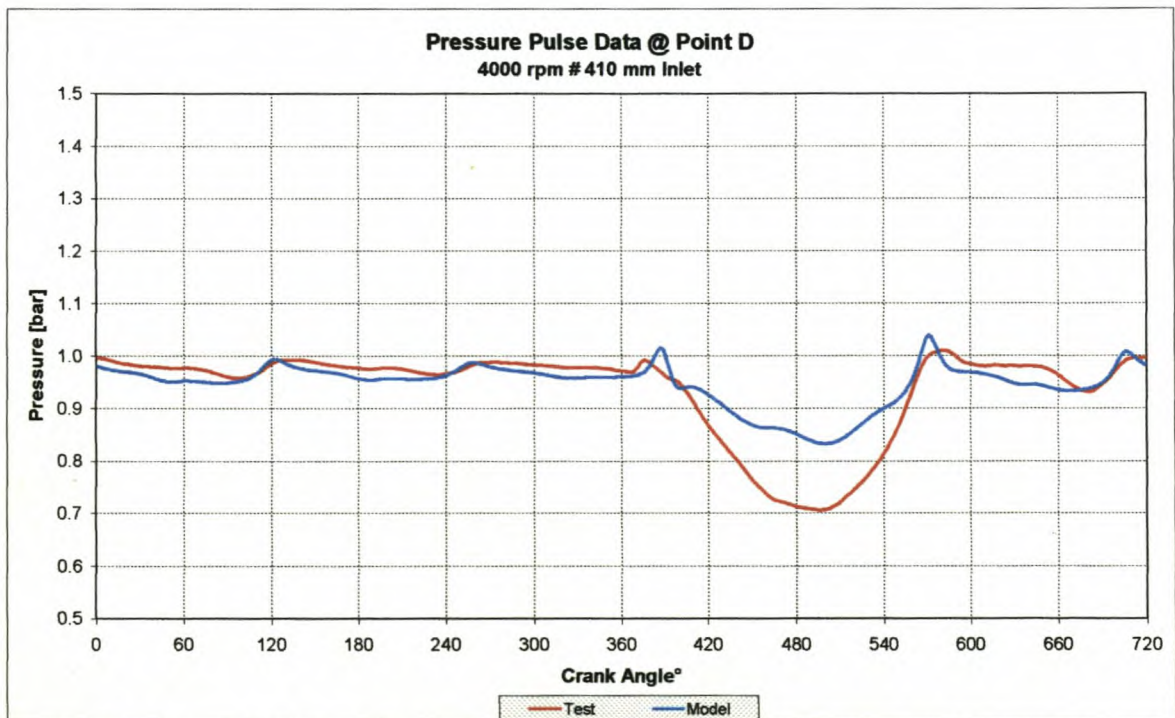


Figure I-39: Measured and modelled pressure pulse data at point D @ 4000rpm

Appendix I

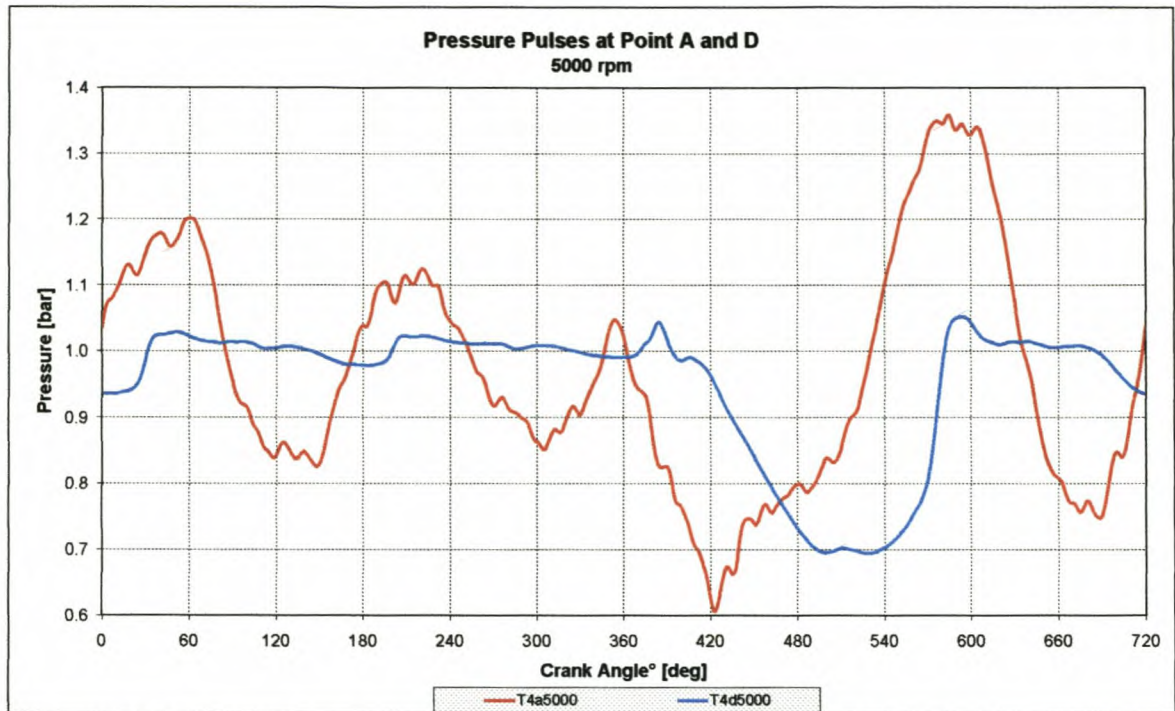


Figure I-40: Pressure pulse data measured at points A and D @ 5000rpm

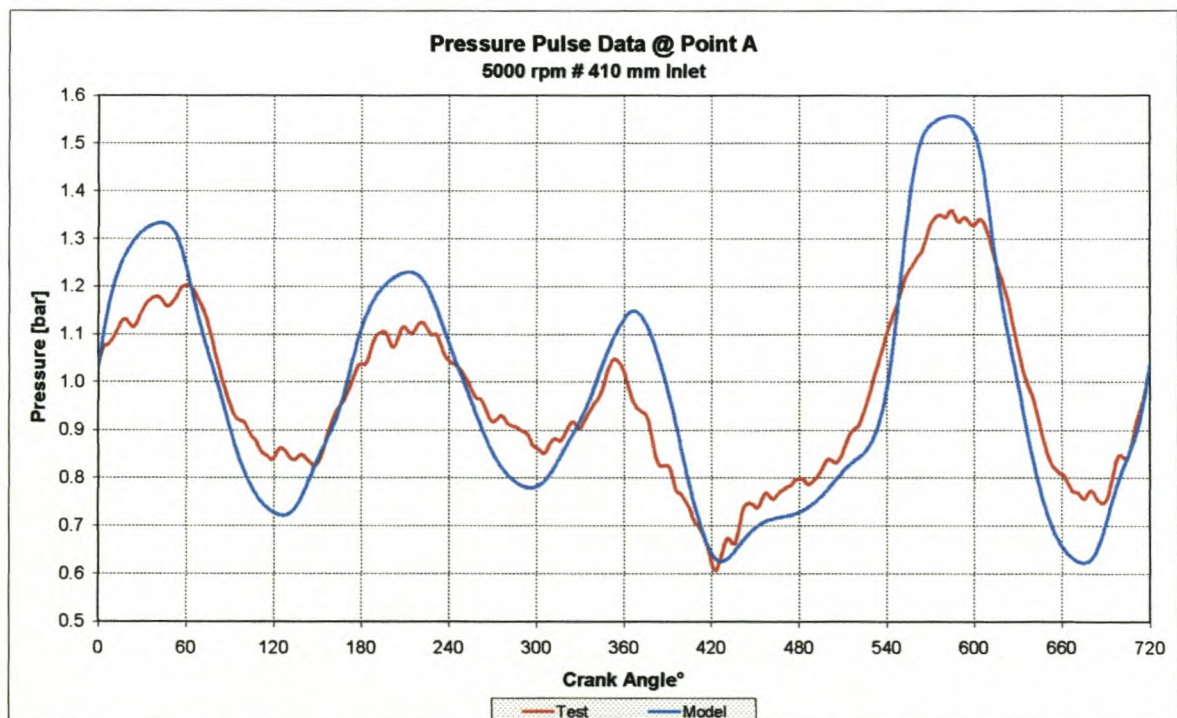


Figure I-41: Measured and modelled pressure pulse data at point A @ 5000rpm

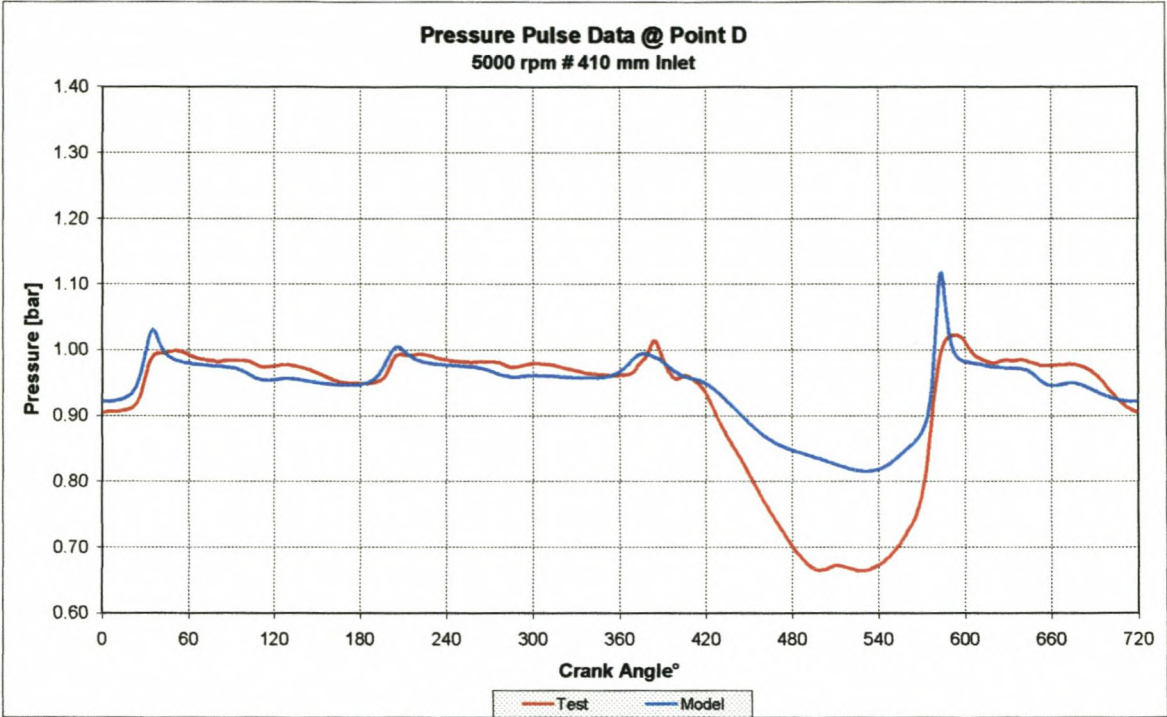


Figure I-42: Measured and modelled pressure pulse data at point D @ 5000rpm

I-5: Test 5 engine performance and pressure data, tested vs. modelled

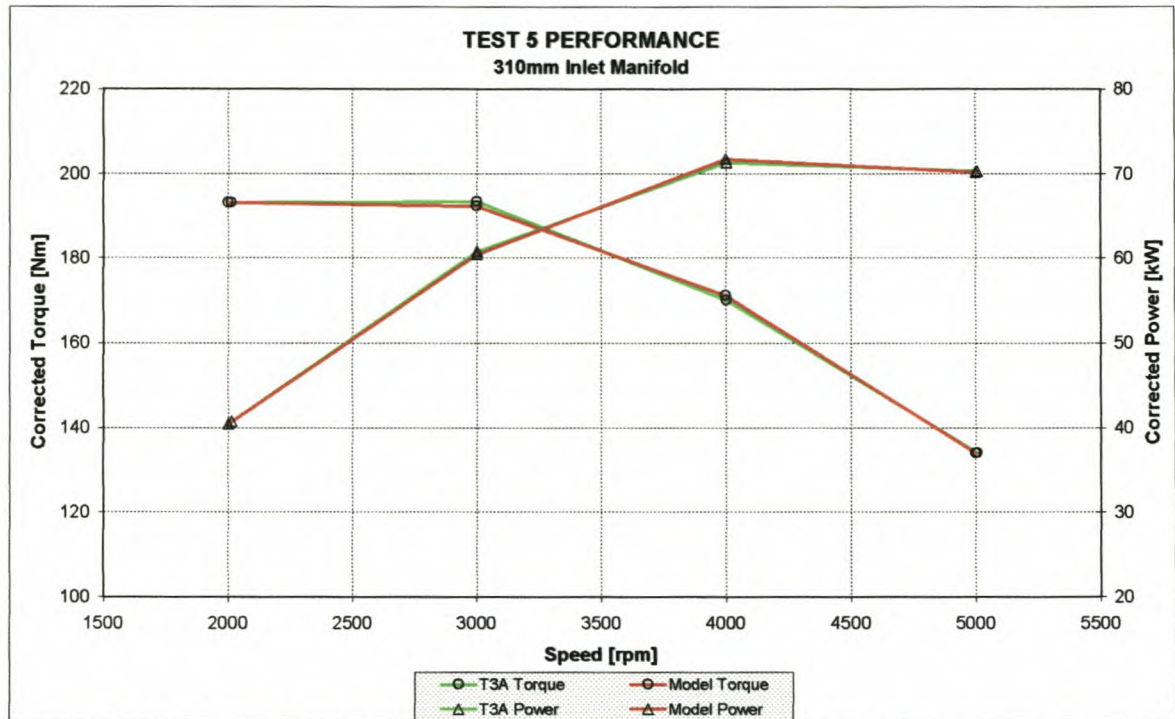


Figure I-43: Test 5 performance on a 310mm inlet manifold, tested vs. modelled

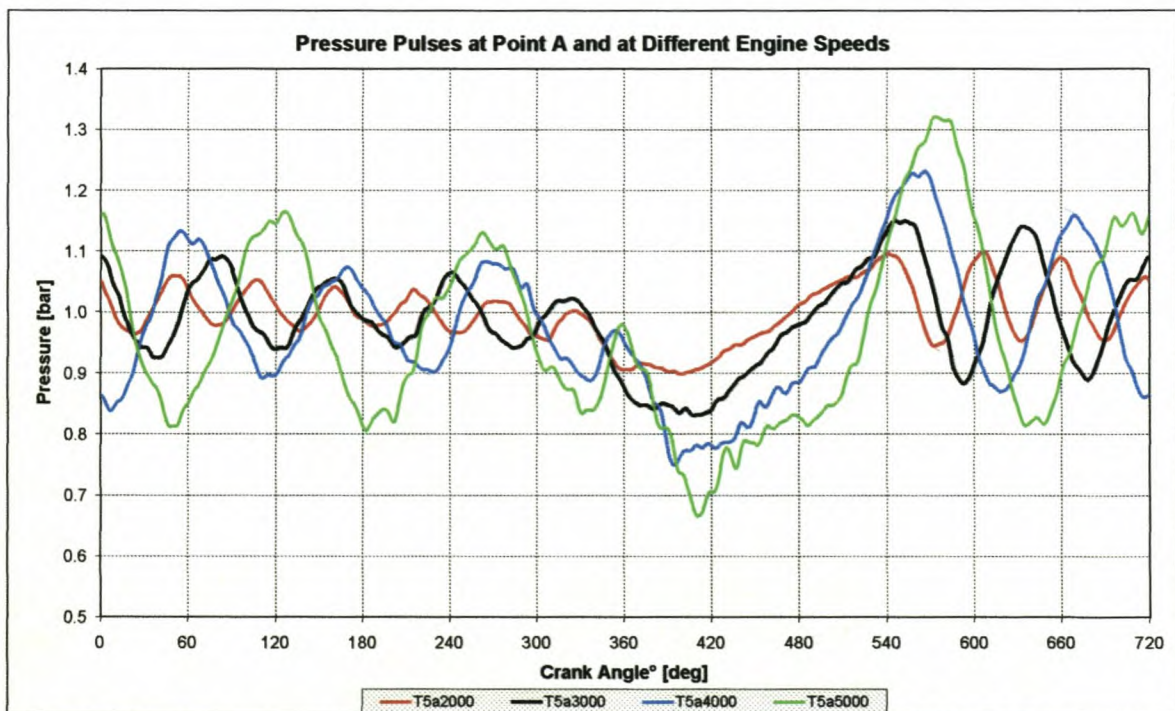


Figure I-44: Pressure pulse data measured at point A at different engine speeds

Appendix I

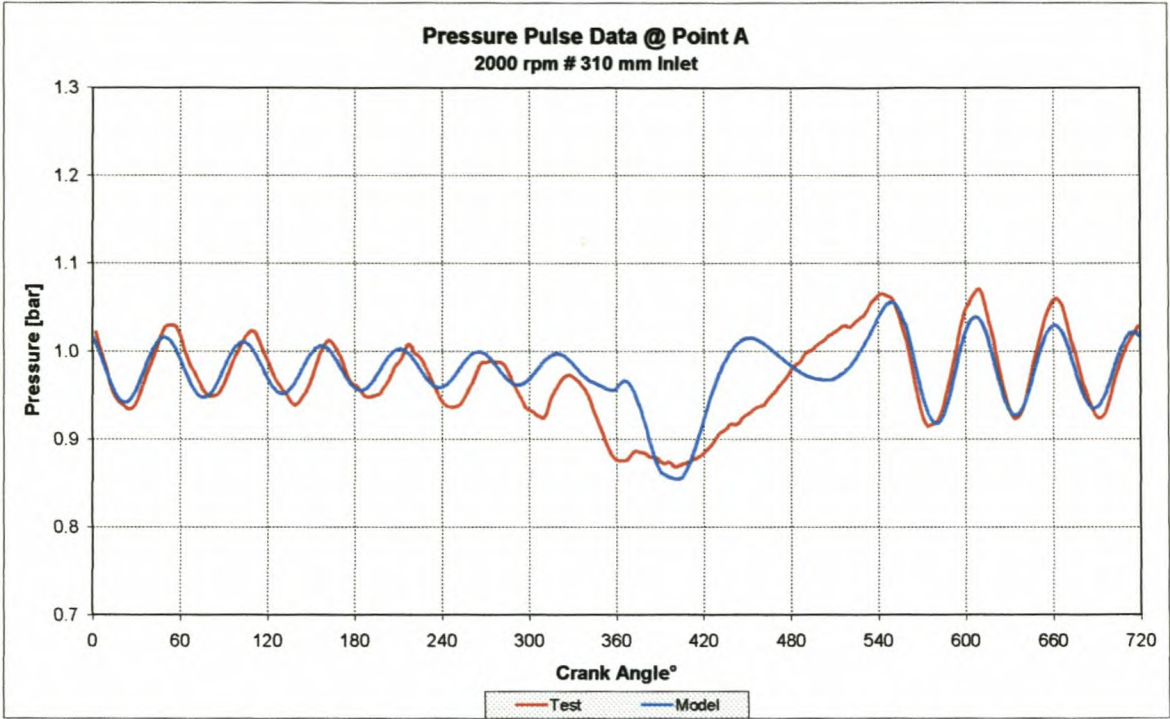


Figure I-45: Measured and modelled pressure pulse data at point A @ 2000rpm

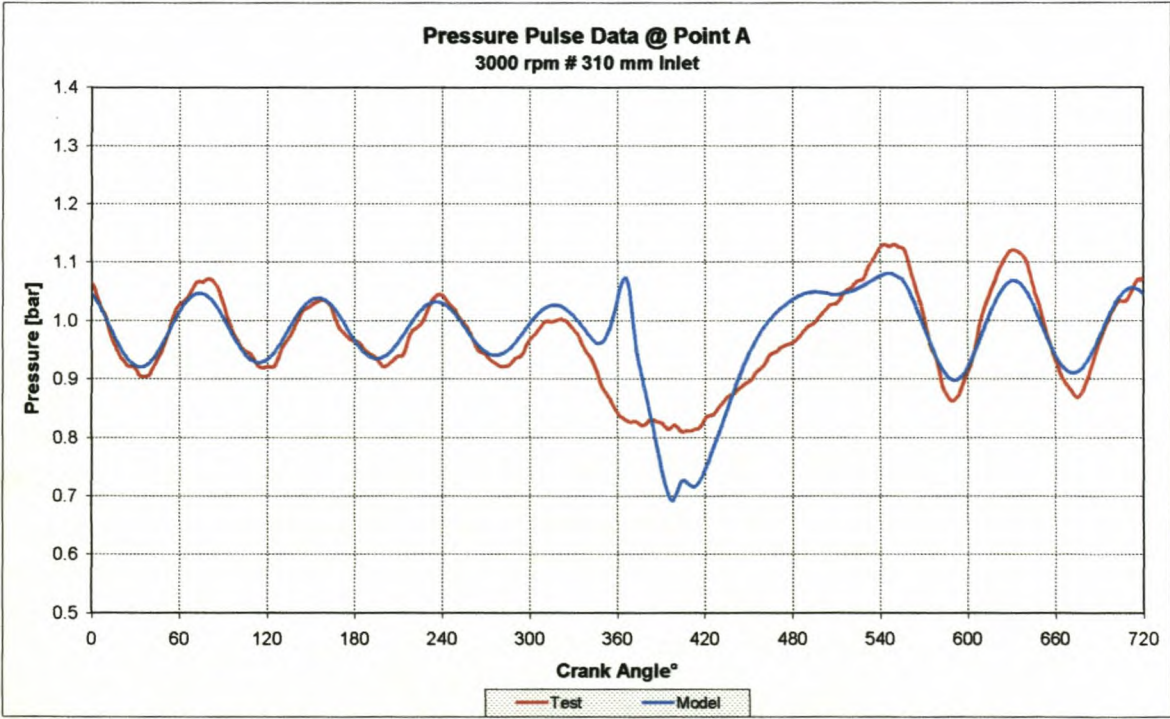


Figure I-46: Measured and modelled pressure pulse data at point A @ 3000rpm

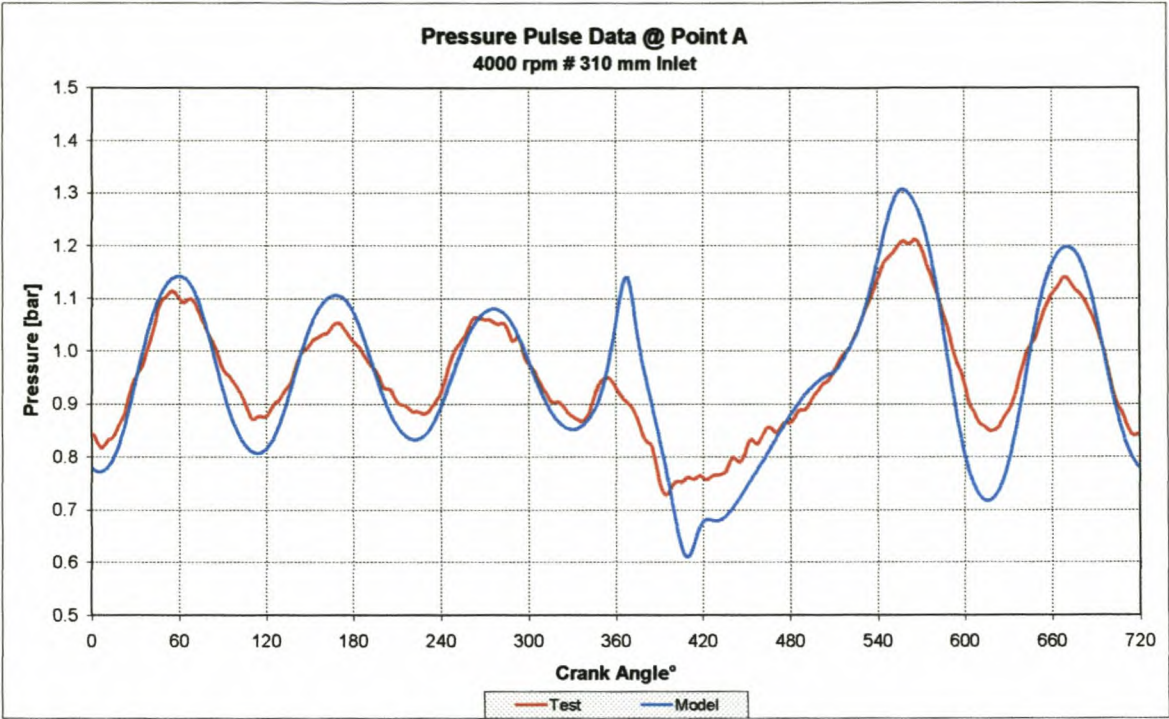


Figure I-47: Measured and modelled pressure pulse data at point A @ 4000rpm

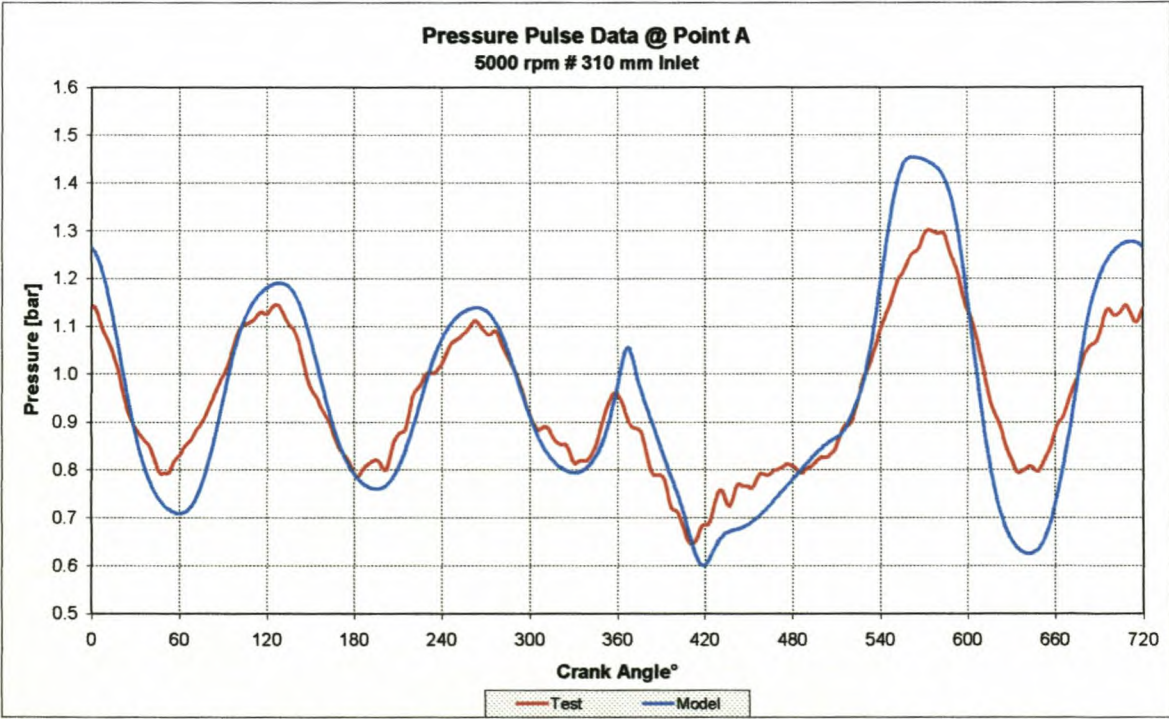


Figure I-48: Measured and modelled pressure pulse data at point A @ 5000rpm

I-6: Test 6 engine performance and pressure data, tested vs. modelled



Figure I-49: Test 6 performance on a 210mm inlet manifold, tested vs. modelled

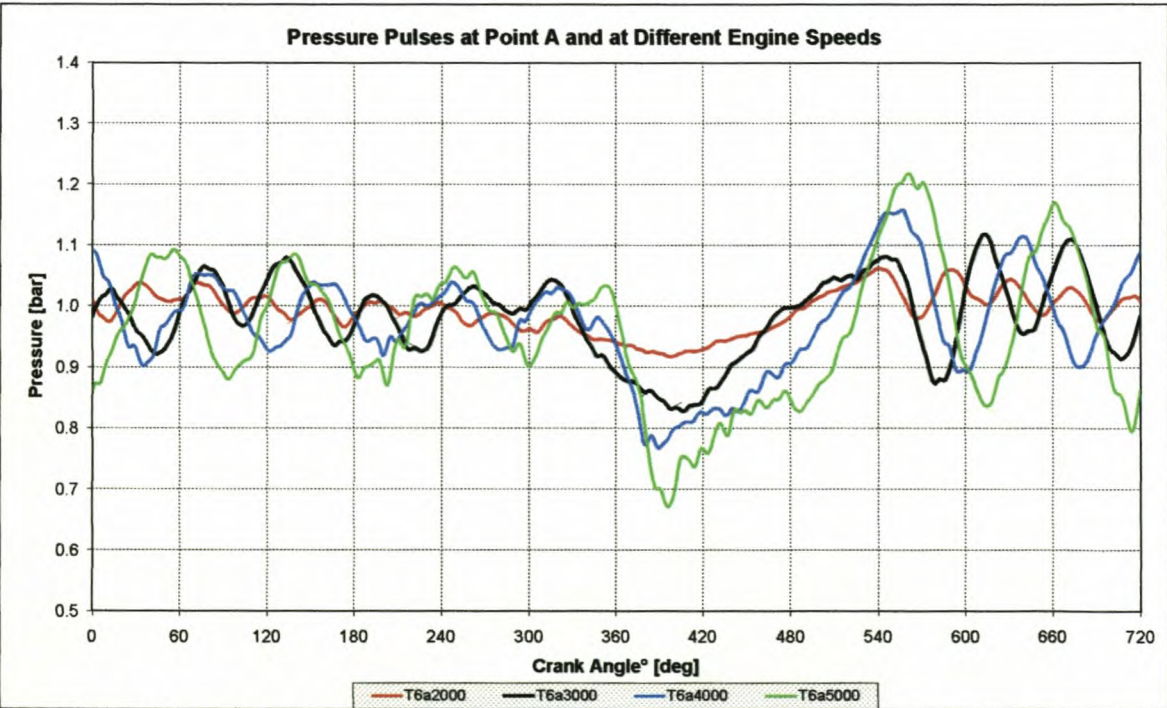


Figure I-50: Pressure pulse data measured at point A at different engine speeds

Appendix I

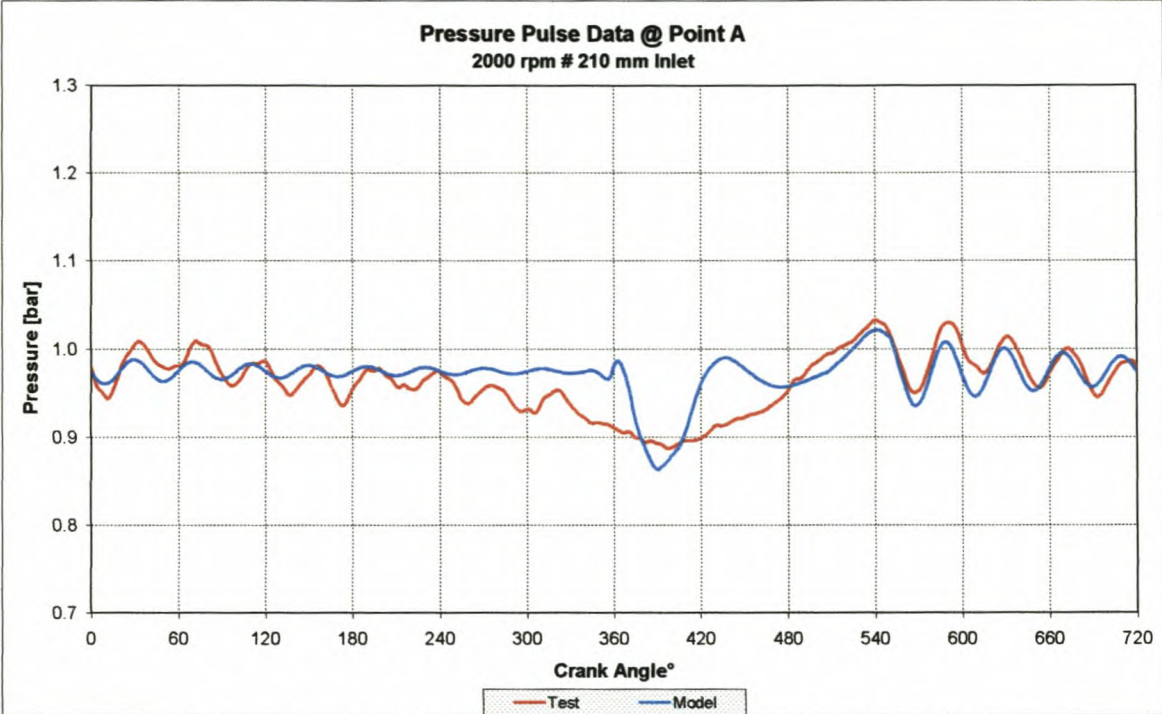


Figure I-51: Measured and modelled pressure pulse data at point A @ 2000rpm

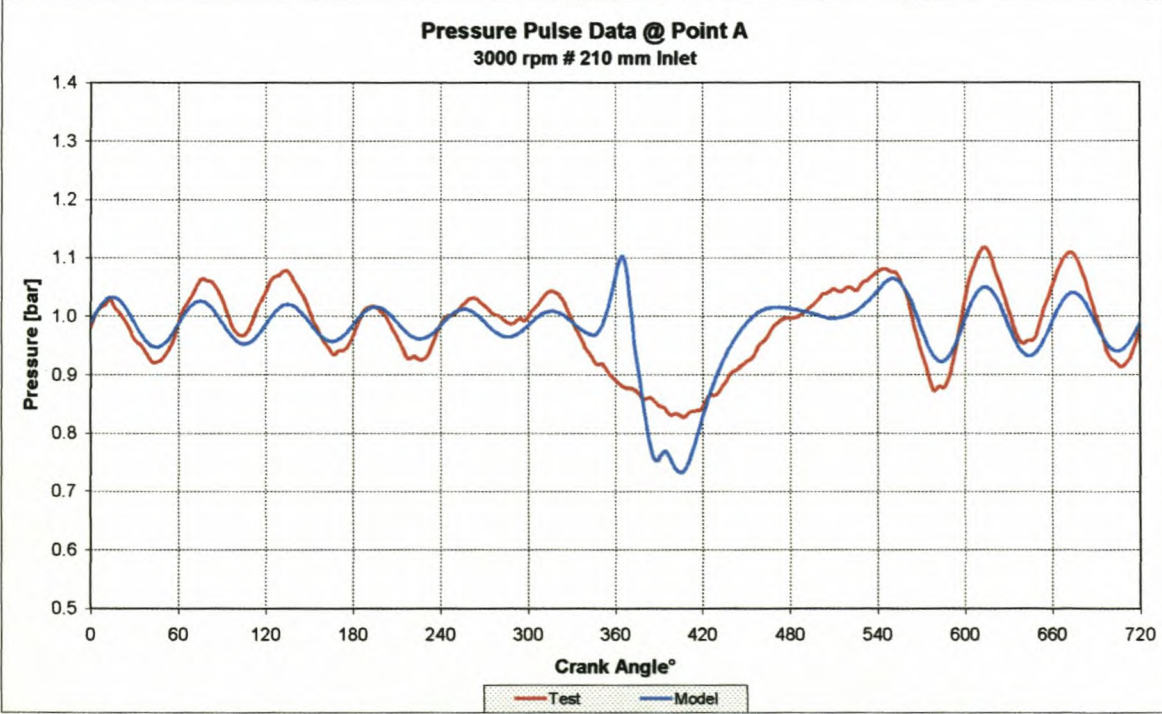


Figure I-52: Measured and modelled pressure pulse data at point A @ 3000rpm

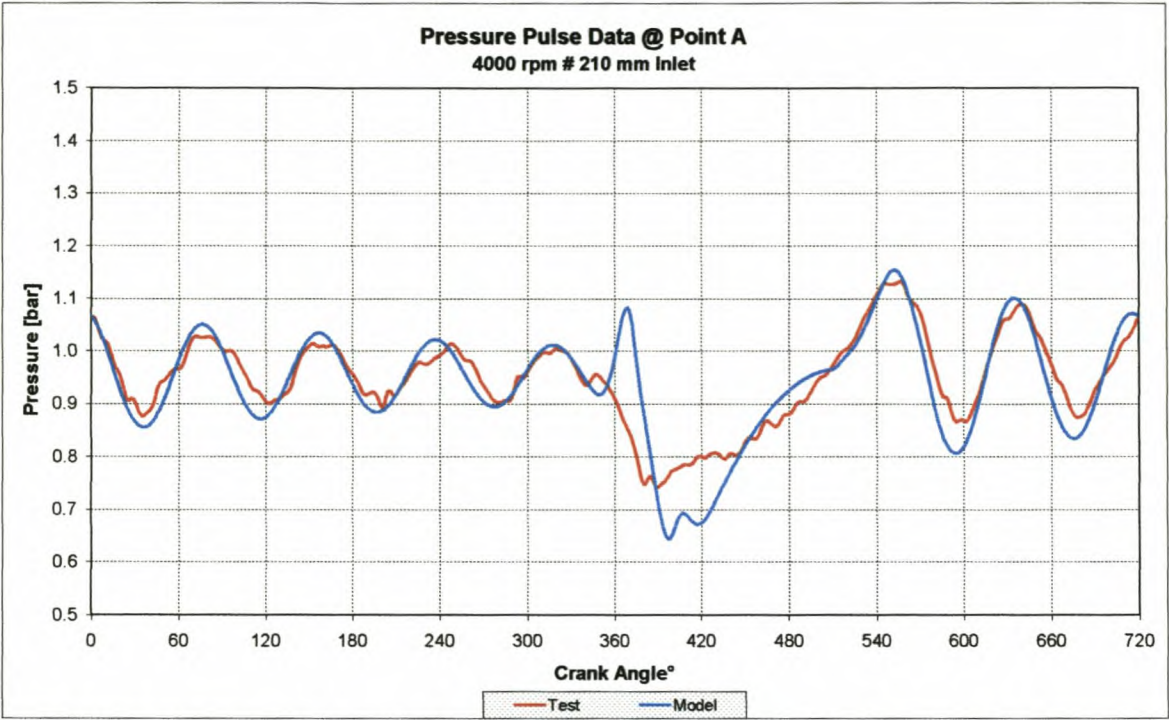


Figure I-53: Measured and modelled pressure pulse data at point A @ 4000rpm

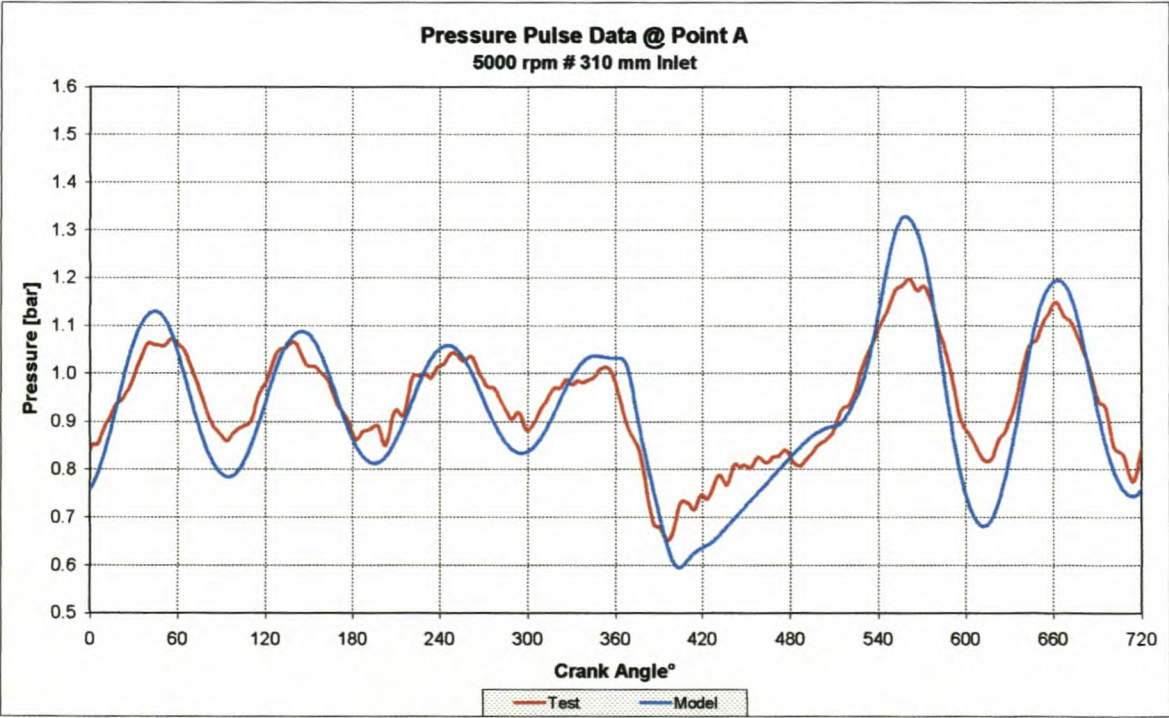


Figure I-54: Measured and modelled pressure pulse data at point A @ 5000rpm

I-7: Test 7 engine performance and pressure data, tested vs. modelled



Figure I-55: Test 7 performance on a 210mm inlet manifold with the camshaft advanced by 12° crank angle, tested vs. modelled

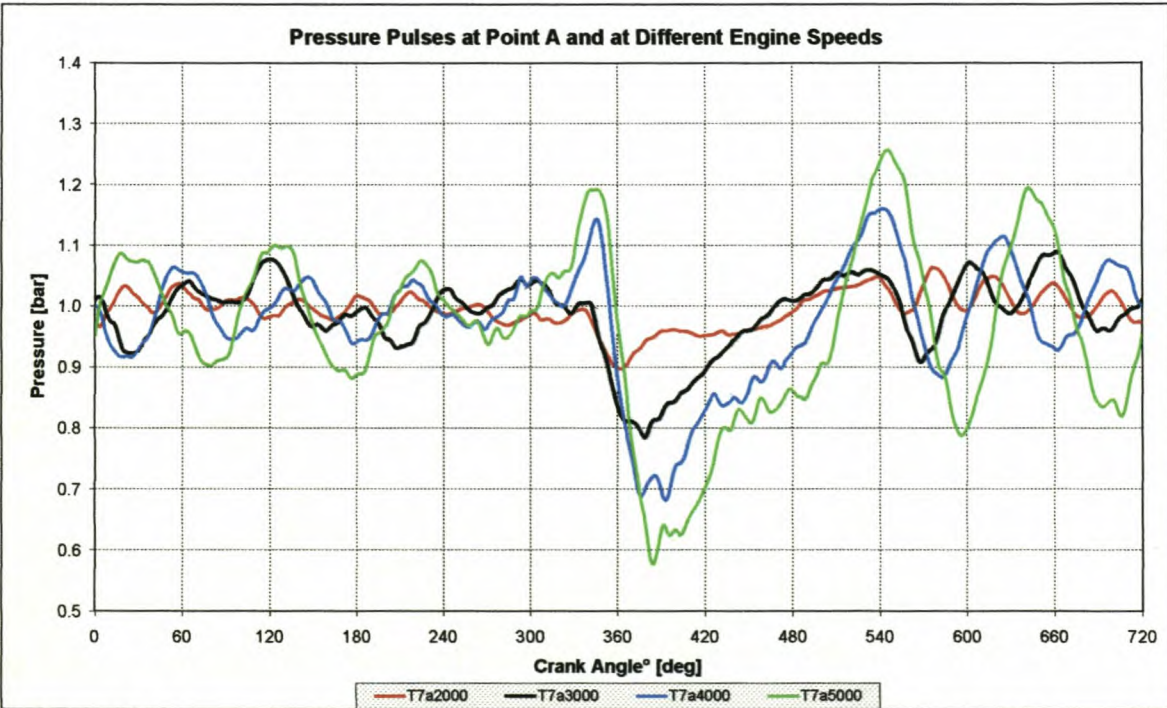


Figure I-56: Pressure pulse data measured at point A at different engine speeds

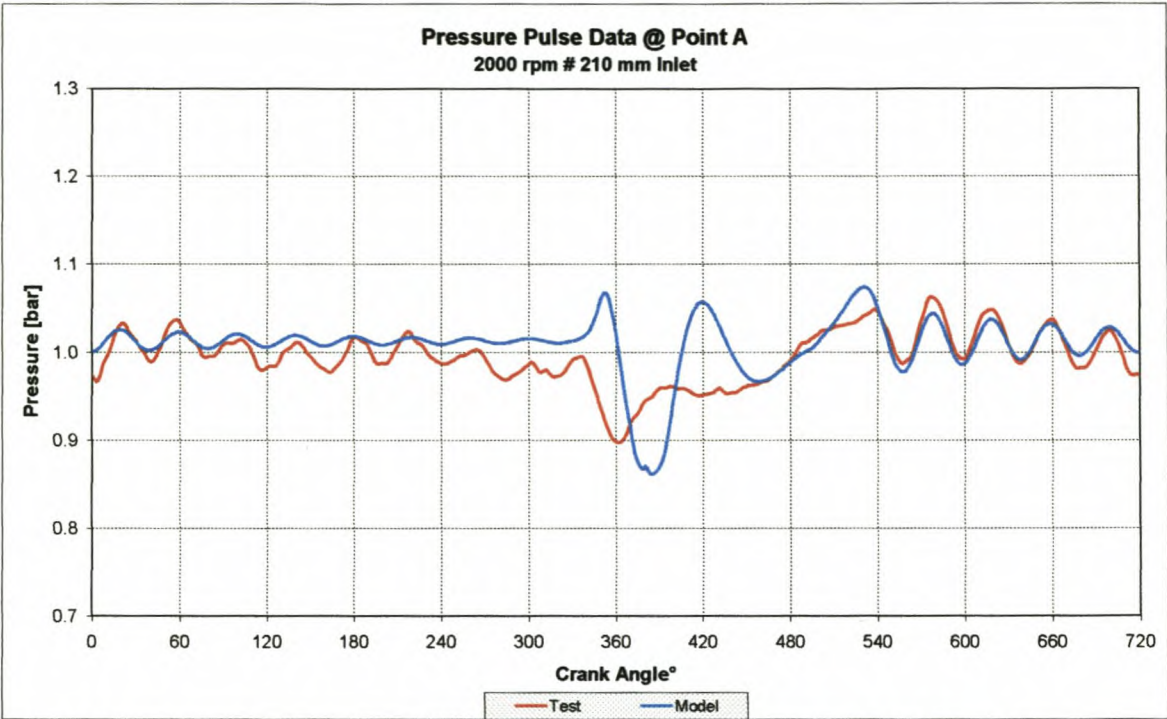


Figure I-57: Measured and modelled pressure pulse data at point A @ 2000rpm

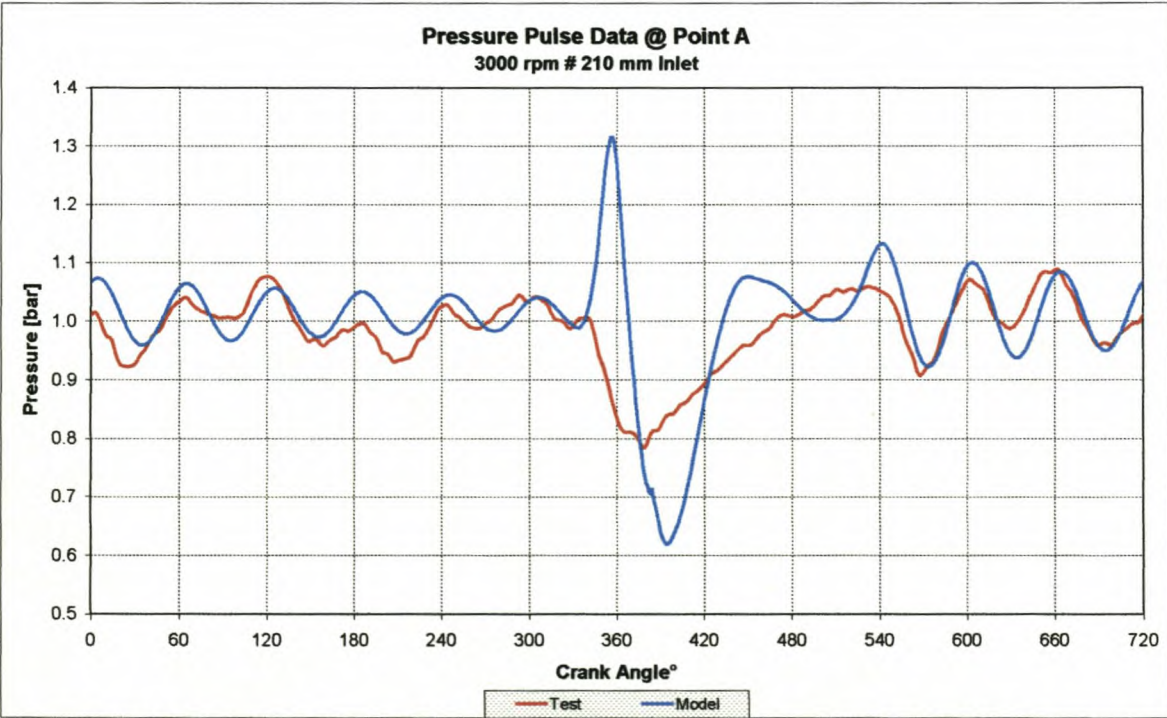


Figure I-58: Measured and modelled pressure pulse data at point A @ 3000rpm

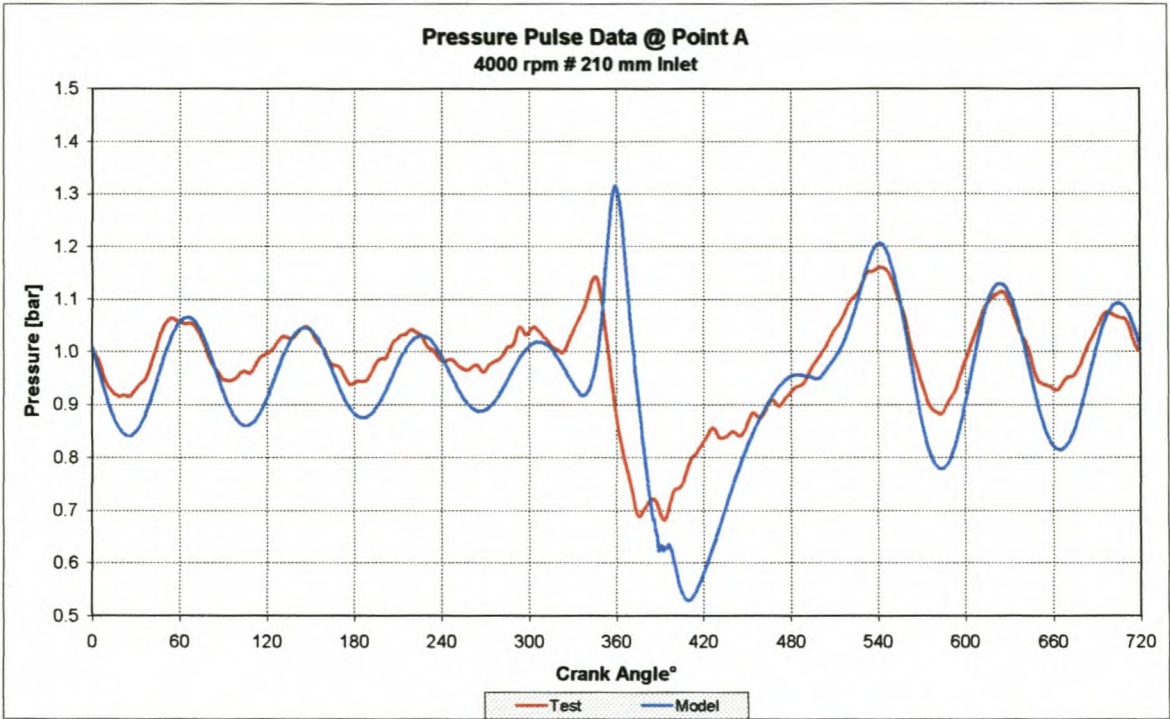


Figure I-59: Measured and modelled pressure pulse data at point A @ 4000rpm

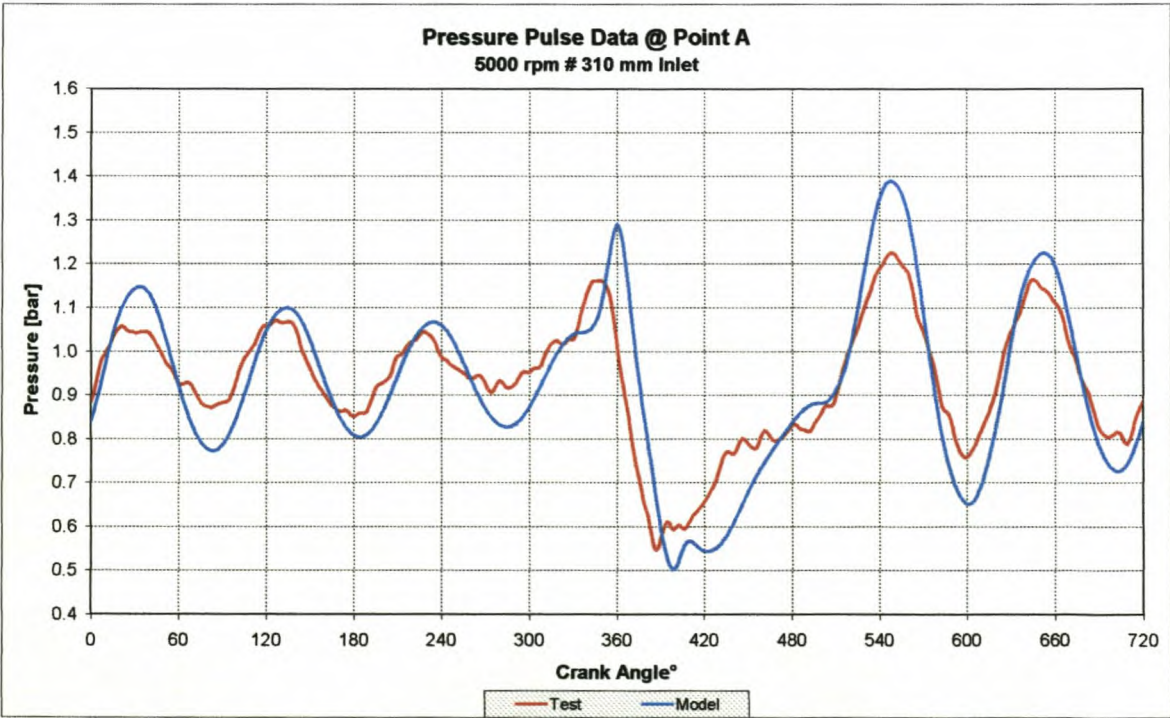


Figure I-60: Measured and modelled pressure pulse data at point A @ 5000rpm

I-8: Inlet pressure pulse interference comparison between Tests 1 and 6

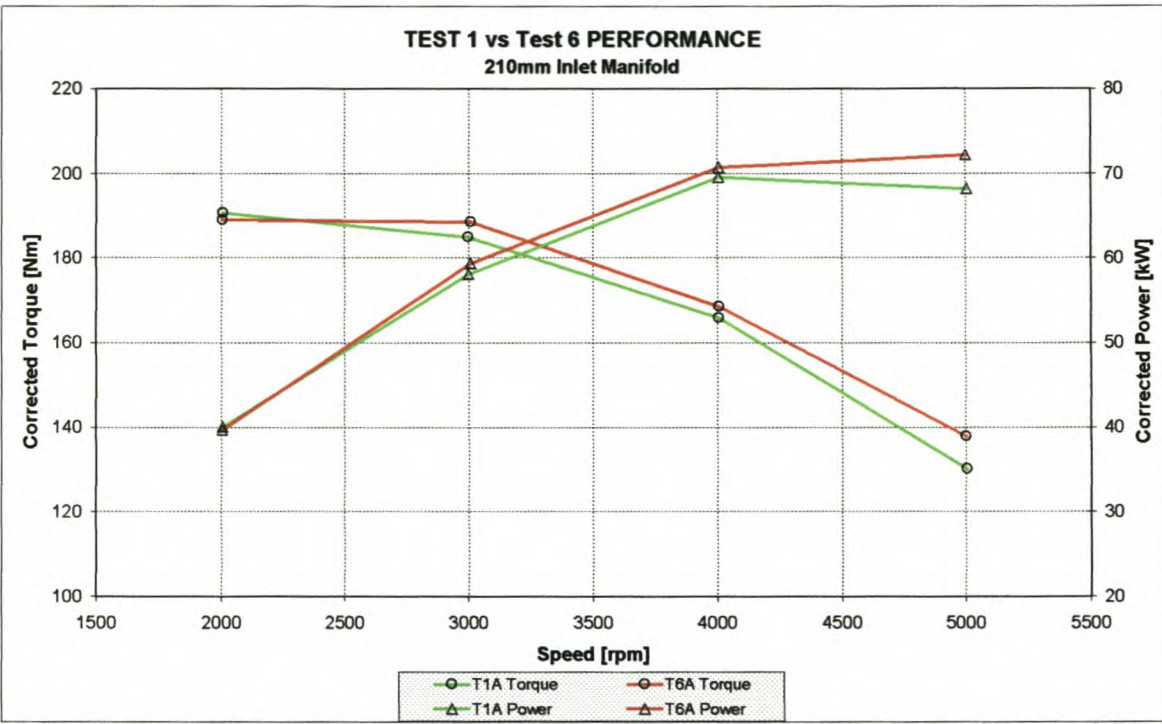


Figure I-61: Measured performance with cylinder 1 connected to the plenum in Test 1 and disconnected in Test 6

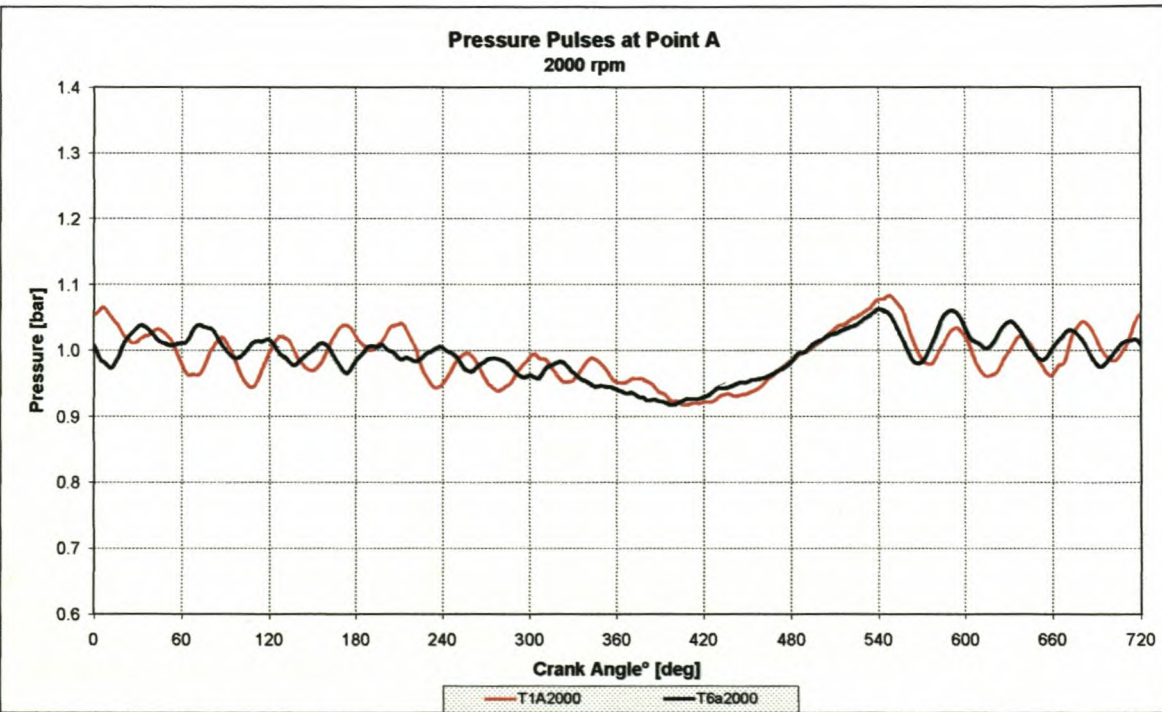


Figure I-62: Measured pressure pulse data at point A @ 2000rpm for Tests 1 and 6

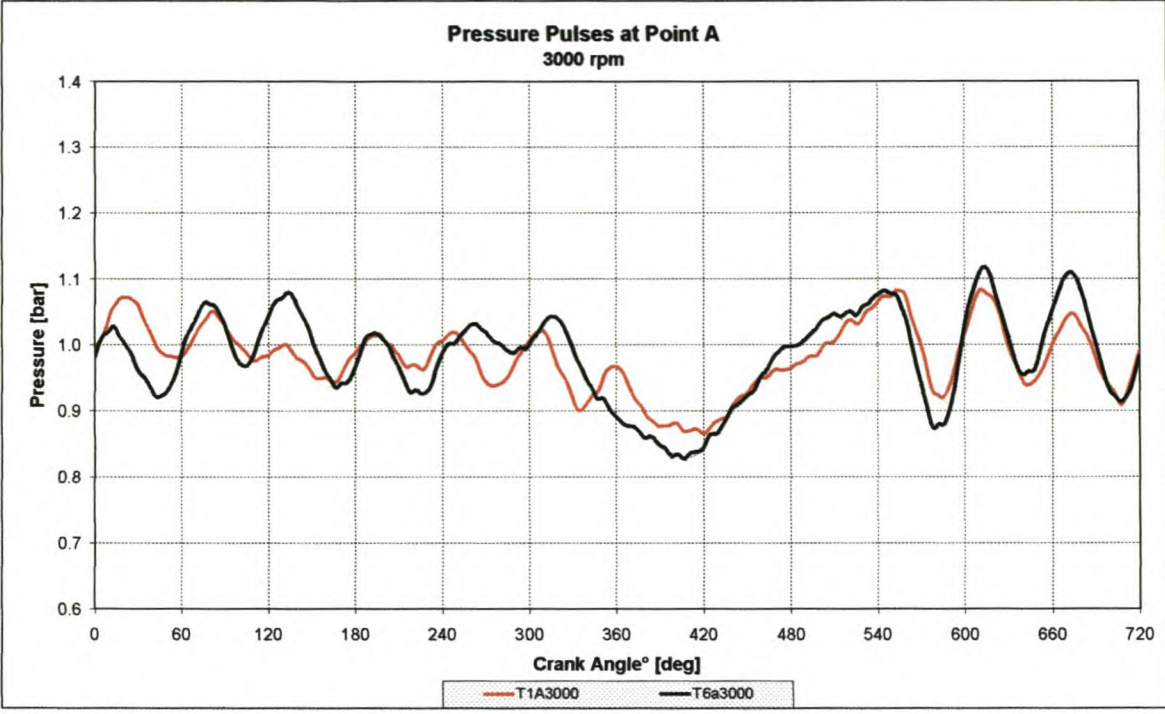


Figure I-63: Measured pressure pulse data at point A @ 3000rpm for Tests 1 and 6

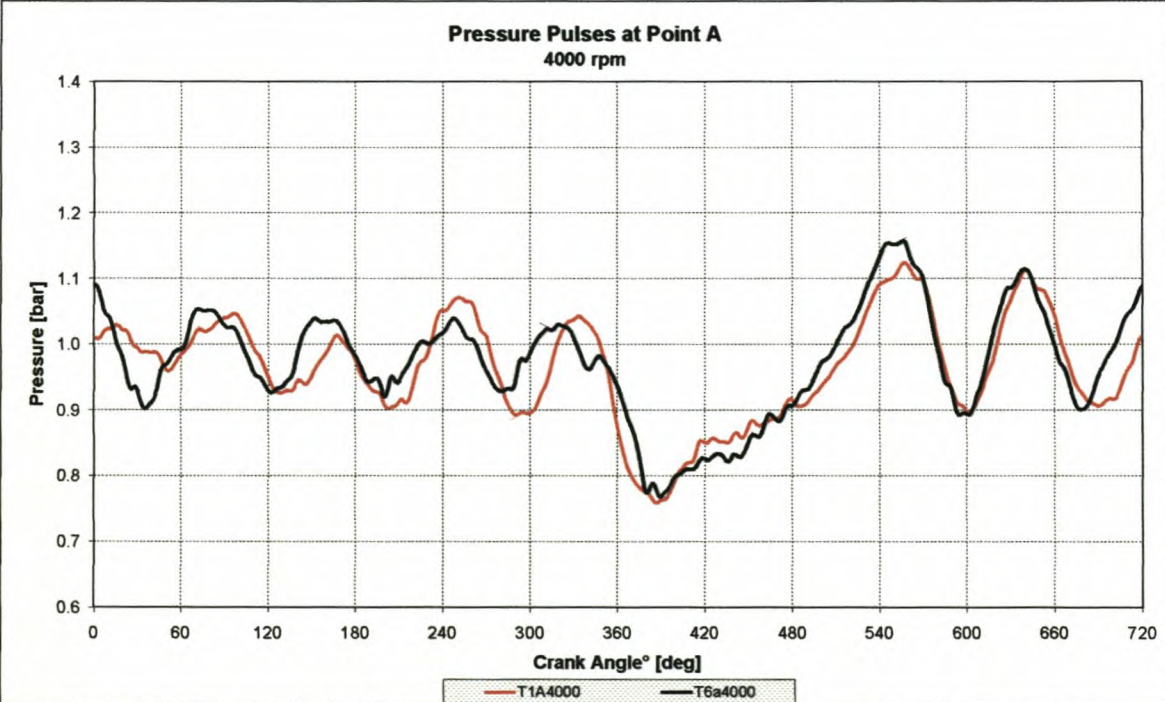


Figure I-64: Measured pressure pulse data at point A @ 4000rpm for Tests 1 and 6

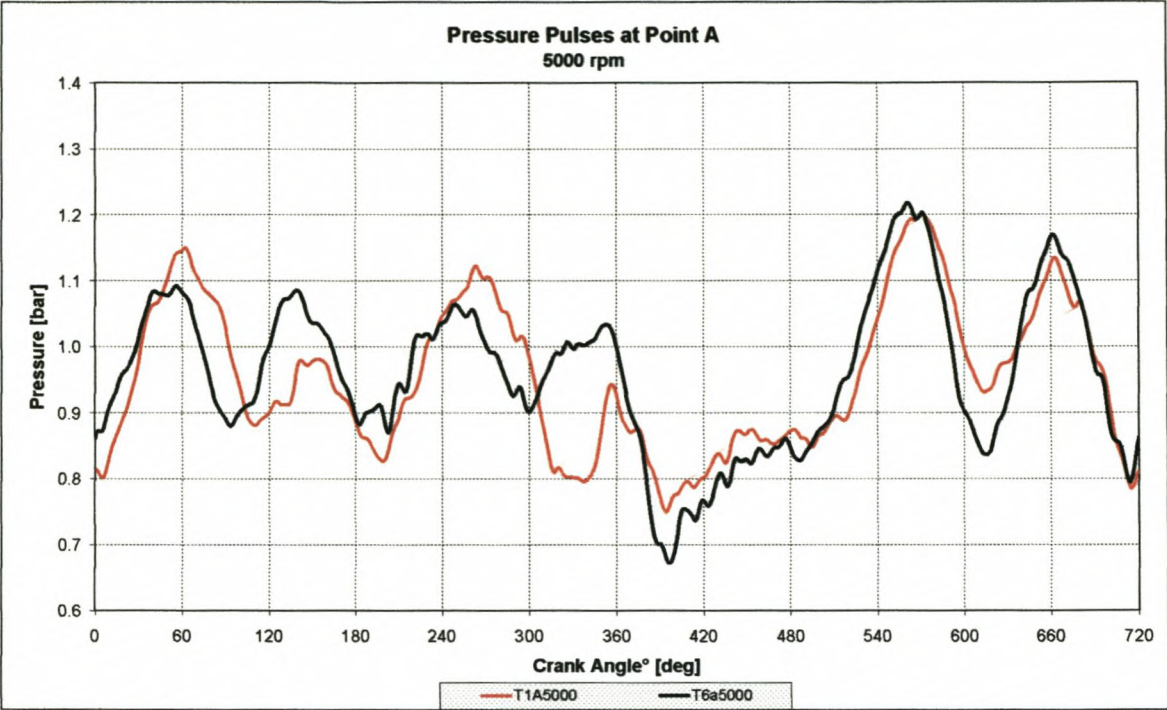


Figure I-65: Measured pressure pulse data at point A @ 5000rpm for Tests 1 and 6

I-9: Inlet pressure pulse interference comparison between Tests 2 and 5

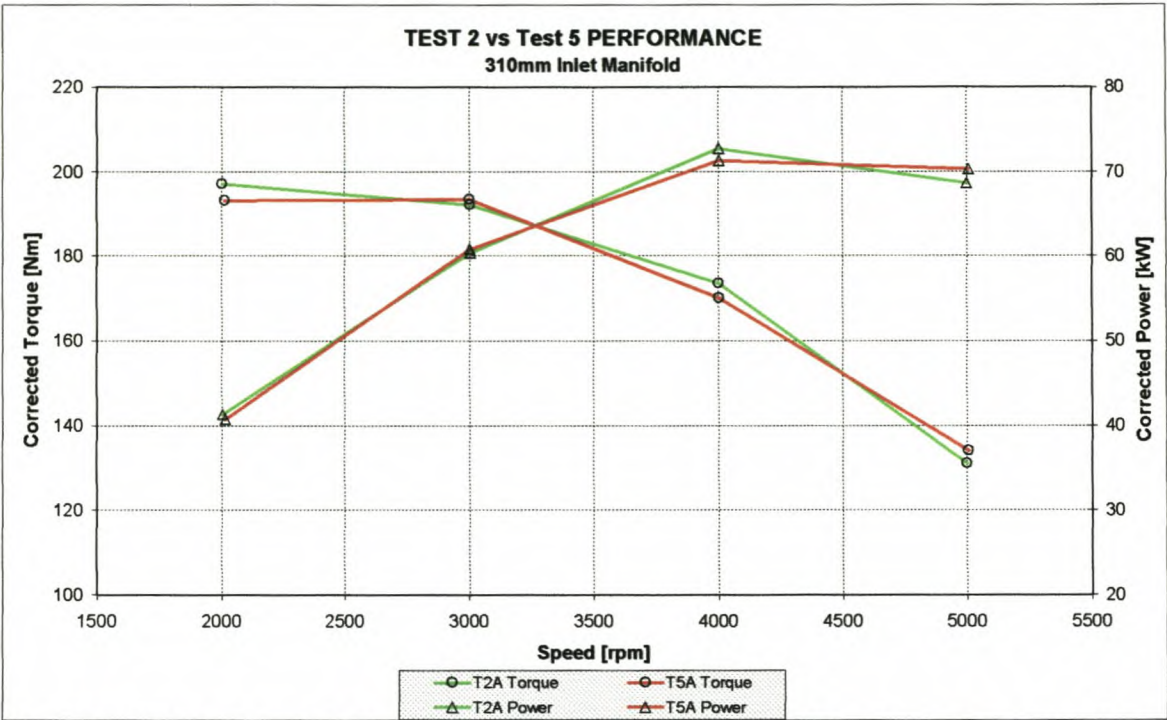


Figure I-66: Measured performance with cylinder 1 connected to the plenum in Test 2 and disconnected in Test 5

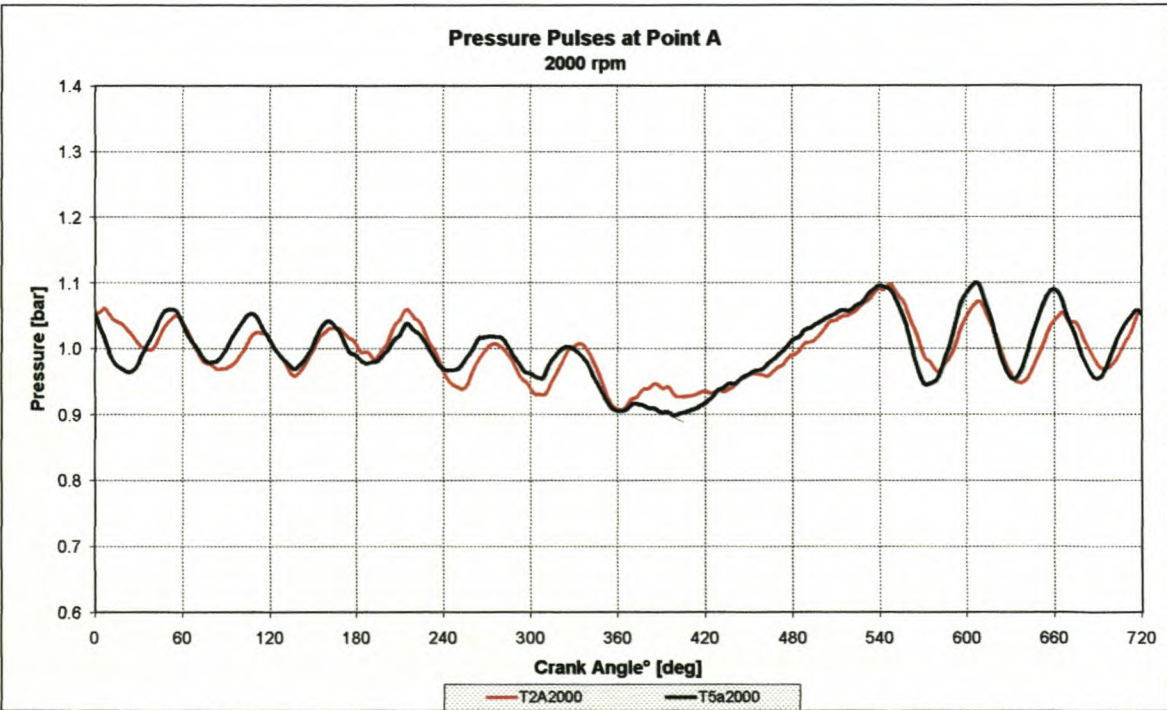


Figure I-67: Measured pressure pulse data at point A @ 2000rpm for Tests 2 and 5

Appendix I

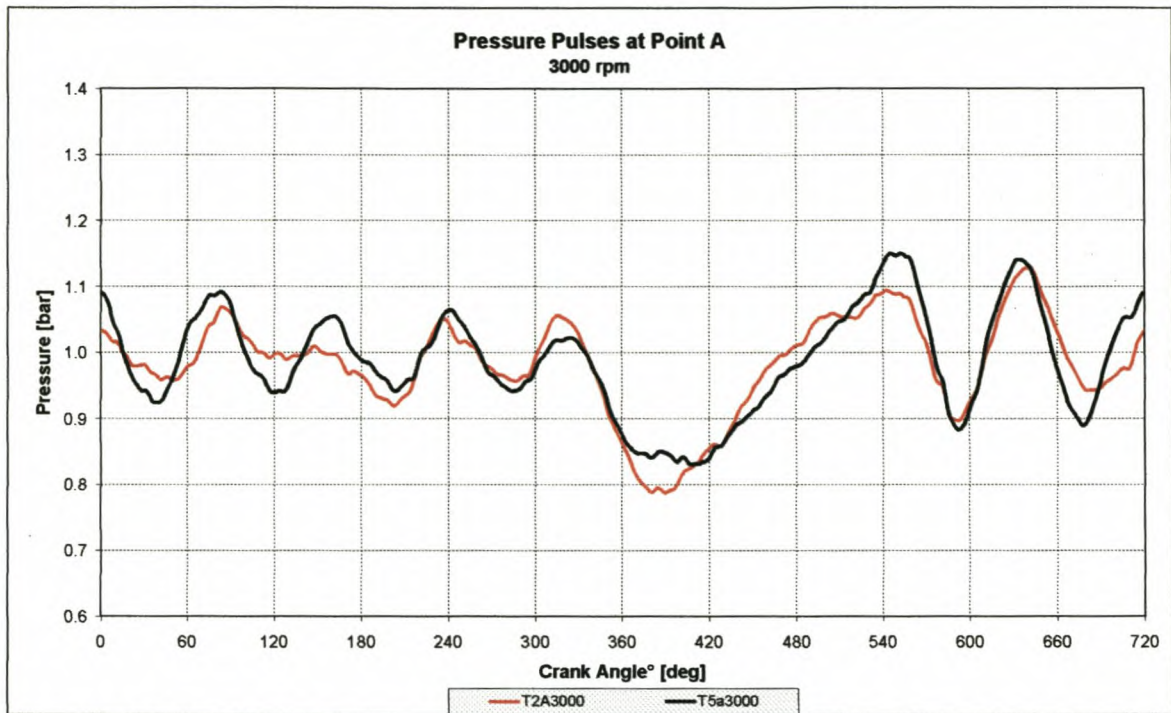


Figure I-68: Measured pressure pulse data at point A @ 3000rpm for Tests 2 and 5

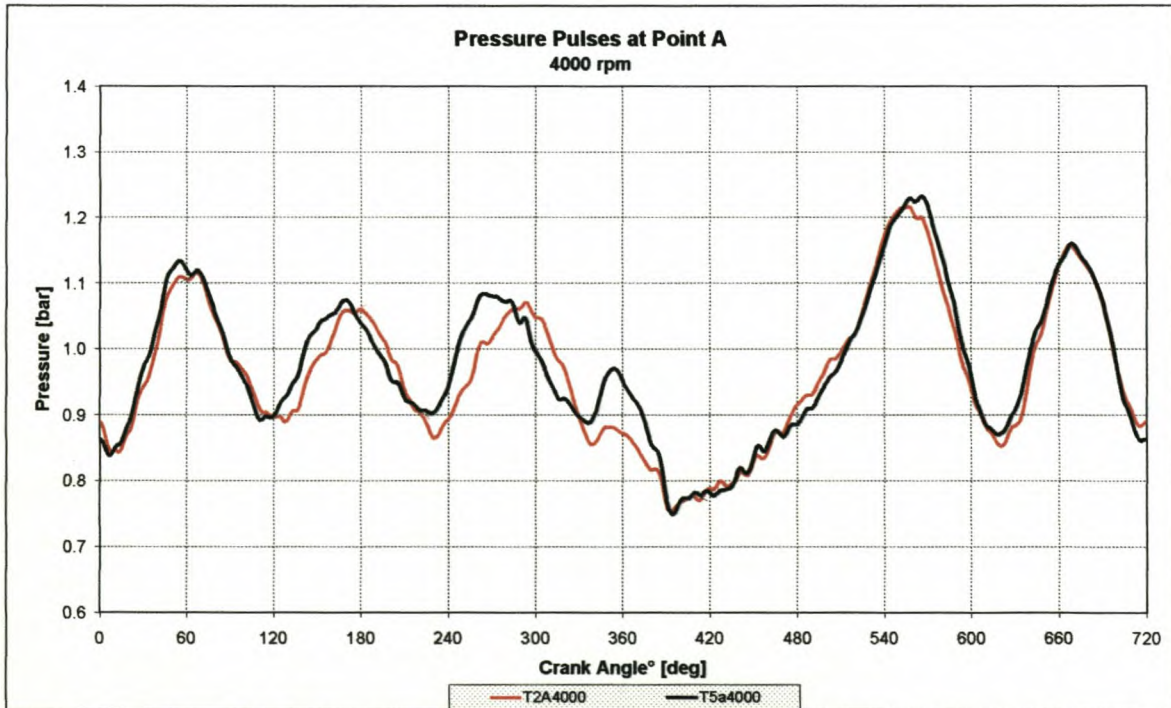


Figure I-69: Measured pressure pulse data at point A @ 4000rpm for Tests 2 and 5

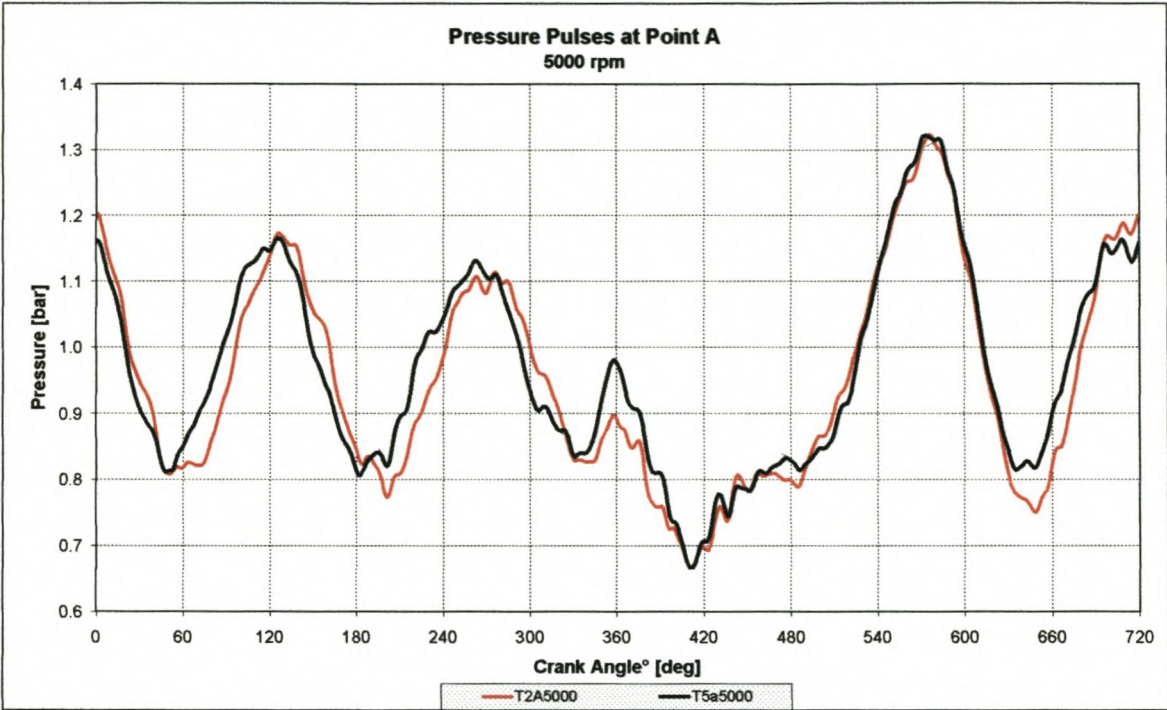


Figure I-70: Measured pressure pulse data at point A @ 5000rpm for Tests 2 and 5

I-10: Inlet pressure pulse interference comparison between Tests 3 and 4

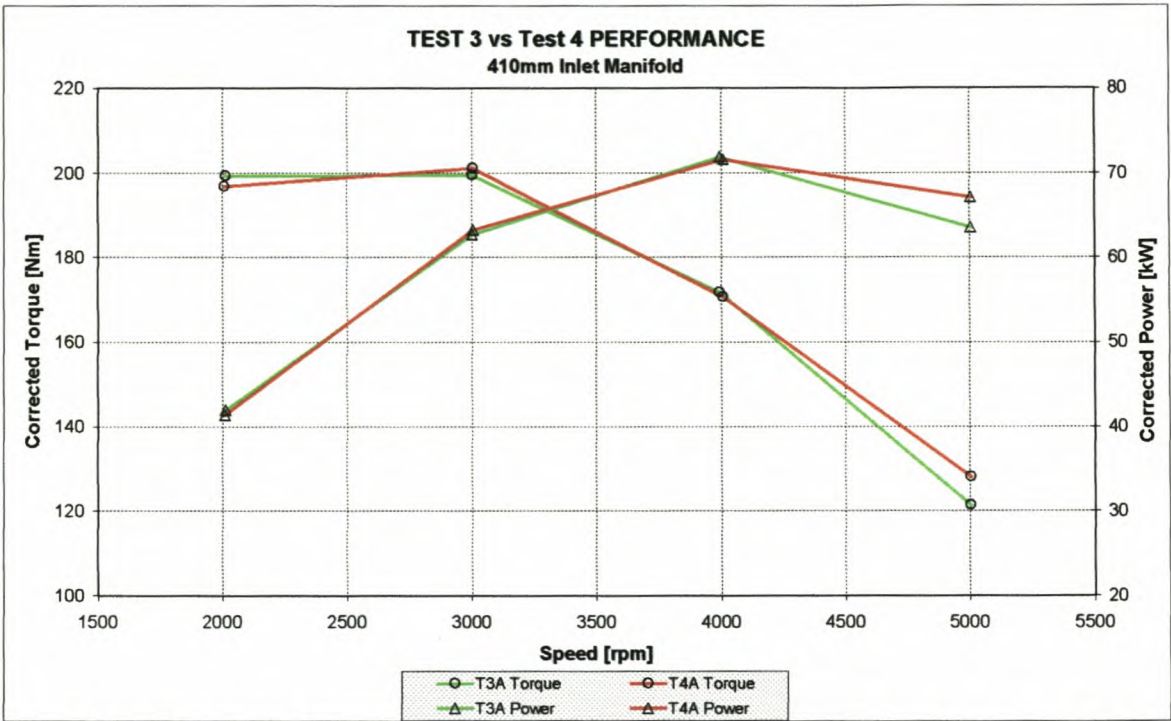


Figure I-71: Measured performance with cylinder 1 connected to the plenum in Test 3 and disconnected in Test 4

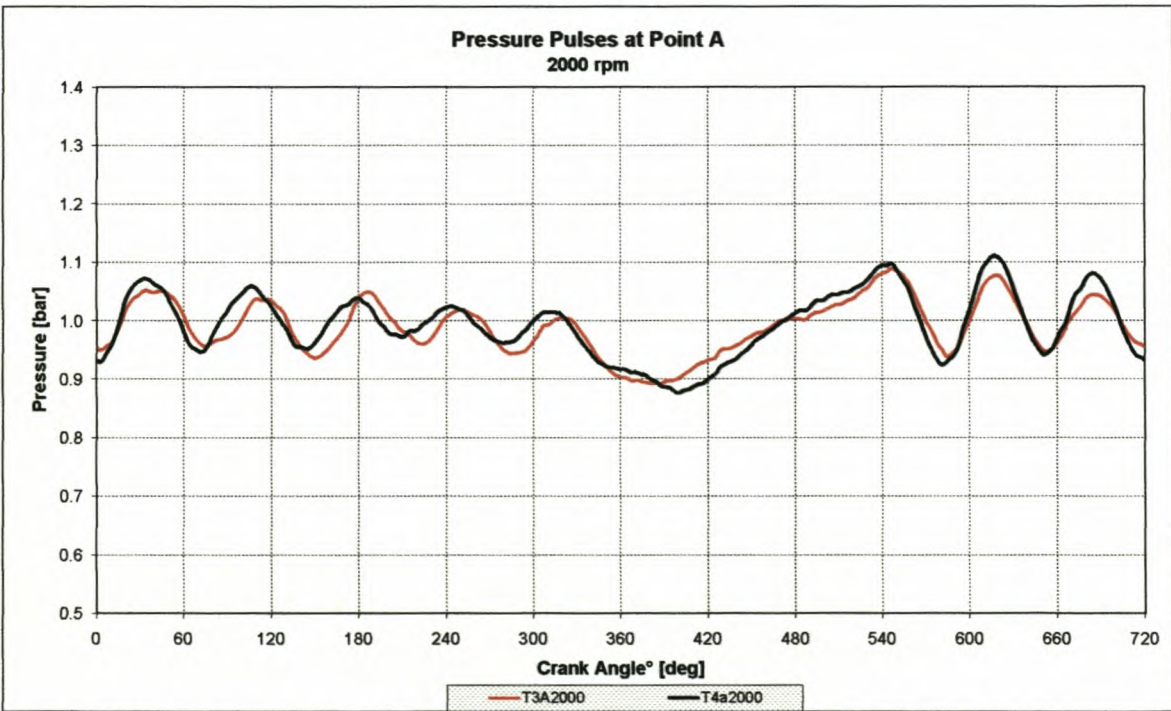


Figure I-72: Measured pressure pulse data at point A @ 2000rpm for Tests 3 and 4

Appendix I

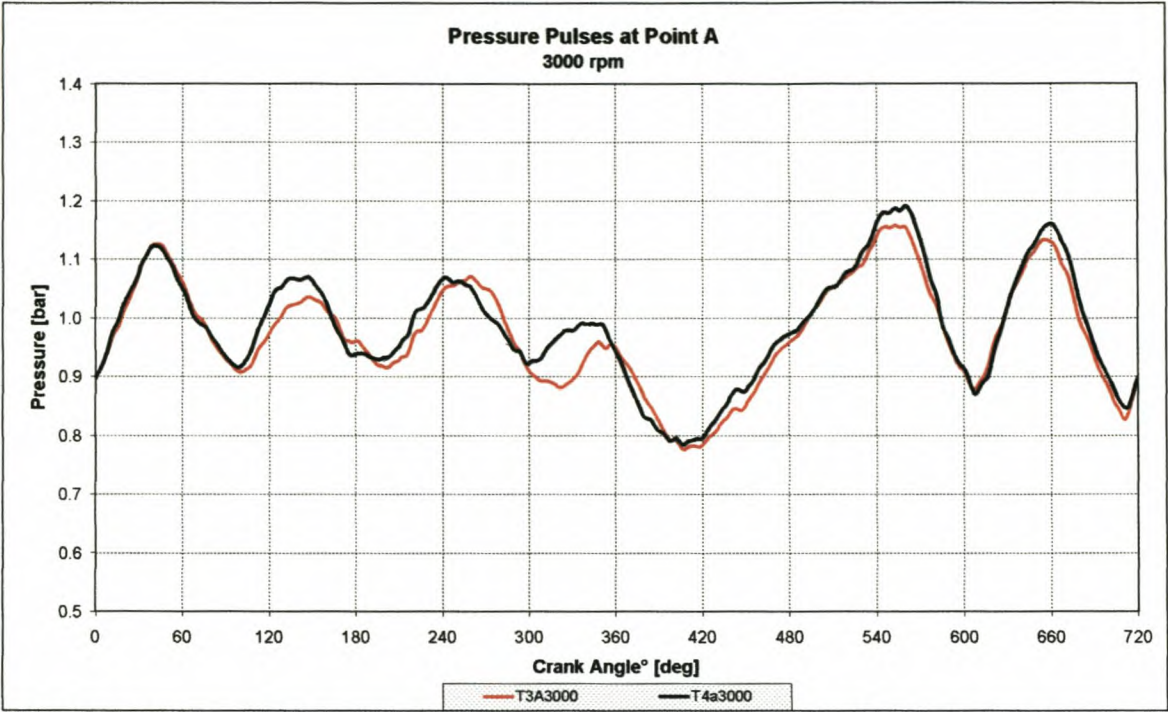


Figure I-73: Measured pressure pulse data at point A @ 3000rpm for Tests 3 and 4

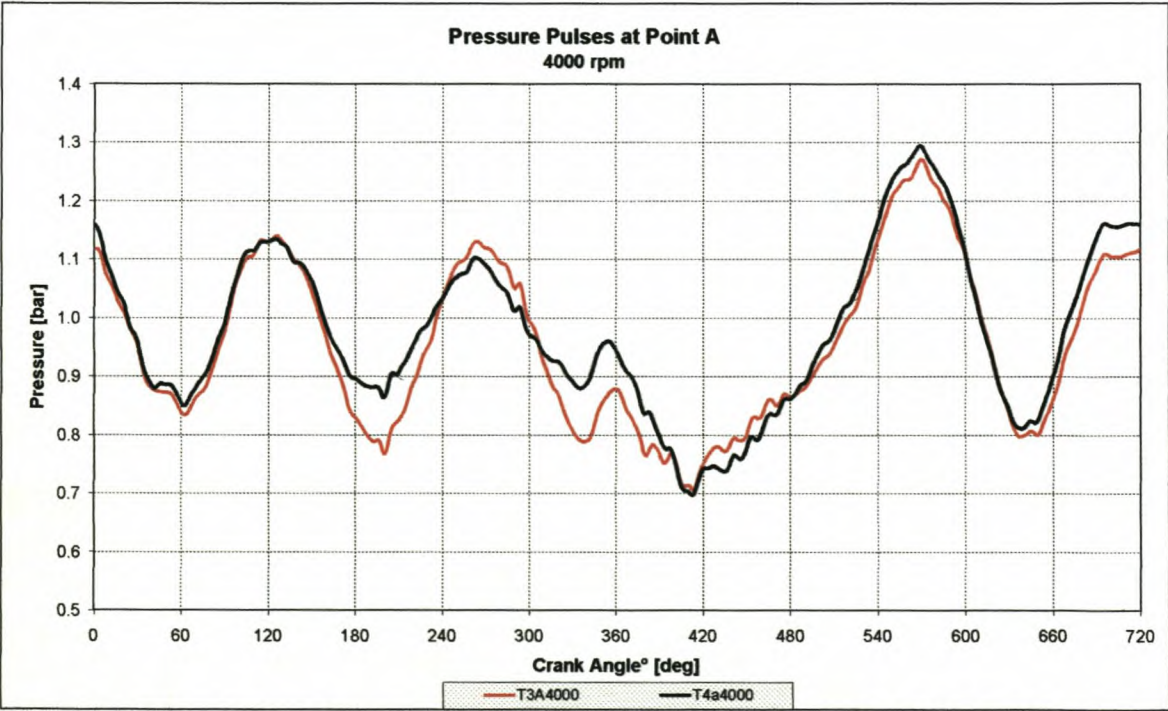


Figure I-74: Measured pressure pulse data at point A @ 4000rpm for Tests 3 and 4

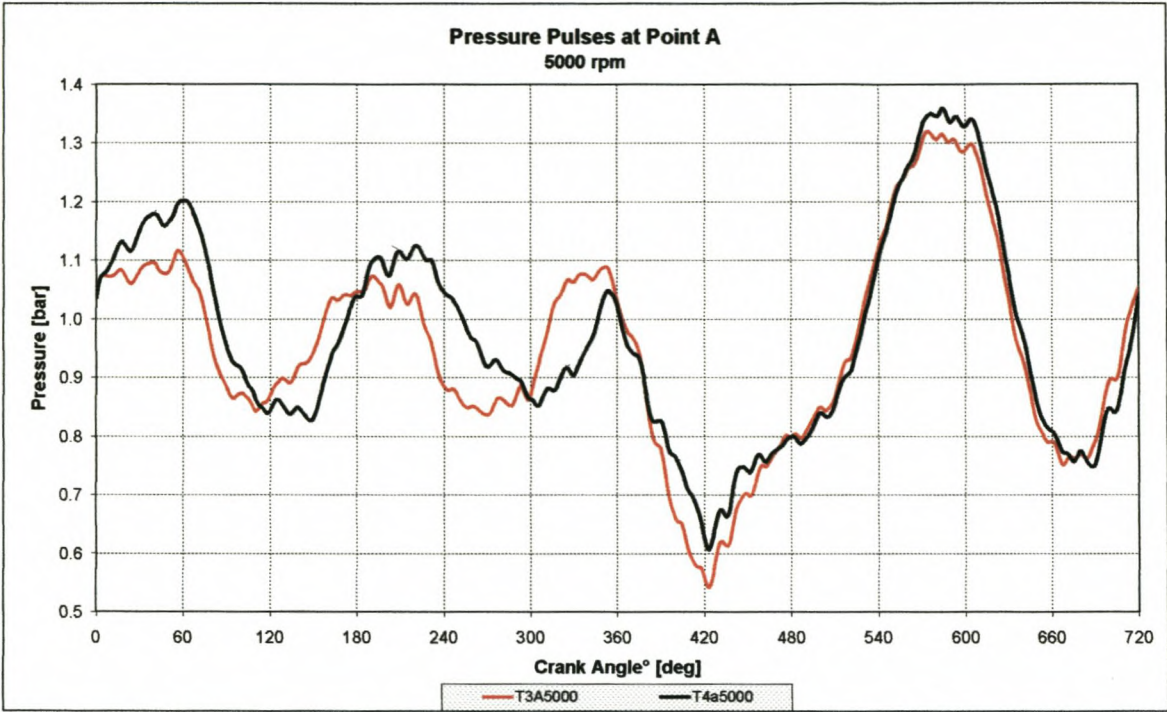


Figure I-75: Measured pressure pulse data at point A @ 5000rpm for Tests 3 and 4

Appendix J

Inlet manifold prototype pictures

Appendix J

J-1: FAW-VW China Jetta inlet manifold development



Figure J-1: Glass fibre prototype 1 installed on engine



Figure J-2: Glass fibre prototype 10 with carbon fibre finish

Appendix J

J-2: FAW-VW China Bora inlet manifold development



Figure J-3: CAD model of final inlet manifold



Figure J-4: Glass fibre prototypes 1 & 2

Appendix J

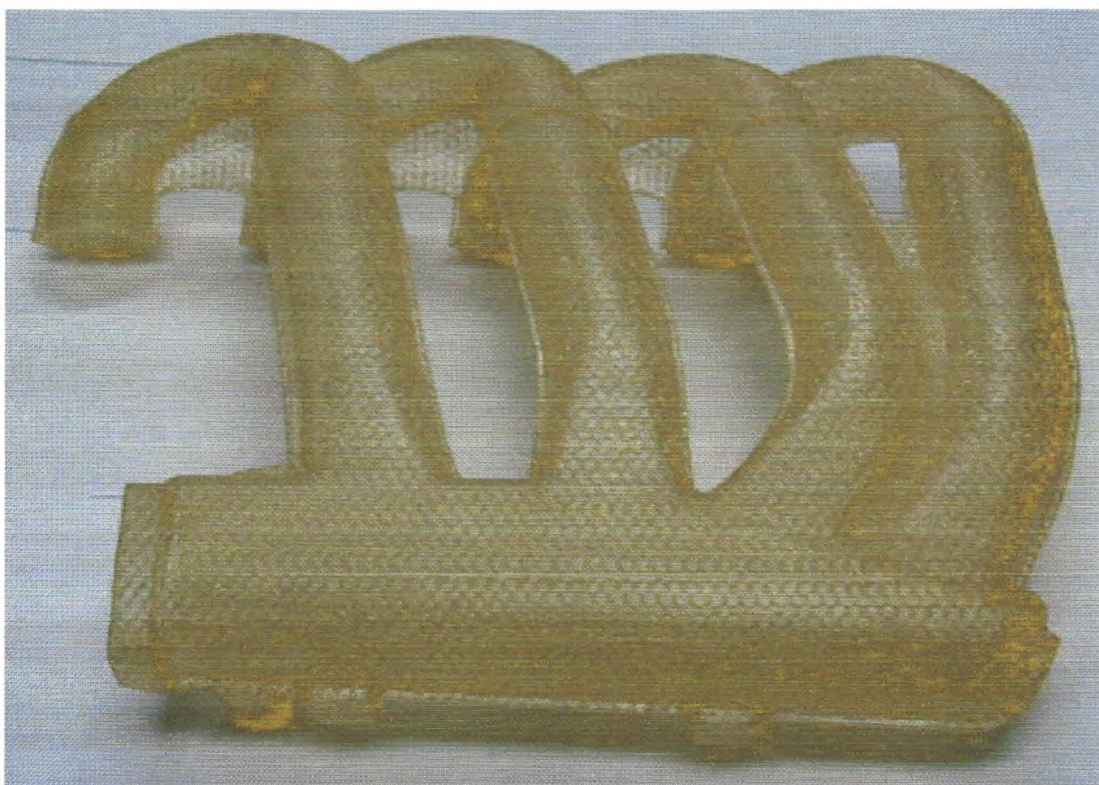


Figure J-5: Stereolithography (SLA) inlet manifold

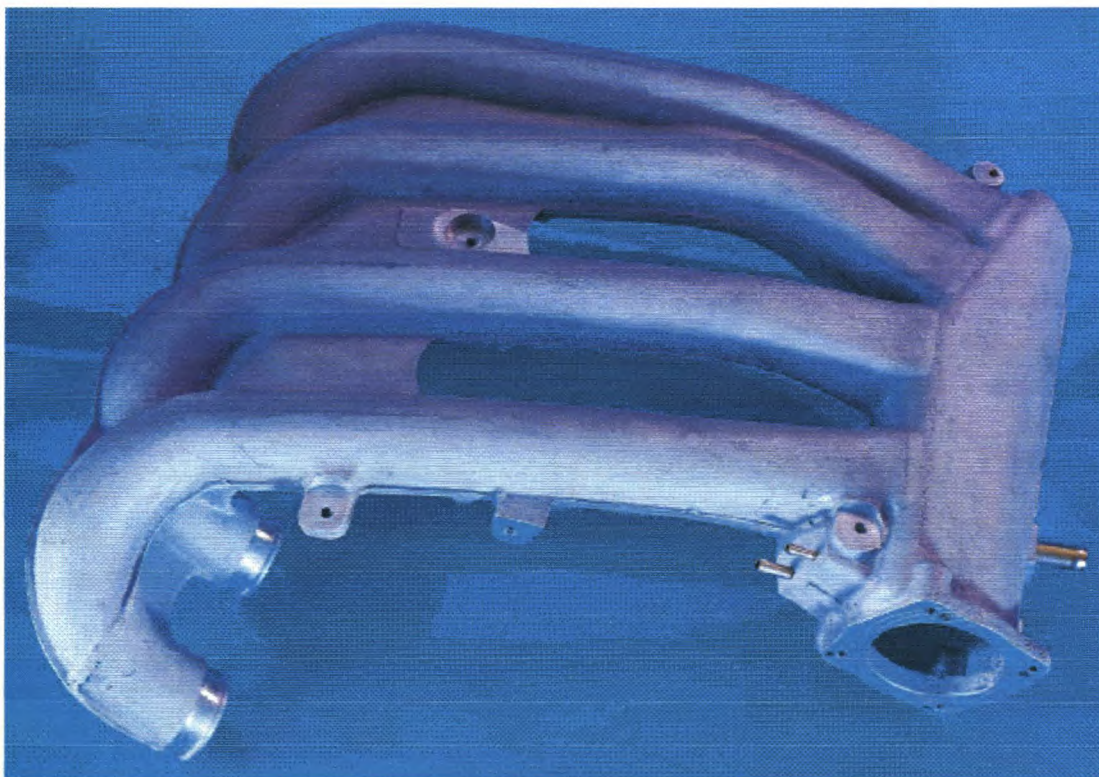


Figure J-6: Final aluminium prototype of inlet manifold

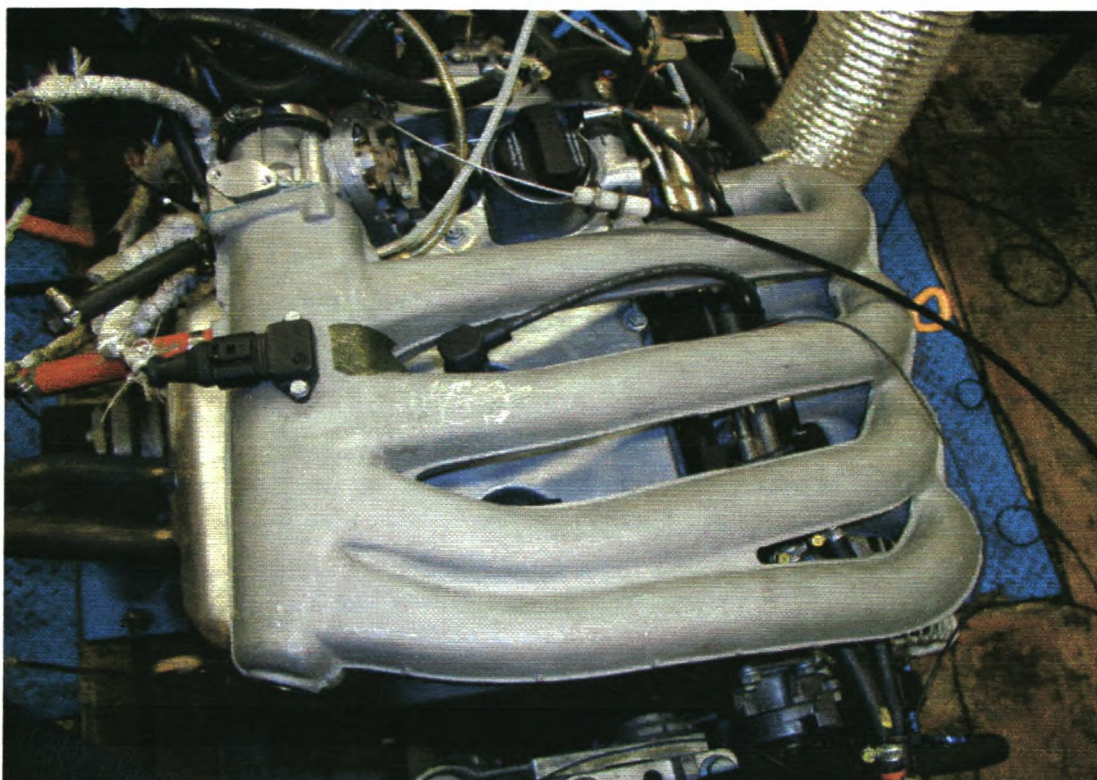


Figure J-7: Final aluminium prototype installed on engine

Appendix K

Inlet manifold pressure and velocity graphs

Appendix K

K-1: VW Bora inlet manifold pressure graphs

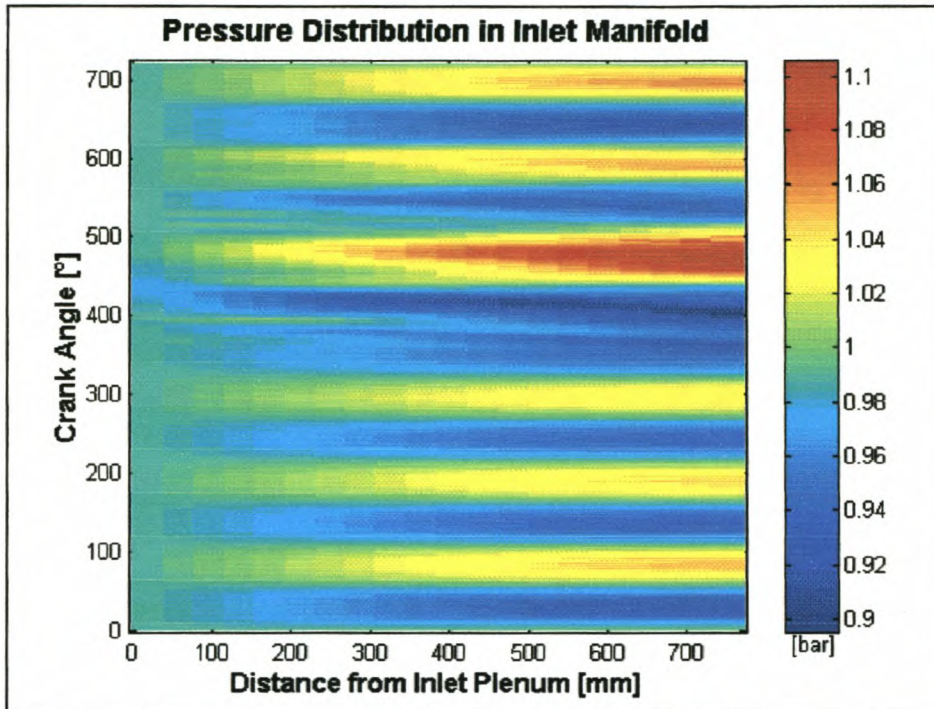


Figure K-1: Pressure distribution in inlet manifold @ 2000rpm

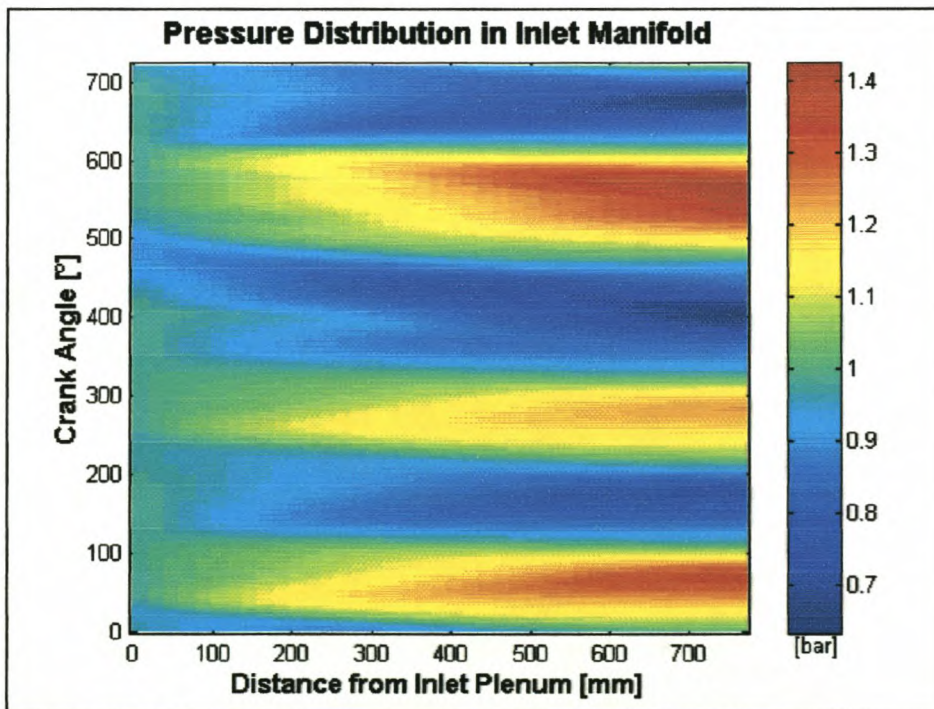


Figure K-2: Pressure distribution in Inlet manifold @ 4000rpm

Appendix K

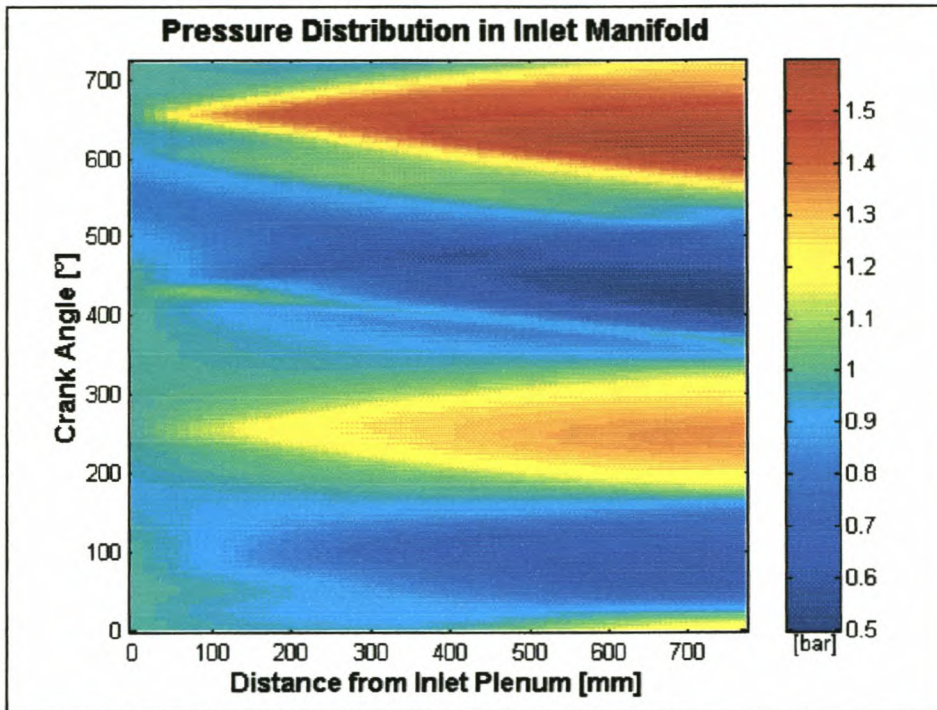


Figure K-3: Pressure distribution in inlet manifold @ 6000rpm

K-2: VW Bora inlet manifold velocity graphs

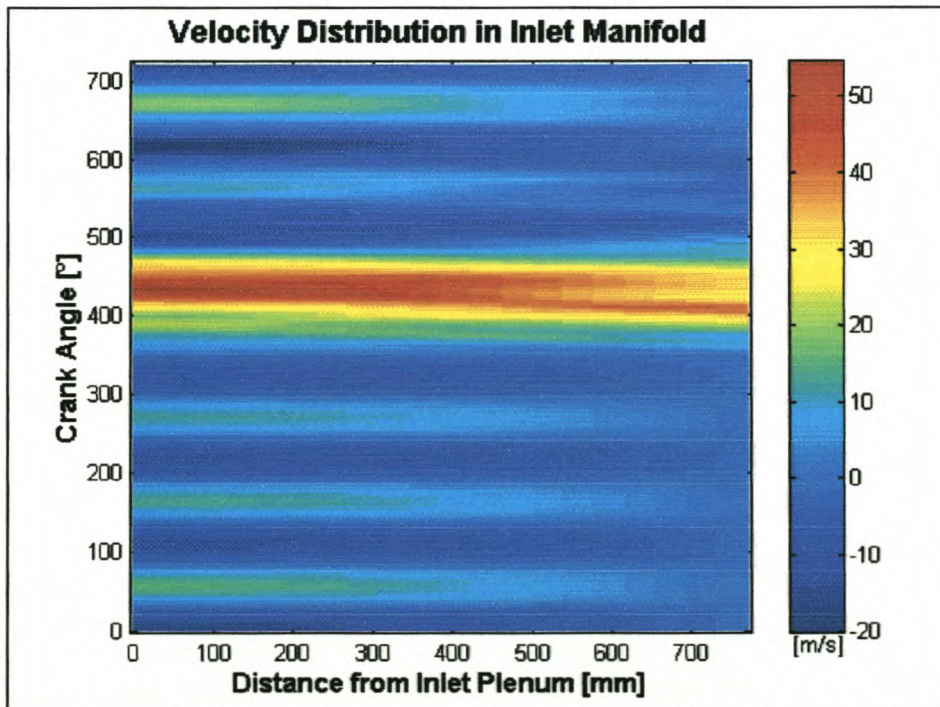


Figure K-4: Velocity distribution in inlet manifold @ 2000rpm

Appendix K

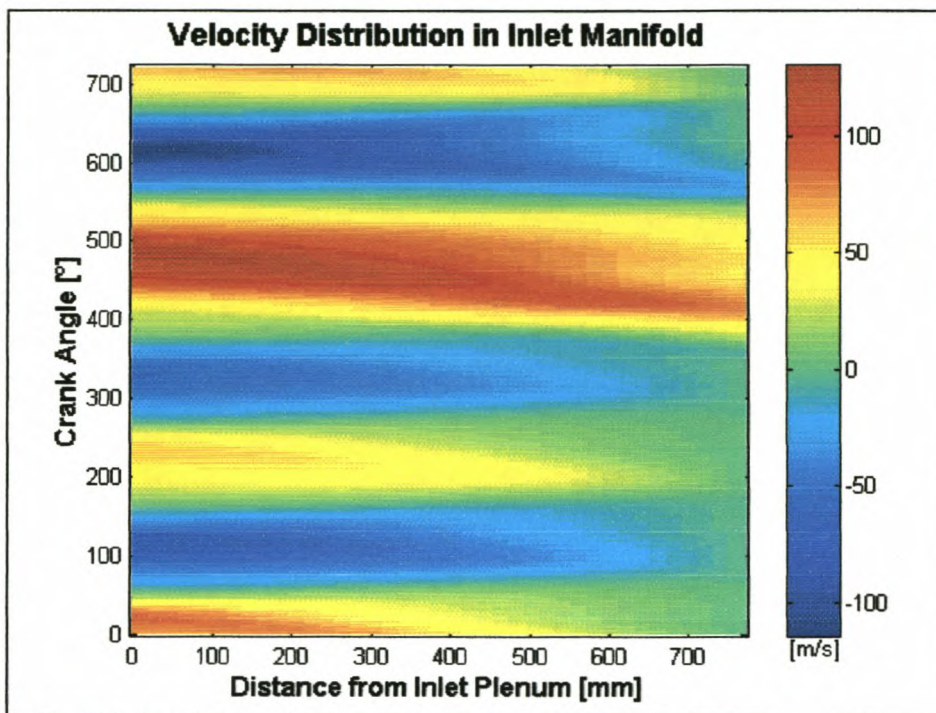


Figure K-5: Velocity distribution in inlet manifold @ 4000rpm

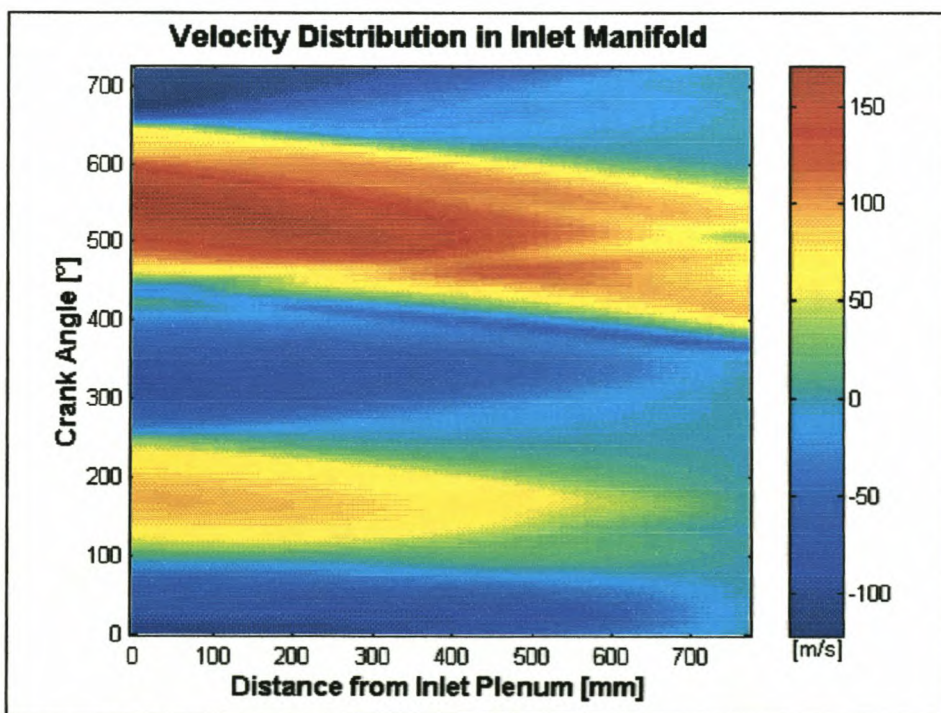


Figure K-6: Velocity distribution in inlet manifold @ 6000rpm

REFERENCES

1. Ferguson, C. R., *"Internal Combustion Engines: Applied Thermosciences"*, John Wiley & Sons, 1986
2. Heywood, J. B., *"Internal Combustion Engine Fundamentals"*, McGraw-Hill, 1988
3. Heisler, H., *"Advanced Engine Technology"*, Edward Arnold, 1995
4. BENSON, R. S., *"The Thermodynamics and Gas Dynamics of Internal-Combustion Engines: Vol. I"*, Clarendon Press (Oxford), 1982
5. Imperial College CFD software, *"STAR-CD v3.10"*, Computational Dynamics Ltd., London
6. Molvig, K., *"PowerFLOW"*, Exa Corporation, Lexington, 1991
7. Shapiro, A. H., *"The Dynamics and Thermodynamics of Compressible Fluid Flow: Vol. II"*, Ronald Press, 1954
8. Ohata, A. and Ishida, Y., *"Dynamic Inlet Pressure and Volumetric Efficiency of Four Cycle Four Cylinder Engine"*, SAE Paper No. 820407, 1982
9. Wright, E. J., *"Computer Simulation of Engine Gas Dynamic Processes: A Design Package"*, SAE Paper No. 710174, 1971
10. ZUCROW, M. J. and HOFFMAN, J. D., *"Gas Dynamics: Vol. II"*, John Wiley & Sons, Inc., 1976
11. ZUCROW, M. J. and HOFFMAN, J. D., *"Gas Dynamics: Vol. I"*, John Wiley & Sons, Inc., 1976
12. Charlton, Dr. S. J., *"SPICE II – Simulation Program for Internal Combustion Engines"*, University of Bath, 1990
13. Audie Technology Inc. and V.P. Engineering Inc., *"DYNOMATION – Four Cycle Wave Action Simulator"*, Audie Technology Inc. and V.P. Engineering Inc., 1994
14. Williams, P. N. T., *"Optimisation of Internal Combustion Engine Camshafts for Dynamics and Gas flow"*, Final Year Mechanical Project, 1995

References

15. Williams, P. N. T., *"Development of an Engine Simulation Model with special attention to Valve Dynamics and Flow"*, University of Stellenbosch, Unfinished MSc Engineering Thesis, 2000
16. Heath, W. A., *"The Effect of Valve Angles on Engine Performance"*, University of Stellenbosch, Final Year Mechanical Project, 1996
17. Rossouw, M. A., *"An Analysis of Gas Servo-Mechanism Behaviour"*, University of Stellenbosch, Master of Engineering Thesis, 1988
18. Kirkpatrick, S. J., Blair, G. P., Fleck, R. and McMullen, R. K., *"Experimental Evaluation of 1-D Computer Codes for the Simulation of Unsteady Gas Flow Through Engines – A First Phase"*, SAE Paper No. 941685, 1994
19. Low, S. C. and Baruah, P. C., *"A Generalised Computer Aided Design Package for I.C. Engine Manifold System"*, SAE Paper No. 810498, 1981
20. Gerald, C. F. and Wheatley, P. O., *"Applied Numerical Analysis"*, Addison-Wesley, 1992
21. Takizawa, M., Uno, T., Oue, T. and Yura, T., *"A Study of Gas Exchange Process Simulation of an Automotive Multi-Cylinder Internal Combustion Engine"*, SAE Paper No. 820410, 1982
22. Blair, G. P. and McConnel, J. H., *"Unsteady Gas Flow through High-Specific-Output 4-Stroke Cycle Engine"*, SAE Paper No. 740736, 1974
23. Ohata, A. and Ishida, Y., *"Dynamic Inlet Pressure and Volumetric Efficiency of Four Cycle Four Cylinder Engine"*, SAE Paper No. 820407, 1982
24. Endo, M. and Iwamoto, J., *"Extension of One-Dimensional Boundary Conditions for Junction to Those of Other Pipe Elements"*, SAE Paper No. 961821, 1996
25. Endo, M. and Iwamoto, J., *"A Numerical Study of Pulsating Flow in a Duct with a Junction"*, SAE Paper No. 911783, 1991
26. Sung, N. W. and Choi, J. S. and Jeong, Y. I., *"A Study on the Flow in the Engine Intake System"*, SAE Paper No. 952067, 1995

References

27. Pearson, R. J. and Winterbone D. E., *"A Rapid Wave Action Simulation Technique for Intake Manifold Design"*, SAE Paper No. 900676, 1990
28. Blair, G. P., Kirkpatrick, S. J., Mackey, D. O. and Fleck, R., *"Experimental Validation of 1-D Modelling Codes for a Pipe System Containing Area Discontinuities"*, SAE Paper No. 950276, 1995
29. Streit, E. E. and Borman, G. L., *"Mathematical Simulation of a Large Turbo-charged Two-Stroke Diesel Engine"*, SAE Paper No. 710176, 1971
30. Sung, N. W. and Song, J. W., *"Flow Analysis for a Chamber Type Intake Manifold Engine"*, SAE Paper No. 961824, 1996
31. Blair, G. P. and Cahoon, W. L., *"A More Complete Analysis of Unsteady Gas Flow through a High-Specific-Output Two-Cycle Engine"*, SAE Paper No. 720156, 1972
32. Winterbone, D. E. and Yoshitomi, M., *"The Accuracy of Calculating Wave Action in Engine Manifolds"*, SAE Paper No. 900677, 1990
33. Blair, G. P., *"An Alternative Method for the Prediction of Unsteady Gas Flow through the Internal Combustion Engine"*, SAE Paper No. 9911850, 1991
34. Chen, C., Veshagh, A. and Wallace, F. J., *"A Comparison Between Alternative Methods for Gas Flow and Performance Predictions of Internal Combustion Engines"*, SAE Paper No. 921734, 1992
35. Stone, C. R. and Etminan, Y., *"Review of Induction System Design and a Comparison Between Prediction and Results from a Single Cylinder Diesel Engine"*, SAE Paper No. 921727, 1992
36. Smith, P. H. and Morrison, J. C., *"The Scientific Design of Exhaust and Intake Systems"*, Robert Bentley, 1971
37. Iwamoto, J. and Deckker, B. E. L., *"Application of Random-Choice Method to Calculation of Unsteady Flow Pipes"*, SAE Paper No. 851561, 1985
38. Kays, W. M. and Crawford, M. E., *"Convective Heat and Mass Transfer"*, McGraw-Hill, 1993
39. Holman, J. P., *"Heat Transfer"*, McGraw-Hill, 1992

References

40. Blair, G. P., *"Design and Simulation of Four-Stroke Engines"*, SAE International, 1999
41. Olikara, C. and Borman, G. L., *"A Computer Program for Calculating Properties of Equilibrium Combustion Products with some Applications to I. C. Engines"*, SAE Paper No. 750468, 1975
42. Bell, A. J., *"The Effect of Fuel Formulation on the Exhaust Emissions of Spark Ignition Engines"*, University of Stellenbosch, Unfinished MSc Engineering Thesis, 2000
43. Bell, A. J., *"RACER (Rapid Acquisition of Combustion and Engine Results)"*, University of Stellenbosch, Unfinished PhD research, 1998
44. Ricardo Software, *"WAVE (One Dimensional Gas Dynamics and Engine Simulation Code)"*, Ricardo Plc., Chicago Technical Center